Organic thermoelectric materials : A novel approach to improve performances using quantum dots

Shivani Shisodia

Thèse de Doctorat

Mention : Sciences physiques
Spécialité : Milieux denses, matériaux et composants

présentée à *l'Ecole Doctorale en Sciences Technologie et Santé (ED 585)*

de l'Université du Littoral Côte d'Opale

par

Shivani SHISODIA

pour obtenir le grade de Docteur de l'Université du Littoral Côte d'Opale

Amélioration des performances de matériaux thermoélectriques organiques : nouvelle approche basée sur l'utilisation de quantum dots

Encadrée par :

M. Abdelhak HADJ SAHRAOUI	**Professeur, Université du Littoral Côte d'Opale, France**	**Co-Encadrant**
M. Michael DEPRIESTER	**MCF-HDR, Université du Littoral Côte d'Opale, France**	**Directeur de thése**

Soutenue le 14 Octobre 2022, après avis des rapporteurs, devant le jury d'examen :

M. Yogendra K. MISHRA	**Professeur , University of Southern Denmark, Denemark**	**Rapporteur**
M. Andrés E. SOTELO MIEG	**Professeur, Universidad Zaragoza, Espagne**	**Rapporteur**
M. Andreas ZEINERT	**Professeur, Université de Picardie Jules Verne, France**	**Examinateur**
M. Stéphane PAILHES	**Chercheur-HDR, Institut Lumière Matière-CNRS, France**	**Examinateur**
M. Dharmendra P. SINGH	**MCF, Université du Littoral Côte d'Opale, France**	**Examinateur**
M. Michael DEPRIESTER	**MCF-HDR, Université du Littoral Côte d'Opale, France**	**Directeur de thése**

Doctoral Thesis

Major : Physical Sciences
Specialty: Dense Media, Materials and Components

Presented at the Doctoral School ***Sciences Technologie et Santé (ED 585)***

From the Université du Littoral Côte d'Opale

by

Shivani SHISODIA

To obtain the degree of **Doctor of Philosophy in Physics**

Organic thermoelectric materials: A novel approach to improve performances using quantum dots

Supervised by:

M. Abdelhak HADJ SAHRAOUI	**Professor, Université du Littoral Côte d'Opale, France**	**Co-Encadrant**
M. Michael DEPRIESTER	**MCF-HDR, Université du Littoral Côte d'Opale, France**	**Thesis Director**

Defended on 14 October 2022, after reviewers evaluation, in front of the examination jury:

M. Yogendra K. MISHRA	**Professor, University of Southern Denmark, Denmark**	**Referee**
M. Andrés E. SOTELO MIEG	**Professor, Universidad Zaragoza, Spain**	**Referee**
M. Andreas ZEINERT	**Professor, Université de Picardie Jules Verne, France**	**Examiner**
M. Stéphane PAILHES	**Researcher-HDR, Institut Lumière Matière-CNRS, France**	**Examiner**
M. Dharmendra P. SINGH	**MCF, Université du Littoral Côte d'Opale, France**	**Examiner**
M. Michael DEPRIESTER	**MCF-HDR, Université du Littoral Côte d'Opale, France**	**Superviser**

Abstract

The growing need for energy and the scarcity of fossil fuels drive us to seek out alternative energy sources. Additionally, a substantial portion of the energy spent is lost as heat. Thermoelectric (TE) materials have attracted considerable interest in a variety of applications, including cooling, power generation, sensors, aviation, etc., due to their capacity to convert waste heat into electrical energy and vice versa [1–5]. The efficiency of thermoelectric materials is determined using the dimensionless TE *figure of merit* parameter $\mathrm{ZT} = \mathrm{S}^2\sigma\mathrm{T}/\kappa$, where S, σ , T, and κ denote the Seebeck coefficient, electrical conductivity, absolute temperature, and thermal conductivity, respectively. The term $S^2\sigma$, often known as the thermoelectric power factor (PF), is used to determine the efficiency of materials with poor thermal conductivities, such as, polymers. For convincing TE performance, high electrical conductivity and Seebeck coefficients with low thermal conductivity are required; however, in bulk materials, these parameters exhibit a trade-off relationship. Nevertheless, materials behave differently at the nanoscale due to their high surface-to-volume ratio, which allows for these interrelationships to be broken [6].

In the current thesis, efforts have been made to increase TE efficiency by simultaneously increasing electrical conductivity and the Seebeck coefficient while decreasing the phonon contribution to thermal conductivity. We chose a conduct-

ing polymer matrix filled with heterogeneous nanostructures for this purpose. The polymer poly (3,4-ethylene dioxythiophene): polystyrene sulfonate (PEDOT: PSS) has been chosen as a polymer matrix because of its outstanding electrical conductivity. The titanium di-oxide quantum dots decorated graphene oxide (TQDGO) was chosen as the filler due to its high surface to volume ratio and its ability to serve as energy filtering and phonon scattering sites. The literature on quantum dot embedded polymers for thermoelectric (TE) applications is, however, extremely limited. Therefore, the TE properties of TQDGO/PEDOT: PSS nanocomposite have been investigated in the thesis. In addition, their performances in thin films were compared with those of bulk pellets and it was found that the thin films undergo better TE performance than their bulk counterparts. The current thesis presents a two-step facile approach for the synthesis of polymer nanocomposites as a cost-effective and scalable outcome for future TE applications. The resulting hybrid material can be used in a variety of applications, including power generation, cooling and refrigeration, printing, and so on. The main goals of the thesis are, in brief, as follows:

- Synthesis of non-toxic organic polymer nanocomposite for thermoelectric applications.
- Break the interdependence of thermoelectric parameters.
- Enhance the thermoelectric performance by using quantum dots.

Amélioration des performances de matériaux thermoélectriques organiques : nouvelle approche basée sur l'utilisation de quantum dots

Résumé étendu de la thèse

Contexte générale et objectifs

Le besoin croissant en énergie et la rareté des hydrocarbures nous poussent vers la recherche de sources d'énergie alternatives. Par ailleurs, une grande partie des combustibles utilisés est perdue sous forme de chaleur (chaleur fatale). Dans ce contexte, les matériaux thermoélectriques (TE) ont suscité un grand intérêt du fait de la capacité qu'ils présentent de convertir la chaleur en énergie électrique et vice versa. Ils sont utilisés dans différentes applications dans des domaines tels que le

refroidissement, le production d'électricité, les capteurs, l'aéronautique, etc [1–5].

Le rendement de conversion des matériaux thermoélectriques est évalué à travers le paramètre, sans dimension, appelé *figure de mérite* $\mathrm{ZT} = \mathrm{S}^2\sigma\mathrm{T}/\kappa$, où S, σ , T, and κ sont respectivement le coefficient Seebeck, la conductivité électrique, la température absolue et la conductivité thermique. Le terme $S^2\sigma$, connu sous le nom de facteur de puissance (FP), est utilisé pour rendre compte du rendement de matériaux avec une faible conductivité thermique tels que les polymères. L'amélioration des performances TE nécessite donc une conductivité électrique et un coefficient Seebeck élevés et une faible conductivité thermique. Cependant, dans le cas de matériaux massifs, ces paramètres sont interdépendants : l'optimisation de l'un des paramètres induit une évolution défavorable de l'un ou des deux autres paramètres (fig.1) . En revanche, cette optimisation reste possible dans le cas de matériaux nanostructurés. Ces matériaux ont un comportement différent à l'échelle nanoscopique, dû a leur grand rapport surface/volume, qui permet de briser cette interdépendance [6].

L'objectif que nous nous sommes fixé dans le cadre de cette thèse, pour améliorer l'efficacité TE, est d'augmenter la conductivité électrique et le coefficient Seebeck tout en diminuant simultanément la conductivité thermique à travers sa composante phononique dans un matériau nanocomposite nanostructuré. Nous avons orienté notre travail vers un système hybride organique-inorganique où l'on combine des polymères à bas coût avec des inclusions inorganiques présentant des propriétés de transport avantageuses. Le nanocomposite que nous avons choisi et élaboré est une matrice polymère contenant des inclusions hétérogènes nanostructurées. Le mélange de polymères poly (3,4-ethylene dioxythiophene): polystyrène sulfonate (PEDOT: PSS) a été choisi comme matrice au vu de sa remarquable conductivité électrique. Le choix de quantum dots de TiO_2 déposés sur des nanofeuillets d'oxyde de graphène (QTDOG) comme inclusions est lié au grand rapport

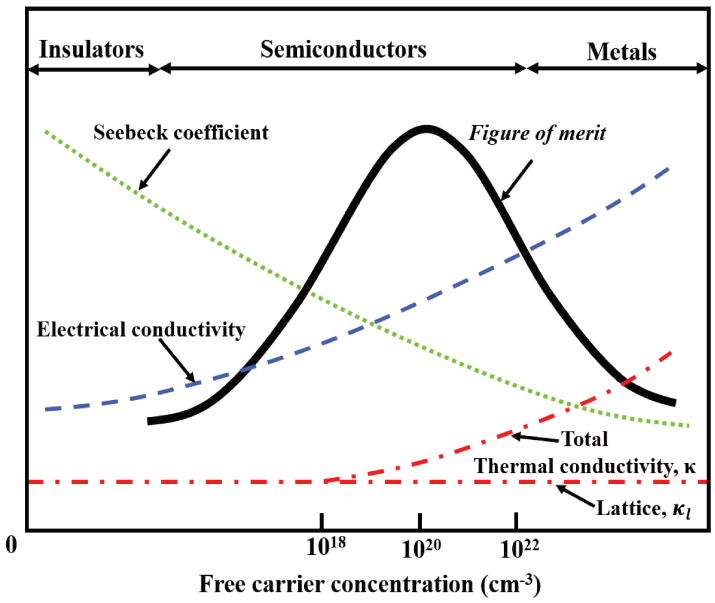

Figure 1: Interdépendance des paramètres thermoélectriques : conductivité électrique (σ), conductivité thermique (κ), et coefficient Seebeck S pour les isolants, semi-conducteurs, et métaux en fonction de la concentration des porteurs de charges.

surface/volume de ces inclusions et à la possibilité de les utiliser comme sites de diffusion des phonons et comme barrière sélective des niveaux d'énergie électronique. Il est à noter que les travaux sur les propriétés thermoélectriques de composites polymères/quantum dot sont assez rares.

Notre travail a concerné l'élaboration de ces nanocomposites QTDOG/PEDOT: PSS et l'étude de leurs propriétés thermoélectriques. L'ensemble des constituants de ces nanocomposites polymères ont été synthétisés dans le laboratoire. Une méthode de synthèse des échantillons, en deux étapes, rentable et évolutive est présentée. Par ailleurs, nous avons, d'une part, procédé à des analyses chimiques et structurales (DRX, MEB, EDS, FTIR, spectroscopie UV-Vis et ATG) et d'autre part mesuré les propriétés de transport de ces matériaux (conductivité électrique, thermique et coefficient Seebeck). Les rendements thermoélectriques de films minces de ces composites ont été comparés à ceux d'échantillons massifs.

Synthèse des nanocomposites

Synthèse de nanofleurs de quantum dots de TiO_2 déposés sur oxyde de graphène (QTDOG)

Les inclusions, constituées de quantum dots (QD) de TiO_2 déposés sur oxyde de graphène (OG), ont été synthétisées en utilisant un précurseur de dioxyde de titane, l'isopropylate de titane (Ti^{4+}), et l'oxyde de graphène comme matériaux initiaux pour induire le dépôt des quantum dots de TiO_2 sur les nanofeuillets d'OG par le biais de liaisons oxo et hydroxyl stables [7]. Ce processus chimique est montré dans la figure 2 : durant la réaction, l'isopropylate de titane (IV) a été utilisé comme précurseur et l'OG comme gabarit. Les ions Ti^{4+} positivement chargés sont déposés sur un des groupes fonctionnels de l'oxyde de graphène chargé négativement. Ces sites vont alors agir comme points d'activation pour initier le processus de nucléation et permettre la croissance des quantum dots de TiO_2 sur les nanofeuillets (2D) d'oxyde de graphène [8]. Les inclusions ainsi synthétisées présentent une morphologie qui rappelle celle des hortensias, on parle de nanostructures floriformes.

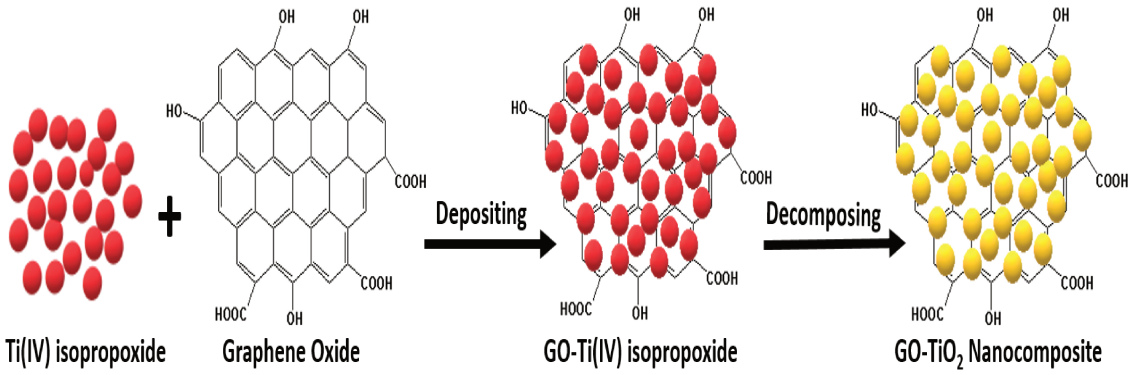

Figure 2: Diagramme schématique de la synthèse des inclusions par décomposition d'un précurseur du titane, l'isopropylate de titane (Ti^{4+}), pour former des quantum dots de TiO_2 déposés sur la surface de l'oxyde de graphène (QTDOG)

Synthèse in situ des nanocomposites QTDOG/ PEDOT: PSS

Les nanocomposites à matrice polymère QTDOG/PEDOT: PSS ont été synthétisés en utilisant la polymérisation chimique oxydative du 3,4-Ethylenedioxythiophene (EDOT) en présence de PSS et de QTDOG. Durant la polymérisation les chaînes EDOT chargées positivement sont combinées avec les chaînes PSS chargées négativement à travers des interactions coulombiennes pour former le composé intermédiaire EDOT: PSS [9] comme décrit dans la figure 3. A partir de la poudre nanocomposite ainsi synthétisée, nous avons réalisé, d'une part, des pastilles par pressage uni-axial sous une pression de 8 kPa durant une minute et d'autre part des films minces par voie sol-gel. Une partie des nanocomposites obtenus a été traitée à l'acide chlorhydrique HCl (6 mol/l), les propriétés thermoélectriques des nanocomposites traités et non traités à l'acide sont présentées et discutées . Par ailleurs, nous avons aussi utilisé du PEDOT : PSS commercial (Sigma Aldrich) comme matrice pour élaborer les nanocomposites afin de comparer leurs propriétés avec ceux élaborés avec du PEDOT : PSS synthétisé au laboratoire.

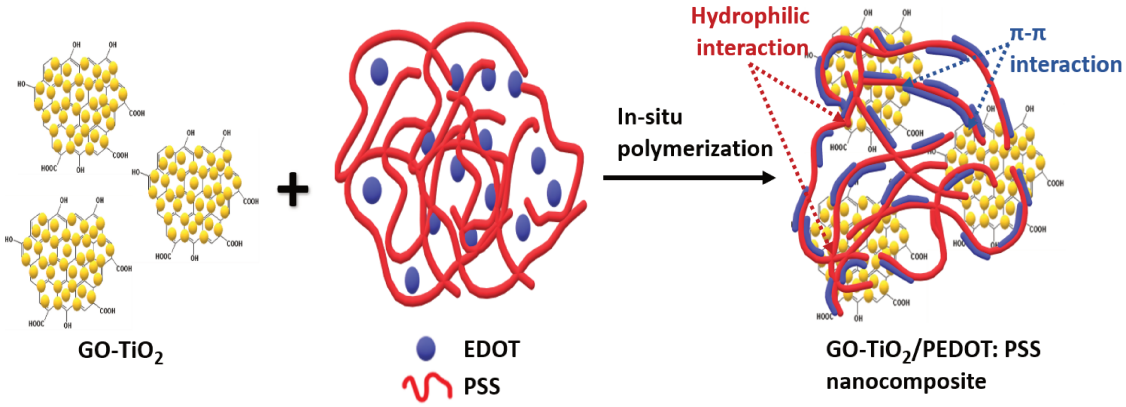

Figure 3: Schéma de la polymérisation chimique oxydative in situ de l'EDOT en présence de PSS et de QTDOG pour former les nanocomposite QTDOG/PEDOT: PSS

Caractérisation structurale des nanocomposites

Analyse morphologique des nanocomposites par microscopie électronique à balayage (MEB)

Il est connu que les propriétés thermique et électrique des nanocomposites sont directement liés à leur caractéristiques morphologiques [10, 11]. Par conséquent, une étude morphologique des nanocomposites ainsi que des inclusions a été réalisée à l'aide d'un microscope électronique à balayage à émission de champ (FE-MEB). La figure 4 montre les images MEB des inclusions formées de quantum dots de dioxyde de titane déposés sur oxyde de graphène (QTDOG). On y observe une morphologie qui rappelle celle de l'hortensia (photo en insert), on parle de nanostructures floriformes. Ces images indiquent que la méthode de synthèse utilisée permet d'obtenir une distribution uniforme de nanoparticules. Elles montrent aussi l'ancrage réussi des quantum dots de TiO_2 sur les nanofeuillets d'oxyde de graphène, ce qui augmente de façon probante le rapport surface/volume de l'inclusion. Ces micrographies MEB laissent voir une distribution dense du TiO_2 sur les feuillets d'oxyde de graphène avec la présence de quelques agrégats. Il est à noter qu'il n'a pas été observé de quantum dots individuels ailleurs que sur les feuillets d'OG, ce qui indique la forte interaction des QD avec l'OG. Ce réseau constitué de QD et d'OG peut avantager le transfert de charge et induire une diffusion de phonons [12].

La figure 5 montre les images MEB du PEDOT: PSS et celles de nanocomposites QTDOG / PEDOT: PSS à différentes concentrations en inclusions. Le mélange de polymère sans inclusions montre une morphologie lisse et régulière comparée à celle des nanocomposites. Dans ces derniers, on observe une distribution uniforme des inclusions (QTDOG) recouvertes complètement par le polymère. Une croissance réussie de la matrice polymère conductrice autour des inclusions renforce les chemins de conduction électrique. [12, 13]. Au vu de l'hétérogénéité

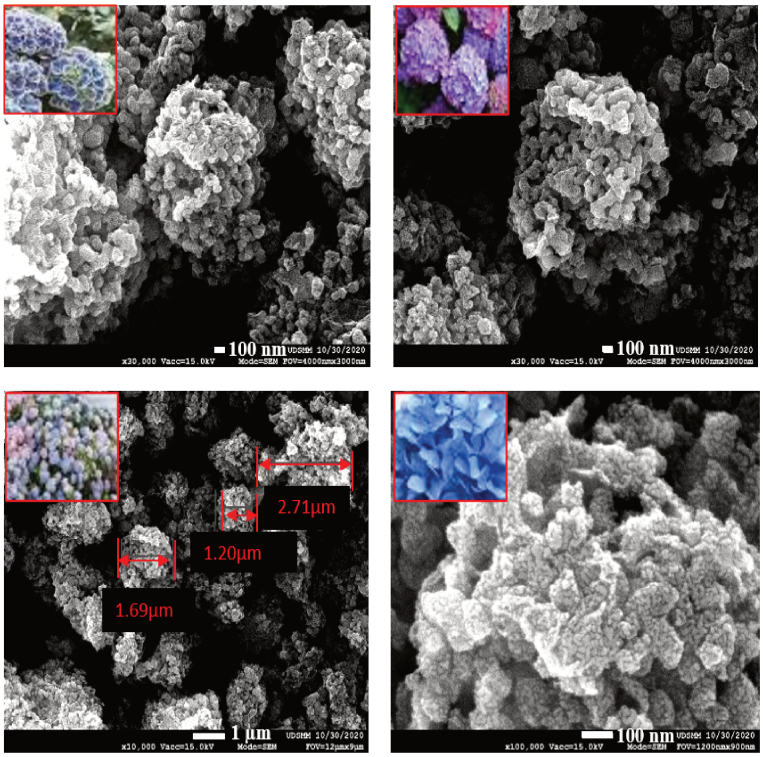

Figure 4: Images MEB des inclusions formées de quantum dots de dioxyde de titane déposés sur oxyde de graphène (QTDOG). Leur morphologie rappelle celle de l'hortensia comme montré en insert.

morphologique observée, la diffusion des phonons sera accentuée aux niveau des différentes interfaces. Nous pouvons nous attendre à ce que ce composite hybrides organique/inorganique synthétisé présente simultanément une bonne conductivité électrique et une faible conductivité thermique phononique.

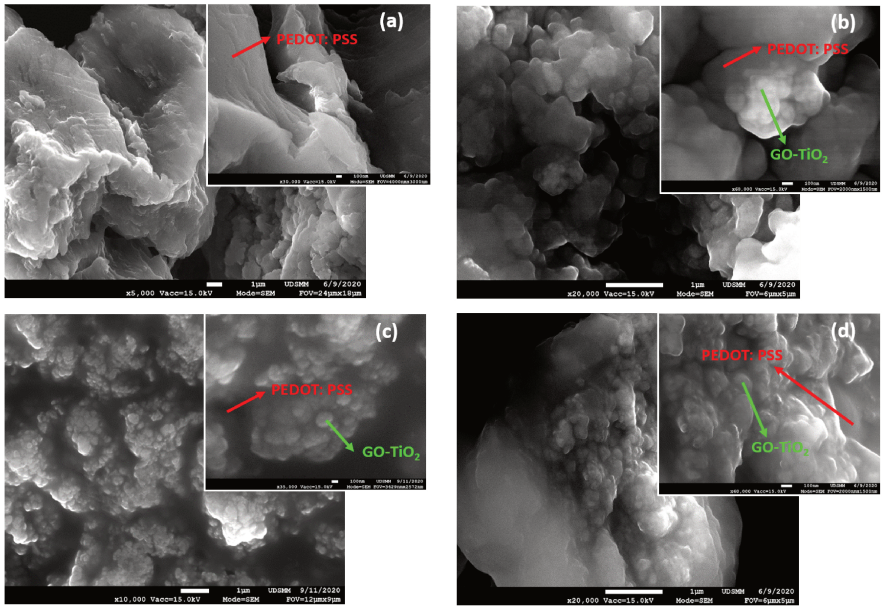

Figure 5: Image MEB de nanocomposites (a) PEDOT: PSS, (b) 0,5 %m QTDOG/PEDOT: PSS, (c) 2 %m QTDOG/PEDOT: PSS, et (d) 5 %m QTDOG/PEDOT: PSS,

Cartographie des éléments chimiques par spectrocopie à rayons X à dispersion d'énergie (EDS)

La composition chimique des QTDOG a été étudiée en réalisant une cartographie par EDS. La figure 6 montre la cartographie et la distribution du carbone (C), oxygène (O), et titane (Ti) en rouge, vert, et jaune, respectivement. Ici le carbone et le titane représente respectivement l'oxyde de graphène et le dioxyde de titane.

La figure 7 montre la cartographie et la distribution dans les nanocomposites du carbone (C), de l'oxygène (O), et du titane (Ti) en rouge, vert, et jaune,

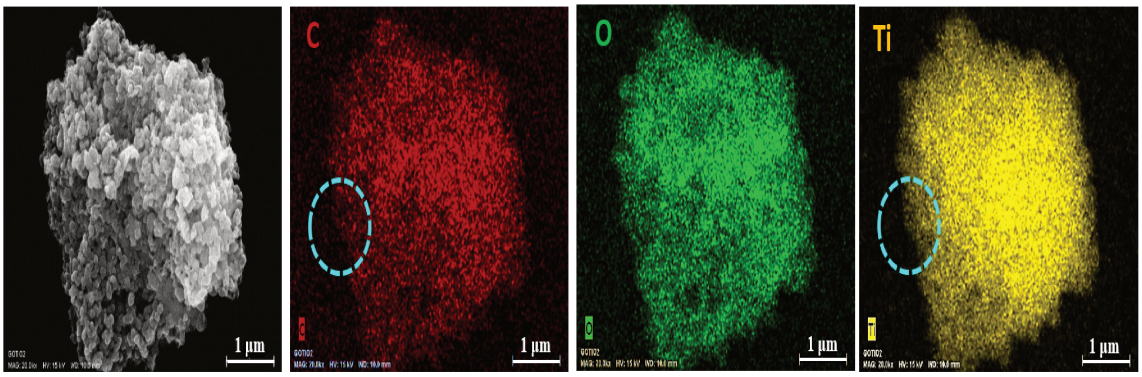

Figure 6: Images MEB avec cartographie, par spectrocopie à rayons X à dispersion d'énergie (EDS), des éléments chimiques présents dans les inclusions QTDOG . La distribution du carbone (C), oxygène (O), et titane (Ti) est respectivement en rouge, vert, et jaune.

respectivement. La cartographie EPS confirme la distribution uniforme du titane dans les nanocomposites où la concentration en QTDOG est de 2 %m et 5 %m. En revanche, on observe que la distribution en titane n'est pas uniforme dans les échantillons à 0,5 %m, cela est dû probablement à la faible quantité des inclusions. Les images EPS confirment aussi la distribution dense des inclusions (QTDOG) avec la présence de quelques agrégats.

Microscopie électronique à transmission (TEM) avec spectrocopie à rayons X à dispersion d'énergie (EDS)

L'analyse par TEM a été utilisée pour étudier la morphologie des inclusions QTDOG à l'échelle nanométrique. La figure 8 (a-b) révèle une monodispersion des QD, une morphologie sphérique des QD et un ancrage à la surface de l'oxyde de graphène tel qu' attendu. La figure 8 (c) présente un histogramme de distribution en taille de 400 QD avec une taille moyenne de 3,75 ±0,92 nm. La taille de ces particules est plus petite que le rayon de Bohr d'un exciton, ce qui indique la formation effective de QD [14–16]. La Figure 8 (e) est une image TEM haute résolution

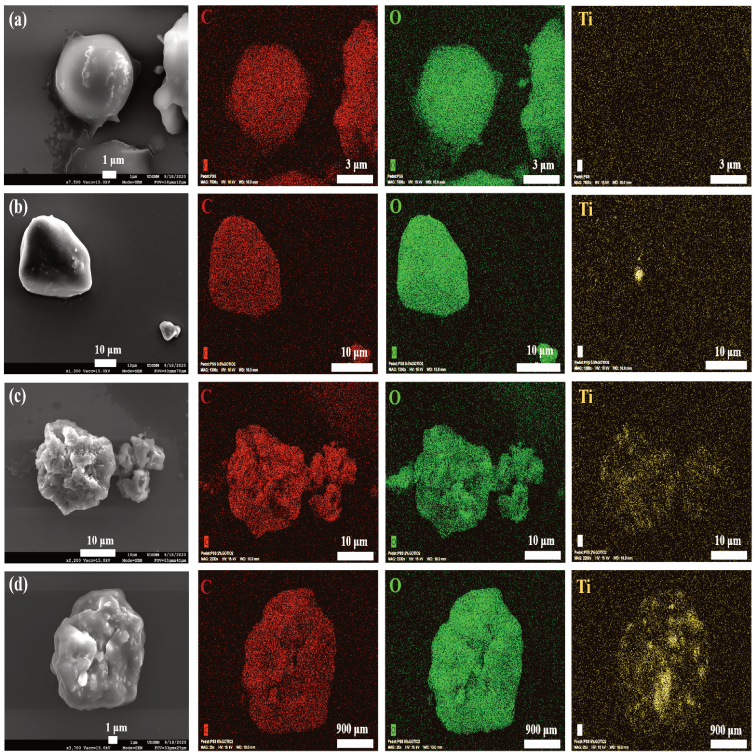

Figure 7: Images MEB et cartographie, par spectrocopie à rayons X à dispersion d'énergie (EDS), des éléments chimiques présents dans les nanocomposites (a) PEDOT: PSS, (b) 0.5 %m QTDOG/PEDOT: PSS, (c) 2 %m QTDOG/PEDOT: PSS, , and (d) 5 %m QTDOG/PEDOT: PSS.

(HRTEM) qui montre les plans réticulaires correspondant à l'oxyde de graphène (vert) et les quantum dots de TiO_2 (rouge). Les figures 8 (d) et (f) montrent la transformée de Fourier rapide (FFT) (diagramme de diffraction) et la FFT inverse pour l'oxyde de graphène ($d_{001} = 0,22$nm) et les QD de TiO_2 ($d_{101} = 0,34$nm) respectivement. Le plan d_{10l} correspondant à une distance interréticulaire de 0,34 nm confirme la phase anatase du TiO_2. La figure 8 (g-j) est une image obtenue par imagerie annulaire en champ sombre (HAADF) et réalisée en parallèle avec l' acquisition par spectroscopie de rayons X à dispersion d'énergie. On y observe une cartographie des différents éléments tels que le carbone, l'oxygène, et le titanium représentés respectivement en rouge, vert et jaune. Cela confirme une distribution

homogène des QD de TiO_2 sur la surface de l'oxyde de graphène.

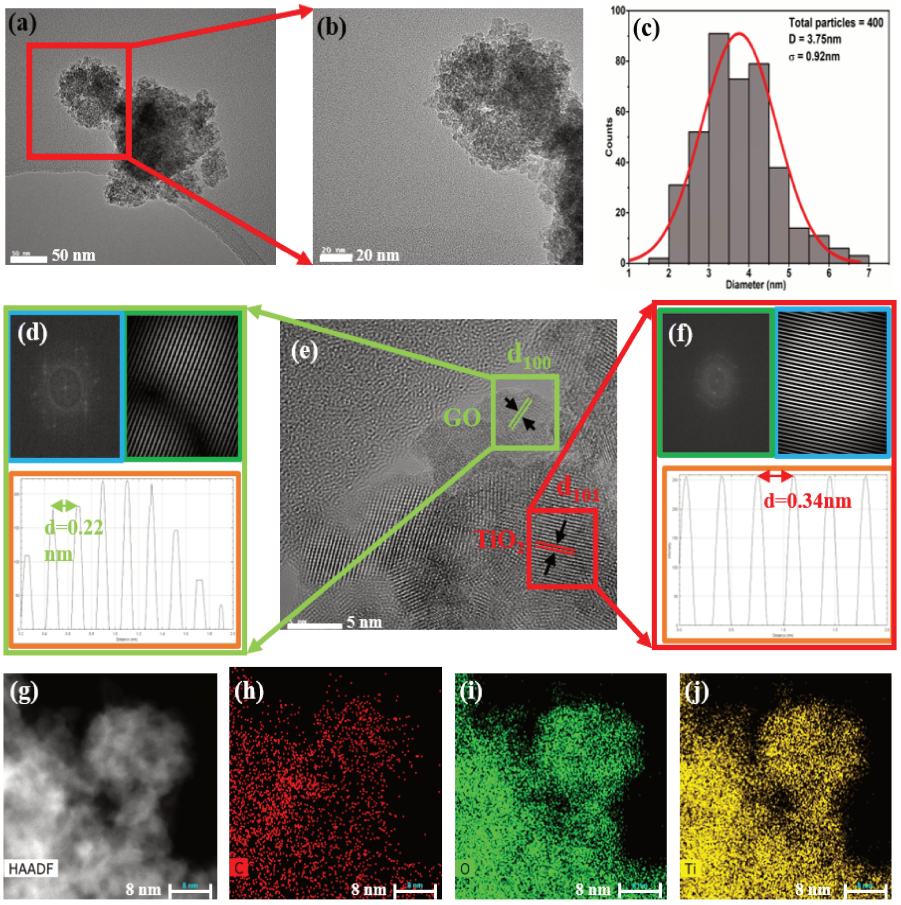

Figure 8: (a,b) Images TEM de QTDOG avec des barres d'échelle de 50nm et 20nm, (c) Histogramme de distribution en taille des QD, (e) Image TEM haute résolution montrant les plans TiO_2 et oxyde de graphène. FFT, FFT inverse obtenu en utilisant Image J software pour (d) OG and (f) QD de TiO_2 respectivement. (g) Image HAADF et cartographie EDX du (h) carbone , (i) oxygène, et (j) titane

.

Propriétés de transport des nanocomposites polymères

Afin d'évaluer le rendement de conversion thermoélectrique des nanocomposites élaborés, nous avons étudié leurs propriétés de transport en mesurant la conduc-

tivité électrique, la conductivité thermique et le coefficient Seebeck des différents échantillons. Cela a nous a permis de comparer leur facteur de puissance (FP) thermoélectrique.

Conductivité électrique

Deux techniques ont été utilisées pour la mesure de la conductivité électrique σ : la spectroscope d'impédance et la méthode de mesure 4 pointes. La première a été utilisée pour les échantillons massifs tandis que la seconde est appropriée à la caractérisation des couches minces. Différentes mesures ont été menées sur les échantillons suivants :

1. Sans traitement additionnel.
2. Avec traitement à l'acide hydrochlorique.
3. Avec matrice polymère PEDOT: PSS commerciale.
4. Sous forme de films minces sans traitement .

Nanocomposites sous forme de pastille

Nous avons mesuré initialement la conductivité électrique des nanocomposites massifs, sous forme de pastilles, en utilisant la spectroscopie d'impédance dans un intervalle de fréquence compris entre 100Hz et 1MHz (fig.9).

La conductivité électrique présente une évolution telle que prévue par Jonscher [17] : un plateau à basses fréquences et une dispersion à hautes fréquences. La conductivité électrique a été obtenue en ajustant les données expérimentales de la figure 9 par la loi de puissance de Joncher.

La figure 10 montre l'évolution, en fonction de la concentration en inclusions QTDOG, de la conductivité électrique des **nanocomposites non traités** . On

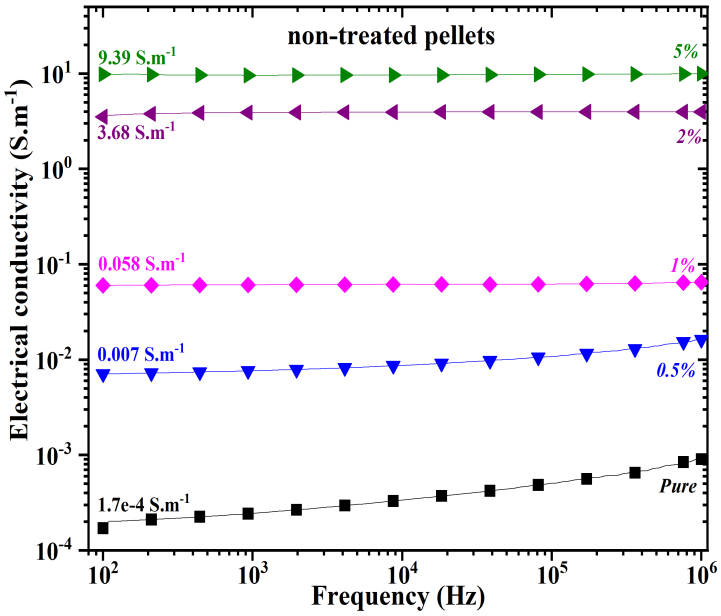

Figure 9: Conductivités électriques en fonction de la fréquence de pastilles non traitées de PEDOT: PSS avec des inclusions QTDOG à différentes concentrations.

y observe une augmentation de plusieurs ordres de grandeur de la conductivité électrique (de $1,7\ 10^{-4}$ à 9,84 $S.m^{-1}$) à une concentration volumique en inclusions de 1,5 % en volume. Cette évolution suggère la possibilité d'une percolation. Malgré cela, la valeur maximale atteinte reste insuffisante pour induire de bonnes performances TE.

La même procédure de mesure de la conductivité a été utilisée pour les **nanocomposites traités à l'acide**, la figure 11 montre, à la fois, une augmentation de la conductivité électrique de la matrice polymère de $1,7x10^{-4}$ (non-traité) à 0,03 $S.m^{-1}$ (traité à l'acide) ainsi qu'une augmentation de celle des nanocomposites, en fonction de la concentration en inclusions, qui passe de 0,03 à 97,58 $S.m^{-1}$ pour une concentration volumique de 1,5 %. Le traitement à l'acide des nanocom-

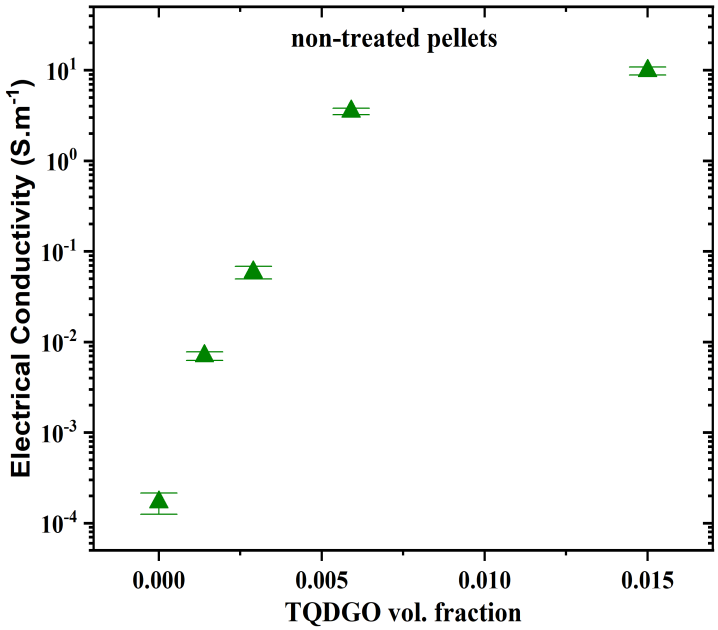

Figure 10: Évolution de la conductivité électrique en fonction de la concentration des inclusions QTDOG dans des pastilles PEDOT: PSS non traitées.

posites à été une étape positive pour l'amélioration des propriétés électriques des échantillons, cependant cela reste insuffisant pour des performance TE élevées.

Enfin, les résultats obtenus ci-dessus ont été comparés à la conductivité électrique mesurée pour des nanocomposites élaborés **avec une matrice polymères PEDOT: PSS commerciale** (fournie par Sigma-Aldrich). La conductivité électrique augmente de 16 Sm^{-1} pour les échantillons sans inclusions à 253 Sm^{-1} pour les nanocomposites à 1,5 % d'inclusions. Ces propriétés de conduction restent, en dépit de cette amélioration, en deçà de ce que l'on attend de matériaux thermoélectriques performants.

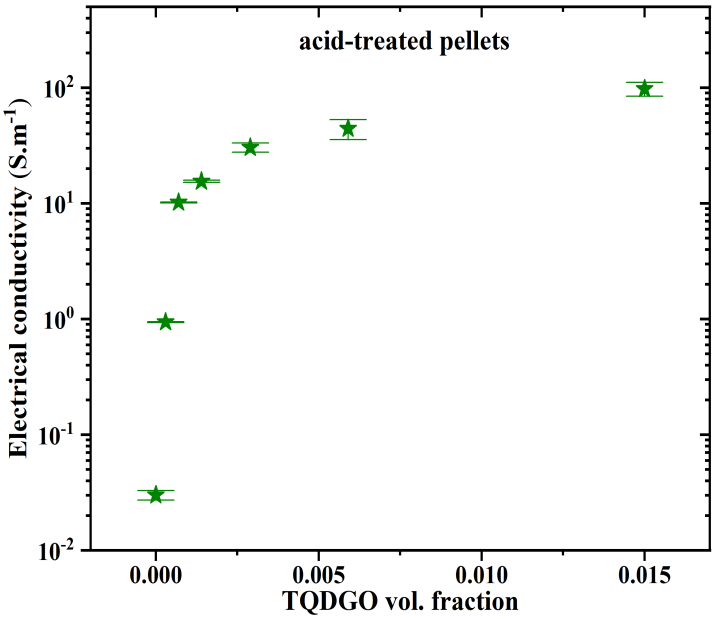

Figure 11: Évolution de la conductivité électrique en fonction de la concentration des inclusions QTDOG dans des pastilles PEDOT: PSS traitées à l'acide.

Nanocomposites sous forme de films minces

Notre attention s'est portée ensuite sur la conductivité électrique des nanocomposites en films minces (sans traitement acide). Nous avons utilisé pour ces mesures la technique des 4 pointes. La figure 12 montre l'évolution de σ pour ces films minces. La matrice de polymère sans inclusions présente une conductivité électrique très faible, éloignée de celle de la matrice sous forme de pastille. En revanche, avec l'ajout d'inclusions, σ augmente plus vite que dans le cas des pastilles et atteint la valeur de 3,69 10^5 S.m^{-1} à une concentration volumique de 1,5 % (équivalent à 5 % massique).

Cette accroissement remarquable de la conductivité électrique peut être ex-

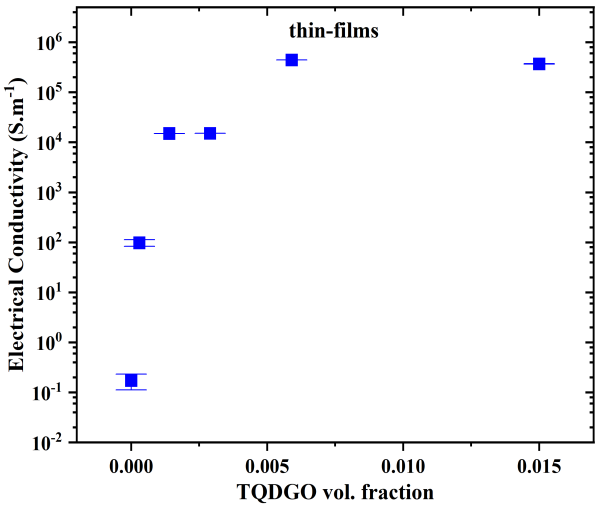

Figure 12: Évolution de la conductivité électrique en fonction de la concentration des inclusions QTDOG dans des films minces de PEDOT: PSS.

pliqué par la formation de réseaux PEDOT-QTDOG-PEDOT tels que décrits dans la figure 13. La percolation est induite par l'établissement d'un ordre à longue distance, une cristallinité accrue [18, 19] , qui se traduit par un chemin conducteur ininterrompu favorisant la conductivité électrique.

La figure 14 compare les résultats obtenus pour les films minces à ceux des échantillons sous forme de pastilles. Il en résulte que les films minces, au vu de leur conductivité électrique la plus élevée, sont les plus appropriés pour des applications TE.

Conductivité thermique

Nous avons utilisé une technique photothermique pour la mesure des propriétés thermiques des nanocomposites. Il s'agit de la radiomètrie infrarouge (PTR) [20], une technique développée au sein de notre laboratoire (UDSMM). Elle permet la mesure simultanée de la diffusivité (d) thermique et de l'effusivité thermique (e)

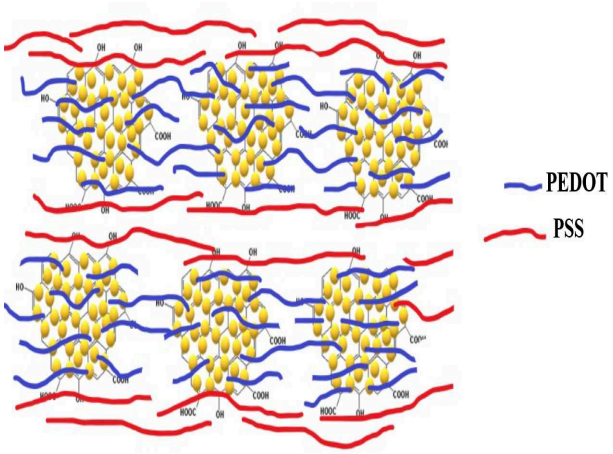

Figure 13: Schéma du changement conformationnel dans les chaînes PEDOT et formation d'un réseau PEDOT-QTDOG-PEDOT à longue distance dans les films minces.

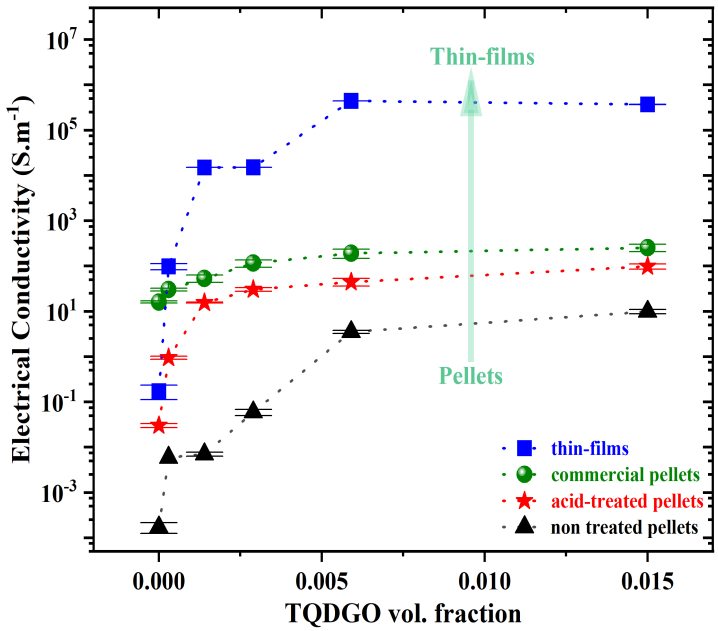

Figure 14: Évolution de la conductivité électrique en fonction de la concentration des inclusions QTDOG dans les pastilles et les films minces.

et par conséquent de la conductivité thermique $\kappa = e\ /\sqrt{d}$.

Le principe de cette technique consiste à illuminer la surface d'un échantillon opaque en utilisant un faisceau laser modulé. L'absorption de la lumière se traduit par une élévation locale de la température. En réponse à cette excitation, le matériau émet une radiation infrarouge dont l'intensité, mesurée à l'aide d'une photodiode, est proportionnelle à la température. L'analyse de la variation de cette température en fonction de la fréquence de modulation permet la détermination des paramètres thermiques [21].

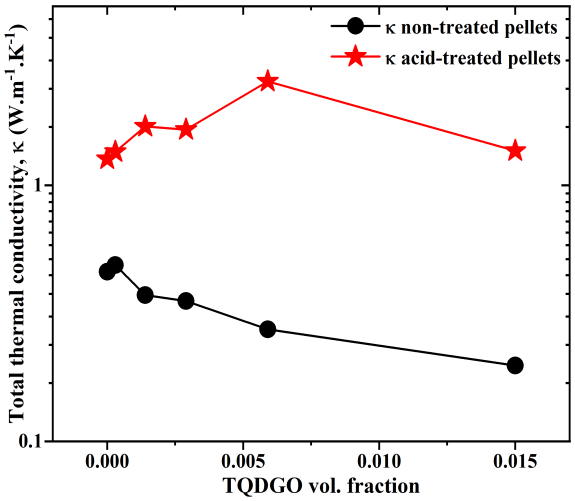

Figure 15: Effet des inclusions QTDOG sur la conductivité thermique de pastilles traitées à l'acide et non traitées.

La figure 15 montre l'évolution de la conductivité thermique κ en fonction de la concentration en inclusions pour les nanocomposites en pastilles traités à l'acide et non traités. On y observe une diminution pour les échantillons non traités où κ prend la valeur de 0,46 $\mathrm{Wm^{-1}K^{-1}}$ en l'absence d'inclusions et diminue jusqu'à 0,19 $\mathrm{Wm^{-1}K^{-1}}$ lorsque la concentration massique en QTDOG atteint 5 %. On observe aussi que la conductivité thermique des échantillons traités est plus

grande que celle des échantillons non traités et que l'ajout d'inclusions se traduit d'abord par une augmentation, peut être due à l'augmentation de la conduction ionique, ensuite une diminution avec l'ajout de 5 % (massique) de QTDOG. La composante électronique de la conductivité thermique a été estimée à l'aide de la loi de Wiedemann-Franz $\kappa_e = L\,\sigma\,T$ où, κ_e, L, et T sont la conductivité thermique électronique, le nombre de Lorenz, et T la température absolue, respectivement. La valeur maximum atteinte par cette composante, quelque soit le type d'échantillon et la concentration en inclusions, est de 10^{-3} W m^{-1} K^{-1}. Ainsi, la contribution de la conductivité thermique électronique à la conductivité thermique totale est très faible et négligeable devant la contribution phononique. Nous pouvons en déduire que la diminution de la conductivité thermique totale dans les nanocomposites est due seulement à la composante phononique qui diminue avec l'ajout des inclusions.

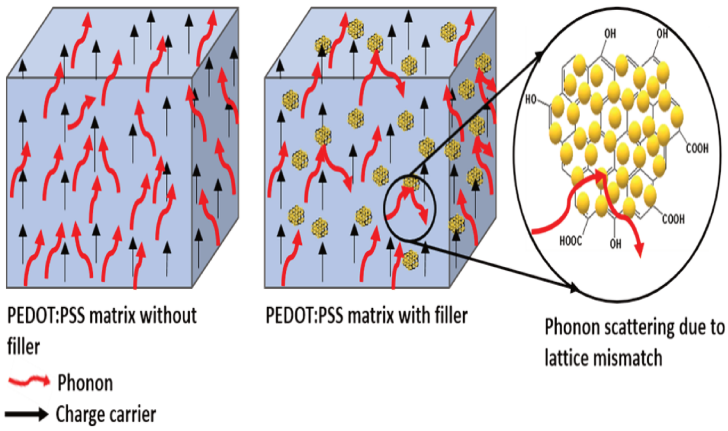

Figure 16: Représentation Schématique de la diffusion des phonons par la phase hétérogène des QTDOG dans la matrice polymère PEDOT: PSS.

Cette diminution de la composante phononique peut être expliquée par le fait que les phonons de faible énergie sont diffusés à l'interface matrice-inclusion par la structure hétérogène des inclusions [22, 23] tel que illustré dans la figure 16.

Coefficient Seebeck

Le banc de mesure du coefficient Seebeck S a été mis au point est développé au laboratoire. Il a permis de mesurer ce coefficient à température ambiante en fonction de la concentration en inclusions pour les différents types de nanocomposites (pastilles traitées à l'acide ou non, avec PEDOT-PSS commercial ou non et films minces). Les résultats de ces mesures sont synthétisés dans la figure 17. On note une augmentation de S en fonction de la concentration en inclusions, plus ou moins importante suivant le type de nanocomposite. On observe ainsi pour ces nanocomposites que l'augmentation de S n'induit pas forcément une diminution de σ comme cela se produit généralement.

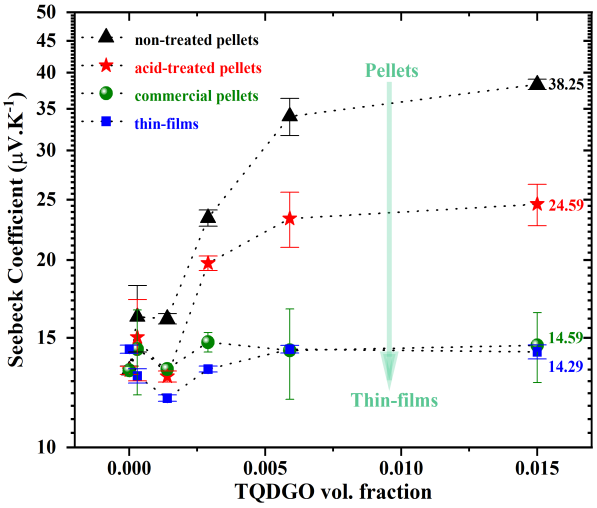

Figure 17: Effet des inclusions QTDOG sur le coefficient Seebeck de pastilles PEDOT: PSS non traitées (triangles noirs), traitées à l'acide (étoiles rouges), pastilles commerciales (sphères vertes), et films minces (carrés bleus).

Cette augmentation du coefficient Seebeck S peut être attribuée à l'interaction forte entre les inclusions QTDOG et le PEDOT-PSS au niveau moléculaire. En l'occurrence, cette interaction est à l'origine, comme observé sur les pastilles non

traitées, d'une barrière sélective des niveaux d'énergie électronique, induite par les interfaces inhomogènes des inclusions avec la matrice [24–27]. Cette barrière ne permet que le passage des porteurs de charge de niveaux d'énergies les plus élevés et a donc pour effet d'accroître le coefficient Seebeck. La sélection des niveaux d'énergie électronique survient lorsqu'il y a une différence entre la valeur de la fonction de travail (énergie nécessaire pour extraire un électron du matériau) de la matrice et celle des inclusions (fig.18).

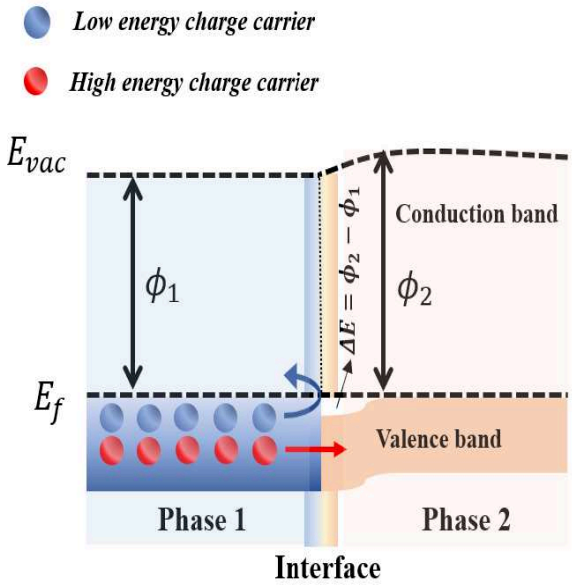

Figure 18: Schéma représentatif d'une barrière sélective des niveaux d'énergie électronique induite par la différence des fonctions de travail de la matrice et des inclusions.

Le transfert de charge entre matrice et inclusions est à l'origine d'un champ électrique [28]. Alors, l'accumulation des porteurs de charge de basses énergies aux extrémités de l'échantillon est inhibée par la présence de ce champ électrique à l'interface polymer/inclusion. Seul le passage des porteurs de charge de haute énergie est alors permis, ce qui accroît le coefficient Seebeck sans pour autant diminuer la conductivité électrique, c'est ce qui est observé dans les pastilles que

nous avons élaborées.

Performances thermoélectriques

A partir des mesures des propriétés de transport des différents nanocomposites, nous avons calculé le facteur de puissance (FP) pour chacun des échantillons. La figure 19 décrit l'effet des inclusions QTDOG sur le facteur de puissance. Une augmentation de ce facteur a été constatée pour l'ensemble des nanocomposites. Cependant, le facteur de puissance maximum obtenu pour les pastilles reste en deçà de ce qui est attendu pour des applications TE. En revanche la valeur du FP obtenue pour les films minces est remarquable, elle atteint 91,26 $\mu Wm^{-1}K^{-2}$ avec une concentration volumique en QTDOG de 0,6 %. Cette valeur de FP est largement supérieure à celle obtenue pour des nanocomposites polymère/quantum dots décrits dans la littérature [18, 29–31]. Un résultat similaire au notre (116 $\mu Wm^{-1}K^{-2}$) a été obtenu dans des nanocomposites composés de nanoparticules SnOx dans une matrice PEDOT: PSS [32].

Conclusion

Dans le cadre de cette thèse, des nanocomposites ont été élaborés à partir d'une matrice PEDOT: PSS contenant des inclusions composées de quantum dots de TiO_2 déposés sur des nanofeuillets d'oxyde de graphène (QTDOG). Ces composites ont été préparés via un processus de polymérisation oxydative. Différents types d'échantillons (pastilles, films minces) ont été soumis à des analyses chimiques et structurales (DRX, MEB, EDS, FTIR, spectroscopie UV-Vis et ATG). L'objectif était d'étudier les performances thermoélectriques de ces nanocomposites hybrides. Leur propriétés de transport, conductivité électrique, thermique et

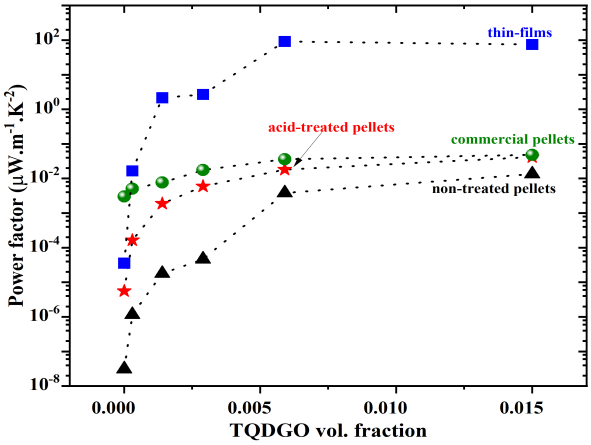

Figure 19: Effet des inclusions QTDOG sur facteur de puissance de pastilles PEDOT: PSS non traitées (triangles noirs), traitées à l'acide (étoiles rouges), pastilles commerciales (sphères vertes), et films minces (carrés bleus).

coefficient Seebeck, ont été étudiées. La conductivité électrique a été mesurée à l'aide de la spectroscopie d'impédance ou de la méthode de mesure 4 pointes. La conductivité thermique a été mesurée en utilisant la radiomètrie infra rouge. Un dispositif à 2 pointes, mis au point au laboratoire, a permis la mesure du coefficient Seebeck.

Dans ce travail nous avons tenté de contourner la difficulté qui réside dans l'interdépendance des paramètres de transport qui interviennent dans la performance thermoélectrique. Il a été ainsi possible d'augmenter de manière importante la conductivité électrique des nanocomposites en évitant une augmentation de la conductivité thermique et une diminution du coefficient Seebeck. Cela a été possible par le biais des inclusions QTDOG qui ont constitué, d'une part, une barrière électronique sélective, filtrante, n'autorisant le passage que des électrons de plus hautes énergies et permettant ainsi l'amélioration du coefficient Seebeck. D'autre part, ces inclusions se sont avérées des sites de diffusion de phonons efficients, permettant la diminution de la composante phononique de la conductivité

thermique. Cette nanostructuration des QTDOG a ainsi permis l'amélioration des performances de ces nanocomposites qui présentent les facteurs de puissance parmi les plus élevées de la littérature pour des composites polymères-quantum dots.

Bibiliographie

[1] Shiho Kim, Soonseo Park, SunKook Kim, and Seok Ho Rhi. A Thermoelectric Generator Using Engine Coolant for Light-Duty Internal Combustion Engine-Powered Vehicles. *Journal of Electronic Materials*, 40(5):812–816, 2011.

[2] D. Samson, T. Otterpohl, M. Kluge, U. Schmid, and Th. Becker. Aircraft-Specific Thermoelectric Generator Module. *Journal of Electronic Materials*, 39(9):2092–2095, 2010.

[3] Pawel Ziolkowski, Knud Zabrocki, and Eckhard Müller. TEG design for waste heat recovery at an aviation jet engine nozzle. *Applied Sciences*, 8(12):2637–2658, 2018.

[4] Saniya LeBlanc. Thermoelectric generators: Linking material properties and systems engineering for waste heat recovery applications. *Sustainable Materials and Technologies*, 1:26–35, 2014.

[5] Fengjiao Zhang, Yaping Zang, Dazhen Huang, Chong-an Di, and Daoben Zhu. Flexible and self-powered temperature–pressure dual-parameter sensors using microstructure-frame-supported organic thermoelectric materials. *Nature Communications*, 6(1):8356–8366, 2015.

[6] Shuankui Li, Zhongyuan Huang, Rui Wang, Chaoqi Wang, Wenguang Zhao, Ni Yang, Fusheng Liu, Jun Luo, Yinguo Xiao, and Feng Pan. Precision grain boundary engineering in commercial bi2te2.7se0.3 thermoelectric materials towards high performance. *Journal of Materials Chemistry A*, 9:11442–11449, 2021.

[7] Amr Tayel, Adham Ramadan, and Omar El Seoud. Titanium dioxide/graphene and titanium dioxide/graphene oxide nanocomposites: Synthesis, characterization and photocatalytic applications for water decontamination. 8(11):491–536, 2018.

[8] Shivani Shisodia, Benoit Duponchel, Gérard Leroy, Abdelhak Hadj Sahraoui, Dharmendra Pratap Singh, Christophe Poupin, Lucette Tidahy, Renaud Cousin, Patrick Ropa, and Michael Depriester. Synthesis of quantum dot-based polymer nanocomposites: assessment of their thermoelectric performances. *Sustainable Energy Fuels*, 6:3158 – 3168, 2022.

[9] Jianyong Ouyang. "secondary doping" methods to significantly enhance the conductivity of PEDOT:PSS for its application as transparent electrode of optoelectronic devices. *Displays*, 34(5):423–436, 2013.

[10] Addis Tessema, Dan Zhao, Joseph Moll, Shansan Xu, Ronggui Yang, Chen Li, Sanat K. Kumar, and Addis Kidane. Corrigendum to "Effect of filler loading, geometry, dispersion and temperature on thermal conductivity of polymer nanocomposites" [Polym. Test. 57 (2017) 101–106]. *Polymer Testing*, 73:448–449, February 2019.

[11] Nikhil Satyala and Daryoosh Vashaee. The effect of crystallite size on thermoelectric properties of bulk nanostructured magnesium silicide (Mg $_2$ Si) compounds. *Applied Physics Letters*, 100(7):073107–073112, February 2012.

[12] Yi Zhang, Adam M. Schwartzberg, Kevin Xu, Claire Gu, and Jin Z. Zhang. Electrical and thermal conductivities of gold and silver nanoparticles in solutions and films and electrical field enhanced Surface-Enhanced Raman Scattering (SERS). volume 5929, pages 592912–592920, San Diego, California, USA, 2005.

[13] Yandong Sun, Yanguang Zhou, Ramya Gurunathan, Jin-Yu Zhang, Ming Hu, Wei Liu, Ben Xu, and G. Jeffrey Snyder. Phonon scattering in the complex strain field of a dislocation in PbTe. *Journal of Materials Chemistry C*, 9(27):8506–8514, 2021.

[14] Sofia Javed, Mohammad Islam, and Mohammad Mujahid. Synthesis and characterization of TiO2 quantum dots by sol gel reflux condensation method. *Ceramics International*, 45(2):2676–2679, 2019.

[15] Swati Sood, Sandeep Kumar, Ahmad Umar, Amandeep Kaur, Surinder Kumar Mehta, and Sushil Kumar Kansal. TiO2 quantum dots for the photocatalytic degradation of indigo carmine dye. *Journal of Alloys and Compounds*, 650:193–198, 2015.

[16] Lalitha Gnanasekaran, R. Hemamalini, and K. Ravichandran. Synthesis and characterization of TiO2 quantum dots for photocatalytic application. *Journal of Saudi Chemical Society*, 19(5):589–594, 2015.

[17] Andrew K. Jonscher. Dielectric relaxation in solids. *J. Phys. D. Appl. Phys.*, 32(14):57–70, jul 1999.

[18] Fei-Peng Du, Nan-Nan Cao, Yun-Fei Zhang, Ping Fu, Yan-Guang Wu, Zhi-Dong Lin, Run Shi, Abbas Amini, and Chun Cheng. PEDOT:PSS/graphene quantum dots films with enhanced thermoelectric properties via strong inter-

facial interaction and phase separation. *Scientific Reports*, 8(1):6441–6453, 2018.

[19] Sung Hyun Kim. Control of the charge carrier concentration and hall mobility in PEDOT:PSS thermoelectric films: Control of the charge carrier concentration and hall mobility in PEDOT:PSS thermoelectric films. *Bulletin of the Korean Chemical Society*, 38(12):1460–1464, 2017.

[20] M. Depriester, P. Hus, S. Delenclos, and A. Hadj Sahraoui. New methodology for thermal parameter measurements in solids using photothermal radiometry. *Review of Scientific Instruments*, 76(7):074902–074909, July 2005.

[21] M. Depriester, P. Hus, S. Delenclos, and A. Hadj Sahraoui. Study of thermal parameters' temperature dependence in solids using photothermal radiometry. *Review of Scientific Instruments*, 78(3):036101–036105, March 2007.

[22] Scott T. Huxtable, David G. Cahill, Sergei Shenogin, Liping Xue, Rahmi Ozisik, Paul Barone, Monica Usrey, Michael S. Strano, Giles Siddons, Moonsub Shim, and Pawel Keblinski. Interfacial heat flow in carbon nanotube suspensions. *Nature Materials*, 2(11):731–734, November 2003.

[23] Ce-Wen Nan, Gang Liu, Yuanhua Lin, and Ming Li. Interface effect on thermal conductivity of carbon nanotube composites. *Applied Physics Letters*, 85(16):3549–3551, October 2004.

[24] Haijun Song, Qiufeng Meng, Yao Lu, and Kefeng Cai. Progress on PEDOT:PSS/nanocrystal thermoelectric composites. *Advanced Electronic Materials*, 5(11):1800822–1800840, 2019.

[25] Biplab Paul, Ajay Kumar V, and P. Banerji. Embedded ag-rich nanodots in PbTe: Enhancement of thermoelectric properties through energy filtering of the carriers. *Journal of Applied Physics*, 108(6):064322–064328, 2010.

[26] Haijun Song and Kefeng Cai. Preparation and properties of PEDOT:PSS/te nanorod composite films for flexible thermoelectric power generator. *Energy*, 125:519–525, 2017.

[27] Jaeyoo Choi, Jang Yeol Lee, Sang-Soo Lee, Chong Rae Park, and Heesuk Kim. High-performance thermoelectric paper based on double carrier-filtering processes at nanowire heterojunctions. *Advanced Energy Materials*, 6(9):1502181–1502189, 2016.

[28] Hao He and Jianyong Ouyang. Enhancements in the mechanical stretchability and thermoelectric properties of PEDOT:PSS for flexible electronics applications. *Accounts of Materials Research*, 1(2):146–157.

[29] Kongli Xu, Guangming Chen, and Dong Qiu. Convenient construction of poly(3,4-ethylenedioxythiophene)–graphene pie-like structure with enhanced thermoelectric performance. *Journal of Materials Chemistry A*, 1(40):12395–12402, 2013.

[30] Chuizhou Meng, Changhong Liu, and Shoushan Fan. A promising approach to enhanced thermoelectric properties using carbon nanotube networks. *Advanced Materials*, 22(4):535–539, 2010.

[31] Ahmed Gamal El-Shamy. New free-standing and flexible PVA/carbon quantum dots (CQDs) nanocomposite films with promising power factor and thermoelectric power applications. *Materials Science in Semiconductor Processing*, 100:245–254, 2019.

[32] Jingjin Dong, Dominic Gerlach, Panagiotis Koutsogiannis, Petra Rudolf, and Giuseppe Portale. Boosting the thermoelectric properties of PEDOT:PSS via low-impact deposition of tin oxide nanoparticles. *Advanced Electronic Materials*, 7(5):2001284–2001292, 2021.

Contents

List of Figures

List of Tables

Acknowledgements

The work presented in this thesis was done at the Unité de Dynamique et Structure des Matériaux Moléculaires (UDSMM) laboratory of Université du Littoral Côte d'Opale (ULCO), Dunkerque. I acknowledge Université du Littoral Côte d'Opale and Université de Lille for providing financial support to carry out this work. I am grateful to everyone who guided, supported, motivated, and assisted me during the three-year PhD program. The completion of this thesis would not have been possible without the contributions of a large number of people.

First, I would like to acknowledge my thesis supervisor, Michael Depriester, for believing in me and welcoming me to work with him in this laboratory. I cannot thank him enough for his unwavering support throughout the thesis process and for his endless support. His expertise and professionalism made my PhD journey more enjoyable despite numerous obstacles. After each setback I encountered during my PhD, he encouraged me to stay strong and never gave up on me. He is an excellent mentor and a good person. He is so friendly that I was never hesitant to share my ideas with him.

I would like to greatly thank Prof. Abdelhak Hadj Sahraoui, the former director of the UDSMM, for his scientific input, discussions, and suggestions, all of which have helped to improve the quality of this thesis. I am grateful to him for having faith in me and for his endless encouragement.

My gratitude extends to Dr. Dharmendra Pratap Singh, Assistant Professor at UDSMM, for the insightful conversations and fruitful discussions during this project. His scientific knowledge assisted me in selecting materials, characterizing them, and enhancing the quality of my research. I would like to thank Mr. Benoit Duponchel, Research Engineer at UDSMM, for his dedication and cooperation. He helped me during many experimental techniques and discussions. Without

his experience and understanding, the current thesis would not be conceivable. I thank Dr. Lucette Tidahy, UCEIV, for the TG-DSC measurements.

I would like to thank Prof. Gerard Leroy for his assistance in electrical conductivity measurements by the four-point probe method. Dr. Benoit Escorne for his technical support in the Seebeck coefficient measurement cell. Prof. Amaury Kasprowiak for his assistance in FTIR and UV-Vis spectroscopies. Manuel Mascot for thin-film thickness measurement by using a profilometer.

I would like to thank Prof. Abdelylah Daoudi, the current director of the UDSMM, for encouraging me and granting me permission to attend several international conferences.

Working with MREI1 coworkers was an incredible experience. I thank Fabrice Goutier, Stéphane Longuemart, Mathieu Bardoux, Yahia Boussoualem, Christophe Poupin, Abdelaziz Elass, Corinne Kolinsky, Renaud Cousin, and Patrick Ropa for sharing the good moments at work.

I want to express my sincere appreciation to Véronique Vanvincq, France Folatre, and Virginie Bal Picotin for the invaluable assistance they provided in the administrative process.

I am extremely grateful to Dr. Nassima Radouane, my colleague and close friend, for guiding me throughout my PhD. Because of her, I was able to work independently on complex techniques such as, photothermal radiometry and Seebeck coefficient measurements. She assisted me with MATLAB programming and data analysis. Now that she has completed her PhD, I miss our late-night lab conversations over pizza and snacks.

I appreciate my coworker, Qingyu Tian, for being a kind friend at work. I enjoyed having long conversations with her over a cup of tea in our free time. I thank

my fellow PhD candidates, Miriam Achkar, Abir Moghnieh, Layla Farhat, Dr. Atul Shankar Mani Tripathi (former post-doc), Asmita Shah, Soukaina Chahib, Parthiban Palani, Nouha Drame, Mamadou Barry, Bouchra Asbani, Mireille Bader, and others for the pleasant moments that will always be remembered.

I would like to take this opportunity to express my gratitude to Saurabh Kejriwal for his assistance with the grammar and editing of the article that I just recently published. I want to thank you for the time and effort that you have put into it.

To my Lille family, Sumit Sood, Manarshjot Singh, Sepal Dhaliwal, Raman Dhaliwal, Anuradha Tewari, Archana Sankhyan, and Shilpa Sonar, you guys are all amazing. I'm so grateful for all the fun times we had together. To my friends Anjali Sharma, Deepak Gupta, and Sugandha Sharma, I say thank you for always being there for me.

I thank Nishant Tuteja for proofreading my manuscript and helping me with my writing. I appreciate him for being patient with me and the encouragement he provided during this time. Finally, I would like to thank my parents, grandparents, sister, and brother for loving me and supporting my decision to pursue my PhD overseas, as well as every other decision I have made in my life.

Nomenclature

α	Thermal diffusivity
A	Surface area of the sample
C	Capacitance
C_0	Air capacitance
D	Spacing between two successive tips in four-point probe method
η_{max}	Thermoelectric conversion efficiency
ϵ^*	Dielectric permittivity
$\epsilon^{'}$	Real part of dielectric permittivity
$\epsilon^{"}$	Imaginary part of dielectric permittivity
e	Elementary charge
e'	Thermal effusivity
δE	Barrier energy
EG	Ethylene glycol
E_f	Fermi energy
EMT	Effective medium theory
f	Frequency
$\overrightarrow{F_i}$	Thermodynamic affinity
G	Conductance
h	Planck's constant
$\overrightarrow{J_e}$	Electric flux density
$\overrightarrow{J_i}$	Thermodynamic flux density
$\overrightarrow{J_Q}$	Heat flux density
k_B	Boltzmann constant
κ	Total thermal conductivity
κ_e	Electronic component of thermal conductivity
κ_l	Lattice component of thermal conductivity
κ_J	Intrinsic thermal conductivity
κ_m	Thermal conductivity of the matrix
κ_f	Thermal conductivity of the filler
L	Lorenz number

$\overrightarrow{L_{ij}}$	Kinetic coefficient
M	Thermal wave number
$m*$	Effective mass
μ	Mobility
μ_e	Electrochemical potential
μ_C	Chemical potential
n	Charge carrier concentration
ρ	Electrical resistivity
ϕ	Work function
ϕ_c	Percolation threshold
ϕ_σ	Percolation threshold for electrical conductivity
$\phi_{\kappa/S}$	Percolation threshold of κ/S
σ	Electrical conductivity
σ_m	Electric conductivity of the matrix
σ_f	Electric conductivity of the filler
σ_{ac}	Electric conductivity due to alternating current
σ_{dc}	Electric conductivity due to direct current
σ_{pol}	Electric conductivity due to polarisation
S	Seebeck coefficient
S_f	Photocell signal as a function of frequency
S_f	Seebeck coefficient of the filler
S_m	Seebeck coefficient of the matrix
τ	Relaxation time
T	Temperature
ΔT	Temperature difference
t	Sample thickness
T_g	Glass transition temperature
T_f	Melting temperature
V	Electric potential
ΔV	Electric potential difference
ω	Angular frequency
CNT	Carbon nano tubes
CP	Conducting polymer
$DIwater$	De-ionized water
$DMSO$	Dimethyl sulfoxide

DSC	Diffrential scanning calorimetry
$FTIR$	Fourier transform infrared spectroscopy
GO	Graphene oxide
IPA	Isopropyl alcohol
NC	Nanocomposite
NP	Nanoparticle
PA	Polyacetylene
$PANI$	Polyaniline
$PSVA$	polar solvent vapor annealing
PVC	Polyvinyl chloride
$PEDOT$	Poly (3,4-ethylene dioxythiophene)
$PANI$	Polyaniline
$PBTTs$	Poly(2,5-bis (3- alkylthio-phene -2-yl) thieno [3,2-b]thiophenes)
$PBBL$	oly benzimidazobenzophenan-throline (BBL)
$P3HT$	Poly(3-hexylthiophene)
PF	Thermoelectric power factor
$PGEC$	Phonon glass electron crystal
PNC	Polymer nanocomposite
PPy	Polypyrrole
PSS	Polystyrene
QDs	Quantum dots
rGO	Reduced graphene oxide
SEM	Scanning electron microscopy
TEM	Transmission electron microscopy
TE	Thermoelectric
TiO_2	Titanium di-oxide
TGA	Thermogravimetric analysis
$TQDGO$	Titanium di-oxide quantum dot decorated graphene oxide
$UV-Vis$	Ultra-violet visible spectroscopy
UPS	Ultra-violet photoelectron spectroscopy
XRD	X-ray diffraction
ZT	Thermoelectric *figure of merit*

General Overview

Population growth has resulted in a significant increase in energy demand, which requires a higher energy per capita. The world's current energy consumption requirements are increasing day by day and a large part of the current energy supply is highly dependent on fossil fuels as shown in figure 1.

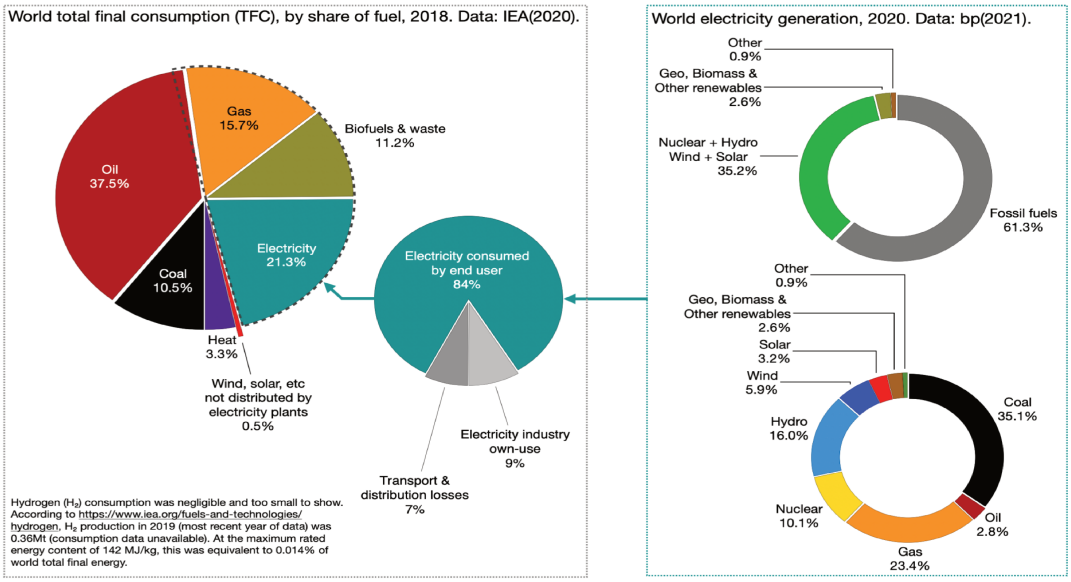

Figure 1: World energy data report 2021, source: [7]

As the name suggests, fossil fuels take millions of years to form and have been consumed a lot faster than that. At the beginning of industrial growth, the amount

of fossil fuel seemed to be inexhaustible, but this is not the case in the 21st century. If we continue to burn them at our current rate, all fossil fuels are expected to be depleted at the end of this century. On the other hand, the burning of fossil fuels emits a large number of greenhouse gases, which are responsible for increasing global warming as shown in figure 2.

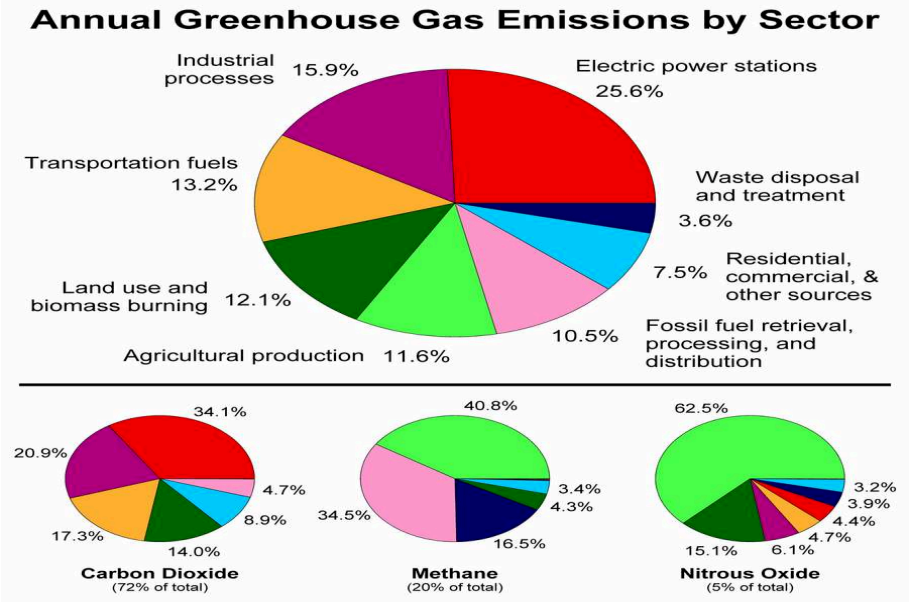

Figure 2: Annual global greenhouse gas emissions by economic sector.

Apart from that, the sea level is also rising due to thermal expansion of water and is expected to cause floods in many cities. The consequences are avoidable only if we limit green house gas emissions and switch to carbon-free green energy sources. Therefore, the world is seeking alternative clean energy options to fulfill the current demands without harmful outcomes. In this case, one of the obvious options to exploit is solar energy. Despite the mature technology of photovoltaics, research is still ongoing in order to achieve cheaper and highly efficient materials [22]. The output of solar panels and wind turbines is just as unpredictable as the weather, yet they are regarded as the epitome of renewable energy solutions. As a result, researchers are working on smart energy grids, clean and more effi-

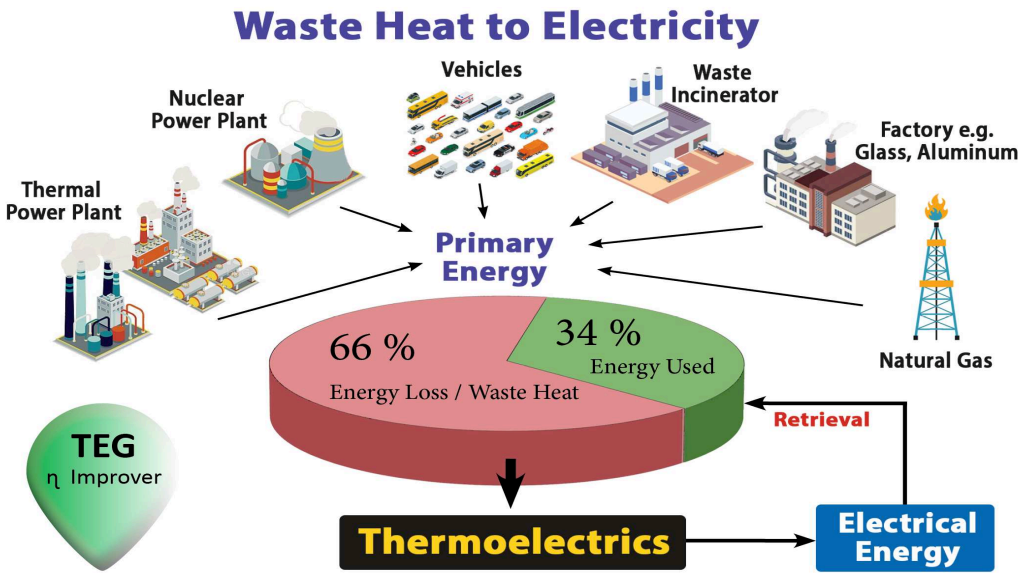

Figure 3: Schematic of the produced waste thermal energy in primary industrial energy sectors [8].

cient batteries and supercapacitors to manage distributed and intermittent power supplies and accelerate the development of electric cars [23, 24]. Nuclear power is another viable option for generating electricity with low emissions, as it emits minimal greenhouse gases and is much safer than fossil fuels [25]. Research into next-generation nuclear power and fusion is crucial to the global energy transition, however, as expanding use of current fission reactors faces a variety of economic and social obstacles [26]. This mix of innovative technologies will unavoidably be the key component of a decarbonized economy, [27] including geothermal [28] and waste heat management by using thermoelectric modules [29].

As shown in figure 3, about 66% of the energy used in primary energy sectors like airplanes, transportation, industries, power plants, etc. is lost as heat [30]. Here, thermoelectric (TE) materials can play an important role by converting heat loss into electricity. Thermoelectric materials have the ability to convert heat into electricity and vice versa. These materials work on the principle of the Seebeck

and Peltier effect. This allows us to take advantage of using waste thermal energy to generate useful electrical energy. Additionally, traditional cooling to eliminate the waste heat from aircraft, automotives, industries, electricity generation, etc. requires additional energy. Therefore, TE materials can be used as an alternative option to the coolant. They have several advantages over conventional coolants, like no requirement for any moving parts, immense reliability, silent operation, no maintenance, etc [31].

Chapter 1

Thermoelectricity: Principles, Materials, and Applications

1.1 Thermoelectric effect

The direct conversion of temperature difference into electrical voltage via a thermocouple is known as the Thermoelectric effect. The scientific and technical branch which studies the thermoelectric effect is known as **Thermoelectricity**. A thermoelectric generator (TEG) creates a potential difference in response to the temperature difference on two sides. Similarly, when the electric potential difference is applied, a temperature difference is built up on the two sides due to the heat transfer from one side to the other. At the atomic scale, the applied temperature difference causes the charge to transfer from the hot side to the cold side. As a result, this effect can be used in generating electricity, measuring the temperature difference or potential difference between the two sides of materials. Thermoelectric materials can be used as temperature controllers as well, because the direction of the cooling and heating is dependent on the polarity of the applied electrical voltage. The thermoelectric effect is based on two fundamental effects, namely, the

Seebeck effect and the Peltier effect. The Seebeck effect was first discovered by the German physicist Thomas Seebeck in 1821, and the Peltier effect was discovered by the French watchmaker Jean Peltier in 1834. Later, in 1851, the link between these two effects was discovered by the W. Thomson (Lord Kelvin) and named after him. In this chapter, we will discuss these three thermoelectric effects briefly.

1.2 Thermodynamic approach of thermoelectric effect

The 1931 theory of Onsager describes a general theory for coupled irreversible thermodynamic processes, such as, electrical conductivity and thermal diffusion in the thermoelectric effect. Onsager considered a non-equilibrium thermodynamic medium with local equilibrium, i.e., the system can be divided into sub-systems in equilibrium with their environment. Onsager's relations connect thermodynamic flows to thermodynamic forces, or affinities. Onsager's relations are obtained by considering the fact that the studied medium is a continuous medium in local equilibrium. The quantities defining the system vary slowly in space and time. Thus, the thermodynamic flows $\overrightarrow{J_i}$, or more precisely, the thermodynamic flow densities, are expressed by a linear combination of the affinities $\overrightarrow{F_j}$, resulting in Onsager relations:

$$\overrightarrow{J_i} = \sum_j L_{ij} \overrightarrow{F_j}, \tag{1.1}$$

where L_{ij} are known as the kinetic coefficients. For example, in the case of two flows $\overrightarrow{J_1}$ and $\overrightarrow{J_2}$ induced by the affinities $\overrightarrow{F_1}$ and $\overrightarrow{F_2}$, we have the following relations:

$$\begin{cases} \overrightarrow{J_1} = L_{11}\overrightarrow{F_1} + L_{12}\overrightarrow{F_2}, \\ \overrightarrow{J_2} = L_{21}\overrightarrow{F_1} + L_{22}\overrightarrow{F_2}. \end{cases} \tag{1.2}$$

Considering the microscopic reversibility [32], Onsager assumed that the action of affinity $\overrightarrow{F_2}$ on flow $\overrightarrow{J_1}$ is identical to the action of affinity $\overrightarrow{F_1}$ on flow $\overrightarrow{J_2}$. This reciprocity is expressed by the relationship below:

$$L_{12} = L_{21}, \tag{1.3}$$

and in general, $L_{ij} = L_{ji}$ for $i \neq j$.

Onsager relations applied to thermoelectricity

The Onsager formalism was first applied to isotropic thermoelectric materials by H. Callen in 1948 [33] and then presented in more detail by S.R. De Groot [34]. Using Onsager's formalism for thermoelectric systems, considering only a gas of electrons, leads to the following two coupled equations:

$$\begin{aligned} \overrightarrow{J_N} &= \frac{\sigma T}{|e|^2}\left(-\frac{\overrightarrow{\nabla}(\mu_e)}{T}\right) + \frac{T^2\sigma S}{|e|}\overrightarrow{\nabla}\left(\frac{1}{T}\right), \\ \overrightarrow{J_Q} &= \frac{T^2\sigma S}{|e|}\left(-\frac{\overrightarrow{\nabla}(\mu_e)}{T}\right) + \left[T^3\sigma S^2 + T^2\kappa\right]\overrightarrow{\nabla}\left(\frac{1}{T}\right), \end{aligned} \tag{1.4}$$

considering,

$$\overrightarrow{\nabla}\left(\frac{1}{T}\right) = -\frac{1}{T^2}\overrightarrow{\nabla}(T) \tag{1.5}$$

where $|e|$ is the elementary charge, μ_e is the electrochemical potential, T is the temperature and $\overrightarrow{\nabla}$ is the gradient operator. The flux density of charged particles

$\overrightarrow{J_N}$ and the thermal flux density $\overrightarrow{J_Q}$ are associated to the associated generalized affinities $-\frac{1}{T}\overrightarrow{\nabla}(\mu_e)$ and $\overrightarrow{\nabla}\left(\frac{1}{T}\right)$, respectively.

The parameters σ, κ, and S are the electrical conductivity, the thermal conductivity, and the Seebeck coefficient, respectively. By analogy with a traditional steam engine, entropy is transported in a thermoelectric system by an electron gas, also known as Fermi gas. The equivalent in a thermoelectric material of a fluid's partial pressure in a steam engine is the electrochemical potential μ_e.

The kinetic coefficients can be identified in accordance with the system of equations, (1.2) [35], by:

$$\begin{aligned} L_{11} &= \frac{\sigma T}{|e|^2}, \\ L_{12} = L_{21} &= \frac{T^2\sigma S}{|e|}, \\ L_{22} &= T^2(T\sigma S^2 + \kappa). \end{aligned} \tag{1.6}$$

where, κ is the thermal conductivity and is written as:

$$\kappa = \kappa_e + \kappa_l, \tag{1.7}$$

where κ_l is the lattice thermal conductivity due to the atomic networks (phonons).

One can also express the electric current flux density $\overrightarrow{J_e}$ instead of the flux density of charged particles by posing $\overrightarrow{J_e} = e\overrightarrow{J_N}$,

$$\begin{aligned} \overrightarrow{J_e} &= -\sigma\left(\frac{\overrightarrow{\nabla}(\mu_e)}{|e|}\right) + T^2\sigma S\overrightarrow{\nabla}\left(\frac{1}{T}\right), \\ \overrightarrow{J_Q} &= -T\sigma S\left(\frac{\overrightarrow{\nabla}(\mu_e)}{|e|}\right) + \left[T^3\sigma S^2 + T^2\kappa\right]\overrightarrow{\nabla}\left(\frac{1}{T}\right), \end{aligned} \tag{1.8}$$

If we consider:

$$\overrightarrow{\nabla}\left(\frac{1}{T}\right) = -\frac{1}{T^2}\overrightarrow{\nabla}(T), \tag{1.9}$$

then, a more convenient form of equation 1.8 can be derived for the equations of thermal current density $\overrightarrow{J_Q}$ and charge current density $\overrightarrow{J_e}$ in a thermoelectric leg:

$$\begin{aligned} \overrightarrow{J_e} &= \sigma \overrightarrow{E} - \sigma S \overrightarrow{\nabla}(T), \\ \overrightarrow{J_Q} &= ST\overrightarrow{J_e} - \kappa \overrightarrow{\nabla} T \end{aligned} \tag{1.10}$$

where,

$$\overrightarrow{E} = -\frac{\overrightarrow{\nabla}(\mu_e)}{|e|} = -\frac{\overrightarrow{\nabla}(\mu_c)}{|e|} - \overrightarrow{\nabla}(V) \tag{1.11}$$

where E is the electric field, μ_{C} is the chemical potential, V is the electrical potential. The second term in first equation 1.10 comes from the Seebeck effect, however the first term in the second equation 1.10 comes from the Peltier effect. The subsequent sections will describe these two effects.

1.3 Thermoelectric Modules: Device performance and *figure of merit ZT*

The Seebeck and Peltier effects are the fundamental principles of the thermoelectric refrigeration and power generation modules, respectively. Figure 1.1 shows the working principle of the thermoelectric power generation module and the same module can be used for the thermoelectric refrigeration as well. The thermoelectric module is made up of an array of these devices connected electrically in series and thermally in parallel. It consists two segments of a p-type (hole carriers) and an n-type (electron carriers) thermoelectric materials to re-enforce the generated current due to Seebeck effect. These two legs exploits the temperature difference between heat sink ($\mathrm{T_C}$) and heat source ($\mathrm{T_H}$) just like the heat engine. These

segments are placed in between the heat sink and source. They are linked to each other and to an external charge resistance (R_C) by a metalized electrical pads. A part of the heat flux (ϕ) exchanged from heat source to the heat sink, through the p and n-type segments is converted into electrical current I, contributes to a power generation (I^2R_C) while ignoring the heat loss by any means. Therefore, the efficiency of the thermoelectric device is given by:

$$\eta = \frac{I^2 R_C}{\phi} \tag{1.12}$$

On solving the equations 1.10 along with the governing equations of charge conservation $\overrightarrow{\nabla}.\overrightarrow{J} = \overrightarrow{0}$ and energy conservation $\overrightarrow{\nabla}.(\overrightarrow{J_Q} + V.\overrightarrow{J_e}) = \overrightarrow{0}$ gives the expression for heat flux ϕ and electrical current assuming constant Seebeck coefficients and conductivities in the thermoelectric legs [36, 37]:

$$\phi = \kappa(T_H - T_C) + ST_H I - \frac{RI^2}{2} \tag{1.13}$$

$$I = \frac{S(T_H - T_C)}{R + R_C} \tag{1.14}$$

where κ, S, and R, are the thermal conductivity, Seebeck coefficient, and electrical resistance of thermoelectric material. T_H and T_C are the temperatures of the heat source and the heat sink. The first term on the right-hand side in equation 1.13 is simply the heat diffusion from heat source to the heat sink in absence of any electrical current. While the second term is related to the Peltier effect and the third term is half of the dissipated energy due to Joule heating in the thermoelectric legs and the remaining half is refused to the heat sink. Electrically, a thermoelectric module is identical to a DC voltage generator of the amplitude $S(T_H - T_C)$ in series with the resistance R, which yields the equation of thermoelectric efficiency, η. On replacing electrical current I and heat flux ϕ in equation

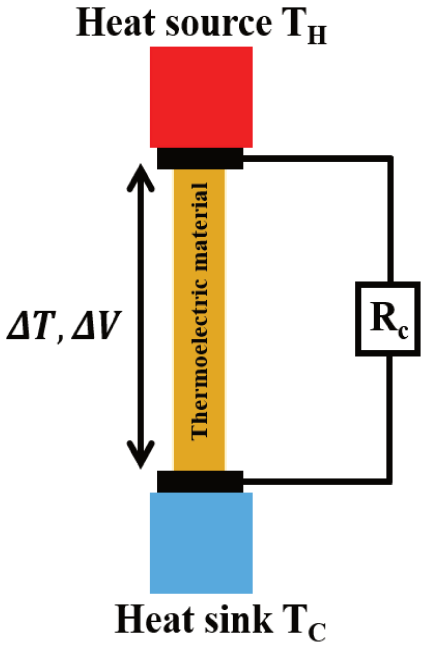

Figure 1.1: Illustration of single leg thermoelectric generator under the influence of applied temperature gradient with external electrical load.

1.12 gives the thermoelectric material efficiency which depends on the resistance (R_C). The efficiency optimization with respect to the resistance (R_C) gives the same order of magnitude as ($R_p + R_n$) and the optimal efficiency as:

$$\eta = \frac{T_H - T_C}{T_H} \frac{\sqrt{1+ZT}-1}{\sqrt{1+ZT}+\frac{T_C}{T_H}} \tag{1.15}$$

where $T = \frac{T_H+T_C}{2}$ and $Z = \frac{S^2}{R\ \kappa}$. By further optimizing the sections of the thermoelectric material to minimize R κ, the thermoelectric ZT becomes:

$$ZT = \frac{S^2\sigma}{\kappa}T \tag{1.16}$$

Similarly, the efficiency of the thermoelectric generator consisting two thermoelectric n-type and p-type legs (schematic shown in figure 1.2) can be obtained by solving the equations 1.10 along with the governing equations of charge conserva-

tion $\vec{\nabla}.\vec{J}=\vec{0}$ and energy conservation $\vec{\nabla}.(\vec{J_Q}+\mathrm{V}.\vec{J_e})=\vec{0}$ gives the expression for heat flux ϕ and electrical current assuming constant Seebeck coefficients and conductivities in the thermoelectric legs [36, 37]:

$$\phi = (\kappa_p + \kappa_n)(T_H - T_C) + (S_p - S_n)T_H I - \frac{(R_p + R_n)I^2}{2} \tag{1.17}$$

$$R_p + R_n + R_C \tag{1.18}$$

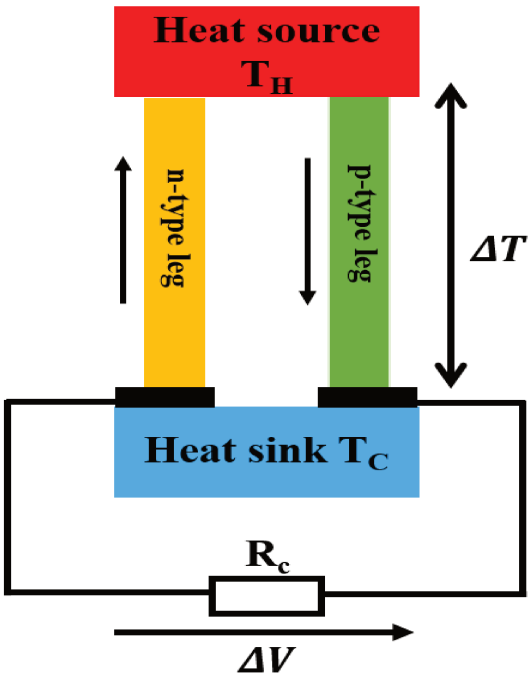

Figure 1.2: Illustration of two leg (n-type and p-type legs) thermoelectric generator under the influence of applied temperature gradient with external electrical load.

Electrically, a thermoelectric module is identical to a DC voltage generator of the amplitude $(\mathrm{S_p} - \mathrm{S_n})(\mathrm{T_H} - \mathrm{T_C})$ in series with the resistance $(\mathrm{R_p} + \mathrm{R_n})$, which yields the thermoelectric efficiency equation. On replacing electrical current I and heat flux ϕ in equation 1.12 gives the device efficiency of the thermoelectric

module which depends on the resistance (R_C) that needs to be dimensionalized according to the thermoelectric module. The efficiency optimization with respect to resistance (RC) provides the same order of magnitude as Rp+ Rn and the optimal efficiency as:

$$\eta = \frac{T_H - T_C}{T_H} \frac{\sqrt{1+\overline{ZT}} - 1}{\sqrt{1+\overline{ZT}} + \frac{T_C}{T_H}} \tag{1.19}$$

where $T = \frac{T_H + T_C}{2}$ and $Z = \frac{(S_p - S_n)^2}{(R_p + R_n)(K_p + K_n)}$. By further optimizing the sections of the legs to minimize $(R_p + R_n)(\kappa_p + \kappa_n)$, the thermoelectric ZT becomes:

$$ZT = \frac{(S_p - S_n)^2}{(\sqrt{\frac{\kappa_p}{\sigma_p}} + \sqrt{\frac{\kappa_n}{\sigma_n}})^2} \overline{T} \tag{1.20}$$

where S_p, κ_p, and σ_p (similarly S_n, S_n, and σ_n) are the Seebeck coefficient, thermal and electrical conductivities of the p-type thermoelectric leg (similarly n-type thermoelectric leg). Here in the equation 1.20, ZT is known as the ***figure of merit*** of the device, and it depends only on intrinsic bulk properties of the thermoelectric material of the legs. It was calculated assuming that the Seebeck coefficients, thermal and electrical conductivities of these materials are uniform, but in reality they are not constant as they are temperature dependent. Therefore, the relevant value is the temperature-average *figure of merit*, ZT. For a given values of T_C and T_H, the optimal efficiency increases with the ZT, and the thermoelectric efficiency η is limited by the Carnot efficiency when $ZT \to \infty$.

The illustrative image of the thermoelectric device and its efficiency as a function of heat source temperature T_H are shown in figure 1.3 and 1.4, respectively. Figure 1.3 shows the thermoelectric device sand-witching many TEM generators connected electrically in series and thermally in parallel through the metal interconnections. These modules are surrounded with the ceramic platings acting as the substrate and encasing. Sometimes the heat exchangers are used to bring

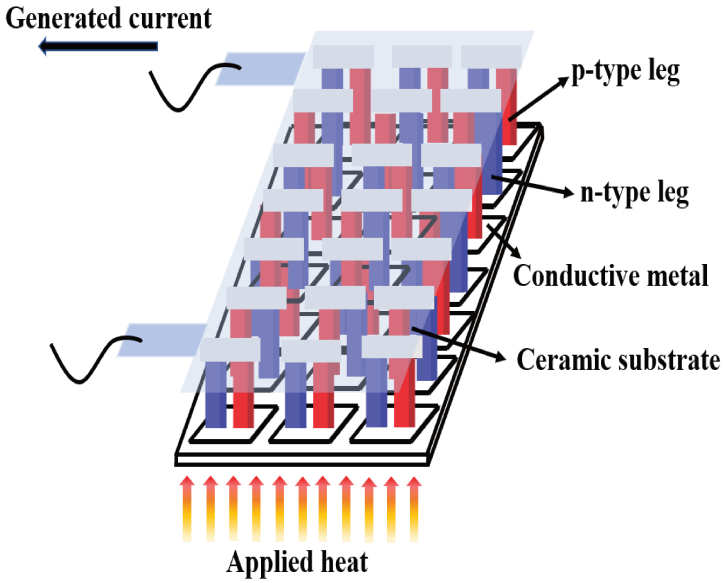

Figure 1.3: Schematic image of a thermoelectric device consisting thermoelectric modules connected through electrical connections and plating from ref. [9].

heat to the heat source and to remove heat from the heat sink in many applications. The material of the legs are optimized in a clever way to attain the better performances, keeping the thermal expansion of p-type and n-type legs in mind. Therefore, these legs are composed of two very similar materials [38, 39].Thermoelectric generators are extremely beneficial, robust, reliable, and highly scalable, with applications ranging from small-scale household appliances to large industries and spacecraft power systems. Yet, their high cost and low efficiency have confined their applications to remote areas or space exploration due to their small size and high reliability.

Figure 1.4 shows the power generation efficiency of thermoelectric module as a function of heat source temperature T_H (considering room temperature as the heat sink temperature i.e. $T_C = 300K$). Currently, the commercially used TEG devices have a *figure of merit* $ZT = 1$, making them much lesser efficient as compared to the

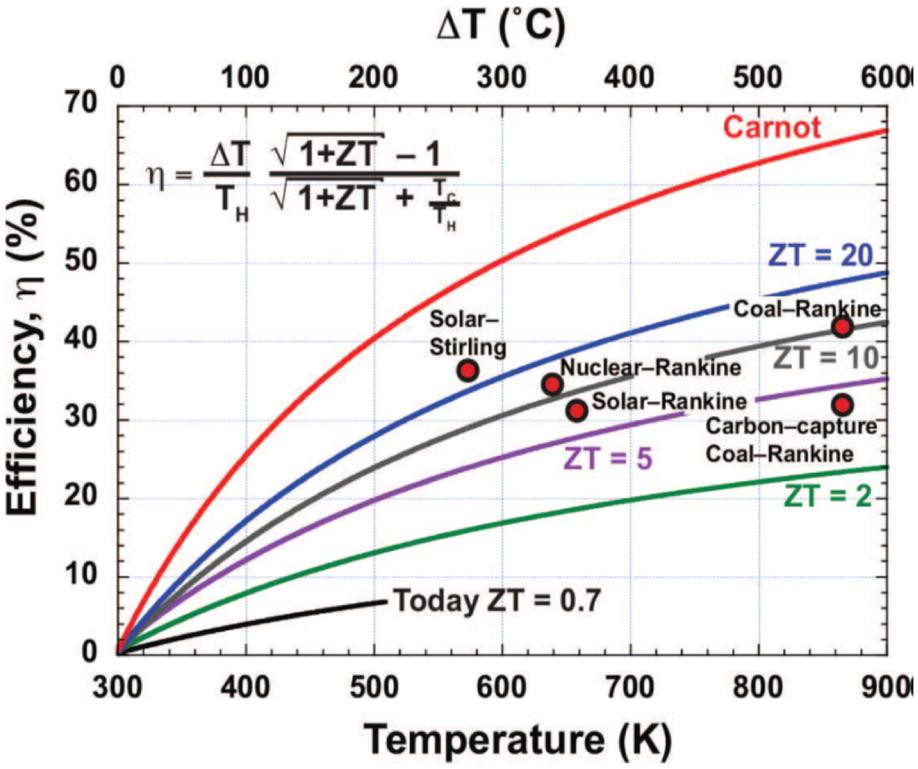

Figure 1.4: Comparison of thermoelectric efficiency as a function of heat source temperature T_H (considering room temperature as the heat sink temperature i.e. $T_C = 300K$) with the efficiency of traditional mechanical engines. Image shows various thermoelectric ZT values with the Carnot limits. The images are taken from the references [10, 11].

heat engines [40,41]. The thermoelectric modules can replace the conventional heat engines in large scale applications only if a remarkable breakthrough will happen, until then they have the advantages limited to the small-scale production [42].

Figure 1.5 shows the applications of thermoelectric generator in various wearable devices as body heat is a sustainable energy source and could be used in small scale day to day life applications and implanted medical devices (IMDs) [43–45]. These medical devices are suitable to track the health conditions of the patients at home or in the hospitals or healthy people to track their daily routine activities. The normal temperature of a human body varies from 27.1°C to 35.2°C depending on the body activity and environmental conditions [46, 47]. There-

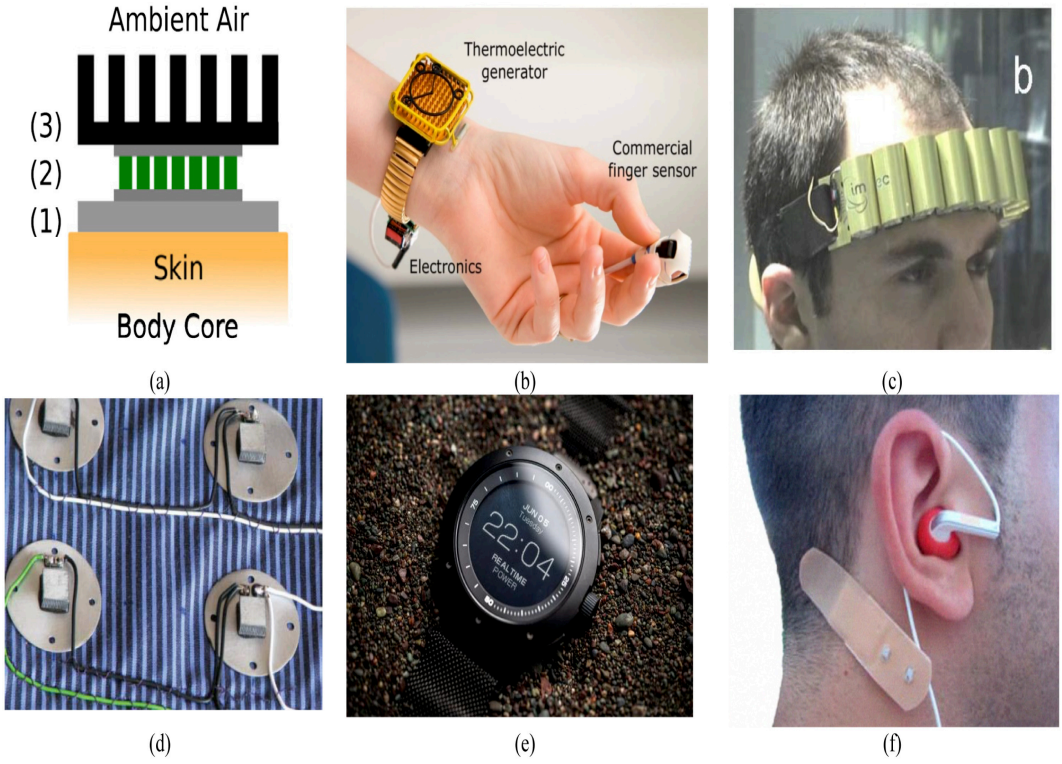

Figure 1.5: Wearable applications of thermoelectric generators (TEG): (a) schematic of a TEG module powered by the body heat with (1) thermal interface between skin and TEG's hot side, (2) TEG module, and (3) heat sink providing the heat dissipation to the ambient air [12], (b) pulse oximeter with CMOS-based TEG made of poly-SiGe TCs [13], (c) Electroencephalography (EEG) headband [13], (d) Electrocardiography (ECG) shirt [14], (e) Matrix Watch powered by body heat and TEG [15], and (f) Biomedical hearing device [16].

fore, the body and the environment have a temperature gradient of around 13°C which is sufficient for the power supply to the wearable devices; especially the implanted medical devices since their maintenance is expensive and time consuming [48]. Figure 1.5(a) shows the schematic for the wearable applications of TEGs where the device is ideally placed vertically in between the skin (heat source) and the environment (heat sink). Figure 1.5(b) shows the wearable pulse oximeter to monitor and control the oxygen saturation in the body operated with the body heat through a watch [49]. Figure 1.5(c) shows the electroencephalography (EEG)

headband device composed of BiTe-based thermoelectric generator, recording the electrical activities of the brain [50]. Additionally, the TEGs are also used in the wearable fabrics and garments [50, 51]. Leonov et al. [52] fabricated a planner CMOS-based thermoelectric generator placed between the skin and the T-shirt as shown in figure 1.5(d). The "Matrix Power Watch" was the first commercialized "Internet of Things" (IoT) smart watch running with the body heat as shown in figure 1.5(e) [53]. Figure 1.5(f) shows the hearing aid device fabricated from a thin film based TEG [54].

1.3.1 Seebeck effect

The phenomenon behind the thermoelectric power generation was discovered by the German scientist Thomas Johann Seebeck in 1821. He discovered that a direct current flows through the closed loop when the junctions of two dissimilar metals are at different temperatures. This effect was named after him and known as **Seebeck effect**. The material could be metal or semiconductor. The current produced through Seebeck effect is however very small and usually measured in μVK^{-1} or mVK^{-1}. Seebeck coefficient is an important parameter to investigate thermoelecrtic properties and is utilized to measure on-site temperature precisely.

During the process, when a temperature gradient is applied across the sample, an induced voltage is developed in response, and majority charge carriers (electrons and holes) start to migrate from hot side (T_H) to cold side (T_H) generating a charge current density $\overrightarrow{J_T}$. The produced current causes an accumulation of charge carriers at the cold side and a depletion at the hot side till a counter-posing voltage difference (ΔV) is induced and further migration of charge carriers is prohibited by the induced electromotive force. Sometimes, apart from the charge carriers, phonons also contribute to Seebeck coefficient. If the phonon-electron interaction is predominant, phonon drags electrons from one side to other and contributes to

Seebeck coefficient. This phenomenon is known as **'Phonon drag effect'**.

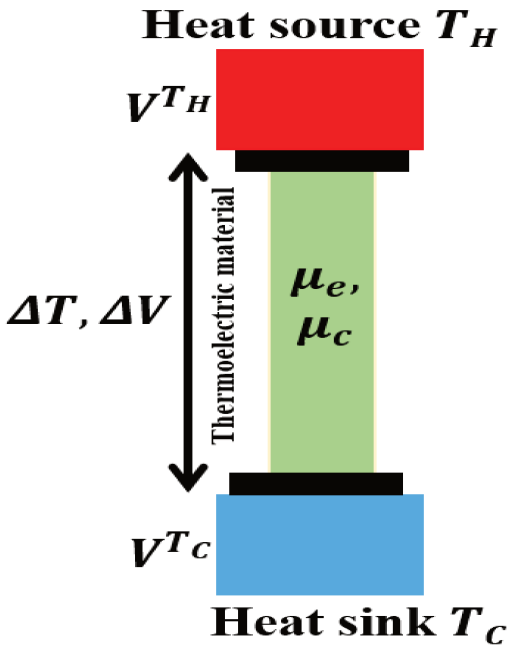

Figure 1.6: Schematic of the thermoelectric circuit with one leg under the influence of temperature difference. The chemical μ_C and electrochemical potential μ_e of the material are also indicated.

Starting from equation 1.10, we have:

$$\overrightarrow{J_e} = \sigma \overrightarrow{E} - \sigma S \overrightarrow{\nabla}(T) \tag{1.21}$$

For a homogeneous material with an electrical conductivity σ:

$$\overrightarrow{J_V} = \sigma \overrightarrow{E} \tag{1.22}$$

and

$$\overrightarrow{J_T} = -\sigma S \overrightarrow{\nabla}(T) \tag{1.23}$$

Considering a thermoelectric material in open circuit and thermodynamically in equilibrium as shown in figure 1.6, the generated current due to the thermal

gradient $\overrightarrow{J_T}$ can be obtained from the balanced equation,:

$$\overrightarrow{J_e} = \overrightarrow{J_V} + \overrightarrow{J_T} = \overrightarrow{0}. \tag{1.24}$$

Now, by separating the electrochemical potential μ_e into chemical potential μ_C and electrostatic potential V for a one-dimensional system, we have:

$$d\mu_e = d\mu_C + |e|\ dV = -|e|\ S\ dT. \tag{1.25}$$

Dividing the above equation 1.25 by |e| and taking the integration on both sides:

$$\frac{1}{|e|}\int_{T_C}^{T_H} d\mu_e = \frac{1}{|e|}\int_{T_C}^{T_H} d\mu_C + \int_{T_C}^{T_H} dV = -\int_{T_C}^{T_H} S\ dT. \tag{1.26}$$

On solving the above equation, we get:

$$\frac{1}{|e|}\left[{\mu_e}^{T_H} - {\mu_e}^{T_C}\right] = \frac{1}{|e|}\left[{\mu_C}^{T_H} - {\mu_C}^{T_C}\right] + \left[V^{T_H} - V^{T_C}\right] = -S\ \left[T_H - T_C\right] \tag{1.27}$$

Considering a unique material throughout the leg, the chemical potential at 2 different points and temperatures will be identical i.e. ${\mu_e}^{T_H}={\mu_e}^{T_C}$ and hence,

$$S = -\frac{V^{T_H} - V^{T_C}}{T_H - T_C} \tag{1.28}$$

This simplified physical picture provides various valuable information. Firstly, the generated potential difference by the Seebeck effect is static. Secondly, the positive or negative sign of the Seebeck coefficient, S, defines the nature of the majority of charge carriers. For instance, the positive and the negative values of the Seebeck coefficient defines the majority of charge carriers due to the holes and electrons, respectively, confirming the p-type and the n-type nature of the material. Thirdly, the bipolar conduction where the minority charge carriers diffuses in the opposite direction to the majority charge carriers reduces the Seebeck coefficient

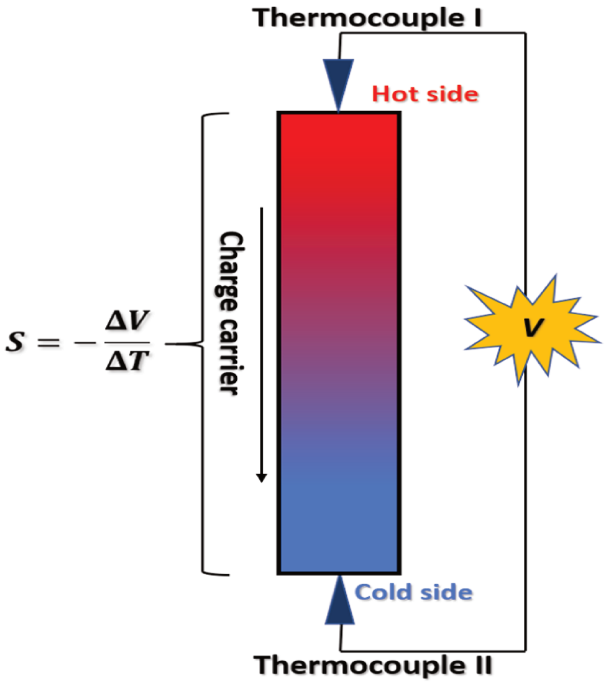

Figure 1.7: Schematic of the Seebeck coefficient measurement cell including the thermocouple used to measure the temperature and potential difference across the sample.

magnitude. As a matter of fact, the bipolar conduction is one of the major limitation of thermoelectric effect at high temperature. At last, good metals suffers from a low Seebeck coefficient since a large compensating current $\overrightarrow{J_V}$ is produced following a small voltage difference ΔV. For example, the Seebeck coefficient for copper (a good metal) is $\approx$ 1 μVK^{-1}, while for bismuth (a semi-metal) and intrinsic silicon (a semiconductor) is $\approx$ -75 μVK^{-1} and $\approx$ 450 μVK^{-1}, respectively. Consequently, the semi-metals or semiconductors are known for their high Seebeck coefficient.

1.3.2 Peltier effect

The Peltier effect is the opposite of the Seebeck effect. It was discovered in 1834 by the French watchmaker Jean Peltier, a few years after the discovery of the

Seebeck effect. According to the Peltier effect, a heat current $\overrightarrow{J_Q}$ begins to flow besides the current flow in response to the applied potential difference across the thermoelectric material. Onsager showed that there is a symmetry between the two effects [55], so that

$$\overrightarrow{J_Q} = S\ T\ \overrightarrow{J_e} \tag{1.29}$$

where the product of Seebeck coefficient and temperature is known as the Peltier coefficient, π i.e. π = S T. The above equation is only valid when the temperature gradient is zero. Unlike the Joule heating effect, the phenomenon of the Peltier effect is a reversible process. The Peltier effect is utilised in temperature control and refrigeration applications for years, and the evolution in the thermoelectric modules will make them strong candidate in heat pumps and domestic refrigerators.

1.3.3 Thomson effect

The third thermoelectric effect is the link between the Seebeck and Peltier effect and it was observed by William Thomson in 1851. According to the Thomson effect, heat exchange from the environment takes place in a material when subjected to the temperature difference and an electrical current I in order to maintain the temperature difference. If the heat dQ is exchanged from the environment by the material at a temperature between T and T+dT is given by:

$$dQ = -\tau\ I\ dT \tag{1.30}$$

where τ could be positive or negative and is known as the Thomson coefficient. Thomson also proved that the Seebeck, Peltier, and Thomson effects are inter-

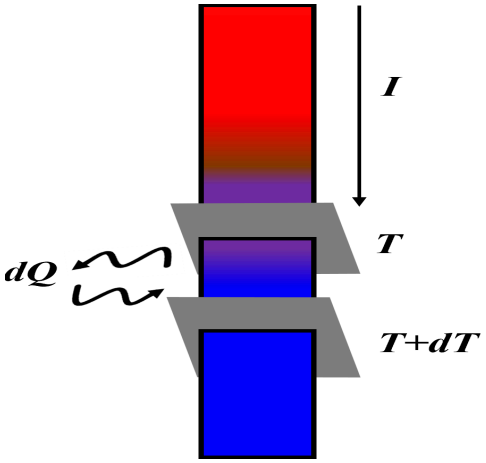

Figure 1.8: Illustration of Thomson effect in a material subjected to the applied current *I* and temperature difference across the sample

related according to the formula:

$$\pi = S\ T \tag{1.31}$$

$$\tau = T\ \frac{dS}{dT} \tag{1.32}$$

These two relations are known as Kelvin's relation. The illustration of Thomson effect in a material is shown in figure 1.8.

1.4 Thermoelectric Materials

As previously discussed, thermoelectric (TE) materials have sparked considerable interest in a wide range of applications, such as, cooling, power generation, sensors, aircraft, etc., due to their ability to convert waste heat into electricity [4, 5, 56, 57]. Refrigerators and generators powered by thermoelectrics were used in specialized applications where their desirable characteristics outweighed their relatively expensive cost and low performance. For instance, thermoelectric generators were

successfully integrated in domestic food refrigerators, stove, air conditioning, mobile charging boots, and cooling of CCD's (charge coupled devices) infrared detectors [58–62]. Radioisotope Thermoelectric Generators(RTG) found their successful application for powering NASA's spacecrafts since 1961 due to their low maintenance and long lifetime, for example Voyager 1 and 2 were launched in 1977 and have already exceeded 37 successful years. Research and development department in the automobile industry are running intensive research programs to recover the waste heat from the exhaust system with an aim to improve the fuel economy by approximately 7-10%. In 2005, BMW has decided to develop a TEG prototype vehicle to transform waste exhaust heat into electrical energy. This project was a part of efficient dynamics program and BMW research team performed the tests on a prototype 5 Series 530i whose exhaust system was equipped with a thermoelectric generator. It generates enough electricity at 125 km/h to keep the car running without an alternator. The concept was applicable on petrol and diesel engines with an advantage of saving 5% fuel i.e. approximately 0.5 liters per 100 km. Initially the manufacturer has planned to begin the production by 2013 [63]. The applicability of the thermoelectric generators (TEGs) in market and industries are shown in figure 1.9.

However, the scientific community is working on finding some more efficient thermoelectric materials for decades. The efficiency of thermoelectric materials is calculated by dimensionless ***figure of merit*** ZT by the following equation:

$$ZT = \frac{S^2 \sigma T}{\kappa} = \frac{S^2 \sigma T}{\kappa_e + \kappa_l} \tag{1.33}$$

Where S, σ, T, and κ are the Seebeck coefficient, electrical conductivity, absolute temperature, and thermal conductivity, respectively. Thermal conductivity has two terms, κ_e and κ_l, associated to the electronic and lattice parameters, re-

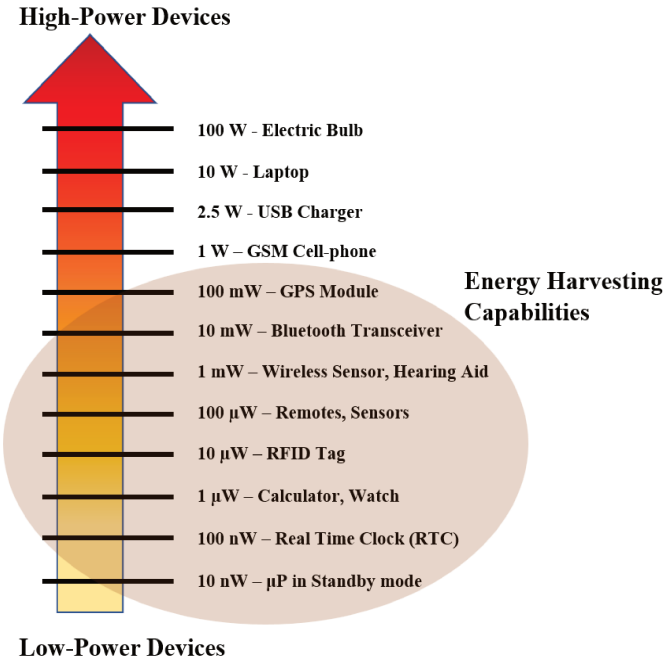

Figure 1.9: A market and industry analysis of subwatt thermoelectric energy harvesting systems. The values are taken from the Tyndall national institute [17].

spectively. The term $S^2\sigma$ is known as thermoelectric ***power factor*** (PF) and plays a very important role in organic TE materials due to their low thermal conductivities. As the upper limit of TE efficiency is given by the Carnot efficiency, however, there is effectively no theoretical limit for ZT and higher values could be achieved by increasing the electrical conductivity and Seebeck coefficient, whilst decreasing the thermal conductivity. Figure 1.10 shows the promising road-map for the thermoelectric technology exploitation over the years. Although, the simultaneous optimization of these parameters at the operating temperature is the main challenge. The contribution of charge carriers to electrical conductivity is linked to the thermal conductivity, according to Wiedemann Franz law, therefore, optimization of the phonon contribution of thermal conductivity is essential to improve thermoelectric ZT.

Moreover, in the bulk state, these three variables are inter-related and a modification in one variable can have an impact on the others. Consequently, a trade-off relationship between thermoelectric parameters is usually sought. However, at the nanoscale, materials behave differently, making it possible to break this correlation and improve TE efficiencies. Therefore, introducing a secondary phase with nano dimensions can do all the work by introducing the lattice mismatch at the interface of matrix and filler. Doping typically increases σ and κ_{e} due to an increase in the number of charge carriers and decreases in κ_l due to phonon scattering [64]. In addition, The Seebeck coefficient could be increased due to the quantum confinement effect, without significantly affecting the electrical conductivity [65]. In the following section, we will discuss the main issues that limit the performance of thermometric materials.

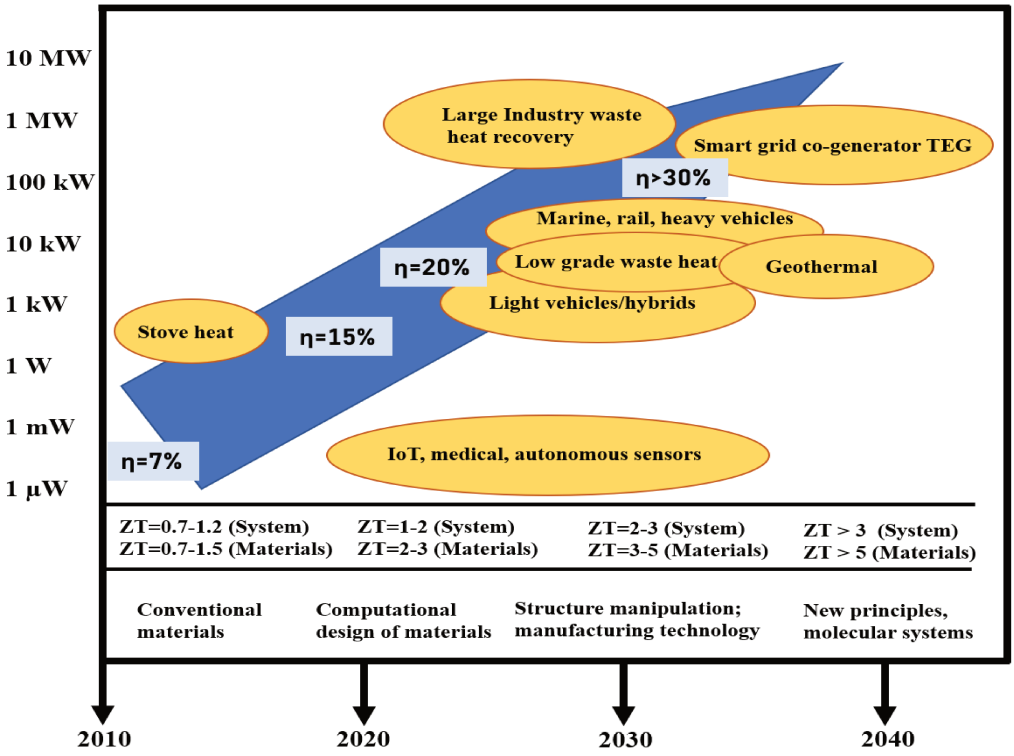

Figure 1.10: The road-map of thermoelectric technology exploitation over the years, where ZT is the thermoelectric *figure of merit* and η is the efficiency [18].

1.5 Challenges

In order to attain a high thermoelectric *figure of merit* ZT, a high Seebeck coefficient (S), electrical conductivity (σ) and low thermal conductivity (κ) is crucial, which is quite challenging in bulk state according to the laws of physics. For instance, in 1853, two German physicists Gustav Wiedemann and Rudolph Franz found out that the ratio of thermal to electrical conductivities ($\frac{\kappa}{\sigma}$) is approximately constant for all the metals at the same temperature. Which means that any material which is good conductor of electricity is also a good conductor of heat and vice-versa. This law was later named after them as Wiedemann-Franz law [66]. This law indicates that the electronic thermal conductivity is directly proportional

to the electrical conductivity as follows:

$$\kappa_e = L\ \sigma\ T, \tag{1.34}$$

where κ_e is the thermal conductivity ($\mathrm{Wm^{-1}K^{-1}}$), σ is the electrical conductivity ($\mathrm{Sm^{-1}}$). The proportionality constant "L" with temperature was firstly discovered by Ludvig Lorenz in 1872 and is known as Lorenz number. Theoretically, Lorentz number is defined by:

$$L = \frac{\kappa_e}{\sigma\ T} = \frac{\pi^2}{3}\ \left(\frac{k_B}{e}\right)^2 \tag{1.35}$$

where $\mathrm{k_B}$ is the Boltzmann's constant ($1.38\mathrm{x}10^{-23}$ $\mathrm{m^2kgs^{-2}K^{-1}}$) and e is the elementary charge ($1.6\mathrm{x}10^{-19}$coulombs). Normally, Lorenz number is treated as a universal factor with $2.44 \times 10^{-8}\mathrm{W\Omega K^{-2}}$ (degenerate limit). However, for non-degenerate semiconductors in which Lorenz number converges to 1.5×10^{-8} $\mathrm{W\Omega K^{-2}}$ for acoustic phonon scattering, it is known that considerable departures from the degenerate limit (about 40 percent or more for Kane bands) can occur. A drop in the Lorenz number is associated with an increase in absolute value of the Seebeck coefficient [67, 68, 68].

In addition to the Wiedmann-Franz law restrictions, Pisarenko's relation restricts the enhancement in S and σ simultaneously. However, this relation is only valid for metals and strongly degenerate semiconductors. The complicated interdependence of these thermoelectric parameters can be summarized as:

$$S = \frac{8\pi^2 k_B^2}{3eh^2}\ m^*T\ \left(\frac{\pi}{3n}\right)^{2/3} \tag{1.36}$$

$$\sigma = ne\mu = \frac{ne^2\tau}{m^*} \tag{1.37}$$

$$\mu = \frac{1}{m^{*5/2}} \tag{1.38}$$

$$\kappa = \kappa_e + \kappa_l = L\ \sigma\ T + \kappa_l \tag{1.39}$$

where, h is the Planck's constant ($6.6210^{-34}\mathrm{m}^2\mathrm{kgs}^{-1}$), m^* is the density of state effective mass, n is the charge carrier concentration, μ is the carrier mobility, τ is the relaxation time, κ is the total thermal conductivity, κ_e is the electronic component of thermal conductivity, κ_l is the lattice thermal conductivity.

The aforementioned relationship explains that the electrical conductivity and Seebeck coefficient share the opposite dependency of charge carrier concentration, mobility, and density of state effective mass. On the other hand, Wiedmann-Franz does not permit increasing electrical conductivity while decreasing thermal conductivity. This complicated relationship between the TE parameters is very strong in the bulk state, which makes it even harder to have a high thermoelectric ZT value. However, great progress has been made in the past few decades by employing various strategies to enhance ZT by switching at least one dimension of the material to the nanoscale. It can break the interdependency of the thermoelectric parameters and make it possible to enhance the thermoelectric ZT [69–71].

1.6 Overview of efficient thermoelectric materials

The urge towards the development of thermoelectric materials began in the mid '90s due to the depletion of fossil fuels and environmental scarcity and interest was shifted towards the search of alternative green and clean energy technologies. In this regard, new projects and concepts were initiated with the aim to break develop

new materials which can break the barrier of ZT $\sim$ 2. In this context, the research areas were explored in the direction of new bulk semiconducting materials with complex and/or open crystal structures, and in the direction of the low dimensional systems such as, quantum dots (0D), quantum wires (1D), and quantum wells (2D), and then the bulk nanostructured materials.

Thermoelectric materials are basically divided into two categories as inorganic and organic materials. Inorganic TE materials include metal chalcogenides (ME_2, where M = a transition metal i.e. Bi, Cr, Pb, Fe etc., and E = S, Se, Te), half Heusler alloys (XYZ, where X and Y are the transition metals and Z is in the p-block i.e. B, C, N, Si etc.), inorganic clathrates (3-D framework with tetravalent and trivalent atoms which enclose guest atoms), skutterudite materials (AB_3 where A is the transition metal element and B is pnictide element such as, P, As, and Sb), metal oxides (M_2O where M is metal such as, Li, Na, Ca etc., and O is oxygen), silicides (MnSi or MS in with $1 \leq n \leq 2$), etc.

The finest compromise for thermoelectric performances is achieved by using semiconductors due to moderate charge carrier concentration as shown in figure 1.11. In past few decades, inorganic materials such as, Bi_2Te_3, PbTeSe, Sb_2Te_3, SiGe, PbTe, PbS, $CdSe_2$, ZnS_2, CdS_2 have been investigated thoroughly due to their high ZT values [72–76]. The alloys such as, $(Bi_{1-x}Sb_x)_2(Te_{1-y}Se_y)_3$ and $Bi_{1-x}Sb_x$ are generally accepted as the state of art materials for effective thermoelectric refrigeration at room temperature and at low temperatures applications, respectively. Additionally, materials such as, $Si_{1-x}Ge_x$ and PbTe were best known for the power generation in high-temperature applications and have a high *figure of merit* ZT of around 2.2 [77]. Figure 1.12 shows the thermoelectric ZT values of the conventional inorganic thermoelectric materials as a function of temperature up-to 1300° C. Despite of all extensive research efforts done on conventional state of art thermoelectric materials, the maximum thermoelectric ZT of around

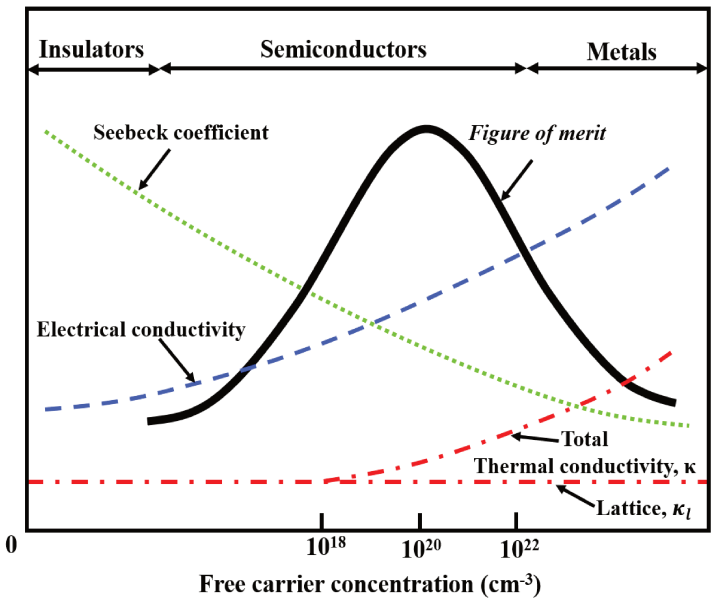

Figure 1.11: Interdependency of thermoelectric parameters, namely, electrical conductivity (σ), thermal conductivity (κ), and Seebeck coefficient S for insulators, semiconductors, and metals as a function of charge carrier concentration.

1 was achieved in the period of 1950 to 1990. The thermoelectric performances were at-least two-times lower than that of the traditional refrigerators. Hence, it is believable the thermoelectric field will bloom in several applications only if the materials with thermoelectric *figure of merit* ZT around 2-3 at low temperatures could be developed. Since 1990's, the thermoelectric performances of Bi_2Te_3, PbTe, and $Si-Ge$ have improved significantly, and many new organic, inorganic, hybrid, etc. compounds have been explored to attain high ZT values. We shall now focus on reviewing the main strategies used for improving the thermoelectric performances.

TE materials have made an amazing progress in past few decades. Most of the conventional inorganic TE materials are based on chalcogenides, for example, Bi_2Te_3, PbTe, SnSe, owing to their high ZT value [78, 79]. The development of efficient inorganic thermoelectric materials is hindered by their high-cost,

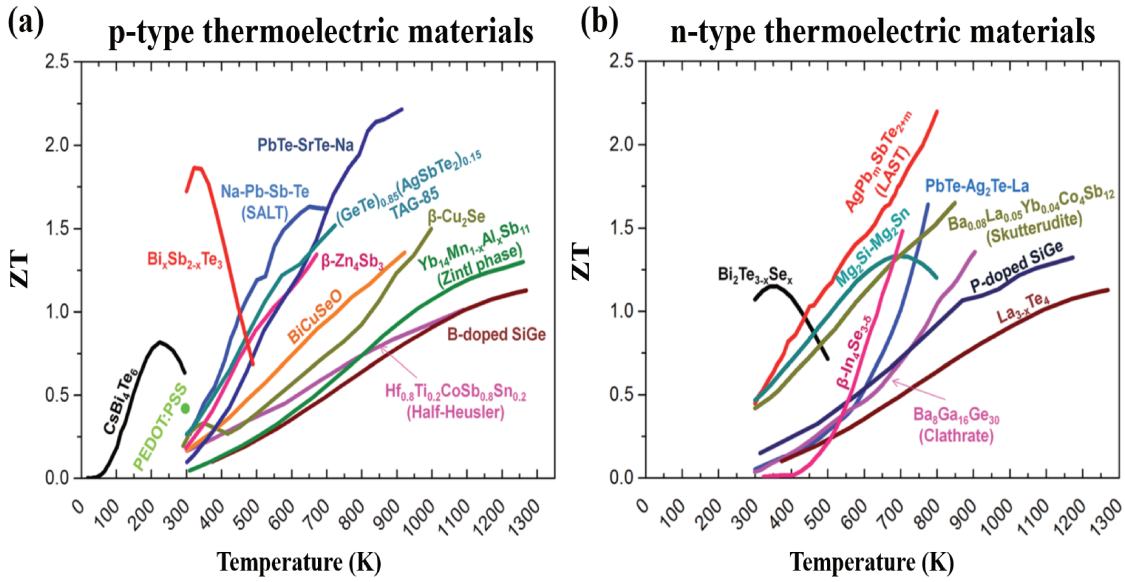

Figure 1.12: Performances of p and n-type thermoelectric materials as a function of temperature [19].

complicated processing, and toxic nature [80, 81]. Hence, to overcome this issue, the focus was shifted towards organic thermoelectric materials. The majority of organic-based thermoelectric studies have been done on conducting polymers, such as, poly(3,4-ethylene dioxythiophene) (PEDOT), polyaniline (PANI), Polypyrrole (PPy), Polyethylene (PE), Polyvinyl chloride (PVC), and their composites due to the ease of processing, low cost, lightweight, and non-toxicity. However, their performances are far behind than those of their inorganic counterparts [82–85]. On contrary, their low thermal conductivity favors gaining a high ZT and can play a vital role in optimizing the thermoelectric parameters. Despite that, enhancement in the electrical conductivity could be emphasized by doping to significantly improve the thermoelectric *figure of merit* ZT.Consequently, utilizing the low thermal conductivity of conjugated polymers and the high Seebeck coefficient of the fillers, the hybrid organic-inorganic approach provides the optimal compromise for producing thermoelectric materials [86, 87]. Therefore, the novel class of conju-

gated/conducting polymers are very popular nowadays due to their high electrical conductivities that make them suitable for thermoelectric applications [88, 89].

Most of the inorganic TE materials are very expensive and toxic in nature. On the contrary, organic materials have several advantages such as, low density, low cost, the ease of synthesis process, low thermal conductivity and non-toxic. However, till date, no organic TE material has achieved the value of ZT of inorganic TE material. Hitherto, best results were obtained on poly(3,4-ethylenedioxythiophene) doped by poly(styrenesulphonate) where a ZT=0.42 was achieved at room temperature.

F. Roussel et al. reported huge enhancement in TE properties of Ag/PANI nanocomposites as compared to pristine PANI samples. Ag/PANI nanocomposites undergoes a percolation type behaviour for electrically conductivity after addition of 16 vol.% of Ag and the best power factor and ZT values of 3 $\mu Wm^{-1}K^{-2}$ and 0.5×10^{-3}, respectively. Usually, the pristine PEDOT: PSS films, prepared from the aqueous solution does not undergo very promising TE properties. Luo et al. treated PEDOT: PSS films with dimethyl sulfoxide (DMSO) and ethylene glycol (EG) to achieve a significant enhancement in electrical conductivity from 0.2 to 900 Scm^{-1}, keeping the Seebeck coefficient almost the same. The obtained P.F. was 30 and 25 $\mu Wm^{-1}K^{-2}$ for DMSO and EG treated films, respectively [90]. Z. Fan et al. reported a maximum power factor of 754 $\mu Wm^{-1}K^{-1}$ and a ZT value of 0.75 for organic TE materials for acid and base treated PEDOT: PSS films, for the first time [91].

Recently, in 2020, W. S. Kim et al., introduced a new approach of tuning the barrier energy to improve the TE behaviour of the PEDOT: PSS/Be_2Te_3 composite by using polar solvent vapor annealing (PSVA). The ratio of PEDOT: PSS was controlled by the exposure timing of PSVA to tune the work function of PEDOT: PSS and ultimately optimize the barrier energy of the thin films [92]. Such

optimization was found very successful and electrical conductivity and Seebeck coefficient were enhanced collaterally up-to 1000 Sm^{-1} and 47μVK^{-1}, respectively for the barrier energy corresponding to 0.11eV. This method allows us not only to tune the work function but also the barrier energy and eventually Seebeck coefficient.

They measured the work function of PEDOT: PSS by using ultraviolet photoelectron spectroscopy (UPS) as a function of PSVA exposure time. The barrier energy between filler Bi_2Te_3 and matrix PEDOT: PSS was calculated by the formula:

$$\Delta E = \phi_{Bi_2Te_3} - \phi_{PEDOT:PSS} \tag{1.40}$$

where, $\phi_{Bi_2Te_3}$ and $\phi_{\text{PEDOT:PSS}}$ are the work functions of Bi_2Te_3 and PEDOT: PSS, respectively.

PEDOT: PSS undergoes semi metallic type band behaviour and the Fermi energy level E_f is situated inside the valence band due to its degenerate semiconductor properties. Initially, for short PSVA timing, there was no energy barrier and all the charge carriers can pass through the barrier due to upward alignment of Bi_2Te_3 valence band. In this region, the Seebeck coefficient as well as the electrical conductivity does not enhanced much. However, for long exposure timings, the downward alignment in Bi_2Te_3 valence band introduces a positive barrier energy and only allows the high energy charge carriers to pass through and scatters off the low energy charge carriers. This facilitates the drastic enhancement in Seebeck coefficient and electrical conductivity. Therefore, the interdependency of Seebeck coefficient and electrical conductivity could be broken by taking advantage of the tuning barrier energy [92].

Carbon-based materials such as, CNTs, graphene, reduced graphene oxide (rGO), and graphene oxide (GO) have high surface to volume ratio and high electrical conductivity [93–95]. Even though, they suffer from a major drawback

of having a high thermal conductivity which acts as a constraint to make them a good TE material [96,97]. X. Tang et al. investigated thermoelectric properties of chiral and zigzag CNTs by using Green's function and non-equilibrium molecular dynamics simulations [98]. Yan et al. synthesized PANI coated CNTs for the first time by an in-situ chemical polymerization process and incorporated them into the PANI matrix by hot pressing method. The observed electrical conductivity, Seebeck coefficient and thermoelectric *figure of merit*, at room temperature, were found to be 2.8×10^3 Scm^{-1}, $21.6\mu\mathrm{VK}^{-1}$ and 1×10^{-3}, respectively, for 30 wt.% of PANI-CNTs loading which is far better than that of the pristine CNTs and neat PANI matrix separately [99]. Sarabia et al. deposited GO doped PEDOT: PSS film on polyethylene terephthalate substrate and treated with hydrazine. The power factor was increased to 47.4 $\mu\mathrm{Wm}^{-1}\mathrm{K}^{-2}$ which is 3.31 times higher as compared to the neat PEDOT: PSS films. The reported value for ZT was 0.084 at 300K, considering the thermal conductivity to be 0.17 $\mathrm{Wm}^{-1}\mathrm{K}^{-1}$ [100].

Similar research has been conducted on CNT/PANI composite with a strong anisotropic thermoelectric behaviour. Chen et al. measured Seebeck coefficient, thermal and electrical conductivities and eventually thermoelectric properties in direction along and vertical to the CNT arrays. The anisotropy in thermal conductivity is way higher ($\kappa_{\parallel}/\kappa_{\perp} = 25$) as compared to electrical conductivity ($\sigma_{\parallel}/\sigma_{\perp} = 6$), where the values were always higher in vertical to CNT arrays. The anisotropy in electrical conductivity was due to the larger carrier mobility in vertical direction as compared to direction along CNT arrays. The possible mechanism was the PANI chain conformation in parallel direction to the CNT due to the $\pi - \pi$ interaction between PANI and CNT [101].

Metal oxides such as, ZnO, TiO_2, MoO_3, MgO etc have been considered as promising TE materials by virtue of their stability, non-toxicity, low cost, easy synthesis process, and tunable transport properties [102–104]. Among all of these

metal oxides, TiO_2 has been extensively studied, benefiting from their tunable semiconductor properties, high Seebeck coefficient, and appealing TE behavior [105, 106].

The importance of TiO_2 in thermoelectrics have been proven by many researches. TiO_2 exhibits very promising TE properties after a proper reduction process to remove the excess oxygen. For instance, J. Tang et al., reported a very large positive Seebeck coefficient of 60,000 μVK^{-1} at 10K with power factor of 170 $\mu WK^{-2}cm^{-1}$ for reduced single crystal of rutile TiO_2. The extraordinarily high Seebeck coefficient values were explained by the phonon drag phenomenon at low temperatures. The observed value for Seebeck coefficient is 4-fold higher than the power factor of Bi_2Te_3 composites near room temperature. They observed a shifting from p-type behaviour to n-type behaviour with increment in temperature which suggested an attractive device application at low temperatures where the same material could be used as n and p type legs in TE generator [107].

L. Xu et al. studied the effect of aluminum doping on TiO_2 nanoparticles. They investigated TE properties at room temperature and at 475 °C. The results indicated that the doping enhanced the electrical conductivity due to the enhancement in charge carrier concentration at the expense of deduction in Seebeck coefficient values. However, they managed to decrease thermal conductivity due to the grain boundary scattering at the interface [108].

Similarly, W. H. Nam et al., proposed an interface controlled strategy to enhance the TE properties of reduced graphene oxide and titanium di-oxide composite ($r - GO - TiO_2$). The composites were prepared by using controlled amount of r-GO content from 0 to 4% by using consolidation of pristine and r-GO coated TiO_2 nanoparticles by plasma sintering technique. The favourable r-GO coating on TiO_2 grain boundaries facilitates the enhancement in electrical conductivity while decreasing thermal conductivity. Their strategy reveals to control the charge and

thermal transport. The electrical conductivity was enhanced upto 20 Scm^{-1} with 4% r-GO content due to the formation of effective charge transport pathways connected by r-GO sheets. Once the percolation is achieved, the enhancement in the electrical conductivity is achieved by the consecutive hopping of the charge carriers from one grain to another at the junction. The maximum TE *figure of merit* ZT of 0.064 was obtained for 4% $r - GO - TiO_2$ nanocomposite [109].

Ali et al. investigated the effect of hydrothermally synthesized molybdenum disulphide nanoparticles (MoS_2) on TE behavior of polyaniline (PANI). The Seebeck coefficient for PANI was observed to be changed from -48.3 to -38.2 $\mu Wm^{-1}K^{-1}$ with 5% doping of MoS_2. In addition, the electrical conductivity was enhanced from 10^{-3} to 0.238 Scm^{-1} and P.F. was increased from 2.99×10^{-4} to 6.3×10^{-2} $\mu Wm^{-1}K^{-2}$ [110].

The Phonon glass electron crystal (PGEC) approach is an interesting strategy for breaking the interdependency of thermolectric parameters, where materials are modified to behave electrically as a crystal and thermally as a glass, helps in accomplishing the desired goal [111]. The aim of this approach is to achieve the decoupling between the electronic and thermal transport quantities by introducing defects acting as phonon back-scattering sites. When the nature and size of the defects are properly selected, the heat transport is then hindered while the electronic transport is not impacted, enhancing the thermoelectric *figure of merit* ZT. A similar approach will be used in this doctoral study, where conducting filler will be embedded in a non-toxic conjugated polymer matrix. We anticipate that the conducting matrix will provide electrically conducting pathways, thereby enhancing the composite's electrical conductivity, while the nanoparticles, acting as defects for thermal transport, will influence the heat flow [112].

1.7 Conclusion

Notwithstanding, many studies have already been done in order to increase the efficiency of organic TE materials, but their performances are far from those currently obtained for inorganic materials. Further investigations are urgently needed in order to improve organic-based thermoelectric systems. To meet the challenge, we combine a low-cost conducting polymer and an inorganic filler with advantageous thermoelectric properties to produce the so-called hybrid organic-inorganic polymeric nanocomposites.

Here in, the goal of this thesis is to enhance the ZT of PEDOT: PSS by incorporating titanium di-oxide quantum-dots decorated graphene oxide (TQDGO) fillers. PEDOT: PSS was used as a matrix due to high electrical conductivity, ease processing, non-toxic nature. Although low Seebeck values of PEDOT: PSS limits the TE performance. Therefore, we chose TQDGO as an inorganic filler in PEDOT: PSS matrix to improve the low Seebeck coefficient. In the present work, TQDGO/PEDOT: PSS polymer nanocomposites have been synthesized by employing oxidative polymerization of EDOT in the presence of titanium di-oxide quantum dot decorated graphene oxide fillers and PSS. As-synthesized samples were characterized by SEM, XRD, TEM, DSC, UV-Vis. spectroscopy, FTIR and their thermoelectric performances were investigated by measuring the thermal conductivity, the electrical conductivity, and the Seebeck coefficient. Sol-gel method has been employed to synthesize TQDGO and it has been used as a template during the polymerization. Thermoelectric behavior of the obtained TQDGO/PEDOT: PSS nanocomposites have been studied for the TE aspects by calculating their thermoelectric ZT [112].

Chapter 2

Polymer nanocomposites for thermoelectric energy conversion

In this chapter, we will discuss the history of conducting polymers. We will focus briefly on Poly (3,4-ethylenedioxythiophene) polystyrene sulphate (PEDOT: PSS) polymer structure, synthesis routes, and thermoelectric applications. The structure and thermoelectric properties of 2-D graphene oxide will then be discussed. Finally, we will concentrate on metal oxide semiconductors, specifically TiO_2 and its molecular structure, as well as various nanostructures, as an efficient means of enhancing their thermoelectric properties. This chapter will provide a concise literature review of the different families of thermoelectric materials implied in this thesis.

2.1 Conducting Polymers

The innovative discovery of conducting polymer poly-acetylene by Hideki Shirakawa, Alan MacDiarmid, and Alan Heerger in 1977 has changed perspectives in the field of organic polymers, which were previously considered non-conducting

plastic materials. In recognition of their discovery, the trio was awarded the Nobel Prize in Chemistry 23 years later. Their collaborative work with MacDiarmid's and Heeger's teams showed that the halogen vapours can enhance the electrical conductivity of trans-poly-acetylene by ten million times. [113]. Since then, remarkable progress in conducting polymers has been made and a lot of research has been conducted on improving the electrical conductivity and stability in the past 30 years [114, 115]. Conducting polymers have been used in various fields such as, photovoltaics, supercapacitors, sensors, biosensors, theromoelectrics, bioelectronics, technical coatings etc [116–122].

These three Nobel Laureates, Shirakawa, MacDiarmid, and Heerger, attempted to dope polyacetylene (PA) by exposing it to halogen vapours in order to decrease the energy gap and increase the carrier density in order to achieve a different level of semiconducting (or even metallic) behavior. The halogenation of the PA is an example of p-type doping where the halogen vapours oxidize the PA chains by extracting electrons and leaving behind positive charges to move freely in the PA to interact with the applied electric field. In general, doping in polymers can reduce the energy band gap and enhance the charge carrier density to make them electrically conducting or semiconducting. Furthermore, organic chemists realized that the use of (hetero)-aromatic rings makes it possible to design undoped polymers with tunable intrinsic (semi)-conducting properties. The field of conducting polymers was flooded with different processing strategies and synthesis routes in order to improve the conductivity right after the initial discovery of conducting polymers in the 1980s.

The term "conducting polymer" is referred to any π-conjugated polymer consisting of an alternating single and double/triple covalent bond backbone which can conduct irrespective of their individual conductivities. For example, polyaniline (PANI), polypyrrole (PPy), Poly (3,4-ethylenedioxythiophene) polystyrene sul-

phate (PEDOT: PSS), Poly (3-hexylthiophene) (P3HT), Poly(2,5-bis (3- alkylthiophene -2-yl) thieno [3,2-b]thiophenes) (PBTTTs), poly benzimidazobenzophenanthroline (BBL) etc [123]. Prior to the discovery of conducting polyacetylene (PA); the conducting polymer prototype was poly(sulfur nitride) $(SN)_x$ which exhibits the intrinsic metallic conductivity where electrons move freely over long (ballistic) distances in a partially filled conduction band [124]. In $(SN)_x$, all bonds are of equal length, which means that the bond length alternation (BLA) along the chain is zero, a crucial characteristic for achieving high conductivity. However, to make polyacetylene (PA) more energetically stable, it has been proposed that the chain should have a BLA $\neq 0$, which creates an energy band gap E_g and makes it electrically insulating.

The macro-molecules in conducting polymer chains are connected via weaker $\pi - \pi$, van der walls, and dipole interactions unlike in the inorganic semiconductors where the strong covalent bonds are holding the atoms together. Such bonds are sufficiently strong to impede solution-based processing of first-generation conducting polymers. However, molecular engineering makes it possible to redesign or rearrange the side chains to enable solution-based processing, thereby conferring several advantages on organic CPs over traditional first-generation inorganic CPs [125, 126].

In-depth understanding of co-relations between molecular and electronic structures allowed the researchers to synthesize intrinsically conducting or semiconducting polymers. In the 1990s, organic conducting polymers flooded the market with various applications due to their excellent mechanical, electrical, optical, optoelectronic, and lighting properties. In the meantime, scientists have found a lot of new organic CPs, like polythiophene (PTH), polypyrrole (PPy), poly (paraphenylene) (PPP), polyaniline (PANI), polyazulene (PAZ), etc [127–132]. Of these, the polyaniline family stands out due to its ability to produce processable conduc-

tive forms in bulk quantities at low cost [133]. Due to the potential presence of benzidine moieties in the polymer backbone, which could produce toxic (carcinogenic) byproducts upon degradation, a number of industrial and academic groups have restricted their polyaniline chemistry research. Although (hetero)aromatic polypyrrole, polythiophene, and poly (p-phenylene vinylene) are potentially more environmentally friendly, however, they are insoluble and infusible. Numerous substituted derivatives of these polymers with alkyl, alkoxy, and other substituents along their backbones have been developed to address these issues [134]. By manipulating the main-chain framework (e.g., regioregularity [127]) and pendant group chemistry (e.g., water-soluble sulfonates [135]), a wide range of properties was availed from the parent structures. Despite the fact that these side-chains provide some degree of control over the physical and electronic properties, the ultimate accessible electronic properties are frequently diminished compared to the parent. In the latter half of the 1980s, researchers at the Bayer AG research laboratories in Germany created a new polythiophene derivative, poly (3,4-ethylenedioxythiophene) (PEDOT).

Among all other organic electrically conducting polymers, PEDOT: PSS is the most successful polymer in terms of several practical applications due to its exceptionally high hole conductivity (300 S cm^{-1}), flexibility, optical transparency for visible light, light weight, commercially available aqueous solution for easy processing, high work function, good thermal and chemical stability, large scale production, tunable conductivity, low surface roughness, and mechanical stability etc [136–139].

2.2 PEDOT: PSS

Poly (3,4-ethylenedioxythiophene) polystyrene sulphate (PEDOT: PSS) is a conducting polymer, benefiting from its electronic and ionic conductivities. PEDOT was first reported by the scientists at Bayer research laboratories in Germany. An effort has been made in order to synthesize a dispersible conducting polymer lacking unwanted α, β- and β, β- coupling in its polymer chain backbone. PEDOT derived from oxidative or electrochemical polymerization was initially discovered to be insoluble despite having very promising properties. In addition to its high electrical conductivity, it was discovered that the oxidized thin film was nearly transparent and extremely stable. Later, the solubility problem was resolved by the addition of a water-soluble counter ion in the form of poly (styrene sulphonic acid) (PSS). The addition of PSS to PEDOT produced a transparent, electrically conductive polymer with excellent stability and film-forming capability [140–145].

2.2.1 PEDOT: PSS Structure

PEDOT: PSS is composed of two ionic polymers, positively charged PEDOT conjugated polymer chains are attached to the negatively charged PSS chains. PEDOT is derived from the monomer ethylene dioxythiophene in the presence of the PSS, acting as a template during the polymerization process. The chemical structure of PEDOT: PSS is shown in figure 2.1. In general, conducting polymers cannot dissolve in solvent, limiting their applications. However, Baytron G changed the whole game after adding PSS and making the PEDOT: PSS dispersible in water and other solvents. PSS in PEDOT not only acts as a counter ion but also as a surfactant, assisting in the dispersal and stabilization of the polymer in water or other solutions such as, water, ethyl alcohol, chloroform, etc. to form uniform thin films [146]. Unlike the other polymer dispersion solutions, PEDOT

does not disperse in the PSS aqueous solution rather PEDOT: PSS as a single entity is captured by the outer PSS- aqueous media. PEDOT:PSS dispersions are composed of gel-like particulates surrounded by a polyanion (PSS)-rich shell that stabilizes PEDOT-enriched particles in aqueous solvents [147]. This is the fundamental reason for the exceptional stability of PEDOT: PSS solution [148]. PEDOT oligomers are assumed to polymerize onto the PSS template, implying that PEDOT is intrinsically ill-defined in terms of molecular weight and polydispersity. These gel-like particulates indicate π-stacking. The PEDOT:PSS structure has been intensively analyzed to examine and improve hole transport for optoelectronic devices [147, 149–152]. Changes in formulation composition, processing, or post-processing have been shown to improve hole conductivity by eliciting conformational changes, reducing surplus dopant phase (i.e., insulating PSS), or both. A comprehensive analysis of the methodologies and suggested mechanisms for enhancing conductivity can be found in the ref. [153]. The aqueous PEDOT: PSS is dark blue opaque solution and it was commercialized for the first time under the name of Baytron P (current name Clevios$^{\text{TM}}$). The aqueous solution is handy and easily forms a thin layer on a solid or flexible surface such as, glass, silicon wafer, PVA film, PC, etc. by using different techniques such as, spin coating, dip coating, slot die coating, doctor blade, screen printing, spray deposition, etc [146].

PEDOT chains are much shorter than PSS chains and contains only a few tens of monomers [154, 155]. Various studies have shown the PEDOT polymer consists of 10–20 monomers by using high angle annular dark-field (HAADF) images of o-CVD PEDOT, scanning tunneling microscopic images of electro-polymerized PEDOT, and transmission electron microscopic images of solution cast polymerized PEDOT [156, 157]. Generally, neutral PEDOT stays in an aromatic state, but distortion caused by doping could result in transformation from aromatic to quinoid states as shown in figure 2.2 [158]. Figure 2.2 shows the molecular struc-

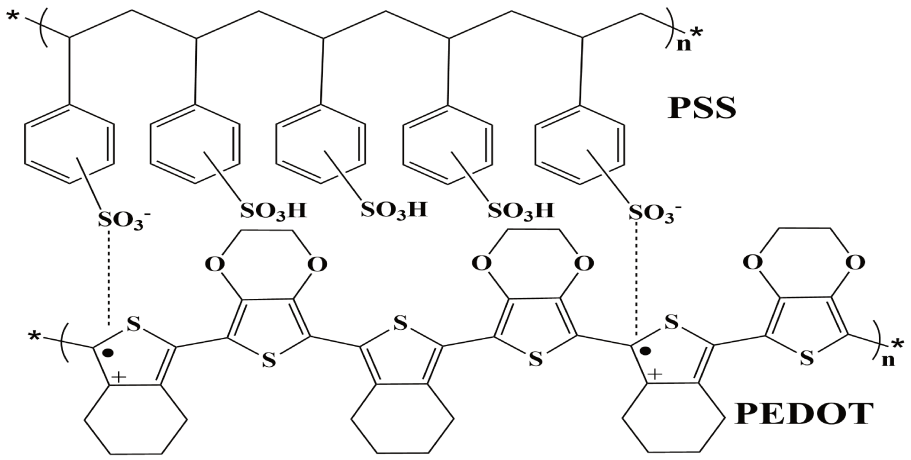

Figure 2.1: Molecular structure of PEDOT: PSS.

ture transformation of PEDOT to form neutral, polaron, and bipolaron states after doping.

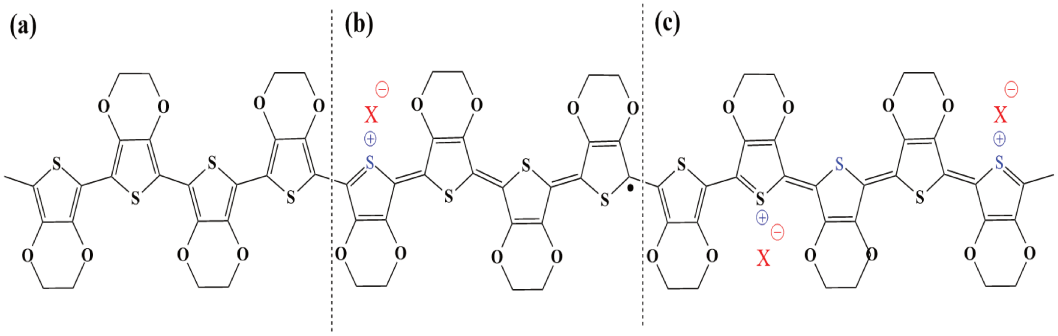

Figure 2.2: Molecular structure transformation of PEDOT from (a) neutral state to (b) polaron, and (c) bipolaron after doping.

2.2.2 PEDOT: PSS synthesis routes

The synthesis route of polymer PEDOT: PSS consists of polymerization of EDOT monomer in presence of PSS and it can be divided into three parts, Oxidative Chemical polymerization, electrochemical polymerization, and transition metal catalysis. Chemical oxidative polymerization is a relatively easy processing route

for the PEDOT: PSS synthesis. Several kinds of processes and oxidative agents can be used during the process. Ferric chloride ($Fe(Cl)_3$) and Iron(III) Tosylate ($Fe(OTs)_3$) are examples of classical oxidizing agents. The final product after polymerization is a deep bluish black solution which is easily dispersible in polar solvents such as, water, tetrahydrofuran, chloroform, dichloromethane, etc.

The ratio of $Fe(Cl)_3$: EDOT also plays an important role. For instance, Kumar and Reynolds showed that if the ratio is greater than two, it makes the final product partially non-dispersible. Also, for $Fe(Cl)_3$/EDOT greater than five, causes a complete non-dispersible polymer in organic solvents [159]. D.M. Leeuw et al. synthesized PEDOT by using $Fe(OTs)_3$ as an oxidizing agent in the presence of imidazole in n-butanol solution. The resultant solution was then filtered and spun on the glass substrate and baked on the hot plate at 110°C for 5 minutes or in a convection furnace. The polymerization process took place during the heating, and the obtained films were washed with n-butanol or water to remove the residual iron (II) salts. The polymerization process is shown in the figure 2.3. The sheet resistance of the above mentioned film was obtained to be 200 Ωsq^{-1} and electrical conductivity of 300 S cm^{-1} [20].

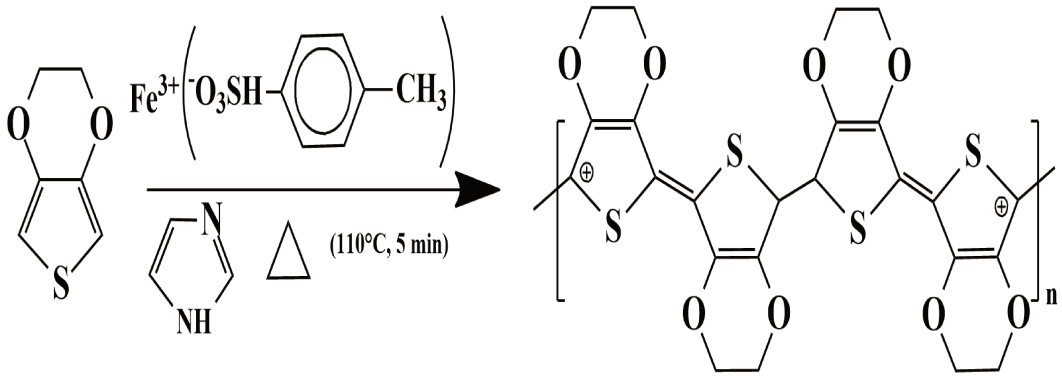

Figure 2.3: Oxidative coupling of edot in the presence of iron (III) p-toluenesulfate leads to the formation of the conducting polymer PEDOT [20].

Similarly, P Sakunpongpitiporn et al. used $Na_2S_2O_8$ as an oxidizing agent for

the polymerization. They optimized the ratio of $Na_2S_2O_8$: EDOT and PEDOT: PSS on the electrical conductivity. For the synthesis, EDOT was mixed with a various amount of PSS (1-13 weight ratios) and the amount of the $Na_2S_2O_8$ was fixed equal to the EDOT molar mass. The ingredients were combined with the water, and the solution was stirred at room temperature for 24 hours. The obtained polymer was centrifuged at 9000 rpm and washed with the mixture of acetone and methanol, and dried at 60°C. The electrical conductivity for EDOT: PSS weight ratios ranging from 1 to 5 was decreased from 452.81 ∓ 31.59 to 250.23 ∓ 13 S cm^{-1} which signifies the low amount of PSS acts as an insulator and inhibits the charge transport. However, the conductivity was observed to be increased from 250.23 ∓ 85.13 to 999.74 ∓ 10.86 S cm^{-1} for EDOT: PSS weight ratios ranging from 5 to 11. The enhancement is justified by the fact that the PSS starts to act as a dopant and enhances the charge carrier concentration. The XPS and UV-vis spectroscopy findings support the above mentioned argument. Nevertheless, the conductivity was decreased for further enhancement in EDOT: PSS weight ratio (1:13) to 524.23 ∓ 42.29 S cm^{-1} due to excessive doping [160].

The optimized value for EDOT: PSS weight ratio of 1:12 was used for the further investigation where the amount of the oxidant was varied. The same synthesis procedure was used with the different values of $Na_2S_2O_8$ ranging from 1:1 to 1:4. Initially, the electrical conductivity was increased from 999.74∓10.86 to 1556.85∓46.84 Scm^{-1} for 1:1 and 1:2, respectively, as the SO_4^{2-} can also acts as dopant. Further enhancement in the oxidant amount produces PSSNa, which in turn reduces the amount of PSS dopant and hence reduces the conductivity to 55.61 ∓0.10 Scm^{-1}. Hence, the maximum electrical conductivity was obtained for the EDOT: PSS and EDOT: $Na_2S_2O_8$ weight ratios were 1:11 and 1:2; respectively [160].

Another method for the polymerization was discovered by Bayer G, which is

the most successful method till date and is known as the BAYTRON P synthesis method. The polymerization of EDOT is conducted in aqueous media containing poly-electrolyte solution, most commonly PSS, by using $Na_2S_2O_8$ as an oxidizing agent. The reaction kept at room temperature forms a deep blue opaque PEDOT: PSS dispersion, which is insoluble in most of the solvents. Interestingly, the dispersion leaves behind a very conducting, transparent, and mechanically durable film after drying. Initially, the commercially available PEDOT: PSS dispersion was only used in the photographic industry; however, as time passed, PEDOT: PSS found many applications in other industries as well, and it is now commercially available in a variety of industries [146, 147, 149–152].

Apart from being utilized in large scale industrial applications, the actual charge transport mechanism in PEDOT: PSS is only partially understood. Various processes have been suggested to optimize the electrical conductivities of PEDOT: PSS, such as, solvent treatment by using ethylene glycol, dimethyl sulfoxide, sorbitol, etc., acid treatment by hydrochloric acid, sulfuric acid, formic acid, etc. Such treatments bring conformational and/or structural and morphological changes in polymer chains. The PSS chains are longer than PEDOT chains, and the resulting conductivity strongly varies with the morphological modifications. For instance, electrical conductivity measurements with temperature show a high in-plane conductivity due to the variable range hopping phenomenon. However, out-of-plane conductivity firmly decreases due to the nearest neighboring hopping. Above mentioned, solvent processing alters the lateral charge transport mechanism from a 3D to a quasi-1D variable range hopping effect [153,161–165]. The challenge to demonstrate the exact mechanism behind the charge transport is that the conductivity (σ) depends on the number of charge carriers (n) and mobility (μ), $\sigma = ne\mu$, where e is the elementary charge. Therefore, it is difficult to find if the enhancement in the conductivity is due to the charge carrier concentration or mobility, especially

in doped materials such as, polymer PEDOT: PSS [166].

2.2.3 Thermoelectric properties of PEDOT: PSS

Researchers have utilized a variety of post-treatments to enhance the TE performance of PEDOT: PSS by increasing its electrical conductivity and Seebeck coefficient. Many studies have suggested that one of the straightforward methods to attain this is the post-treatment with polar solvents with high boiling temperatures, such as dimethyl sulfoxide (DMSO), dimethyl formamide (DMF), ethylene glycol (EG), isopropyl alcohol (IPA), etc. These solvents are capable of initiating a phase separation in PEDOT: PSS to form an interconnected chain network of elongated crystalline PEDOT phase to amplify the electrical conductivities up to 3 times without compensating the Seebeck coefficient [77, 167–170].

Researchers have been investigating the effect of chemical de-doping of PEDOT: PSS to enhance the electrical conductivity in the past decade. H. Park et al. treated PEDOT: PSS thin films by over-coating with a mixture of DMSO and hydrazine. This process removed the excess PSS chains, leaving behind the PEDOT in a neutral state and obtaining the highest power factor of 112 $\mu \mathrm{Wm}^{-1}\mathrm{K}^{-2}$ by optimizing hydrazine concentration in DMSO at room temperature. Apart from the removal of PSS, the enhancement in electrical conductivity was achieved due to the annealing process during the treatment, which modified PEDOT conformation from a densely coiled structure to a linear or expanded coil structure [171].

T. Stoker et al. investigated the effect of PSS on the electrical conductivity of PEDOT: PSS and eventually studied the thermoelectric properties [172]. Electrical conductivity decreases with PSS content, although it is necessary to enhance the processibility of PEDOT. The PEDOT to PSS ratios from 1:2.5 to 1:20 show the conductivities in the range of 1 to 10^{-5} S m^{-1}. The optimized PEDOT: PSS ratio is 1:6 with conductivity around 10^{-3} S m^{-1} for the organic light emitting diodes,

where PEDOT: PSS acts as a hole transport layer. They investigated the PEDOT: PSS ratio from 1:1 to 1:20 and reported the constant carrier concentration despite different PSS content, which suggests that PSS content does not change the doping level in the polymer [172].

Graphene oxide has been studied for TE behaviour by researchers in past decade as it is much cheaper and homogeneously dispersed in PEDOT: PSS as both are hydrophilic in nature. F. Li. et al. [108], investigated the effect of reduced Graphene oxide (r-GO) onto the TE properties of PEDOT: PSS. They reduced GO to r-GO in PEDOT: PSS thin films by using hydrogen iodide (HI).The electrical conductivity of the r-GO PEDOT: PSS thin films was decreased while the Seebeck coefficient was increased due to the decrement in the oxidation level of the polymer as concluded by the XPS studies. However, the electrical conductivity was enhanced with the r-GO content owing to its interaction with the polymer matrix, which provides the conducting channels for charge transport; and also, the sheet-like structure of r-GO pushes PEDOT: PSS to pack more orderly films. The Seebeck coefficient was also increased with the r-GO content due to the synergic effect of the polymer with the filler. Simultaneous increments in Seebeck coefficient and electrical conductivities were expected due to the energy filtering effect due to the nanostructred r-GO sheets. The maximum power factor of 32.6 $\mu \mathrm{Wm}^{-1}\mathrm{K}^{-2}$ was observed for 3% r-GO, which was 50% larger than the neat PEDOT: PSS films. The maximum thermoelectric ZT value of 0.03 was observed for the same sample after considering thermal conductivity to be 0.3 $\mathrm{Wm}^{-1}\mathrm{K}^{-1}$, which is higher than the ZT value (0.021) of graphene-PEDOT: PSS films reported by Y. Du et al. [108].

Fundamental physics suggests that the Seebeck coefficient depends upon the energy band structure and density of states (DOS) near to the Fermi energy level. Doping can tune both of them and facilitate the improvement of the Seebeck

coefficient. It has been observed for the first time in thallium (Tl) doped PbTe, which enhanced the effective mass and elevated the Seebeck coefficient for the first time by introducing distortion in the density of states. It occurs when doping coerces the valence/conduction band to resonate with the energy level of a localized impurity. Such distortion in DOS enhanced TE ZT up to 1.5 at 773 K [173, 174]. Accumulating this new phenomenon with the techniques which lower the thermal conductivity could boost the ZT values and can be directly applied in thermoelectric systems, e.g., aluminium doped PbSe and indium doped SnTe [175–177].

The carrier concentration of PEDOT: PSS is maximized by adding an excessive amount of PSS due to the much lower doping efficiencies of conjugated polymers [178, 179]. The liberated and non complex PSS chains, which are electrically insulating and do not assist in the doping of PEDOT, unnecessary occupies the volume in the polymer. Hence, the electrical conductivity of PEDOT: PSS can be successfully enhanced by removing the extra non complexed PSS chains. The excessive amount of insulating PSS chains can be removed by employing several after treatments such as, ethylene glycol, dimethyl sulfoxide, sulfuric acid, etc. in order to enhance the thermoelectric performance of PEDOT: PSS [72, 180–182].

Gong et al. introduced DMSO and poly (ethylene oxide) (PEO) as binary dopants to PEDOT: PSS and prepared the PEDOT:PSS thin films by spin coating. They observed, for the first time, simultaneous increases in the Seebeck coefficient and electrical conductivity. PEDOT: PSS thin films with 5 wt.% DMSO and 0.3 wt.% PEO exhibited a high Seebeck coefficient of 40 μVK^{-1} and an electrical conductivity of 1300 Scm $^{-1}$ to achieve a high power factor of 157.23 μWm^{-1}K^{-2} [183]. They attributed the enhanced TE property to the polaron to bipolaron conversion due to the PEO [77, 148, 184, 185].

Similarly, Fan et al. accomplished a 2-10 times higher power factor for PEDOT:

PSS thin films by treating them with sulfuric acid and then adjusting the pH values with NaOH. An optimized power factor of 334 $\mu Wm^{-1}K^{-2}$ was achieved by adjusting electrical conductivity and the Seebeck coefficient. They found that the electrical conductivity enhanced up to 3000 S cm^{-1} with acid treatment due to PSS removal and the formation of a nanosized fibrous structure, which enhanced the charge mobility without affecting the Seebeck coefficient. However, NaOH treatment decreased electrical conductivity but enhanced the Seebeck coefficient from 17 to 39 μVK^{-1} due to the execution of low oxidation level [72].

S.K. Kim reported a two-step after treatment of PEDOT: PSS thin films to enhance the power factor from 0.0097 $\mu Wm^{-1}K^{-2}$ to 13.3 $\pm$ 1.5 $\mu Wm^{-1}K^{-2}$. Initially, the thin films were treated with ethylene glycol to reduce the excess amount of PSS, which enhanced the power factor upto 6.31 $\pm$ 0.071 $\mu Wm^{-1}K^{-2}$. After that, the oxidation level of PEDOT was controlled by hydrazine treatment to further enhance the power factor to 13.3 $\pm$ 1.5 $\mu Wm^{-1}K^{-2}$ [186]. Such a chemical de-doping process enhances the TE properties by transforming the bipolaron state of PEDOT to polaron or neutral, which decreases the oxidation level and carrier concentration to tune TE properties.

2.3 Graphene Oxide

Graphene oxide (GO) is a graphene-based material that has gained much attention in the last two decades due to its low cost, scalable and straightforward synthesis process. It is obtained from the oxidation of graphite, and each layer of GO consists of an oxidized graphene sheet [187]. It is a useful and promising material for graphene-based electrical, optical, chemical, energy storage, and biological applications. Due to their exceptional mechanical, electrical, thermal, and barrier capabilities, graphene-based nanocomposites have been a popular topic of study

over the past decade. However, at the beginning of graphene's existence, GO were merely a simple and inexpensive step for the reduction-based synthesis of single and multilayer graphene films and its bulk structures. As a result of flaws in the initial graphite and an incomplete reduction process, additional research indicated that graphene oxide-derived materials have a significantly defective structure. Recent research has proven that graphene oxide possesses a number of unique chemical, optical, and electrical properties that qualify it as an independent nanomaterial with a wide range of uses due to the presence of chemical groups on its surface [188]. In contrast to conventional graphene, it offers an extensive range of chemical techniques for the attachment of functional groups to its surface in order to regulate optical transparency, electrical and thermal conductivity [94].

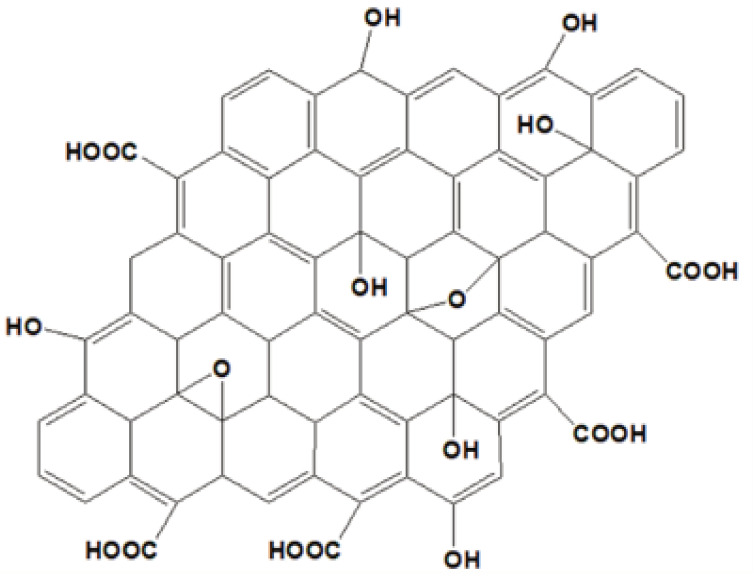

Figure 2.4: Molecular structure of graphene oxide.

2.3.1 Structure of graphene oxide

Graphene oxide (GO) is a 2-dimensional (2D) sheet of sp^2-hybridized (significantly) and sp^3-hybridized (partially) carbon atoms in a honeycomb structure containing hydroxyl (-OH), alkoxy (C-O-C), carbonyl (C=O), carboxylic acid (-COOH), and other oxygen-based functional groups. These oxygenated groups give it many advantages over graphene, such as higher solubility and having functional groups on its surface, which makes it a good choice for use in nanocomposites [189, 190]. It symbolizes the ultra-large organic molecule with a 2D carbon mesh as shown in figure 2.4. sp^3-hybridized carbon atoms that are covalently bonded to oxygen-containing functional groups are considered as the oxidized regions, whereas sp^3-hybridized carbon atoms are considered the unoxidized regions. The sp^3-hybridized carbon clusters are situated at the top and bottom of the sp^2-hybridized carbon atoms. GO is hydrophilic and quickly disperses in aqueous solutions to form stable colloidal suspensions [191–194].

Due to the different chemical groups on the surface, the properties of graphene oxide can vary slightly depending on the synthesis route, starting materials, oxidation time, etc [95, 195, 196]. As a result, there are many different kinds of GO surfaces, with a typical O/C ratio of 28 to 36% [197]. When thermal exfoliation is used to make single sheets of functionalized graphene from GO, this ratio goes down to O/C= 5–10% because of the removal of some chemical functions [198–200].

2.3.2 Thermoelectric properties of Graphene Oxide

Graphene oxide typically has low electrical conductivity and poor thermal stability due to the presence of a large number of defects and oxygen functional groups [201–203]. These groups disrupt the aromatic regions in the basal planes; hence, the graphene oxide layer contains both aromatic regions and oxidized aliphatic six-

membered rings. It results in the distortion of sp^3-hybridized geometry and the insulating properties of graphene oxide. On the other hand, the thermal conductivity can be dramatically reduced due to the phonon scattering associated with the oxygen-containing functional groups at the surface [204, 205]. In addition, these oxygenated functional groups help to attach metal nanoparticles to further form phonon scattering sites, which further reduces thermal conductivity [206].

Feng et al. reported the p-type nanocomposite containing GO with $CoSb_3$ using a solvothermal route at 290 °C for 12 hours and then hot pressing at 600 °C and 80 MPa. The ZT value achieved for the nanocomposite was 0.81 at 800 K with 1.5 wt.% of GO in the $CoSb_3$ matrix, which was more than double that of the pristine $CoSb_3$. The obtained values were due to the enhanced carrier concentration and mobility [207]. Dey et al. embedded GO sheets in the grain boundaries of niobium (Nb) doped $SrTiO_3$ matrix to facilitate charge transfer between the grain boundaries without affecting thermal conductivity. The obtained ZT value of the composites was around 0.5 at 1200 K, which was 50 times higher than Nb-doped $SrTiO_3$ [208]. Similarly, the thermoelectric performance of the GO/CNT membranes was investigated at ambient temperature. The sample GO/CNT(1:2) showed a significant enhancement in the electrical conductivity, Seebeck coefficient, and thermoelectric power factor of 6.52 10^{-1} Scm^{-1}, 28.6 μVK^{-1}, and 5.33 10^{-2} $\mu Wm^{-1}K^{-2}$, respectively [93].

2.4 Titanium di-oxide

Titanium di-oxide (TiO_2) is one of the most prominent commercially available nanomaterials. Titanium di-oxide is an n-type semiconductor and is also known as Titania. Due to its natural abundance, chemical and thermal stability, titanium di-oxide has been well studied for various applications such as photovoltaics,

photo-degradation, dielectrics, sensors, photocatalysts, thermoelectrics, etc. The interesting chemical and physical properties of the TiO_2 depend on the crystal structure, particle size and shape. Recently, it gained much attention in thermoelectric applications after achieving a very high ZT value of around 1.2 after doping.

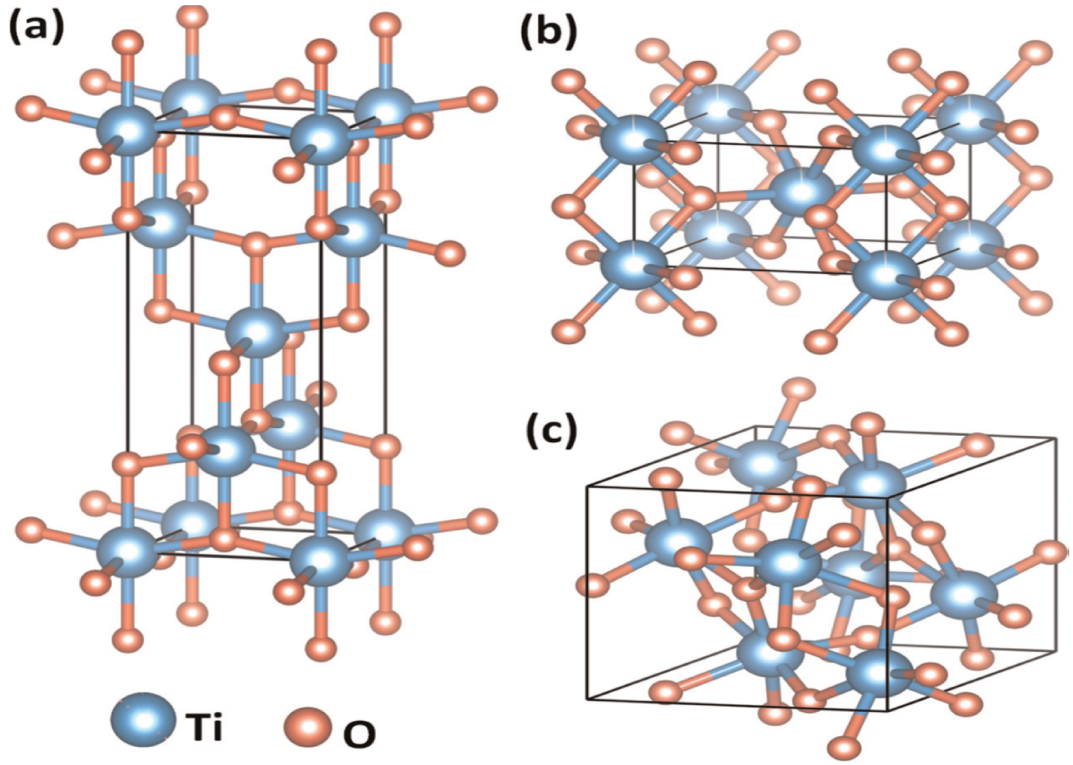

Figure 2.5: Three crystallographic structures of TiO_2 including (a) anatase, (b) rutile, and (c) brookite [21]

2.4.1 Structure of Titanium di-oxide

As shown in figure 2.5, TiO_2 undergoes three structures, namely, anatase, brookite, and rutile. Anatase and brookite are the room temperature forms which are irreversibly transformed to the rutile states upon heating at 700-800 °C [209]. Brookite is the meta-stable state and is found rarely in the naturally obtained TiO_2. The

crystal structure of the Brookite is more complicated than the rutile and anatase states and consists of three orthorhombic structures with a Pbca space group. The Ti-O bond length is the same as that of anatase and rutile, but the six unique lengths (in the range of 1.87 to 2.05 Å) makes the unit cell of brookite larger than the other two forms. There are 12 different O-Ti-O bond angles ranging from 77 to 105 °C. The complicated processing route to obtain the pure brookite phase has limited its applications, and as a consequence, it has gained the least interest compared to the other two forms [210].

The another low temperature form and also the most popular form of TiO_2 is anatase phase as it is highly stable at the nanoscale. Its unit cell structure is tetragonal with I41/amd space group as shown in figure 2.5(a). The unit cell can be explained as the TiO_2 octahedra chains where each chain is surrounded by the 8 others in a manner of 4 edge sharing and 4 corner sharing [211]. The Ti-Ti distances in anatase are 3.79 and 3.05 Å, however, the Ti-O distances are 1.95 and 1.91 Å, resulting from a significant distortion in the octahedra chains.

The third form is the high temperature state of rutile phase. It has a body centred tetragonal (BCT) unit cell structure with a= 4.4923 Å and c=2.8930 Å as shown in figure 2.5 (c). It has the similar structure as of anatase phase with a distorted octahedra around the Ti^{4+} ion formed by the O^{2-} ions. The difference in rutile phase is that the rutile has 2 edge sharing and 8 face sharing neighbours [209].

The most attention has been obtained by the low temperature anatase phase and the research at large scale has been conducted specially in nanotechnology and energy applications. Interesting chemical and physical properties comes in existence when the size of a material smaller down to the nanometer range. Apart from that, the shape of the material at nanoscale also plays an important role. As the material shrinks to the nano scale, the charge transport in semiconductors is controlled by the quantum confinement effect. At the nanoscale where the surface

plays an important role, the transport properties are size and shape dependent [212]. The surface area of TiO_2 based nanomaterials is helpful in running the interaction (which happens at the surface) at the interface of the matrix and filler.

2.4.2 Thermoelectric properties of Titanium di-Oxide

The large Seebeck coefficient of TiO_2 makes it a tantalizing thermoelectric material [213]. However, its low electrical conductivity prevents it from exhibiting desirable thermoelectric properties in its purest form. TiO_2 would be an excellent thermoelectric material if its electrical conductivity could be enhanced, given its non-toxicity, good chemical and thermal stability, and natural abundance. As a result researchers have developed many new structures and composites of TiO_2 to enhance their thermoelectric performances. For instance, the thermoelectric properties of undoped and doped $(TiO_{0.75}Sn_{0.25})O_2$ were studied by Dynys et al., who discovered that the addition of Nb_2O_5 or Ta_2O_5 increased the electrical conductivity by three orders of magnitude, while decreasing the thermal conductivity to below 4 $Wm^{-1}K^{-1}$ [214]. Portehault et al. embedded substoichiometric TiO_2 nanoparticles in carbon matrix to obtain percolated nanocomposites. In comparison to bulk materials, these nanocomposites have a low thermal conductivity (1 $Wm^{-1}K^{-1}$) and a low electrical resistivity ($2x10^{-4}$ Ωm) [215]. Xu et al. reported a decrease in thermal conductivity of TiO_2 due to the phonon scattering at the interface of grain boundaries after the Al doping [216]. Many studies have focused on various methods to improve thermoelectric properties of TiO_2 based composites [217–223]. These studies demonstrate that the properties of these materials are highly dependent on preparation method, particle size, and microstructure, making theoretical methods like first-principles calculations difficult to predict. Hence it is necessary to optimize these parameters in order to achieve high TE *figure of merit* ZT.

Nanostructured TiO_2 has a wide range of potential applications due to its nanoscale characteristics, low toxicity, good biocompatibility, inherent properties, and versatile fabrication methods. In the following section, we will examine various TiO_2 nanostructures and their thermoelectric properties.

2.4.3 Titanium di-oxide nanoparticles

Nanoparticles (NPs) are a broad category of particulate materials with all three dimensions smaller than 100 nm [224]. Researchers realized the significance of these materials when they discovered that the size of a substance can affect its physio-chemical properties, such as its optical properties, electrical properties, thermal properties, etc. NPs consist of three layers: (a) the surface layer, which can be functionalized with a set of different molecules, inorganic compounds, surfactants, and polymers; (b) the shell layer, which is chemically distinct from the core in all respects, and (c) the core, which is primarily the NPs central portion and typically refers to the NP itself [225]. The NPs are utilized in a variety of applications, including drug delivery [226], chemical and biological sensing [227], gas sensing [228, 229], waste water treatment [230, 231], food industries [232], solar cells [233], thermoelectrics [106], and other applications [234–236].

Xu et al. studied the effect of doping on the TE properties of TiO_2 nanoparticles. They reported that Al doping in TiO_2 nanoparticles introduces new grain boundaries, leading to elevated phonon scattering, and ultimately, a decrement in thermal conductivity [216].

Liu et al. reported a very high ZT for n-type thermoelectric material, 0.35 at 700 °C. They synthesized nitrogen (N) and niobium (Nb) co-doped TiO_2 nanoparticles by the fast combustion method. The obtained power factor was 987 $\mu Wm^{-1}K^{-2}$ which is 7 times higher than the pristine TiO_2 nanoparticles sintered under the same circumstances. The enhancement in power factor and ZT with

a decrement in thermal conductivity was attained due to the elevated scattering from point defects and grain boundaries [108].

Ning et al. introduced TiO_2 nanoparticles into the Cu_2SnSe_3 matrix by ball milling followed by the spark plasma sintering process to form the nanocomposite. The 1.0% TiO_2/Cu_2SnSe_3 composite exhibited a maximum ZT of 0.30 at 700 K, which was 17% higher than that of the pure Cu_2SnSe_3 at 700 K [237]. Similarly, Cederkrantz et al. used TiO_2 nanoparticles to enhance the thermoelectric properties of Mg_2Si. The addition of 1% TiO_2 resulted in an optimal thermoelectric *figure of merit* of 0.0042 at 300 °C, which is nearly three times greater than that of pure Mg_2Si. The increase in ZT was the result of a significant decrease in electrical resistivity followed by a less significant decrease in the absolute Seebeck coefficient. However, further addition of TiO_2 led to lower ZT values, and when 3 vol.% TiO_2 was added, the ZT was comparable to that of pure Mg_2Si [238].

Many studies have focused on incorporating TiO_2 nanoparticles into conjugated polymer matrix. Debnath et al. synthesized a hybrid nanocomposite containing TiO_2 nanoparticles in a PANI matrix via chemical polymerization. The TiO_2 nanoparticles were used to introduce the energy filtering effect to enhance the thermoelectric power factor. The presence of TiO_2 led to improved carrier propagation due to the ordered molecular structure of the hybrid composite, resulting in a simultaneous enhancement in electrical conductivity and Seebeck coefficient. The best performance was obtained for 1.5 wt.% TiO_2/PANI nanocomposite with a remarkably high electrical conductivity and Seebeck coefficient of 0.052 Scm^{-1} and 1.767 μVK^{-1}, respectively. Thus, the maximum recorded value of the power factor of 16.17 $\mu Wm^{-1}K^{-2}$ was achieved. The incorporation of TiO_2 into PANI reduced the hopping barrier potential, which increased the power factor. Therefore, conjugating polymers containing TiO_2 can be utilized in thermoelectric generators with such improved performance [239].

2.4.4 Titanium di-oxide nanotubes

Nanotubes are a broad category of particulate materials with a tube-like structure and at least two dimensions smaller than 100 nm [224]. The length of nanotubes ranges from ten to several hundred microns. They have several advantages, such as high aspect ratio, high surface to volume ratio, excellent structural integrity, stable chemical and thermal properties. They are beneficial in many applications, such as gas sensing [240], photoelectrochemical water splitting [241], drug delivery [242], antibacterial applications [243], etc. Nanotubes are similar to 1-D nanomaterials such as nanofibers, nanowires, and nanorods.

Low-dimensional nanotubes are preferable for increasing phonon scattering and lowering lattice thermal conductivity. As discussed in earlier sections, limiting the lattice thermal conductivity is a desirable characteristic for enhancing the thermoelectric performance, and a number of strategies have been implemented to address this issue. Enhancing phonon scattering through the use of point defects, vacancies, rattling structures, and nanostructures is a common approach. To fulfill the purpose, L. Su et al. synthesized Te-Bi-Pb decorated TiO_2 nanotubes via an electrochemical route. The purpose of employing the Te-Bi-Pb composite was to boost the Seebeck coefficient in order to improve TE performance further. Following the deposition of the Te-Bi-Pb composite, the Seebeck coefficient of TiO_2 nanotubes increased from 90 μVK^{-1} to 155 μVK^{-1} [244]. They continued their research by incorporating TiO_2 nanotubes into a PANI matrix and analyzing their thermoelectric and photosensitive properties. The optimization of the processing time and voltage, and fluorine ion concentration during the synthesis of TiO_2 nanotubes were investigated. The well organized TiO_2 nanotubes were obtained at 20 V for 60 min with an electrolyte containing 0.2 M fluorine ions. These nanotubes were further embedded in a PANI matrix via a polymerization process of aniline and showed a maximum value of Seebeck coefficient of 124 μVK^{-1} at 30 °C.

2.4.5 Titanium di-oxide quantum dots

Quantum dots (QDs) are 0-dimensional nanomaterials with all 3 dimensions at the nanoscale. These nanoparticles are called quantum dots as their size imposes quantum effects that affect their electronic energies [245]. QDs have gained much attention in various fields due to their high surface to volume ratio, which provides high reactivity and also their properties can be altered by their size, morphology, chemical composition, surface, etc. The synthesis of QDs involves a precursor as an inorganic material source, surfactants acting as ligands, and a solvent. The precursors decompose to form the supersaturation of monomers during the synthesis process. These monomers are the molecular species that emerge out of the precursor, which later on can connect or dissociate the nucleated nanocrystals, ensuring the growth or shrinkage at the end of the reaction. However, the role of a ligand is to passivate the nanocrystal surface. The origin of the monomer is accompanied by the nucleation process. The formed monomers joined the nucleation seeds, which lets the nanocrystals grow into their final shape by moving the atoms around [246].

Despite the numerous reports on the synthesis of TiO_2 nanostructures [247–251], there are few studies on the synthesis of TiO_2 quantum dots. Mechanical grinding [252], surfactant-modulated growth [253], microwave synthesis [254], and hydrothermal processes [255, 256] are a few of the diverse methods for producing TiO_2 quantum dots. In order to detect biomolecules (DNA, proteins) for clinical diagnostics and in vivo imaging, TiO_2 QD arrays were grown with the aid of a template [257]. In quantum-dot dye-sensitized solar cells (QDSSCs), semiconducting QDs supported by a TiO_2 matrix have been investigated for lower recombination rates and increased conversion efficiency [258, 259].

Various synthesis routes are possible for the synthesis of TiO_2 QDs, such as in-situ, ultra-high vacuum, chemical vapor deposition, etc. L. Pan et al. synthe-

sized TiO_2 QDs self-decorated with anatase TiO_2 nanosheets via a hydrothermal method, followed by a defect healing procedure. This method has provided a novel and efficient method for enhancing surface activity [260]. L. Gnanasekara et al. developed a simple in-situ chemical route to synthesize TiO_2 QDs, and their photocatalytic dye degradation properties were investigated under visible light irradiation [253]. Furthermore, these TiO_2 QDs were modified with the MWCNTs to improve the battery performance of the lithium ion batteries. It aided in preventing the expansion of electrodes during the charging and discharging processes and served as an effective battery separator. This composite increased the layer's conductivity and layer separation [253]. Du et al. synthesized PEDOT: PSS with carbon quantum dots and the PF was enhanced up to 1.6 $\mu Wm^{-1}K^{-2}$, which was 500 times higher than that of the pristine polymer [261].

Enhanced surface of QDs have an advantageousness on numerous applications such as, photo-catalytic activity, antibacterial activity, photovoltaics, fuel cells, etc [254, 260, 262]. The TiO_2 QDs offer a wide range of uses, however we found a research void that TiO_2 QDs have never been reported for thermoelectric applications [263].

Notwithstanding, many studies have already been conducted to boost the efficiency of organic TE materials, yet, their performance has not been satisfactory compared to conventional inorganic materials. Therefore, further investigations are needed to improve the efficiency of organic-based thermoelectric materials. Herein, the current work is focused on improving the TE properties of PEDOT: PSS by incorporating TiO_2 quantum dots decorated graphene oxide (TQDGO). The polymer PEDOT: PSS was chosen as the host matrix for the TQDGO as it is very stable and can interact with the quantum dot-based filler through strong $\pi - \pi$ interactions. Moreover, these interactions with TQDGO are expected to construct conducting pathways and facilitate charge carrier transfer [264–266].

The sol-gel method was employed to synthesise TQDGO nanocomposites using Ti^{4+} and GO as the starting materials. Ti^{4+} was used as a precursor to ensure the growth of TiO_2 QDs on the GO surface via relatively stable oxo and hydroxyl bonds [267]. The next step was immersing the TQDGO filler in the PEDOT: PSS polymer matrix using oxidative polymerization of EDOT. The morphology, elemental analysis, chemical functional groups, optical properties, and thermal properties were investigated by employing scanning electron microscopy (SEM) and transmission electron microscopy (TEM) with Energy Dispersive X-ray (EDX) mapping, Fourier transform infrared (FTIR) spectroscopy, UV-Vis spectroscopy, and thermogravimetric analysis (TGA), respectively. The thermoelectric power factor was calculated by measuring the electrical conductivity and Seebeck coefficient. Finally, the TE properties of pellets were compared to those of thin films.

2.5 Conclusion

In this chapter, we have provided a comprehensive literature review of conducting polymers and their remarkable breakthroughs as a result of the collaborative efforts of three Nobel laureates: Shirakawa, MacDiarmid, and Heerger. Due to their high electrical conductivity, non-toxic nature, flexibility, light weight, etc., the polymer poly (3,4-ethylenedioxythiophene) polystyrene sulphate (PEDOT: PSS) and its composites have been extensively discussed. Then, we discussed its molecular structure, as well as its transformation from a neutral state to polaron and bipolaron, synthesis routes, and various applications, including thermoelectricity. Then, we discussed how the imperfect structure of graphene oxide (GO) allows functional groups to be attached to its surface to control its optical and electrical properties. We provided the molecular structure and thermoelectric properties of

graphene oxide. Then, we discussed titanium di-oxide (TiO_2), its molecular structure, and the thermoelectric properties of its various nanostructures, including nanoparticles, nanotubes, and quantum dots. We concluded that the TiO_2 quantum dots have numerous applications. Their thermoelectric properties, however, have not yet been thoroughly studied.

Chapter 3

Materials and methods

In this chapter, we will discuss the experimental materials used for the thesis. Then, we will discuss the synthesis of filler TiO_2 quantum dot decorated graphene oxide (TQDGO) and polymer nanocomposite TQDGO/PEDOT: PSS. The polymerization of the monomer EDOT into PEDOT will be discussed. In addition, we will present the sample preparation in detail, including pellets, thin films, and various chemical treatments. The techniques used for the structural, chemical, and elemental analysis of the samples will then be described.

3.1 Materials

A single-layer graphene oxide (GO) aqueous solution was purchased from the graphene supermarket (www.graphene-supermarket.com/collections/graphene-oxide-go). Ti(IV) isopropoxide solution, sodium hydroxide, EDOT solution, PSS solution, dioctyl sodium sulfosuccinate, ethanol, acetone, methanol, and ferric chloride were purchased from Aldrich. De-ionized water was obtained from the maison de la recherche unit by centre commun de mesure with reverse osmosis. All chemical reagents were of analytical-grade and were used without further modification

unless specified.

3.2 Synthesis

3.2.1 Synthesis TiO_2 quantum dots decorated GO (TQDGO) nanoflowers

The TiO_2 quantum dots decorated GO nanoflowers were synthesized by using titanium isopropoxide precursor (Ti^{4+}) and GO as the starting materials to ensure the growth of the TiO_2 quantum dots on the GO surface via relatively stable oxo and hydroxyl bonds [267].

For the synthesis, firstly, 3 mg of GO were dispersed in 100 ml of ethanol and sonicated for 1 hour. Second, 1.038 ml of titanium (IV) isopropoxide ($Ti[OCH(CH_3)_2]_4$) precursor solution was added drop-wise in GO dispersion, followed by mechanical stirring for 1 h at room temperature. Afterwards, 15 ml of distilled water and 0.5 ml of HCl (1 M) were added drop wise and the reaction was aged for 24 under mechanical stirring. The obtained precipitate was filtered and washed with distilled water, acetone, and methanol to remove the remaining residuals. Finally, the obtained TQDGO composite was dried in an oven at 60 °C overnight [268]. The schematic reaction process is shown in figure 3.1. During the reaction, titanium (IV) isopropoxide was used as the precursor and GO as the template. The positively charged Ti^{4+} ions were deposited on the negatively charged oxide functional group of GO and these sites acted as the activation points to initiate the nucleation process and resulted in the growth of TiO_2 QDs on 2-D GO nanosheets [112].

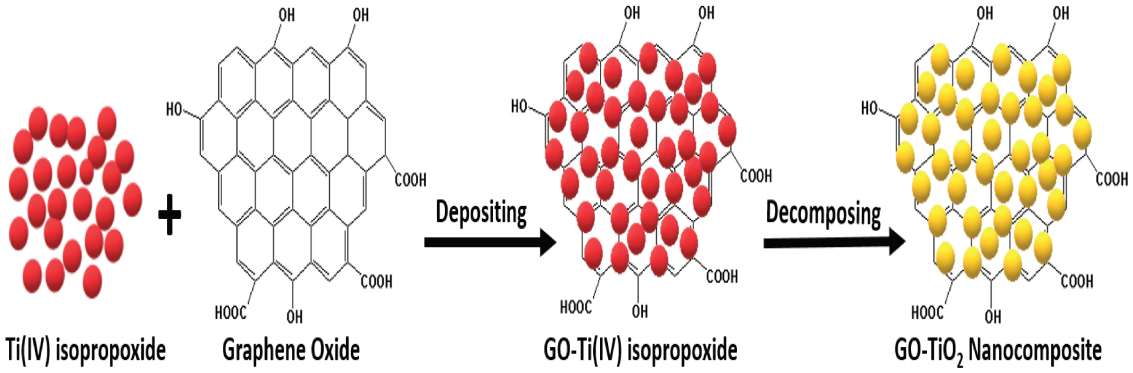

Figure 3.1: Schematic diagram for the synthesis of TiO_2 quantum dot decorated GO (TQDGO) by decomposing the Ti^{4+} precursor to form TiO_2 QDs on GO surface.

3.2.2 In-situ synthesis of TQDGO/ PEDOT: PSS nanocomposites

Generally, PEDOT is derived from the oxidative polymerization of monomer EDOT via an electrochemical method or chemical polymerization process. Figure 3.2 shows the molecular structure of positively charged PEDOT conjugated chains attached to the negatively charged PSS chains to form PEDOT: PSS via Columbic interaction. PSS not only acts as a counterion to balance the charge, but also operates as a polymer surfactant and allows a homogeneous dispersion of PEDOT in aqueous solution.

TQDGO/PEDOT: PSS polymer nanocomposites (PNCs) were synthesized by employing the oxidative chemical polymerization of EDOT in the presence of PSS and TQDGO. In a conical flask, the desired amount of TQDGO filler were dispersed homogeneously in 70 ml of n-hexane and sonicated for 30 min. Then, 6.6495 g dioctyl sodium sulfosuccinate were added as a surfactant and the solution was stirred for 15 min. Afterward, 0.825 g of EDOT and 4.125 g of PSS solutions were added drop-wise with vigorous stirring for 30 min. Subsequently, 2.64 g of anhydrous $FeCl_3$ were dissolved in 3.3 ml of DI water and added to the EDOT: PSS

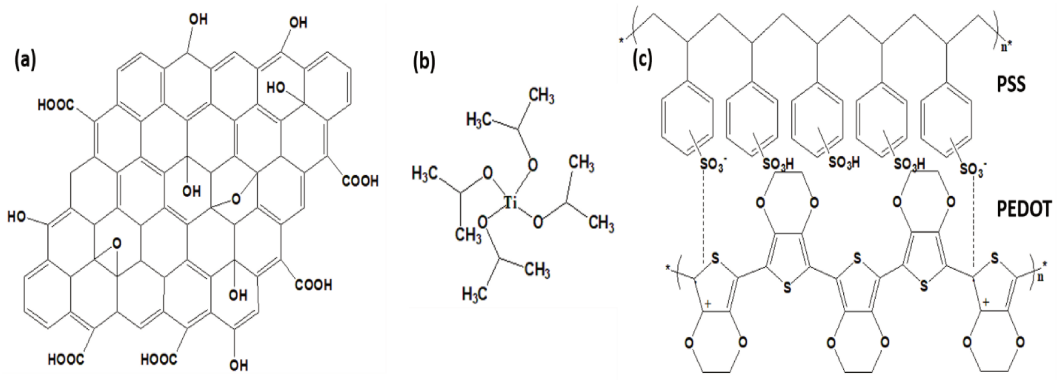

Figure 3.2: Molecular structure of (a) Graphene-Oxide, (b) Ti (IV) isopropoxide, and (c) PEDOT: PSS.

solution as an initiator. For the subsequent polymerization, the obtained solution was stirred at room temperature for 24 hours. The obtained greenish-blue solution was filtered, washed, and dried in an oven at 60 °C overnight, then finey grounded by mortar and pestle for 20 min [269–271].

During the polymerization, the positively charged EDOT chains were combined with the negatively charged PSS chains to form the intermediate product EDOT: PSS via Coulombic interactions [272] as shown in figure 3.3. When $FeCl_3$ is added as an oxidative agent to the above solution, it serves as the electron acceptor and drives the polymerization reaction of EDOT. Keeping in mind that carrier solvent plays an important role during the reaction and EDOT monomer is water-insoluble, we chose n-Hexane to improve the reaction rate and ultimate properties of the composites. Figure 3.5 shows the different stages of polymerization and the color transition from golden yellow to deep greenish-blue signifies successful polymerization [269, 273, 274].

The purpose of introducing TiO_2 QDs on GO sheets was to disrupt the sp^2 carbon atoms in the basal plane and form the potential phonon scattering sites to decrease the lattice thermal conductivity [275] which we will discuss briefly in chapter 6. We chose to conduct the polymerization process of the EDOT in the

presence of TQDGO because the negatively charged oxygen-rich functional groups of GO (within the TQDGO nanoflower structure) make the surface negatively charged, which facilitates the polymerization of EDOT around the nanoflower surface to ensure the intimate bonding between the filler and the matrix. Furthermore, TQDGO interacts with the polymers PEDOT and PSS via π-π and hydrophilic interactions, respectively. The photographic images during the polymerization reaction has been illustrated in figure 3.4.

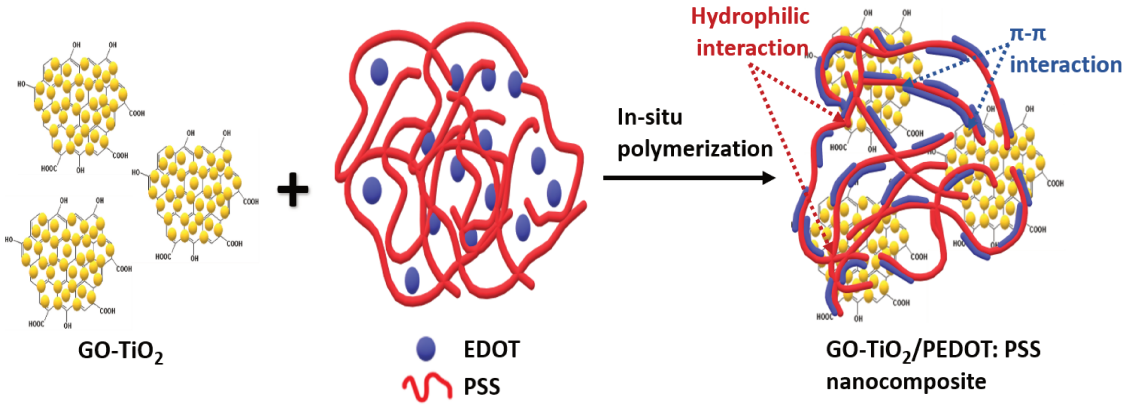

Figure 3.3: Schematic of the chemical in-situ chemical oxidative polymerization of EDOT to form TQDGO/PEDOT: PSS depicting π-π and hydrophilic interactions of TQDGO filler with PEDOT and PSS, respectively.

The obtained PNCs in powder form were used to produce the pellets and thin films. The pellets were formed by using the uniaxial pressing die under the pressure of 8 kPa for one minute. However, the thin films were prepared by dispersing the finey grounded PNCs in ethylene glycol. In the next section, we will discuss various sample preparation methods used in the thesis.

3.3 Acid-treated samples

The above obtained nanocomposites were further treated with 6 M HCl acid. Initially, 50 ml of 6 M HCl acid was mixed with 1 g of dried nanocomposite.

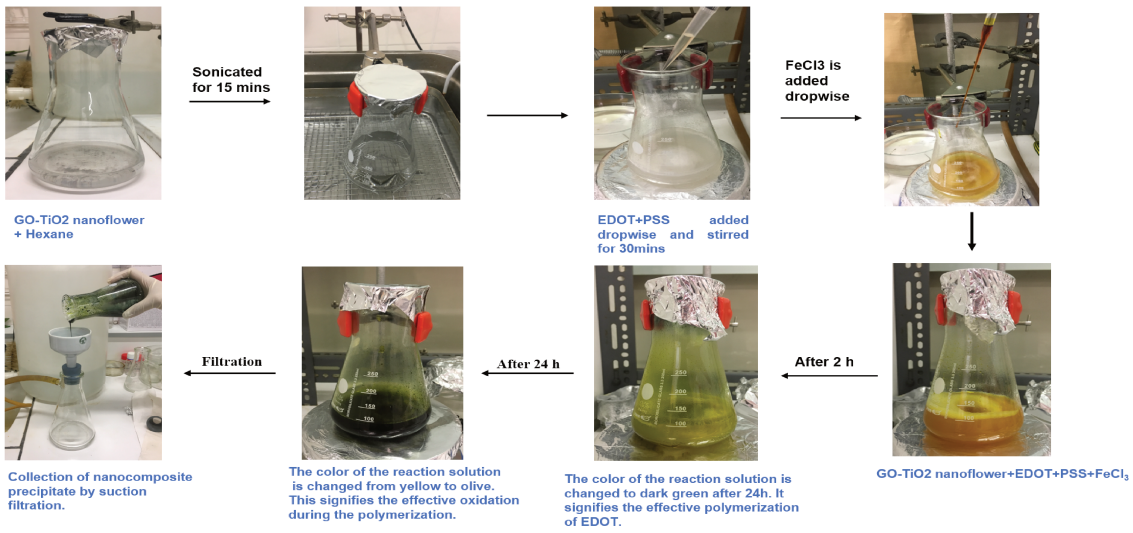

Figure 3.4: Photographic images of TQDGO/PEDOT: PSS nanocomposite chemical in-situ polymerization steps.

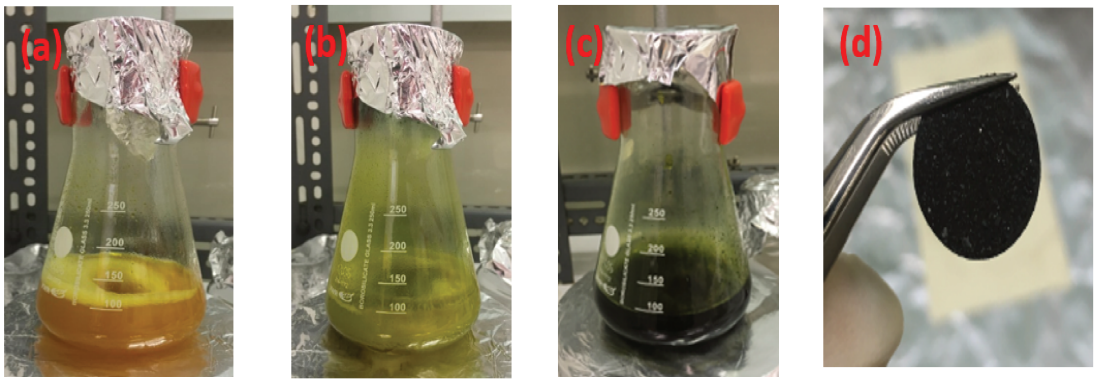

Figure 3.5: Photographic images during the polymerization reaction after (a) 5 min, (b) 2 hours, (c) 24 hours, and the image (d) depicts the TQDGO/PEDOT: PSS nanocomposite in pallet form.

Then, the solution was stirred for 2 h, followed by 1 h of sonication, and then dried in an oven at 60 °C for 24 h. The obtained sample was finey ground by mortar and pestle, and pellets were made by using a uniaxial pressing die (as mentioned above).

3.4 Commercial PEDOT: PSS

In this step, we used the commercially available PEDOT: PSS (from Sigma Aldrich) as a matrix. We took this step in order to compare electrical conductivities of above synthesized samples with the commercially available PEDOT: PSS to ensure the quality of the synthesized polymer composite.

For the process, the desired amount of TQDGO corresponding to the 0.1, 0.25, 0.5, 1, 2, and 5 wt.% of dopant was dispersed homogeneously in 10 ml of commercial PEDOT: PSS and sonicated for 2 h. The obtained solution was dried and collected in form of the powder and then formed into the pellets as mentioned above.

3.5 Thin film fabrication

In the next step, we realized that the electrical conductivities of abovementioned samples in pellet form obtained from the impedance spectroscopy technique were not satisfying, even for the commercial PEDOT: PSS. Hence, we decided to work on thin-films instead of bulk pellets. Impedance spectroscopy sample holder in our lab was not suitable for thin-films. Therefore, four-point probe method was used to measure the electrical conductivities of thin films.

For the thin films, 1 wt.% of the initially synthesized TQDGO/PEDOT: PSS was dispersed in ethylene glycol by sonication for 2 h and then stirring for 24 h to ensure homogeneous mixing. 1 wt.% of PNC was dispersed in 1 ml of ethylene glycol and sonicated for 30 min. The solution was then stirred at 35 °C for overnight. The glass substrate of 2 x 2 cm^2 size was cut with a diamond cutter. The substrates were then thoroughly cleaned with soap solution, followed by an ultrasonicator bath with acetone and isopropyl alcohol for 15 min. The substrates were then dried at 120 °C in an oven overnight to evaporate the solvents. The

next day, the substrates were then used to cast the thin films by the spin coating process. The surface of the substrates was gently covered with the PNC solution and then spun coated at 1500 rpm for 2 min. The films were then annealed on a hotplate at 90 °C for 20 min. The thickness of the prepared films was measured by cross sectional scanning electron microscopy.

3.6 Techniques for fundamental material characterization

3.6.1 X-Ray Diffraction

The crystal structure of the samples was determined by the powder X-ray diffraction method, using the Brüker D8 Advance Diffractometer, equipped with a copper anticathode Cu-Kα ($\lambda = 1.5406$ Å), a monochromator, and a LynxEye detector. The background from the obtained spectra was removed by using Brüker Diffrac plus EVA software. The different crystalline phases were identified by the database PDF (Powder Diffraction Files) established by the ICDD (international center for diffraction data). The recordings were made with a measurement step of $\delta(\theta) = 0.02$ in the range of 2θ from 5 to 80°, with a dwell time of 2 sec per increment.

3.6.2 Scanning Electron Microscopy

Surface morphology followed by the elemental distribution was analysed by scanning electron microscopy (JOEL JSM-7100F) with acceleration voltage (15kV) and energy-dispersive X-ray (EDX) mapping. SEM samples were prepared by dispersing the samples in ethanol and drop casted on a cleaned silicon wafer. The substrates were then placed on the sample holder by using carbon tape to perform SEM followed by EDS and mapping.

3.6.3 Transmission Electron Microscopy

High-resolution transmission electron microscopy (HRTEM) images were used to elaborate the nanoscale morphology and particle size of the filler by using FEI Titan 60-300 kV and FEI TECHAI TEM at 200 kV with LaB6 filament. For the sample preparation, the powdered sample was dusted on a 3 mm carbon-coated TEM grid.

3.6.4 Fourier Transform Infrared Spectroscopy

FTIR spectroscopy is an effective method for determining the molecular structure and composition of any solid, liquid, or gaseous state. Fourier Transform Infrared Spectroscopy (Perkin Elmer Spectrum 2000) in Attenuated Total Reflectance (Specac Golden Gate) mode was used to examine the molecular structures and components of the samples in the 4000-500 cm^{-1} range.

3.6.5 UV-Visible Spectroscopy

UV-visible spectroscopy measurements were done using the Perkin-Elmer Lambda 2S UV-Vis spectrometer system, and the absorption spectra were recorded from 190 to 800 nm. The samples were finey ground and dispersed in ethanol and the background was corrected before each measurement.

3.6.6 Thermogravimetric Analysis (TGA)

Thermogravimetric analysis (TGA) has been employed to analyse the thermal properties of nanocomposites. In an alumina crucible, about 10 mg of dried and ground samples were analysed by Thermogravimetric analysis (NETZSCH STA 409 CD) under the air flow with a heating rate of 5 °C min^{-1}.

3.7 Conclusion

In this chapter, we have discussed the experimental materials and methods used for the thesis. To facilitate the growth of quantum dots on the GO surface, we described the synthesis of the filler TiO_2 quantum dots decorated graphene oxide (TQDGO) extracted from the Ti(IV) isopropoxide precursor. Then, we covered the polymerization of EDOT in the presence of TQDGO and PSS as templates, as well as the synthesis of TQDGO/PEDOT: PSS polymer nanocomposites. Last but not least, we have provided information regarding the sample preparation techniques, including untreated pellets, acid-treated pellets, commercial PEDOT: PSS pellets, thin films, and various chemical treatments. Then, numerous techniques, including X-Ray Diffraction, scanning electron microscopy, transmission electron microscopy, Fourier transform infrared spectroscopy, and UV-Visible spectroscopy, were described.

Chapter 4

Structural characterization of polymer nanocomposites

In this chapter, we will discuss the morphology and elemental distribution of the filler TQDGO and the polymer nanocomposite TQDGO/PEDOT: PSS using the results of scanning electron microscopy and energy dispersed x-ray spectroscopy. Using transmission electron microscopy, the morphology of the filler TQDGO will be analyzed further. Fourier transform infrared spectroscopy will be used to determine the chemical functional groups of the sample, while atomic force microscopy will reveal the surface roughness. In addition, the optical properties will be evaluated using UV-visible spectroscopy, and the thermal stability will be evaluated using thermogravimetric analysis.

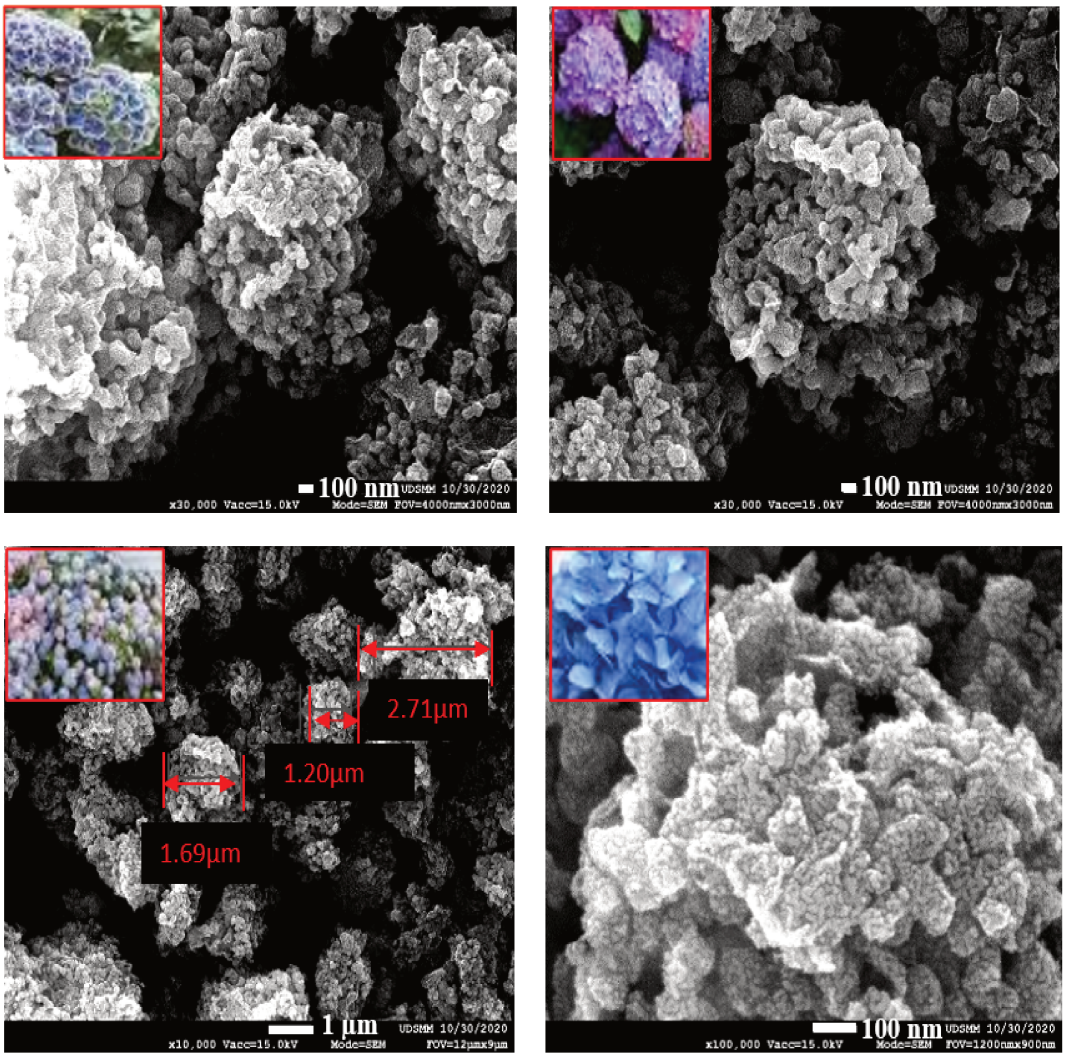

Figure 4.1: SEM micrographs of Hydrangea look-alike nanoflowers titanium di-oxide decorated graphene oxide (TQGDO), image in the inset represents the Hydrangea flower.

4.1 Scanning electron microscopy (SEM) of titanium di-oxide decorated graphene oxide (TQDGO)

The dependence of thermal and electrical conductivities on the filler morphology is a well-known fact [276, 277]. Therefore, the morphology of synthesized nanocomposites was analyzed by using field-emission scanning electron microscopy (FE-SEM). Figure 4.1 represents the SEM images of titanium di-oxide decorated graphene oxide (TQDGO), and the morphology resembles that of the hydrangea flower as shown in the inset image. The shown SEM images demonstrate the methodology used for synthesis was effective to provide the uniform distribution of nanoparticles. The micrographs reveal the successful anchoring of TiO_2 quantum dots on the surface of GO sheets, which convincingly enhances the surface area of the filler. It is noteworthy that GO interacts with TiO_2 via intense chemisorption and physisorption [278].

SEM micrographs also confirm the dense distribution of TiO_2 on GO sheets along with some aggregation. Furthermore, no individual quantum dots were observed elsewhere, apart from the GO surface, which signifies the substantial attachment of decorated quantum dots with GO. Moreover, the strong network between the quantum dots and GO is supposed to expedite charge transfer and phonon scattering [279].

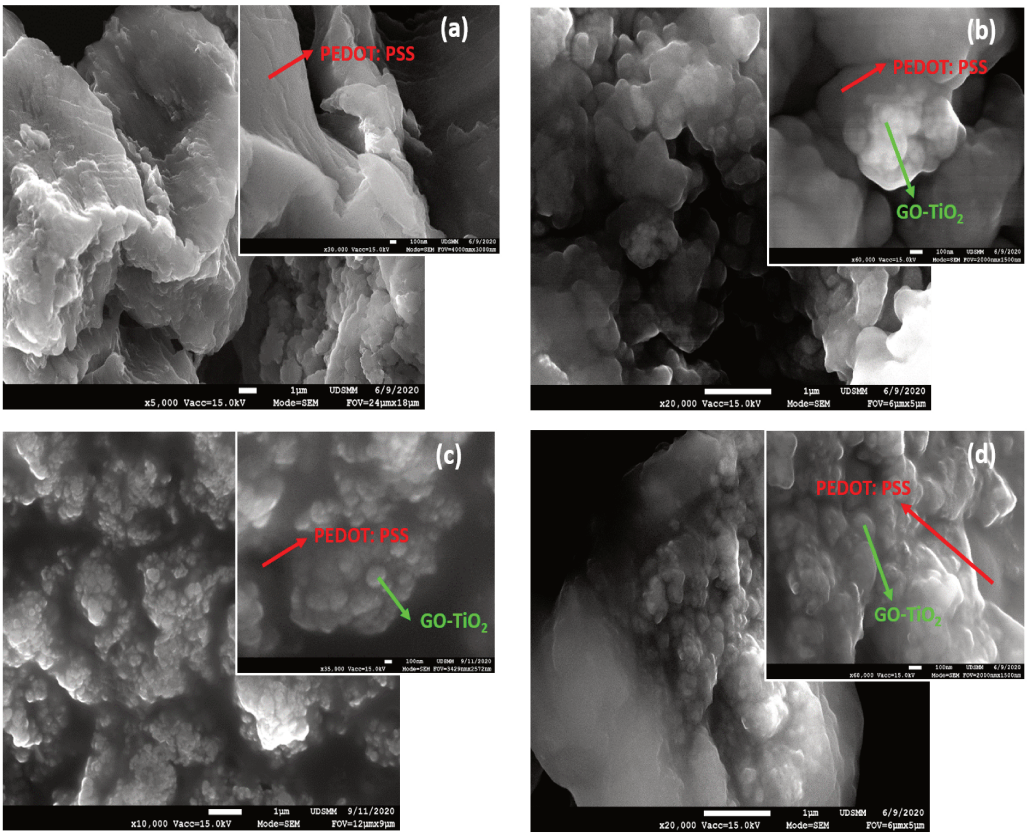

Figure 4.2: SEM micrographs of (a) PEDOT: PSS, (b) 0.5 wt.% TQDGO/PEDOT: PSS, (c) 2 wt.% TQDGO/PEDOT: PSS, and (d) 5 wt.% TQDGO/PEDOT: PSS, nanocomposites.

4.2 Scanning electron microscopy of TQDGO / PEDOT: PSS polymer nanocomposites

Figure 4.2 shows the SEM images of PEDOT: PSS and TQDGO/PEDOT: PSS nanocomposites. The pristine polymer PEDOT: PSS showed a neat and smooth layered morphology of the pristine polymer PEDOT: PSS. Images depict that the polymerization of the EDOT has occurred all around the filler and TQDGO seemed to provide the polymerization activation sites. These images show a uniform distribution of the TQDGO with full coverage of the polymer around it. The

SEM images demonstrate that the methodology used for the synthesis was effective for providing the uniform distribution of QDs. The micrographs reveal the enhanced surface area of PNCs with the addition of the TQDGO. Furthermore, the electrically conductive pathways are supposed to be provided by the successful growth of a conducting polymeric matrix around the filler [279, 280]. Also, the obtained heterogeneous morphology will have a positive impact on phonon scattering due to lattice mismatch at the interface. As a result, the synthesized hybrid organic-inorganic composite is supposed to be helpful in obtaining high electrical conductivity and low lattice thermal conductivity at the same time. In addition, the heterogeneous flower-like structure of the TQDGO is supposed to act as an energy filter to filter out the low energy charge carriers, and as a result, a high Seebeck coefficient is desirable. Overall, this will lead to a high thermoelectric *figure of merit*, which will make our material suitable for TE applications.

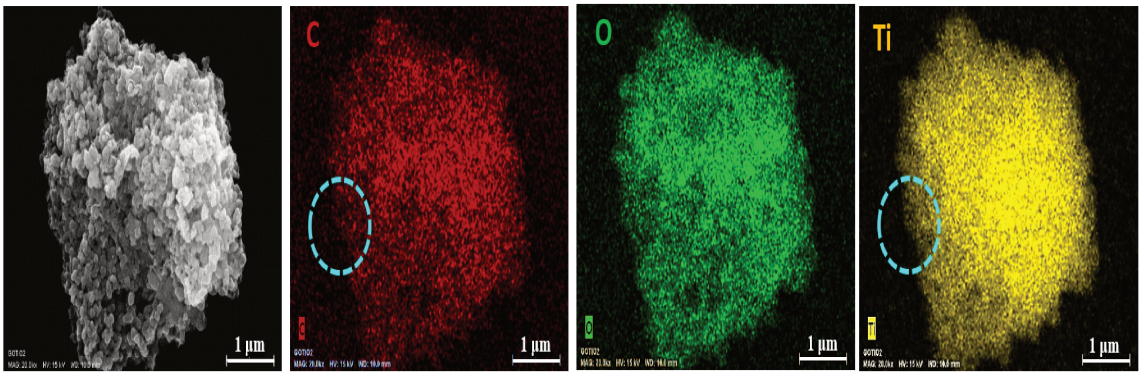

Figure 4.3: SEM micrographs of Hydrangea like titanium di-xoide decorated graphene oxide (TQGDO) nanoflower with the elemental distribution corresponding to red for carbon, green for oxygen, and yellow for titanium.

4.3 Energy dispersive X-ray spectroscopy (EDS) mapping of titanium-di-oxide quantum dots decorated graphene oxide (TQDGO)

The chemical composition of as-synthesized titanium-di-oxide quantum dots decorated graphene oxide (TQDGO) has been studied by EDS mapping. Figure 4.3 shows the elemental mapping and distribution of carbon (C), oxygen (O), and titanium (Ti) with red, green, and yellow colors, respectively. Here carbon and titanium are representing the graphene oxide and titanium di-oxide, respectively. If we look closely at the area surrounded by the cyan color, we can see that the titanium distribution is consistent and that it is only found around/on the carbon rich area, indicating that the reduction of the Ti(IV) isopropoxide precursor occurred over the negatively charged surface of the graphene oxide, as we hypothesized during the synthesis. Additionally, no titanium element has been observed in the carbon abandoned region, which confirms that no loosely bound titanium exists in the filler and reveals the close-knit relationship between titanium di-oxide quantum dots and graphene oxide.

4.4 Energy dispersive X-ray spectroscopy (EDS) mapping of TQDGO/ PEDOT: PSS polymer nanocomposites

Figure 4.4 shows the elemental mapping and distribution of carbon (C), oxygen (O), and titanium (Ti) with red, green, and yellow colors, respectively. EDS mapping confirms the uniform distribution of titanium in 2 wt.% and 5 wt.% of TQDGO/PEDOT: PSS composites in selected microstructural areas. The dis-

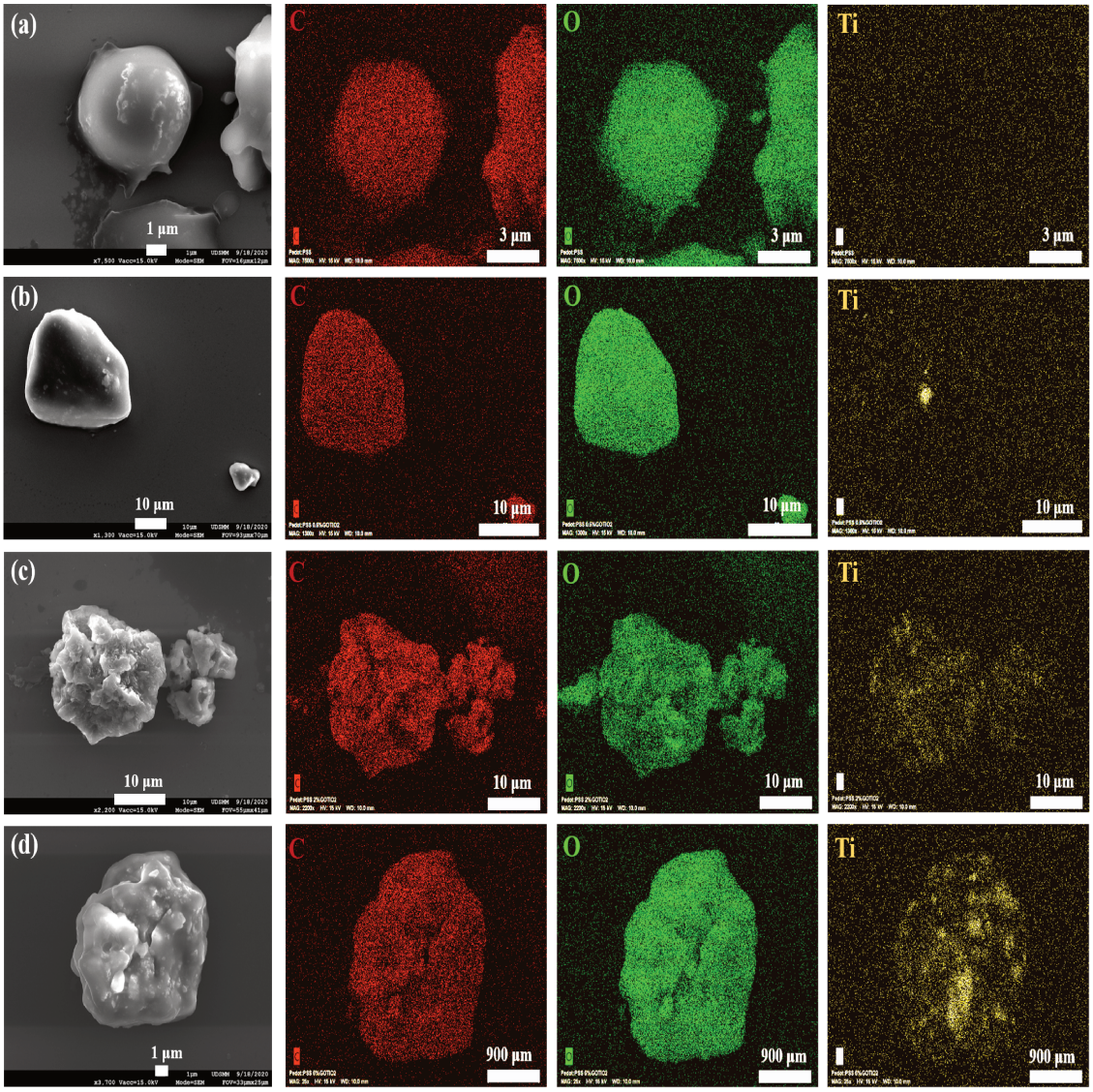

Figure 4.4: SEM EDS mapping of (a) PEDOT: PSS, (b) 0.5 wt.% TQDGO/PEDOT: PSS, (c) 2 wt.% TQDGO/PEDOT: PSS, , and (d) 5 wt.% TQDGO/PEDOT: PSS, nanocomposites.

tribution of titanium is not uniform in the 0.5 wt.% sample, probably due to the small amount of the filler. EDS images also confirm a dense distribution of TQDGO along with some aggregation. Furthermore, no individual filler was observed outside of the polymer matrix, which signifies a substantial attachment.

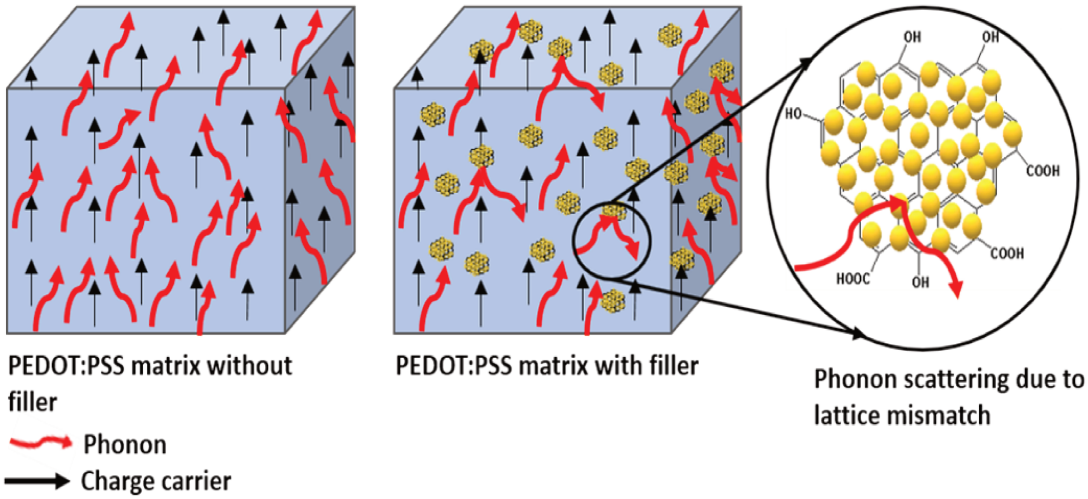

Figure 4.5: Schematic representation of phonon scattering caused by the heterogeneous TQDGO phase in polymer PEDOT: PSS matrix.

However, if we compare the morphology of all the PNCs, the smooth and uniform surface of the pristine polymer in figure 4.4 (a) was transformed to the rough and heterogeneous surface as shown in figure 4.4 (d) with the addition of the filler. This morphological transformation leads us to the hypothesis as shown in figure 4.5. The pristine polymer matrix is shown on the left side with red and black arrows representing the motion of phonons and charge carriers, respectively. Note that here we have considered the ideal case with no inter-particle scattering. The phonons as well as the charge carriers can move under the influence of the temperature difference without any trouble. Nevertheless, when the filler TQDGO is introduced, as shown on the right side of figure 4.5, the charge carriers with certain specific energies (higher than the barrier height) can pass through the filler as they follow the hopping phenomenon (which will be discussed later in the electrical conductivity part). In other words, the filler TQDGO acts as the energy filtering site and allows the high energy charge carriers to pass through and scatter back the low energy charge carriers. On the other hand, the phonons will

PedotPSSnew.spx

Element	At. No.	Netto	Mass [%]	Mass Norm. [%]	Atom [%]	abs. error [%] (1 sigma)	rel. error [%] (1 sigma)
Carbon	6	19588	36.27	36.27	45.42	1.84	5.06
Oxygen	8	42680	52.41	52.41	49.27	2.45	4.68
Titanium	22	0	0.00	0.00	0.00	0.00	2.50
Sulfur	16	39171	11.32	11.32	5.31	0.31	2.77
		Sum	**100.00**	**100.00**	**100.00**		

Pedot:PSS 0.5%GOTiO2 11674

Element	At. No.	Netto	Mass [%]	Mass Norm. [%]	Atom [%]	abs. error [%] (1 sigma)	rel. error [%] (1 sigma)
Carbon	6	31026	35.26	35.26	44.42	1.79	5.07
Oxygen	8	70997	52.94	52.94	50.07	2.47	4.67
Titanium	22	1151	0.43	0.43	0.14	0.04	8.29
Sulfur	16	64517	11.38	11.38	5.37	0.32	2.77
		Sum	**100.00**	**100.00**	**100.00**		

PSS 2%GOTiO2 new.spx

Element	At. No.	Netto	Mass [%]	Mass Norm. [%]	Atom [%]	abs. error [%] (1 sigma)	rel. error [%] (1 sigma)
Carbon	6	13138	44.21	44.21	55.12	2.24	5.07
Oxygen	8	15389	40.89	40.89	38.27	1.99	4.86
Titanium	22	2074	2.25	2.25	0.70	0.08	3.61
Sulfur	16	25042	12.65	12.65	5.91	0.35	2.74
		Sum	**100.00**	**100.00**	**100.00**		

PSS 5%GOTiO2new.spx

Element	At. No.	Netto	Mass [%]	Mass Norm. [%]	Atom [%]	abs. error [%] (1 sigma)	rel. error [%] (1 sigma)
Carbon	6	5009	32.16	32.16	41.54	1.62	5.03
Oxygen	8	11657	54.13	54.13	52.49	2.54	4.70
Sulfur	16	8973	9.63	9.63	4.66	0.27	2.82
Titanium	22	1800	4.08	4.08	1.32	0.13	3.11
		Sum	**100.00**	**100.00**	**100.00**		

Figure 4.6: SEM EDS qualitative analysis of (1) PEDOT: PSS, (2) 0.5 wt.% TQDGO/PEDOT: PSS, (3) 2 wt.% TQDGO/PEDOT: PSS, and (4) 5 wt.% TQDGO/PEDOT: PSS, nanocomposites.

experience the lattice mismatch at the filler-matrix interface and will be scatter off at the polymer-matrix interface. It means that the filler TQDGO will act as the active scattering sites for the phonons and energy filtering sites for the charge carriers. The overall effect of the filler will be different for the phonons and the

charge carriers. It will lead to a higher Seebeck coefficient and lower thermal conductivity.

Figure 4.6 shows the quantitative elemental data of PEDOT: PSS and TQDGO/ PEDOT: PSS nanocomposites. The figure shows the percentage of titanium in 0.5, 2, and 5 wt.% of TQDGO/PEDOT: PSS was found to be 0.43, 2.25, and 4.08 wt.%, respectively. The obtained values are very close to the synthesized values. However, the EDS technique is not very sensitive to low atomic number elements, such as carbon, hydrogen, oxygen, etc., and these are the major elements in our nanocomposite.

4.5 Transmission electron microscopy with energy dispersive X-ray spectroscopy

TEM analysis was employed to analyze the morphology of TQDGO filler at the nanoscale. These images show the monodispersity of TiO_2 QDs on GO [281]. Figure 4.7 (a-b) images reveal the spherical-like morphology of tiny QDs and their successful anchoring onto the GO surface. Such a strong network between QDs and GO sheets is supposed to expedite charge transfer and energy filtering effects [279]. Figure 4.7(c) depicts a particle size histogram of 400 QDs with an average size of 3.75 $\pm$0.92 nm. The particle size is smaller than its exiton Bohr radius, which signifies the successful formation of quantum dots [253, 282, 283].

Figure 4.7 (e) is a High-Resolution TEM (HRTEM) image showing various lattice planes corresponding to GO (green) and TiO_2 quantum dots (red). Figure 4.7 (d) and (f) show Fast Fourier Transform (FFT) (equivalent of diffraction pattern), inverse FFT, and energy distribution images for GO ($d_{001} = 0.22$nm) and TiO_2 QDs ($d_{101} = 0.34$nm) taken by ImageJ software, respectively. The plane d_{10l} corresponding to a 0.34 nm inter-planner distance confirms the anatase phase of

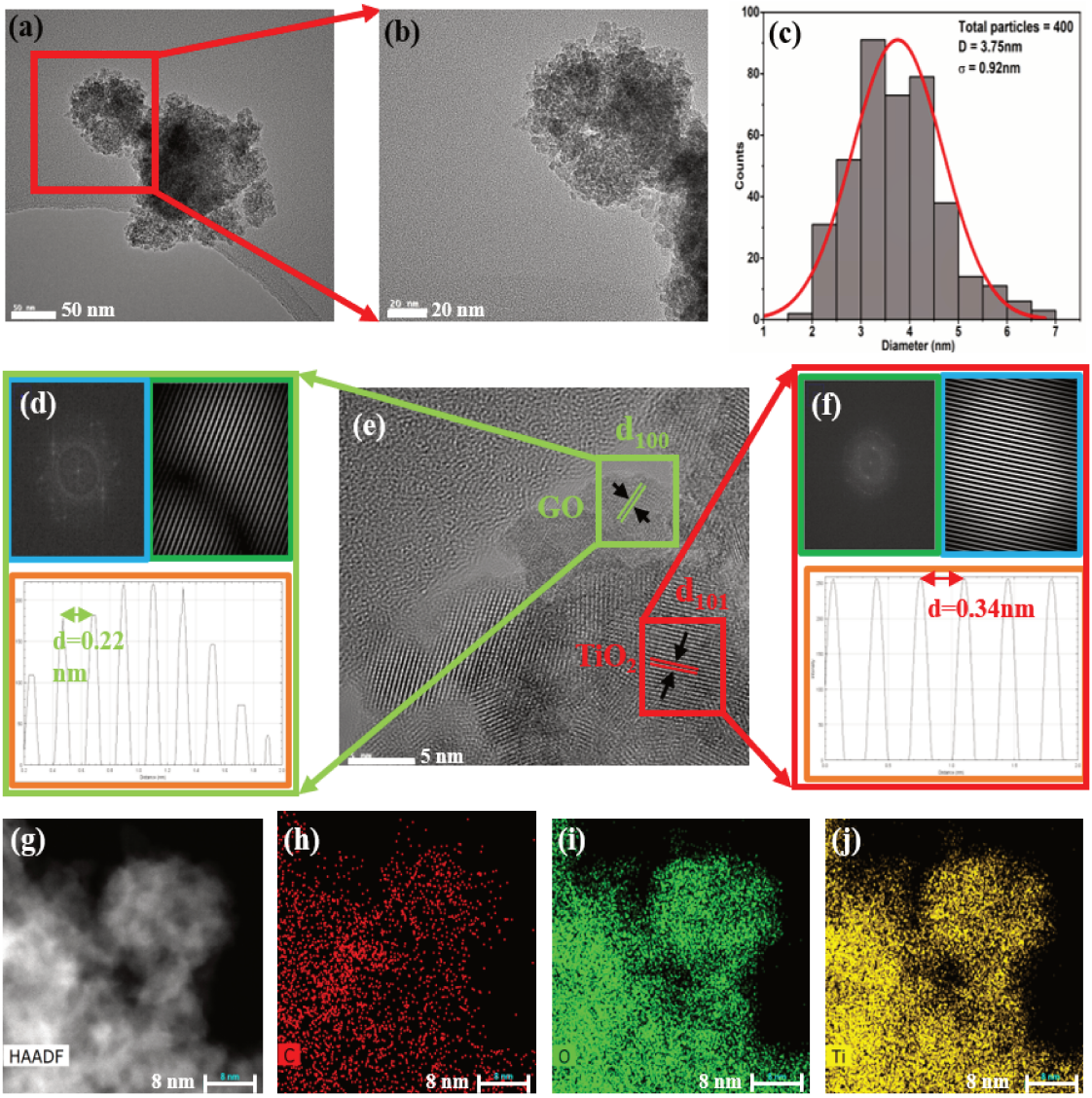

Figure 4.7: (a,b) TEM images of TiO_2 QDs decorated GO with 50nm and 20nm scale bar, (c) QDs size distribution histogram, (e) High-resolution TEM image with GO and TiO_2 planes. FFT, inverse FFT and energy distribution obtained by using Image J software for (d) GO and (f) TiO_2 QDs, respectively. (g) HAADF image for EDX mapping corresponding to (h) carbon , (i) oxygen, and (j) titanium.

.

TiO_2. Figure 4.7 (g-j) represents the EDX spectroscopy of the High-angle Annular Dark-field (HAADF) image.Different elements, such as carbon, oxygen, and

titanium, are represented by the red, green, and yellow colors, respectively. Here, carbon is representing GO and Ti is representing TiO_2, which confirms a consistent distribution of TiO_2 QDs on the GO surface. Additionally, no loosely bounded QDs were observed anywhere.

4.6 Fourier Transform Infrared Spectroscopy

Chemical functional groups present in the sample were revealed by FTIR spectra carried out in the range from 4000-400 cm^{-1}. Figure 4.8 shows the transmittance spectra of the filler and PNC. For the filler TQDGO, peaks from 600 to 900 cm^{-1} are ascribed to the crystalline phase of TiO_2 QDs [284]. The peak at 1632 cm^{-1} refers to the origin of the skeletal vibrations of the C=C bonds of GO. The broadband at ˜2400-3400 cm^{-1} indicates hydrostatic bond stretching and vibration due to hydrogen bonds [285]. The peak located at 1210 cm^{-1} and the broadband centered at 779 cm^{-1} implies a strong chemical bonding between graphene oxide and TiO_2 QDs [285, 286].

The spectra of the polymer nanocomposite consist of the major peaks at 2656, 2386, 2124, and 2005 cm^{-1} assigned to the C=O, O=C=O, C=O, and C=C bonds, whereas the peak at 1629 cm^{-1} is assigned to the C=C bending vibration of the phenyl group. Broadband centered at 3517 and 3813 cm^{-1} are due to the bending and stretching vibration of the O-H bond of trapped water [273, 287]. The region from 580-1750 cm^{-1} is shown in figure 4.9 to visualize the fingerprint region of the polymer nanocomposites. The characteristic peaks for PEDOT are situated at 1503, 1470, 1376, and 1308 cm^{-1} corresponding to the asymmetric stretching vibrations of C=C, C-O-C, C-C, and C-C of thiophene ring, respectively, as shown in fig 4.9. The peak at 1071 cm^{-1} is originated from bond stretching of C-O-C in ethylene-dioxy group [288]. The peaks at 1005, 1028, 1126, and 1170 cm^{-1} are

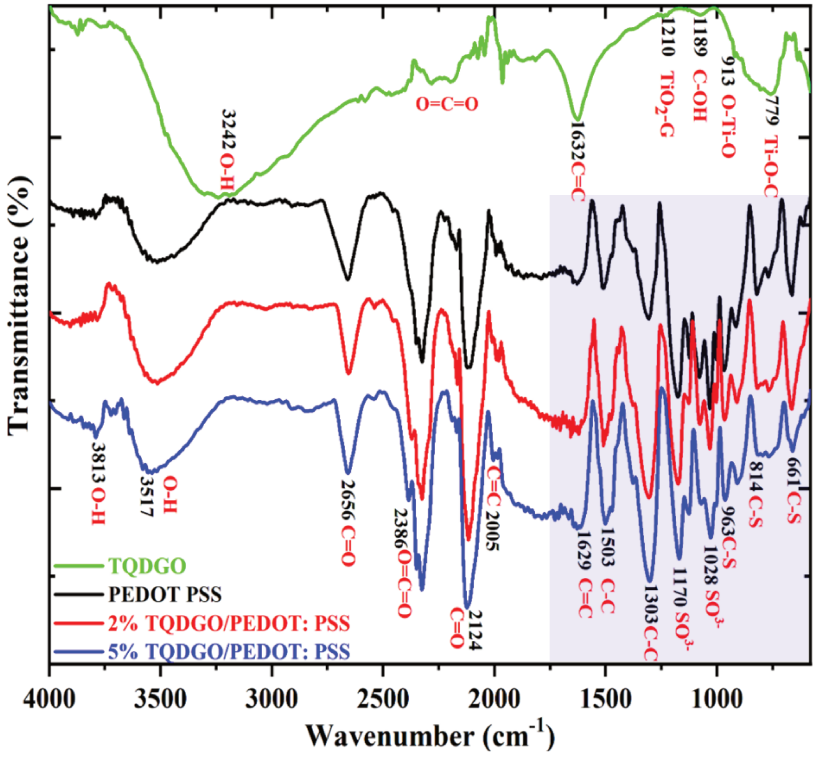

Figure 4.8: FTIR spectrum of TQDGO, PEDOT: PSS, and TQDGO/ PEDOT: PSS polymer nanocomposite. The highlight shows the fingerprint region.

representing the symmetric stretching vibrations of sulfonate group of PSS [289]. Compared to the pristine PEDOT: PSS, the reduction in the intensities of these peaks was observed with the filler, which clarifies the breach in sulfonic acid group out-of phenyl group of PSS chains and confirms the PSS removal. Peaks observed at 963, 909, and 814 cm^{-1} are due to the C-S stretching vibration of the thiophene ring in the PEDOT polymer chain. The analysis showed that the peaks at 1510, 1308, 1177, 1078, 1033, 967, and 823 cm^{-1} showed a blue shift of 3-7 cm^{-1} towards the lower wavenumber. Ouyang et al. investigated that the peak shift towards the lower wavenumber involved the transformation of the benzenoid structure to the quinoid structure PEDOT: PSS [290].

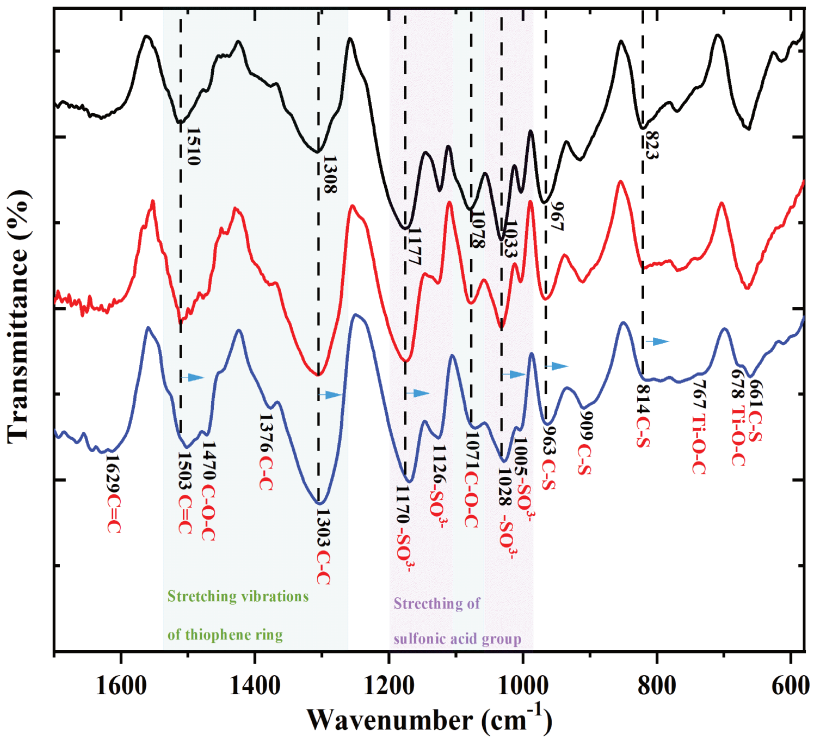

Figure 4.9: FTIR peak shifting in TQDGO/ PEDOT: PSS polymer nanocomposite.

4.7 Atomic Force Microscopy

The morphology of the spin-coated thin-films was analyzed by Atomic Force Microscopy (AFM) using tapping mode. Figure 4.10 shows the AFM images of pristine and 5 wt.% TQDGO/PEDOT: PSS thin-films. Image 4.10 (a) and (b) show the height and 3-D profiles of pristine PEDOT: PSS consisting of 30-40 nm long chains, consistent with the PEDOT: PSS chain length. The polymer entities were found to be scattered everywhere without any visible long-ordered network. The root mean square (RMS) surface roughness and the average roughness (RA) values were found to be 0.909 and 0.640, respectively.

Figure 4.10 shows the AFM images of the PNCs and shows a vast changes in the morphology of the thin films with the filler. Images 4.10 (c) and (d) show the

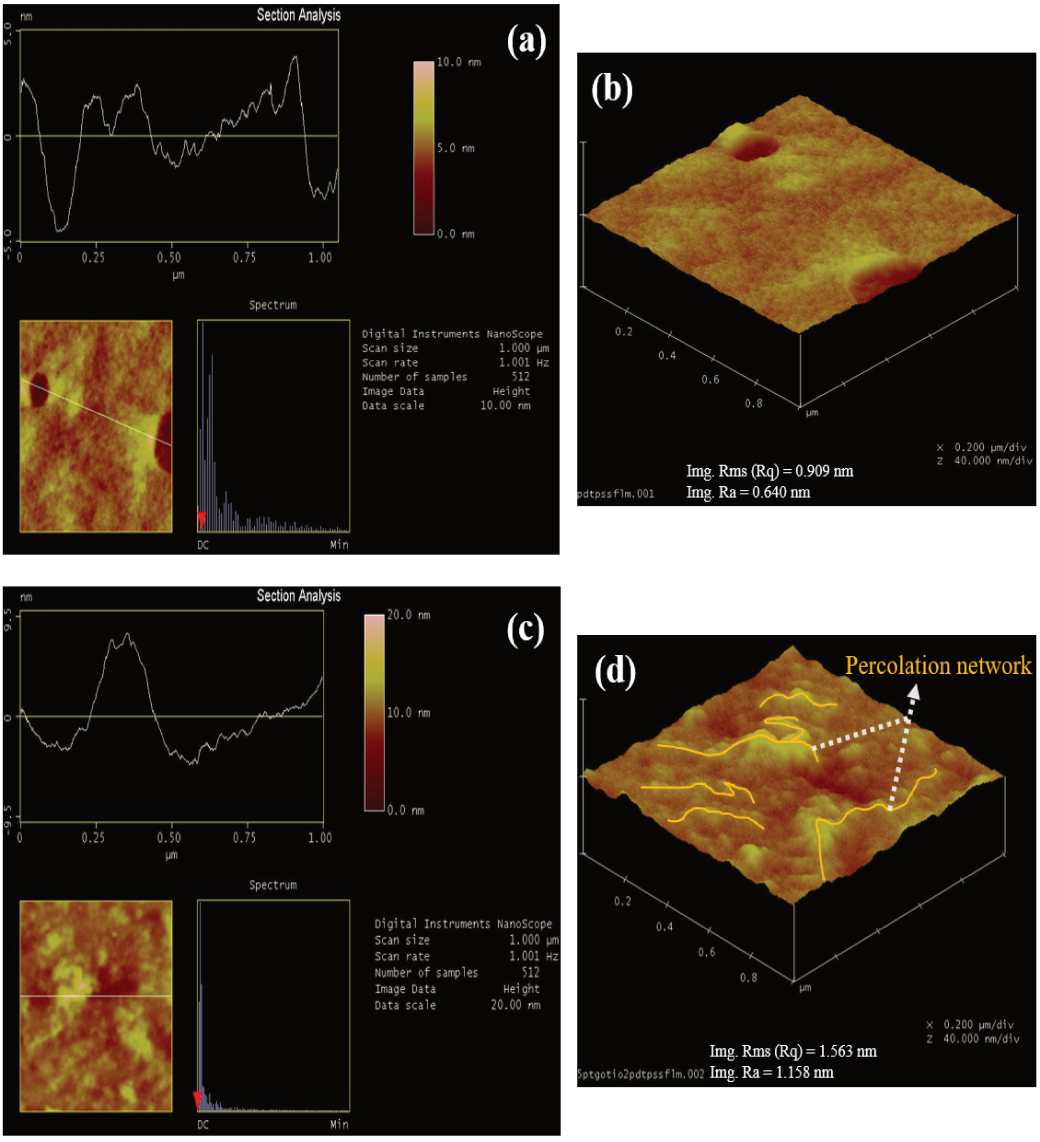

Figure 4.10: AFM with (a,c) height profile and (b,d) 3D image of pristine and 5 wt.% TQDGO/ PEDOT: PSS thin films taken by tapping mode for 1x1 μm^2 area. The black dashed lines in image (f) is showing the PEDOT chain conformation induced by the TQDGO to provide long pathways for the charge transfer.

height and 3-D profiles of 5 wt.% TQDGO/PEDOT: PSS thin films. Generally, the PEDOT: PSS is uniformly distributed over the surface. However, the addition of the filler tends to modify the film morphology. The bright spots correspond to dense materials and higher angles, while the dark spots correspond to mushy material and lower angles. AFM images show that the bright spots increased after the addition of filler, which signifies the accumulation of a thick elongated network of conducting PEDOT after separating with the PSS. The visible long conducting pathways in figure 4.10 (d) indicates that the filler is bringing conducting PEDOT chains closer and connecting them via $\pi - \pi$ interaction. The PEDOT chains become larger (50-60 nm) and more prominent after connecting with the filler. The observed large PEDOT pathways were visible, which could lead to the percolation type network. The formation of a percolation network as observed in the figure 4.10 (d) results in a drastic enhancement in the electrical conductivity. The surface roughness was increased noticeably to 1.563 nm (RMS) and 1.158 nm (RA).

4.8 Thermogravimetric Analysis (TGA)

The thermal stability of the nanocomposites was analyzed by using thermogravimetric analysis (TGA). TGA curves in figure 4.11 shows the mass loss as a function of temperature and time. The mass loss occurred in three steps. The first step started from 40 °C to 120 °C with a mass loss of around 11.9% and 18.1% for pure and 5 wt.% TQDGO/PEDOT: PSS, respectively. This mass loss could be mainly due to the evaporation of adsorbed moisture i.e. the dehydration process. All the samples showed good thermal stability till 270 °C. The continuous heating resulted in the second step from 300 °C to 410 °C with a mass loss of around 15.9% and 17.9% of the initial mass for the pure and 5 wt.% TQDGO/PEDOT: PSS, respectively. It could be due to the rupture of side chains i.e. dissociation of

PSS with PEDOT. It should be noted that the intense PEDOT-PSS interaction in pristine polymer resisted the thermal degradation and showed the least mass loss in this region. This fact was also confirmed by the single polymeric peak in XRD as it will be shown in the discussion part 6.8.

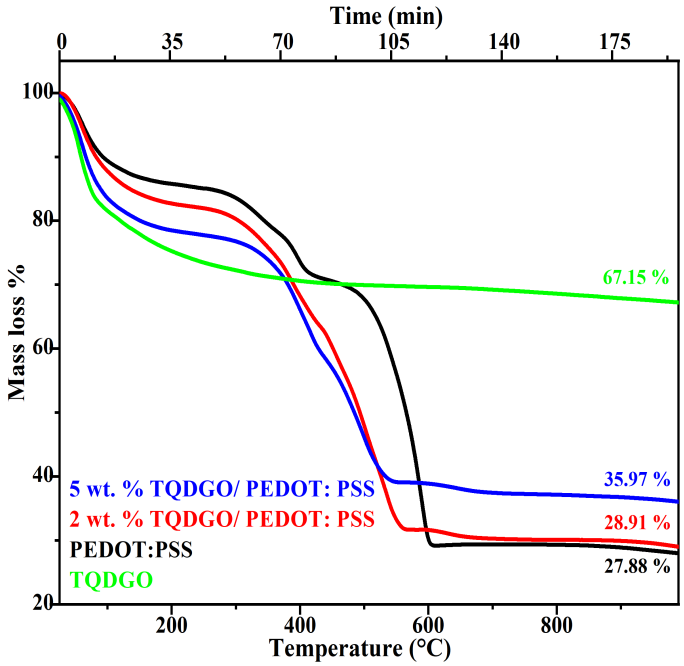

Figure 4.11: Thermogravimetric analysis (TGA) of TQDGO (green), pristine PEDOT: PSS (black), 2 wt.% TQDGO/PEDOT: PSS (red), and 5 wt.% TQDGO/PEDOT: PSS (blue) as a function of temperature and time.

The third and final step started from 420 °C to 600 °C for pristine polymer and 420 ° C to 560 °C for TQDGO/PEDOT: PSS with a mass loss of 42.2% and 24.8% of initial mass for pure and 5 wt.% TQDGO/PEDOT: PSS, respectively. It could be ascribed to the partial melting and decomposition of PEDOT skeletal and PSS polymer backbone chain structure. Since the filler weakened the PEDOT-PSS interaction, the degradation process terminated earlier in the TQDGO/PEDOT: PSS comparing pristine PEDOT: PSS. However, after the PEDOT-PSS bond rup-

ture, the pristine polymer suffers massive mass losses. The oxidation of the organic species and the formation of the ash cause further mass losses after 600 °C. TGA curves support the fact that the final ash content of the polymer was decreased by 8.09% with the addition of 5 wt.% TQDGO, which could be due to a large amount of the leftover filler as it did not undergo any mass loss except the dehydration process.

The filler undergoes a total mass loss of about 32.85 wt.% due to the decomposition of the oxygen-containing functional groups such as epoxide, hydroxyl, and carboxylic acid. The filler did not show any other mass loss steps due to the absence of any organic species and preserves the maximum thermal stability among all samples [291, 292].

4.9 Conclusion

The filler was successfully synthesised by the sol-gel method and incorporated into the polymer PEDOT: PSS matrix by in-situ chemical oxidation polymerization of EDOT. As evidenced by the SEM and EDS images, we have demonstrated in this chapter that the methodology employed for the synthesis was suitable for the uniform distribution of TQDGO in the matrix PEDOT: PSS. In addition, the TEM images confirmed the particle size of 3.75 nm, which is smaller than the TiO_2 exiton Bohr radius, confirming the formation of quantum dots. Furthermore, the FTIR confirmed the chemical functional groups of the samples and confirmed the efficient removal of PSS by the TQDGO by demonstrating a decrease in the peak intensities corresponding to sulfonate groups. The AFM images illustrated the improvement in surface roughness brought about by the filler. The enhancement in the optical band gap from UV-Visible spectroscopy confirms the synthesis of quantum dots due to the quantum confinement effect. The TGA revealed the

samples' thermal stability up to 270 °C.

Chapter 5

Measurement techniques for transport properties of polymer nanocomposites

As discussed in chapter 1, the thermoelectric performance of a material is determined by the dimensionless *figure of merit*, ZT. The performance of organic materials with a low thermal conductivity can be determined by the thermoelectric power factor. In order to calculate the ZT and power factor, we need to measure the Seebeck coefficient S, the electrical conductivity σ, the total thermal conductivity κ, and the absolute temperature T. These three parameters were used to calculate the thermoelectric properties of the materials at a given absolute temperature. In this chapter, we will discuss the experimental methods employed in the thesis to measure the aforementioned parameters.

5.1 Thermal conductivity measurement by the using Photothermal Radiometry (PTR) method

The thermal conductivity of the samples has been determined by photothermal infrared radiometry [293–295]. It is one of the photothermal techniques developed in the UDSMM laboratory. PTR is a well-known non-destructive technique for measuring thermal parameters such as thermal diffusivity and effusivity [293,296]. The foremost advantages of this method are the non-contact mode, broad frequency response range (mHz to MHz depending upon the sensor), and its ability to determine the thermophysical parameters for submicron thick samples. The PTR technique is based on the detection of infrared (blackbody) radiation, obtained from the sample in response to the exposure of a modulated light source, generally a laser. Thermal parameters of the sample were determined for a three-layered system which included a front medium, an opaque sample, and a substrate.

The principle of the PTR technique consists of illuminating the surface of an opaque sample by using a laser beam modulated in amplitude at a frequency f. The laser illumination leads to a local rise in the temperature of the sample surface. In response to this disturbance, the material emits infrared radiation, which is then transformed into an electrical signal using a photoelectric cell (HgCdTe, PbS, InSb, etc.). The expression of the electrical signal at the output of the detector as a function of the surface temperature of an infrared opaque sample is given by the following expression :

$$\mathrm{S}(f) = \Gamma(f) T_m, \tag{5.1}$$

where, $S(f)$ is the signal from the photocell that has been amplified and filtered using a synchronous lock-in amplifier to determine the amplitude and phase. The term Γ(f) is a transfer function that depends on the electronic measurements and

the device geometry. The thermal parameters are included in the term T_m, which represents the variation of the temperature at the surface of an opaque material to the incident light beam.

The mathematical expression for the temperature of the illuminated surface, in the case of an optically opaque sample at light excitation wavelength, is given by the formula:

$$T_m = \frac{F_0}{2k_s\sigma_s} \quad \frac{1+\gamma_{sb}\exp\left(-2M_sL_s\right)}{1-\gamma_{sb}\exp\left(-2M_sL_s\right)}, \tag{5.2}$$

where, F_0 is the heat flux density generated by the light excitation. The parameter L_s represents the thickness of the sample. The indices s, b indicate the sample and the substrate, respectively; κ_s is the thermal conductivity of the material, γ_{sb} represents the thermal wave reflection coefficient at the sample-substrate interface; and given by the relation:

$$\gamma_{sb} = \frac{e_{sub}/e_{sample}-1}{e_{sub}/e_{sample}+1} \tag{5.3}$$

where, e_{sub} and e_{sample} are the effusivity of the substrate and the sample, respectively.

The thermal wave number of the sample (M_s) which depends on the thermal diffusivity (α_s) is given by the following relation:

$$M_s = (1+i)\sqrt{\pi f/\alpha_s}. \tag{5.4}$$

The expression 5.2 is valid when the material can be considered opaque to incident light and the heat transfer can be considered one-dimensional. The schematic diagram of photothermal detection by infrared radiometry is shown in Figure 5.1. Some parameters are difficult to quantify, such as, the quantity of energy absorbed and the Γ transfer function of the measurement electronics, which is why a normal-

isation procedure is applied. It consists of carrying out successively a frequency scans with and without substrate.

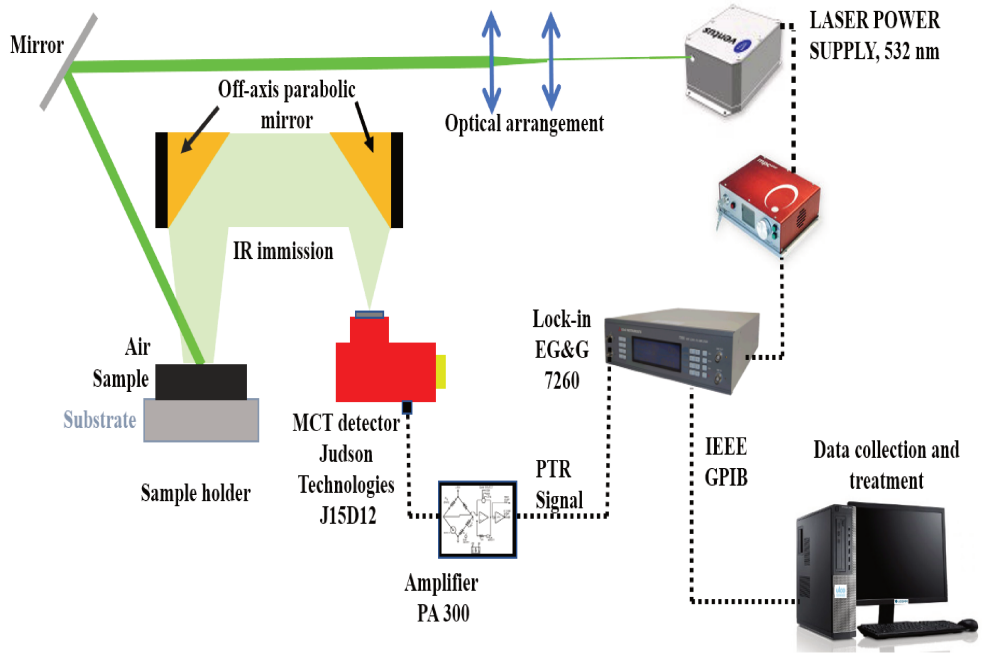

Figure 5.1: Schematic of the photothermal radiometry set-up.

A self-normalization method was used to eliminate the instrument frequency dependence, including the ratio of PTR signals obtained with and without substrate. More details of the method can be found elsewhere [294, 297]. The ratio of the two signals thus obtained gives the normalized signal S_n (f) which depends only on the thermal parameters of the sample. This last is given by the relation:

$$S_n(f) = \frac{S(f)}{S_0(f)} = \frac{1 + \gamma_{sb} \exp(-2M_s L_s)}{1 - \gamma_{sb} \exp(-2M_s L_s)} \times \frac{1 - \exp(-2M_s L_s)}{1 + \exp(-2M_s L_s)}.$$

Working conditions

An opaque sample is required to well absorb the incoming photons from an intensity modulated laser beam and emit an IR PTR signal in response to the periodic

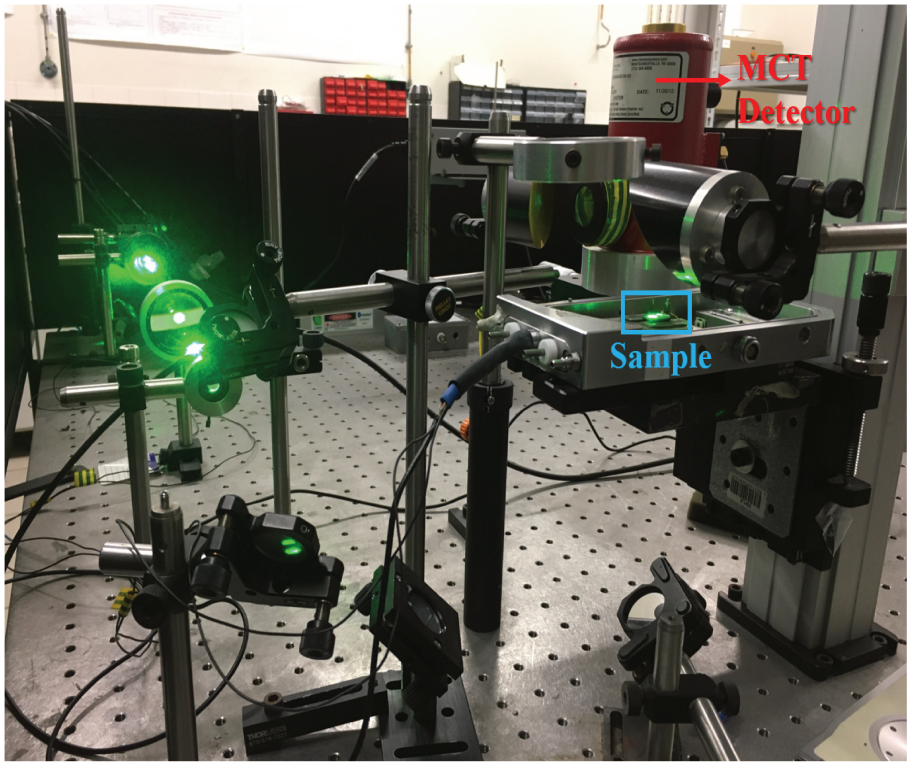

Figure 5.2: Photographic image of the photothermal radiometry set-up.

thermal excitation. A modulated Ventus laser (Laser Power Supply: MPC 6000 quantum laser, Model No. Ventus 532, voltage 11-14V DC, and current rating of 85 A) was used to originate the modulated thermal excitation wave across the sample. The incoming PTR signal has been detected by the nitrogen cooled Mercury-Cadmium-Telluride (MCT) detector and processed by the lock-in amplifier (Model no.: 7225 DSP). The obtained experimental data were analyzed by considering a one-dimensional heat transport model. All the measurements were conducted at the room temperature.

5.2 Electrical conductivity

The electrical conductivity of the sample pellets and thin films was measured by using impedance spectroscopy and four-point probe techniques, respectively. These two techniques are discussed in detail in this section.

5.2.1 Impedance spectroscopy technique

Impedance spectroscopy is a non-destructive technique used in particular to determine the dielectric permittivity of materials. This technique can also be used to measure the electrical conductivity as well. During the measurements, the sample is placed between two metal electrodes (Figure 5.4). An alternating voltage of the frequency f is applied between these two electrodes, which then a current of the same frequency begins to flow through the sample. The analysis of the measured current allows the simultaneous determination of the capacitance C (farads) and the conductance G (siemens) of the sample. The system (sample + the two electrodes) can be linked to a circuit consisting of a resistor and a capacitor connected in parallel and connected to the measuring device as shown in the equivalent circuit diagram in figure 5.3 [298, 299].

Working conditions of impedance spectroscopy technique

The electrical conductivity of the pellets was measured by the impedance spectroscopy and the circuit diagram is shown in figure 5.3. The pellets were 13 mm in diameter and approximately 600 μm in thickness. All the measurements were conducted at the room temperature. The capacitance, C_0 and conductance, G(f) were measured simultaneously as a function of frequency, f by a HP Hewlett Packard 4284A impedance analyser. The AC electrical conductivity σ_{ac} is calculated from the measured value of the conductance G(f) using the following relationship:

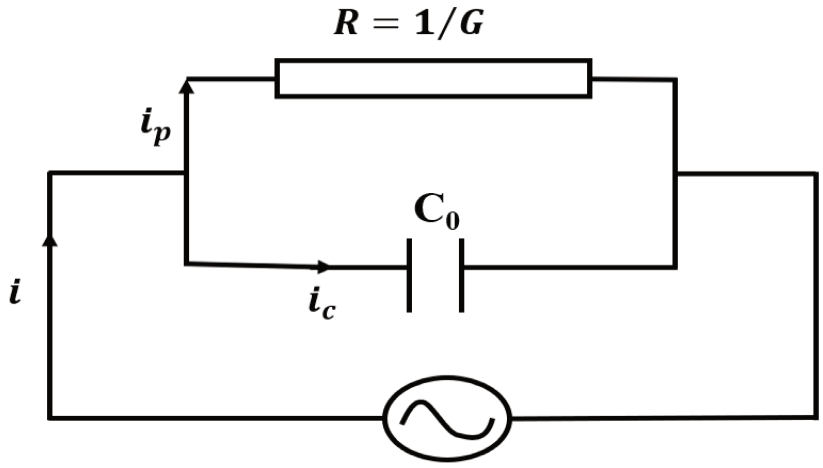

Figure 5.3: Equivalent circuit diagram used in Impedance spectroscopy.

$$\sigma_{ac}(f) = \frac{G(f)\ e}{S}, \tag{5.6}$$

where, S is the cross surface area between sample and electrodes, and e is the thickness of the sample. The electrical conductivity of a dielectric material in the alternating regime σ_{ac} is subdivided into two types as shown by Jonscher [300], a continuous component σ_{dc} and a component known as polarisation σ_{pol} which depends on the frequency [301].

$$\sigma_{ac}(f) = \sigma_{dc} + \sigma_{pol}(f). \tag{5.7}$$

In figure figure 5.5, two zones of the electrical conductivity can be noted. The first zone is observed at the low frequencies, where the electrical conductivity remains almost constant or barely changes, and the second zone, where the electrical conductivity sharply increases with the frequency. The DC electrical conductivity that we are trying to determine $\sigma_{\text{dc}} = \sigma$ by extrapolating the first zone of the curve of the evolution of σ_{ac} according to the frequency up to the y-intercept at f=0.

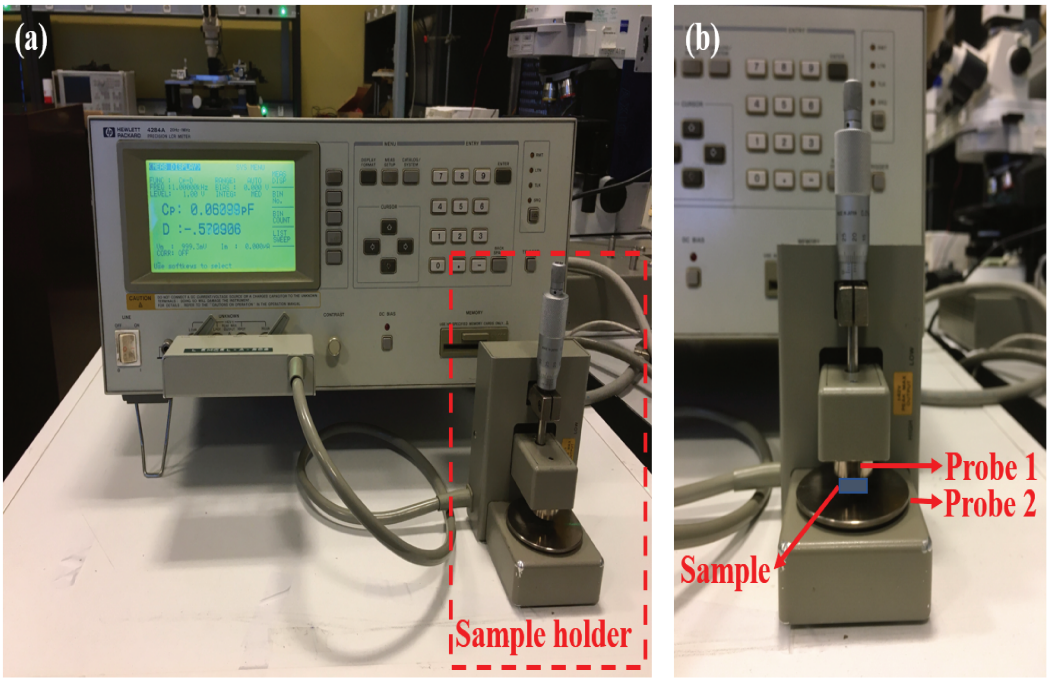

Figure 5.4: Impedance spectroscopy setup including (a) LCR meter and (b) Sample holder.

An example of the evolution of electrical conductivity as a function of frequency σ_{ac} is shown in Figure 5.5.

In addition, we have utilized impedance spectroscopy for the mobility calculations by using the dielectric properties of the material. The complex dielectric permittivity, ϵ^* is given by :

$$\epsilon^* = \epsilon^{'} + i\epsilon^{"} \tag{5.8}$$

where, $\epsilon^{'}$ and $\epsilon^{"}$ are the real and imaginary components of the dielectric permittivity ϵ^*, respectively. The real component, $\epsilon^{'}$, was calculated by :

$$\epsilon^{'} = \frac{C_0\ d}{\epsilon_0\ S} \tag{5.9}$$

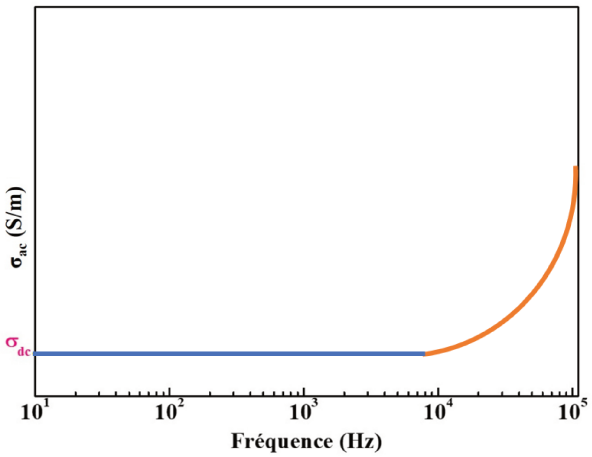

Figure 5.5: Example of the evolution of σ_{ac} as a function of the frequency. The DC component of the electrical conductivity is obtained by extrapolating the low frequency zone of the curve to $f \rightarrow 0$.

and the imaginary component, $\epsilon^{"}$, was calculated by:

$$\epsilon^{"} = \frac{G}{C_0\ \omega} \tag{5.10}$$

5.2.2 Four-point probe technique

The four-point probe method is a non-destructive and rapid technique for the electrical measurements of semiconducting or conducting materials. It was first used by Valdès in 1954 [302]. It was then improved by Smits [303] by using correction factors that take into account the shape of the samples and the arrangement of the tips with finite radius. The major advantage of this technique is that it eliminates the contact and wire resistance when measuring the current-voltage (I-V) characteristics.

The working principle is shown in figure 5.6 is based on the configuration of four equally spaced metal tips aligned on the sample surface. During the measurement, a current I_{14} is made to flow through the outer probes 1 and 4, and the voltage drop V_{23} across the inner probes is measured through a voltmeter with ultra-high

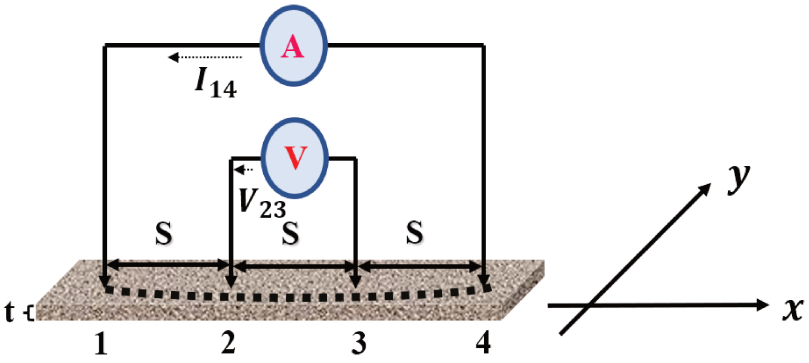

Figure 5.6: The schematic of the four-point probe on line

impedance. The current flowing through the sample results in a voltage drop across the sample surface, and the four-point resistance "R" is given by:

$$R = \frac{V_{23}}{I_{14}} \tag{5.11}$$

Working conditions of four-point probe technique

The four-point probe technique is effective when charge carriers are passing through the surface. The four-point probe technique was employed by using Keysight B2902A as a precision source/measure unit and the under-tip device was used by SIGNATONE. The electrical conductivities were measured by passing a current I_{14} through the outer probes (1 and 4) and measuring the voltage V_{23} between the inner probes (2 and 4). The sheet resistance layers were introduced as

$$R_{sh} = \frac{\rho}{t(\Omega)} \tag{5.12}$$

and the sheet resistance, R_{sh}, was measured for the thickness t of the sample as:

$$R_{sh} = \frac{V_{23}}{I_{14}\ C_{23}} \tag{5.13}$$

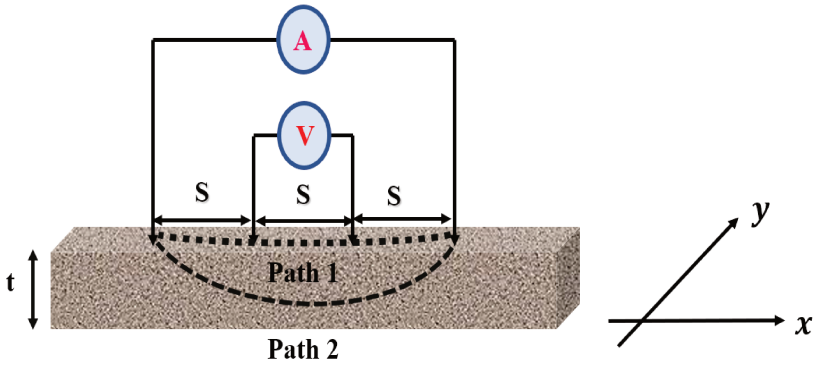

Figure 5.7: Schematic of the issues associated with the four-point probe method while working with the pellets.

where,

$$C_{23} = \frac{\pi}{ln\ 2} = 4.53 \tag{5.14}$$

is the correction factor. Notice that this correction is factor valid only if the thickness "t" of the sample is less than 40% of the distance between the legs, i.e. t$\leq$ 40% S. All the measurements were conducted at the room temperature.

5.2.3 Challenges

During the measurement of the electrical properties of the thin films, the current flows through the surface state and surface-charge layer as shown by the path 1 in figure 5.7. However, this is not the case for the bulk samples, i.e., pellets. In the pellets, the charge flows through the bulk state, i.e., volume via path 2. Therefore, it is then very difficult to precisely analyse the electrical properties of the bulk material owing to the entangled current contributions. As a result, the obtained I-V characteristics are not linear and sheet resistance measurement is not possible. Hence, the electrical conductivity of the pellets could not be measured by the four-point probe technique.

5.3 Seebeck Coefficient

In this section, we describe the methodology used to measure the Seebeck coefficient. In principle, the measurement of the Seebeck coefficient for solid materials is relatively simple. When the temperature difference is small, the Seebeck coefficient is measured by taking the ratio of the induced potential difference (ΔV) in response to the applied temperature difference (ΔT) across the sample. The concept of the Seebeck effect is shown in the figure 1.7. It shows a simple schematic for the Seebeck coefficient measurement by using two probes, which remain in direct contact with the sample during measurement. It shows the ideal measurement geometry where two probes make point contact with the material. The probes, usually thermocouples, serve as temperature sensors as well as electrodes to measure the potential and the temperature at the point of contact. Seebeck coefficient can be positive or negative depending on the nature of the majority charge carriers, e.g. positive for holes and negative for electrons. Thermocouples were used as probes, serving a dual purpose of measuring temperature difference and potential difference. The current configuration of measurement implies three assumptions:(a) the device is in steady state during the measurement of temperature and voltage simultaneously, (b) the voltage response to the temperature gradient is linear; and (c) temperature and voltage were measured at the same point on the sample surface. When these conditions cannot be perfectly fulfilled, non-negligible measurement errors can be expected. The details of the on-site Seebeck measurement cell can be found elsewhere [304].

Figure 5.8 depicts the schematic of the Seebeck coefficient measurement cell, including the sample in contact with two cylinders (I and II) acting as hot and cold sources. This configuration involves a nozzle heater with each cylinder to maintain the temperature difference. Two type T thermocouples (I) and (II) composed of copper/constantan are buried inside each cylinder and measure the temperature

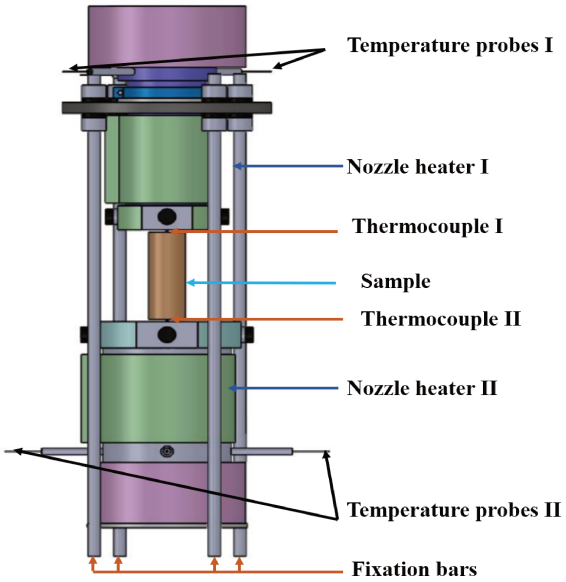

Figure 5.8: Schematic representation of the uniaxial 2-point Seebeck instrument cell.

and voltage at the hot and cold sides of the sample. For temperature control purposes, inside each cylinder there are two temperature probes of type Pt1000. Figure 5.9 represents the photographic image of the setup in the laboratory. It is composed of two generators to maintain a specified temperature and a multiplexer to measure the temperature and potential differences across the sample. The setup is controlled by a computer using the Labview program, which is based on applying a temperature difference (5 °C) between the two sides of the sample and then measuring the potential difference.

During the measurement, the majority of charge carriers begin to migrate from the hot to cold side of the sample until a counter-posing voltage difference is induced and further charge carrier migration is prevented by the induced electromotive force. Sometimes, apart from the charge carriers, phonons also contribute to Seebeck coefficient. If the phonon-electron interaction is predominant in TE material, phonon drag electrons from one side of the material to the other and

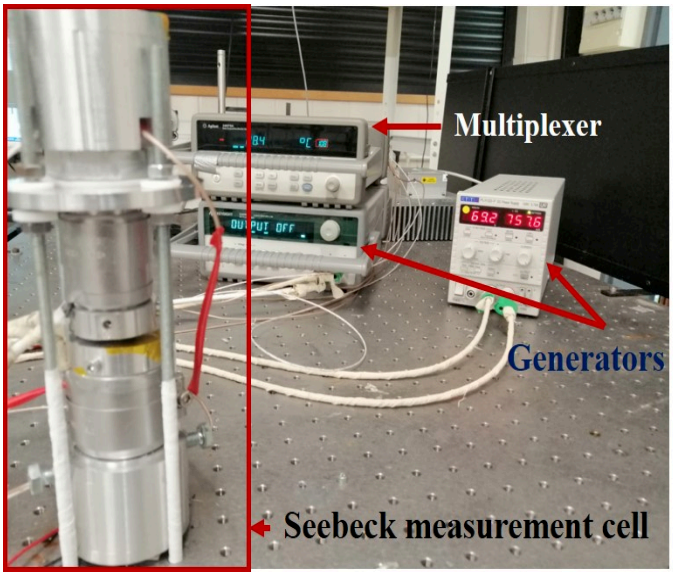

Figure 5.9: Photographic image of the home-made Seebeck cell measurement set-up.

contribute to the Seebeck coefficient. This phenomenon is known as 'phonon drag effect' [305]. Seebeck coefficient can be positive or negative depending on the nature of majority charge carriers, e.g. positive for holes and negative for electrons.

Working conditions

Seebeck coefficient measurement cell includes two cylinders surrounded by the nozzle heater to maintain a steady temperature difference. These heaters were connected to the two power sources (KEYSIGHT E3645A and TTI PLH120-P). Inside each cylinder, there is a type T thermocouple composed of copper/constantan. Thermocouple temperature and potential differences were measured by a multiplexor (Agilent 34970A) and transmitted to a Labview program for recording voltage and temperature control. The constant temperature difference is ensured using a Proportional Integral Derivative (PID) controller. The controlled temperature was indicated by the same multiplexor (Agilent 34970A) connected to the Pt1000 probes inside cylindrical ends. All the measurements were conducted at

the near ambient temperature.

5.4 Conclusion

Several methods for measuring thermoelectric parameters such as, the Seebeck coefficient S, electrical conductivity σ, and total thermal conductivity κ have been covered in this chapter. The Seebeck coefficient was measured by a home-made setup. The electrical conductivity of the thin-films was measured using the four-point probe method. However, this technique was unsuitable for measuring the electrical conductivity of the pellets, so impedance spectroscopy was used. Photothermal radiometry was utilized to determine the thermal conductivity.

Chapter 6

Transport properties of polymer nanocomposites for thermoelectric energy conversion

In this chapter, we will thoroughly discuss the transport properties, such as, electrical conductivity, thermal conductivity, and Seebeck coefficient, of polymer nanocomposites. Then we will discuss the thermoelectric efficiency of the polymer nanocomposites calculated from the thermoelectric power factor, PF. The results obtained from the transport properties will then be analysed with the help of the X-ray diffraction method and UV-Visible spectroscopy. The phenomenon behind it will be elaborated on in detail.

6.1 Electrical conductivity

The electrical conductivity of the nanocomposites has been determined by using two techniques, namely, impedance spectroscopy and the four-point probe method. The samples for impedance spectroscopy were used in a pellet form with a 13 mm

diameter and approximately 800 μm thickness. The surface of the pellet has been metalized by depositing a thin layer of silver paste to ensure better contact between pellets and metal probes. On the other hand, the four-point probe technique is suitable for the thin films as discussed in 5. Steps to fabricate the thin film have already been described in section 3.5. We made many modifications to get better results, which we will discuss here. We measured the electrical conductivity of the TQDGO/PEDOT: PSS nanocomposites with:

1. No additional treatment (section 3.2.2) and naming the samples as non-treated pellets,

2. Acid treatment with hydrochloric acid (section 3.3) and naming the samples as acid-treated pellets,

3. Commercially available PEDOT: PSS as a matrix (section 3.4), and naming the samples as commercially available PEDOT: PSS,

4. Non-treated pellets were transformed to thin films (section 3.5) and naming the samples as thin-films.

6.1.1 Non-treated PEDOT: PSS pellets

Initially, we measured the electrical conductivities of the non-treated TQDGO/ PEDOT: PSS nanocomposites in pellet form by using impedance spectroscopy in the frequency range from 100 Hz to 1 MHz. The electrical conductivities for non-treated TQDGO/PEDOT: PSS pellets as a function of frequency are shown in figure 6.1. The pristine PEDOT: PSS and 0.5 wt.% TQDGO/PEDOT: PSS samples showed the two components of the electrical conductivity as described by Jonscher [300]. It was observed that the ac electrical conductivity increased with

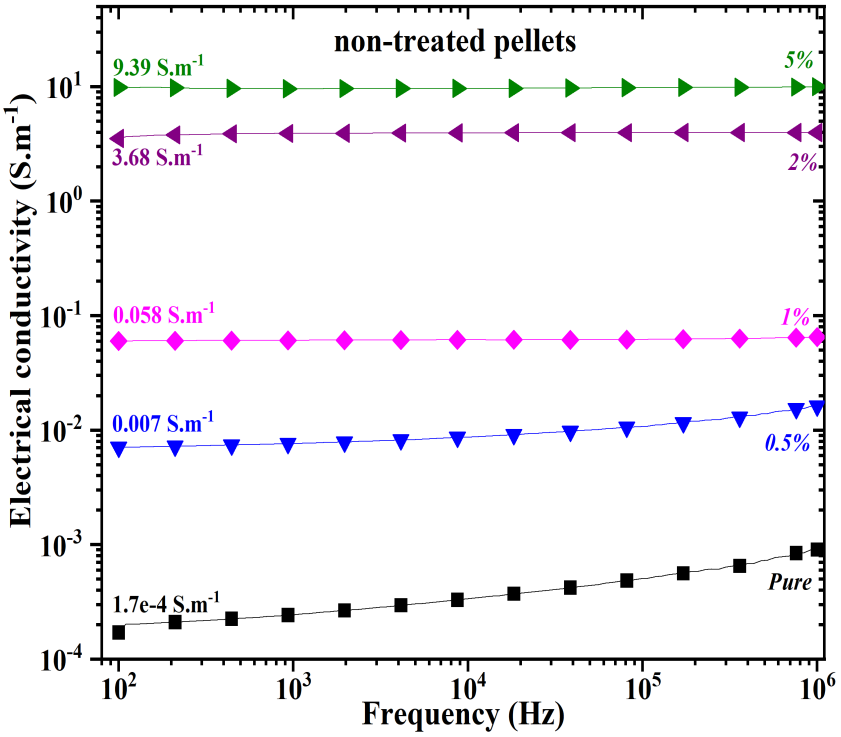

Figure 6.1: The electrical conductivities of non-treated pellets of PEDOT: PSS with TQDGO filler as a function of frequency.

frequency, which is typical of disordered materials such as, oxides and nanocomposites. The conductivity has two characteristic regimes, including a plateau region and a dispersion region, as depicted in figure 6.1. The conductivity was found to be frequency-independent in the plateau region of the low frequency region. The second region, known as the dispersion region, is located in the high frequency zone, where the conductivity is frequency-dependent and increases sharply with increasing frequency. The observed plateau and dispersion regions correspond, respectively, to the DC and polarization component of electrical conductivities. In the low frequency region, the tunneling of the polaron induces grain boundary po-

larization, which manifests as long-range mobility. In the high frequency region, however, the correlated barrier hopping (CBH) model and short-range mobility are associated with the hopping phenomenon, which is primarily responsible for conduction. The DC conductivity in the low frequency range is caused by the polarization of the grain boundaries.

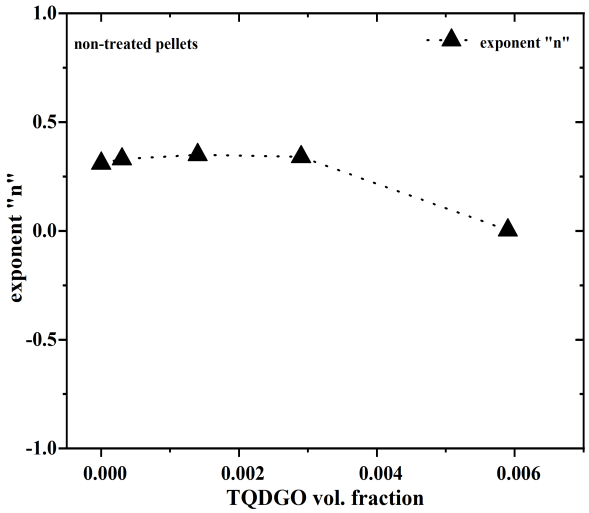

Figure 6.2: The value of exponent in Jonscher power law for non-treated pellets as a function of TQDGO vol. fraction in PEDOT: PSS.

However, the non-linear behavior was observed to decrease with the addition of the filler TQDGO, and it disappeared entirely after the addition of 1 wt.% TQDGO to the PEDOT: PSS matrix. This means that for 1 wt.% doped samples, impedance spectroscopy shows almost a constant value of electrical conductivity over the entire frequency range from 10 Hz to 1 MHz. The DC conductivity σ_{DC} was calculated by fitting the experimentally obtained data with Jonscher's power law using the formula:

$$\sigma_{AC} = \sigma_{DC} + A\ \omega^{n}, \tag{6.1}$$

where, σ_{ac} is the frequency-dependant ac electrical conductivity, ω is the angular frequency, A is the characteristic parameter, and n is the exponent which defines the conduction mechanism. If the value of n lies between 0 and 1, a hopping mechanism is expected for the electrical conduction. If it lies between 1 and 2, the superlinear power law defines the electrical conduction. The experimentally obtained data is shown by the symbols, while the theoretical fit data is represented by the solid lines in figure 6.1. The best-fitting data values estimate the DC electrical conductivity σ_{DC} and the exponent "n".

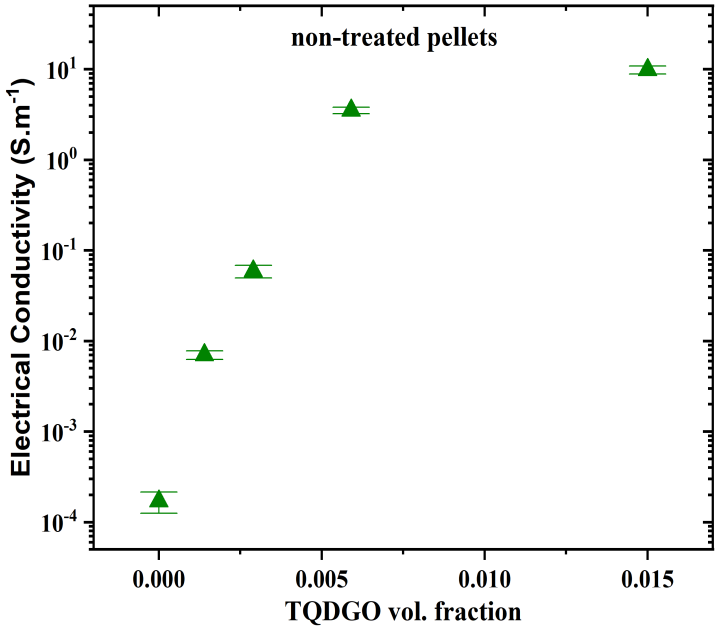

Figure 6.3: Evolution of electrical conductivity as a function of TQDGO filler for non-treated PEDOT: PSS pellets.

The value of the exponent "n" for polymer nanocomposites as a function of TQDGO vol. fraction is depicted in 6.2. It indicates that the value lies between 0 and 1, indicating that the samples' conduction mechanism is a hopping phe-

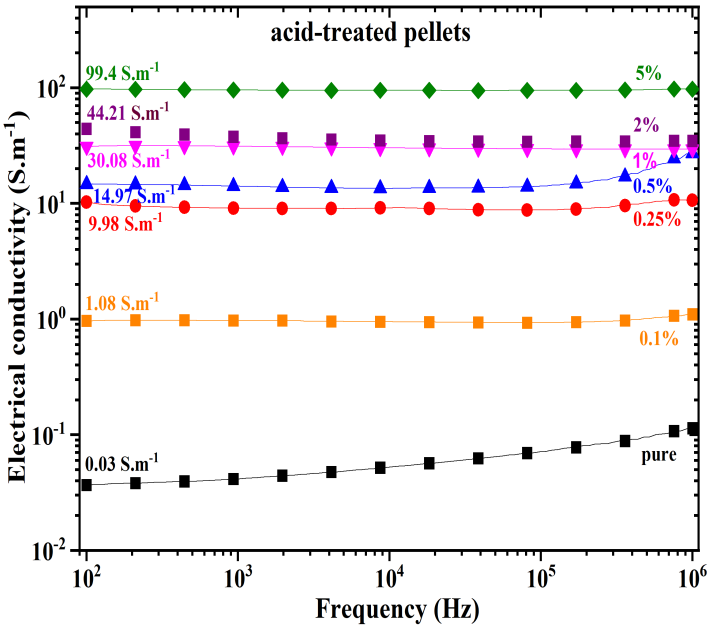

Figure 6.4: The electrical conductivities of acid-treated pellets of PEDOT: PSS with TQDGO filler as a function of frequency.

nomenon. The obtained electrical conductivities for untreated TQDGO/PEDOT: PSS are depicted in figure 6.3. A multiple-fold enhancement in the DC conductivity (σ_{DC}) has been observed with the addition of 0.015 volume fraction of the filler (from 1.7 10^{-4} to 9.84 Sm^{-1}). After the addition of 0.0014 volume fraction of the filler, the electrical conductivity begins to increase dramatically, suggesting the possibility of a percolation-like behavior. Although the PEDOT: PSS matrix has relatively low values in comparison to the scientific literature. With the highest concentration of TQDGO in the polymer matrix, electrical conductivity reached a maximum of 0.098 Scm^{-1}. However, the obtained electrical conductivities were quite low compared to the literature [306], and such small values were insufficient to demonstrate good TE behavior, so we attempted to optimize the material. In

the subsequent step, we acid-treated the aforementioned polymer nanocomposites, as described in section 3.3 of chapter 3.

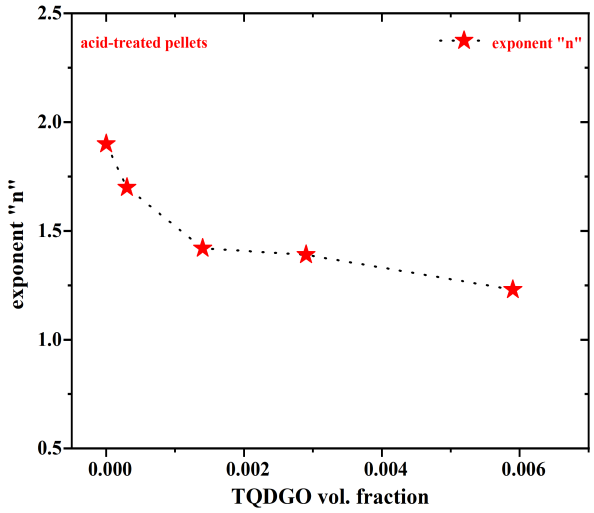

Figure 6.5: The value of exponent in Jonscher power law for acid-treated pellets as a function of TQDGO vol. fraction in PEDOT: PSS.

6.1.2 Acid-treated PEDOT: PSS pellets

Figure 6.4 shows the frequency dependent electrical conductivity (σ_{AC}) of the 6 M HCl treated samples using impedance spectroscopy. Similar to untreated pellets, acid-treated PEDOT: PSS and 0.5 wt.% TQDGO/PEDOT: PSS exhibited frequency-dependent nonlinear conductivity. Figure 6.4 displays experimentally obtained data by symbols and Jonscher's fit data according to equation 6.1 by connecting lines. The best fit data was provided with the DC electrical conductivity and the values of the exponent "n" as shown in figure 6.5. The electrical conductivities as a function of TQDGO vol. fraction are shown in figure 6.6. It shows that the electrical conductivity was enhanced with the filler and also the

electrical conductivity for the matrix PEDOT: PSS has increased from 1.7x10^{-4} (for non-treated) to 0.03 Sm^{-1} (acid-treated). As shown in this figure, the DC electrical conductivity σ_{DC} has been enhanced with the filler from 0.03 to 97.58 Sm^{-1} for 0.015 filler volume fraction.

The acid-treatment of the samples was a positive step in enhancing the samples' electrical conductivity, although the values obtained were insufficient for high TE performance. Next, we compared the obtained results to the commercially available PEDOT: PSS (supplied by Sigma-Aldrich).

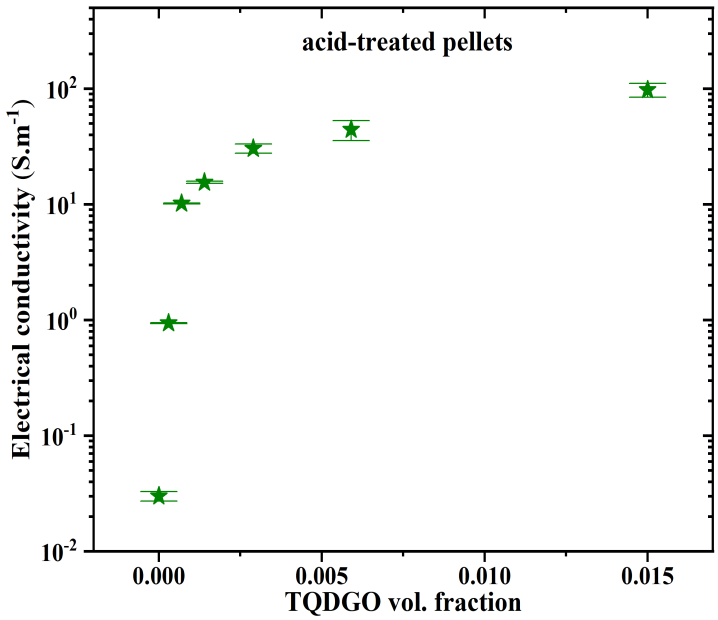

Figure 6.6: Evolution of electrical conductivity as a function of TQDGO filler for acid-treated PEDOT: PSS pellets.

6.1.3 Commercially available PEDOT: PSS

In the next step, we synthesize TQDGO/PEDOT: PSS nanocomposites from commercially available PEDOT: PSS as a matrix (the synthesis process is described in section 3.4 of chapter 3). Figure 6.7 shows the variation in electrical conductivities as a function of frequency and filler volume fraction. Unlike the non-treated and acid-treated sample pellets, the commercial composite does not undergo the variation in conductivity at higher frequencies. Additionally, the obtained conductivity values were greater than those of the previous samples. The pristine matrix has a conductivity of 16 Sm^{-1}, which enhances 15.81 times to 253 Sm^{-1}.

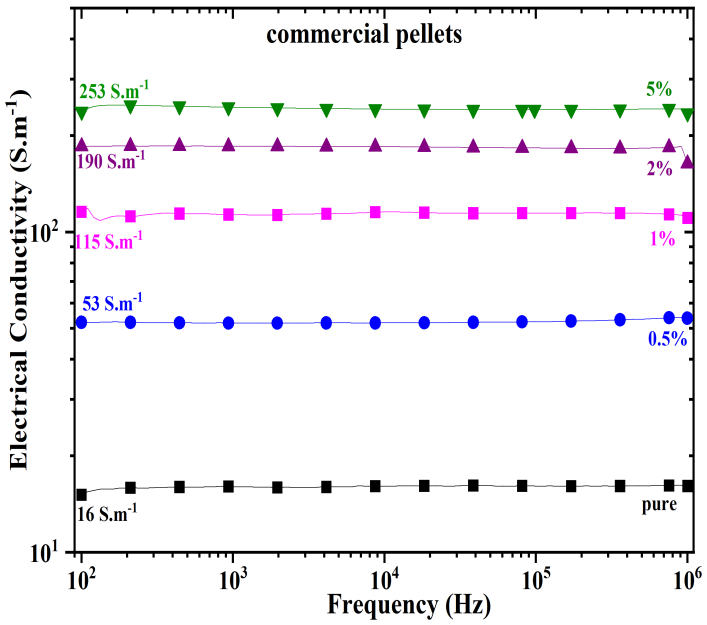

Figure 6.7: Electrical conductivities of commercial available PEDOT: PSS pellets with TQDGO filler as a function of frequency.

Similar to previous samples, the shape of the curve appears unchanged and shows a drastic enhancement after the addition of 0.0014 volume fraction of filler.

This kind of behavior could be explained by the percolation theory. Even so, the electrical conductivity values that were found were not enough to make the nanocomposite a good TE material.

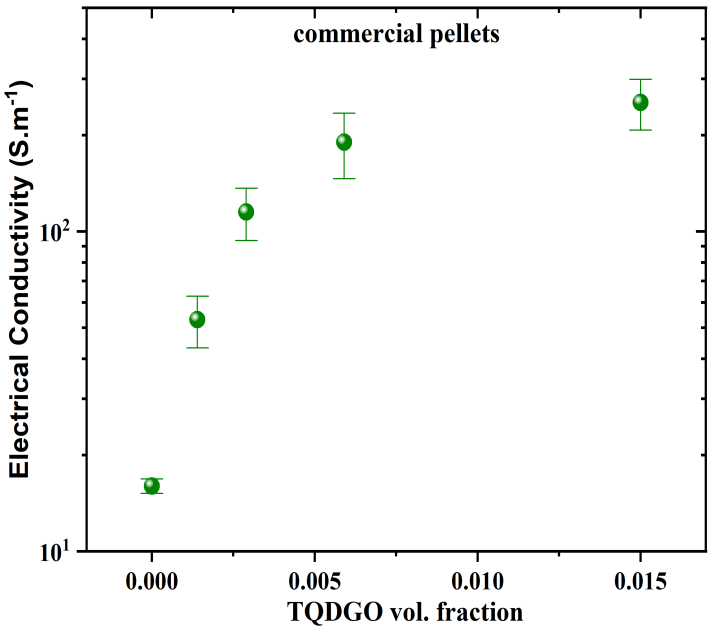

Figure 6.8: Evolution of electrical conductivity as a function of TQDGO filler for commercial PEDOT: PSS pellets.

6.1.4 Thin films of non-treated PEDOT: PSS

In the next step, we decided to try the thin-films of the non-treated samples (the process is explained in section 3.5 of chapter 3). The electrical conductivity of thin films could not be measured by impedance spectroscopy, hence the four-point probe technique was employed. Figure 6.9 shows the sheet resistances of the thin films as a function of filler volume fraction. The pristine PEDOT: PSS thin film has a high sheet resistance of 2.2 10^7 Ωsq^{-1}, leading to a low electrical conductivity

of 0.04 Sm^{-1}. Despite that, the conductivity starts to enhance very fast with the addition of a 0.0014 vol. fraction of the filler, similar to all other samples as shown in figure 6.10. The maximum electrical conductivity of 3.69 10^5 Sm^{-1} was observed for 5 wt.% TQDGO/PEDOT: PSS.

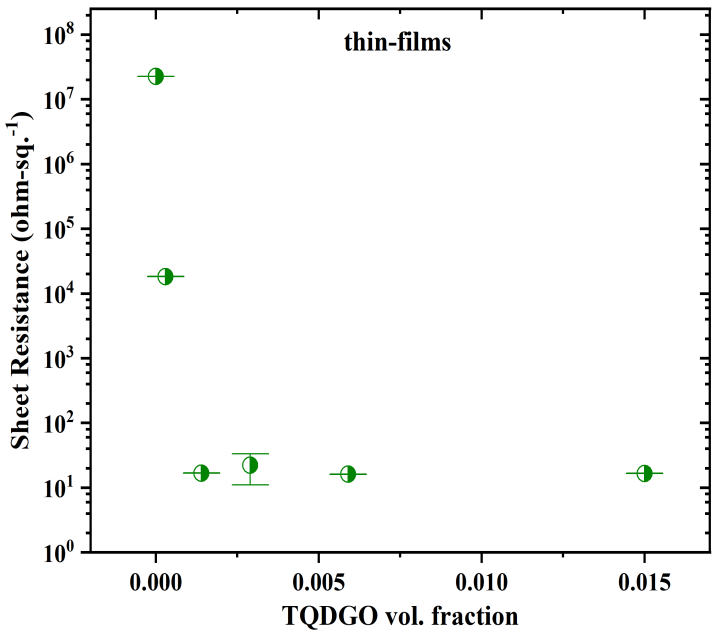

Figure 6.9: Sheet resistance as a function of TQDGO filler for PEDOT: PSS thin films.

6.1.5 Comparison of electrical conductivities

Figure 6.11 illustrates a comparison of the electrical conductivities of each sample. It shows that the non-treated pellets are the least electrically conducting and showed a maximum value of 9.84 Sm^{-1} for 5 wt.% TQDGO/PEDOT: PSS. However, a 10-fold enhancement in the electrical conductivity was observed after the acid-treatment and reached a maximum value of 97.58 Sm^{-1} for 5 wt.%

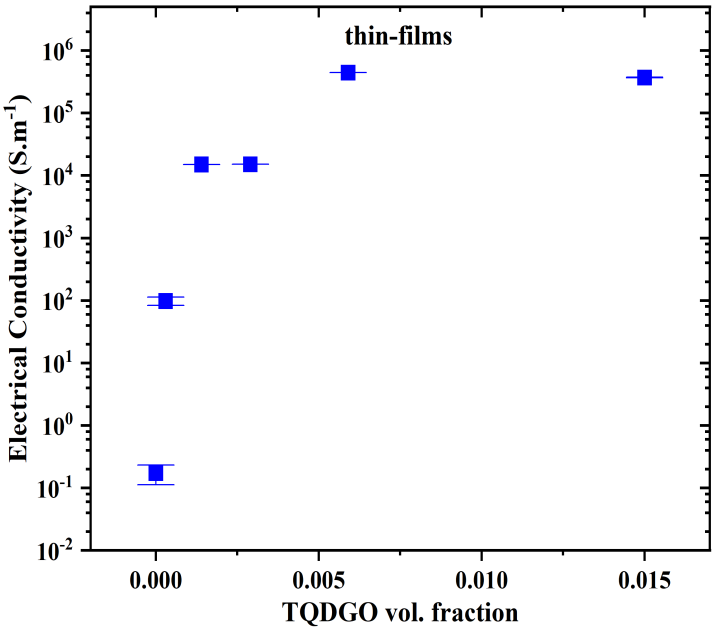

Figure 6.10: Evolution of electrical conductivity as a function of TQDGO filler for PEDOT: PSS thin films.

TQDGO/PEDOT: PSS. The commercial PEDOT: PSS samples showed further enhancement and reached up to 253 Sm^{-1} for 5 wt.%. However, when compared to the literature [307], the obtained electrical conductivities were quite low, and such low values are insufficient to demonstrate good TE behavior. Nevertheless, the thin-film showed a gigantic enhancement of up to 4.4 10^5 Sm^{-1} for 2 wt.% TQDGO/PEDOT: PSS. We believe that the aforesaid consequence could be due to the formation of the PEDOT-TQDGO-PEDOT network as shown in figure 6.12. Many researchers used similar treatments to achieve astonishingly high electrical conductivities [308, 309]. Bae and co-workers reported an electrical conductivity of 4.83 $10^5 Sm^{-1}$ for PEDOT: PSS by using simple chemical treatment [310].

In the present work, TQDGO interacted with PEDOT and PSS via $\pi - \pi$ and

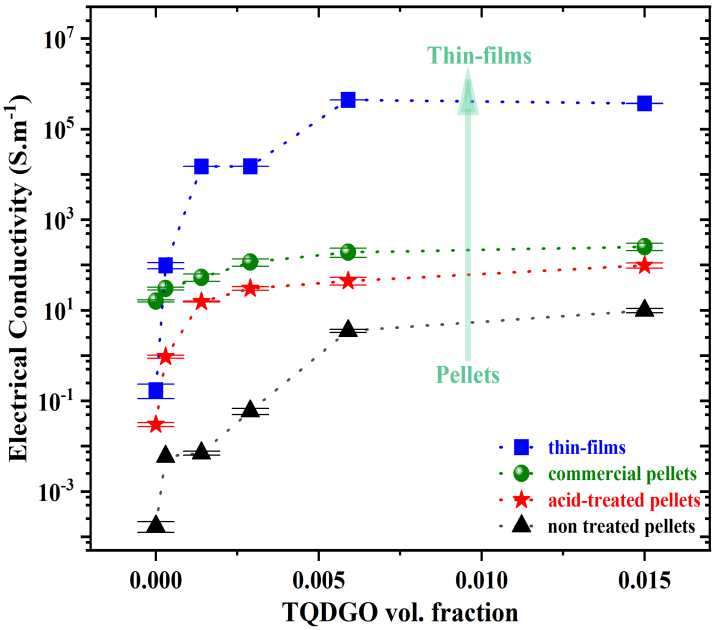

Figure 6.11: Evolution of electrical conductivity TQDGO/ PEDOT: PSS in pellets and thin films.

hydrophilic interactions, respectively, and managed to keep the EDOT and PSS phases separate during the polymerization process. Furthermore, TQDGO formed a conducting network by acting as a building block to connect the PEDOT chains and allowed the PSS phase to tangle around itself, as shown in figure 6.12. By this, a long-range ordered percolation network was established, and a higher crystallinity was induced [261,311]. Hence, the existing conducting pathways provided uninterrupted charge transfer and enhanced electrical conductivity.Furthermore, numerous studies have shown that the addition of polar solvents, such as, ethylene glycol, dimethyl sulfoxide, isopropanol, methanol, dimethylformamide, and others, improve the electrical conductivity of PEDOT: PSS [312–316]. Interaction of polar solvents with PEDOT: PSS is supposed to alter the benzenoid structure

to the quinoid structure and introduce conformational changes in PEDOT chains to improve the electrical conductivity [317–319]. Therefore, the ethylene glycol and annealing process during the thin film formation eliminated the insulating PSS chains and enforced the PEDOT chain's conformation, and finally, straightened them to create longer conducting paths to further contribute to electrical conductivity [151, 320–322].

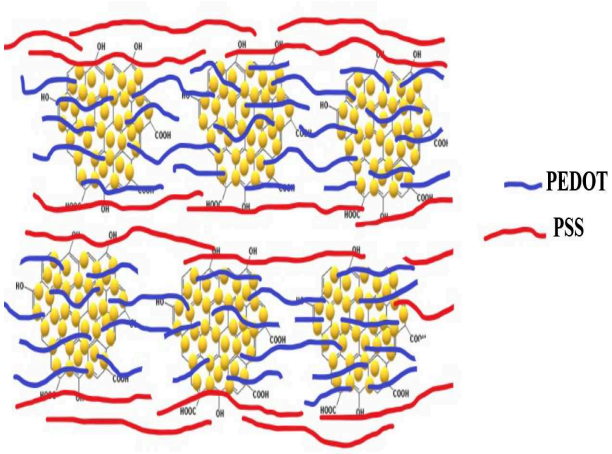

Figure 6.12: Schematic of the conformational changes in PEDOT chains and formation of long range PEDOT-TQDGO-PEDOT network in thin-films.

6.2 Thermal Conductivity by Photothermal Radiometry

The experimental data obtained from the photothermal radiometry is shown in figure 6.13 by triangles, while the fitted data is shown by solid lines. The initially obtained data were converted into normalized data by taking the ratio of signals obtained with and without substrate. The thermal diffusivity and thermal effusivity of samples were determined simultaneously by fitting the normalized phase. The thermal conductivity (κ) of the sample can be calculated by using the formula:

$$\kappa = e\ \sqrt{d} \tag{6.2}$$

Where e, and d are the thermal effusivity and diffusivity of the samples, respectively.

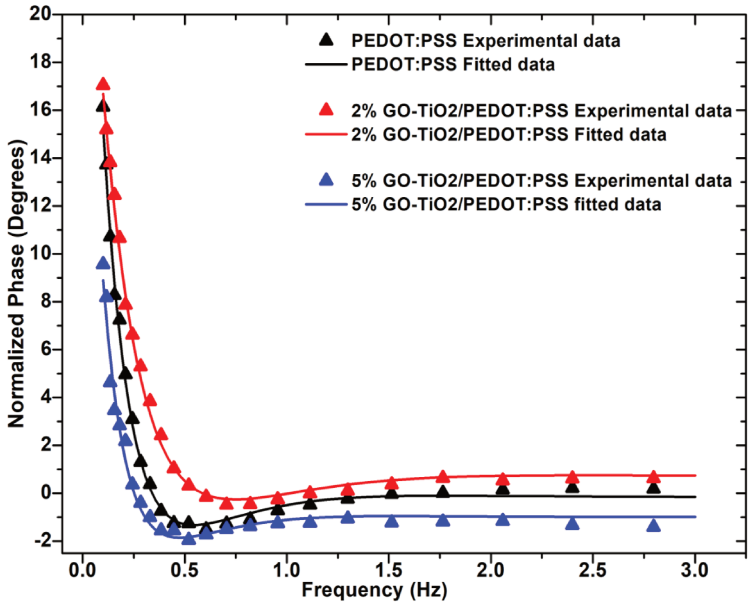

Figure 6.13: Normalized phase vs frequency curves for pure PEDOT: PSS and TQDGO/PEDOT: PSS nanocomposites. The solid lines represent the best fit for the corresponding PTR data.

Figure 6.14 shows the thermal conductivities of non-treated and acid treated pellets. It shows a decreasing trend for the total thermal conductivities with the addition of filler. The total thermal conductivity for the non-treated PEDOT: PSS pellet was 0.46 $Wm^{-1}K^{-1}$, which was decreased to 0.19 $Wm^{-1}K^{-1}$ with addition of 5 wt.% TQDGO. However, the acid treated pellets showed an enhancement in the total thermal conductivity from 1.26 $Wm^{-1}K^{-1}$ to 2.5 $Wm^{-1}K^{-1}$ with 2 wt.% TQDGO of the filler, and then reduced to 1.36 $Wm^{-1}K^{-1}$ with 5 wt.% TQDGO. It could be due to the increased ionic contribution to the total thermal conductivity initially; but, after the addition of 5 wt.%, phonon scattering

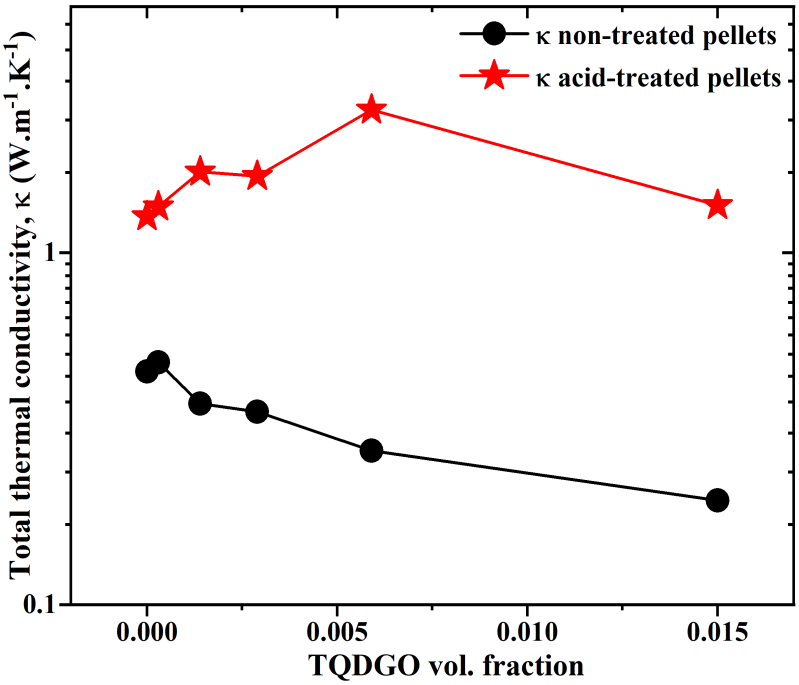

Figure 6.14: Effect of TQDGO filler on thermal conductivity of non-treated and acid-treated PEDOT: PSS pellets.

through TQDGO became dominant, resulting in a decrease in the total thermal conductivity. Therefore, since low thermal conductivity is required to attain a high thermoelectric performance, the acid treatment had a negative impact on the total thermal conductivity, as the value of 0.46 $Wm^{-1}K^{-1}$ for PEDOT: PSS was enhanced to 1.26 $Wm^{-1}K^{-1}$ after the treatment. Similarly, for the 5 wt.% of TQDGO/PEDOT: PSS, the total thermal conductivity was enhanced from 0.19 $Wm^{-1}K^{-1}$ to 1.36 $Wm^{-1}K^{-1}$ after the acid treatment.

To determine the precise reason behind the decrement in the total thermal conductivity, we used Wiedemann-Franz law to calculate the electronic component of the total thermal conductivity by using:

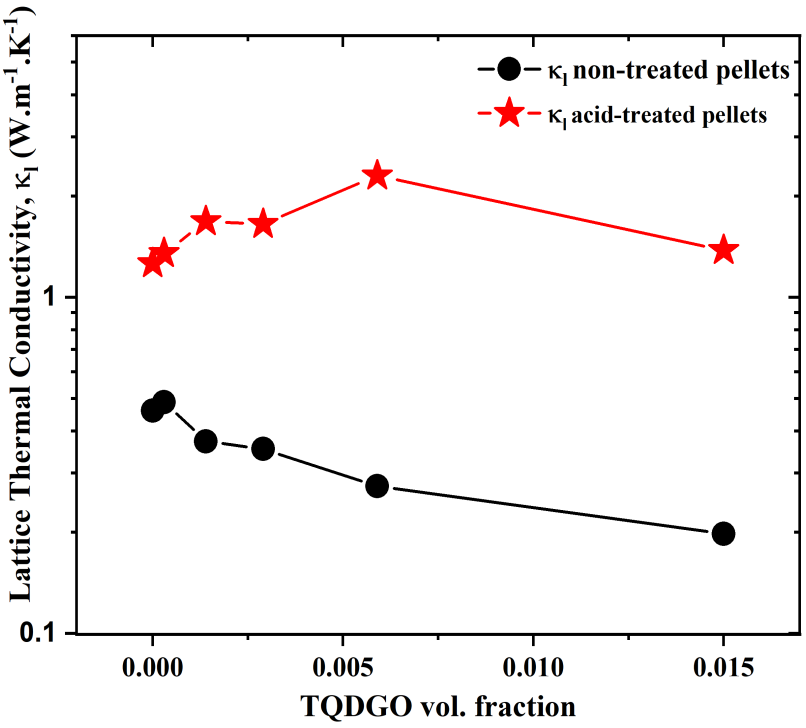

Figure 6.15: The lattice component of total thermal conductivity of non-treated and acid-treated pellets as a function of TQDGO.

$$\kappa_e = L\ \sigma\ T \tag{6.3}$$

where, κ_e, L, and T are the electronic thermal conductivity, Lorenz number, and T is the absolute temperature, respectively. The lattice component of total thermal conductivity is obtained by using:

$$\kappa_l = \kappa - \kappa_e \tag{6.4}$$

Figure 6.15 and 6.16 depict the lattice (κ_l) and electronic (κ_e) components of thermal conductivity, respectively. It indicates that the lattice thermal conductiv-

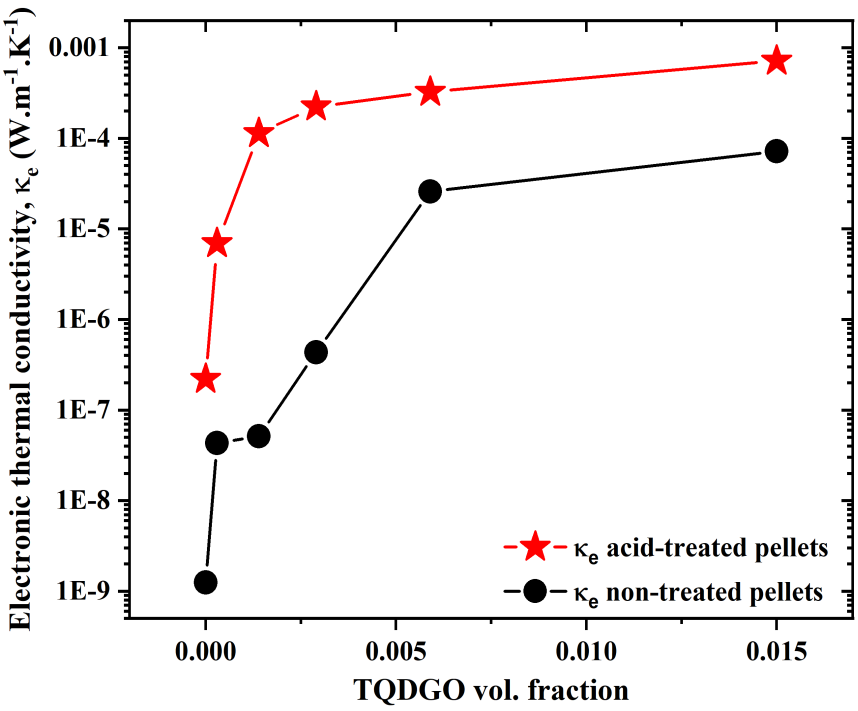

Figure 6.16: The electronic component of total thermal conductivity of non-treated and acid-treated pellets as a function of TQDGO.

ity has a decreasing trend. However, the electronic thermal conductivity has an increasing trend with the filler. Additionally, the contribution of electronic thermal conductivity to total thermal conductivity is insignificant due to the fact that electronic thermal conductivity is extremely low. This indicates that the decrease in total thermal conductivity originates from the lattice portion, most likely as a result of phonon scattering.

These results indicate that the synthesis method used was successful and the filler functions as an effective phonon scattering site to block the phonon pathways [323–325]. The 3-dimensional schematic model for the transport of electrons and phonons is shown in figure 6.17. The thermal behavior of samples could be

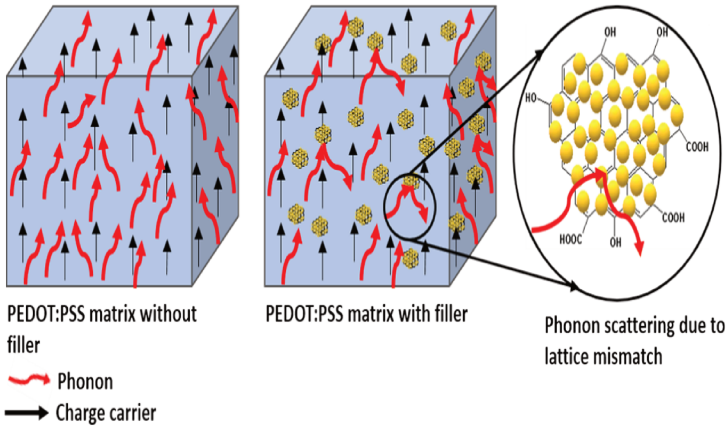

Figure 6.17: Schematic representation of phonon scattering caused by the heterogeneous TQDGO phase in polymer PEDOT: PSS matrix.

explained by the presence of an energy barrier at the interface of the matrix and the filler, preventing low-energy phonons from passing through it and scattering off [323, 324]. The reason for phonon scattering is the existing lattice mismatch provided by the unique structure of TQDGO inclusions, which blocks the phonon pathways, as shown in 6.17.

6.3 Seebeck coefficient

Seebeck coefficient, S, is coming from the build-up of a voltage under a temperature gradient due to the diffusion of charge carriers from hot side to cold side of the sample. The diffusion takes place due to the difference in internal energies of charge carriers, ΔU, between the hot side and the cold side. The Seebeck coefficient was measured at room temperature as a function of filler vol. fraction. Figure 6.18 shows the effect of TQDGO filler on the Seebeck coefficient for pure, acid-treated, commercial PEDOT: PSS pellets and thin films. The non-treated pellets showed ~ 3-fold enhancement in the Seebeck coefficient from 13 to 37 μVK^{-1} with increasing

filler content. The Seebeck coefficient for acid-treated pellets was enhanced from 13.3 μVK^{-1} to 24.59 μVK^{-1} with 5 wt.% TQDGO. However, compared to non-treated pellets, the Seebeck coefficient was decreased to 24.59 μVK^{-1} for the acid-treated pellets. Commercial PEDOT: PSS pellets show a slight enhancement from 13.3 μVK^{-1} to 14.59 μVK^{-1} with 5 wt.% TQDGO.

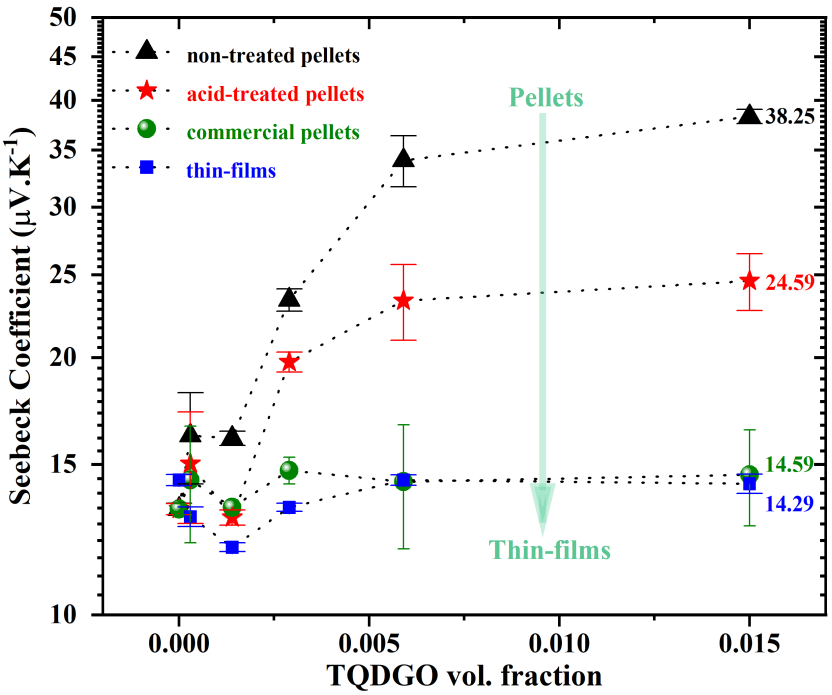

Figure 6.18: Effect of TQDGO filler on Seebeck coefficient of non treated (black triangles), acid treated (red stars), commercial pellets (olive spheres), and thin films (blue squares) of PEDOT: PSS.

The positive values for all the samples indicate a charge transport mainly due to the holes and confirm a p-type behavior. The enhanced Seebeck coefficient is attributed to the strong interaction of TQDGO with PEDOT and PSS at the molecular level. It is evident that the non-treated pellets decoupled the interdependency

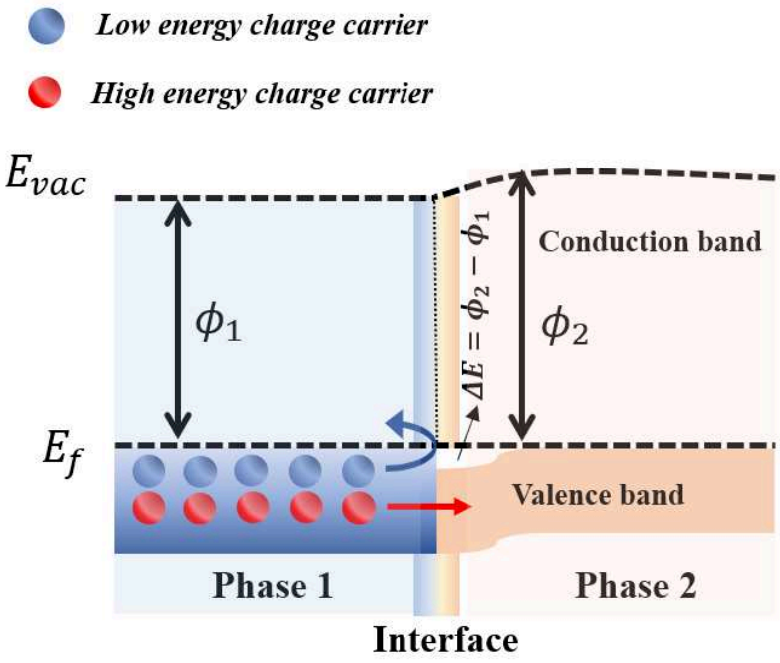

Figure 6.19: Schematic of the energy filtering effect due to the difference in work functions of two phases.

of the Seebeck coefficient and electrical conductivity, which could be ascribed to the energy filtering effect caused by the in-homogeneous grain boundaries of the filler [326–329]. Accordingly, TQDGO acts as a potential barrier (energy filtering sites) at the filler-polymer interface, permitting only charge carriers with higher energy to pass through and led to an increase in the Seebeck coefficient [330]. The energy filtering effect describes that, if there is a difference in the work function levels of the matrix and the filler, the accumulation of the low energy charge carriers at the hot/cold side of the sample is blocked by the internal electric field at the filler-polymer interface. This electric field is induced by the charge transfer between the filler and the matrix [331]. Therefore, only the passage of high energy charge carriers is allowed that can increase the Seebeck coefficient without sacrificing the electrical conductivity as observed in the pellets.

The schematic diagram of the possible energy filtering effect at the polymer-

filler interface is illustrated in figure 6.19. The figure shows the work function of phase 1 and phase 2 as ϕ_1 and ϕ_2, respectively,

On the contrary, thin films did not show any major changes with the filler concentration and offered approximately a constant value of around 13 μVK^{-1}. It indicates that, unlike the pellets, the energy-filtering effect does not exist in the thin films, and it might be due to the large electrical conductivities. In thin films, the TQDGO forms a long-range homogeneous TQDGO-PEDOT-TQDGO network, as shown in figure 6.12, and consequently, TQDGO is no longer effective as energy-filtering sites. Because of this, thin films did not show the energy-filtering effect, and their Seebeck coefficients were low. The increasing trend of electrical conductivity without diminishing the Seebeck coefficient is also attributed to the long-range ordered assembly of TQDGO and PEDOT chains, which facilitates the rapid transit of charge carriers [332] and favors a desired thermoelectric power factor. Note that the trend for the Seebeck coefficient is opposite to the electrical conductivity, as shown in figure 6.11, where the highest values were obtained for the thin films. This fact justifies the tradeoff relationship between electrical conductivity and the Seebeck coefficient [112]. Besides, a similar effect was observed by Z. Fan and co-workers for the acid and base treated PEDOT: PSS thin films [333]. They reported the highest PF and TE ZT values of 754 $\mu Wm^{-1}K^{-2}$ and 0.75, respectively, for polymeric thermoelectric materials.

In order to further analyse the existence of an energy filtering effect, the mobility and carrier concentration were calculated by means of impedance spectroscopy [112].

6.4 Mobility and charge carrier concentration calculation

The dielectric properties in the low frequency region are shown in figure 6.20, 6.21, and 6.22 for 1 wt.%, 2 wt.%, and 5 wt.% TQDGO/PEDOT: PSS pellets, respectively. These properties were analyzed using the Uemura model by using [334–336]:

$$\begin{aligned} \epsilon'(f) &= A\ f^{3/2} + B, \\ \epsilon''(f) &= C\ f^{-1} \end{aligned} \tag{6.5}$$

where, A = $\frac{2nq^2D^{3/2}}{\epsilon_0\sqrt{\pi}dk_BT}$, B = ϵ_∞, and C = $\frac{2nq^2D}{\epsilon_0 k_BT}$

Dividing the coefficient A by C, we can calculate the diffusion coefficient, D, by:

$$D = (\frac{A}{C})^2\ \pi\ d^2 \tag{6.6}$$

And finally, the charge carrier concentration, n, is calculated by:

$$n = \frac{C\ \epsilon_0\ k_B\ T}{2\ q^2\ D} \tag{6.7}$$

And, the mobility μ was calculated from:

$$\mu = \frac{\sigma}{n\ q} \tag{6.8}$$

where, f is the frequency, q is the electronic charge, k_B is the Boltzmann constant ϵ_0 is the permittivity of free space, T is the absolute temperature, d is the sample thickness. The values of the constant A, B, C and the diffusion constant, D, charge carrier concentration, n, and mobility, μ, are given in the table 6.1.

TQDGO wt.%	A	B	C	D (m^2s)	n (m^{-3})	μ ($m^2V^{-1}s^{-1}$)
0%	3.96 x 10^4	0.0015	1.73 x 10^5	7.14 x 10^{-9}	1.74 x 10^{19}	6.10 x 10^{-5}
1%	1.79 x 10^5	0.02	3.37 x 10^6	2.02 x 10^{-9}	1.19 x 10^{21}	3.04 x 10^{-4}
2%	1.09 x 10^6	0.132	6.07 x 10^7	1.6 x 10^{-10}	6.18 x 10^{22}	3.71 x 10^{-4}
5%	9.7 x 10^5	0.043	4.84 x 10^7	5.9 x 10^{-9}	5.8 x 10^{21}	1.0 x 10^{-2}

Table 6.1: The calculated values of the constants A, B, C, dielectric constant (D), carrier concentration (n), and mobility (μ) of the TQDGO/PEDOT: PSS pellets.

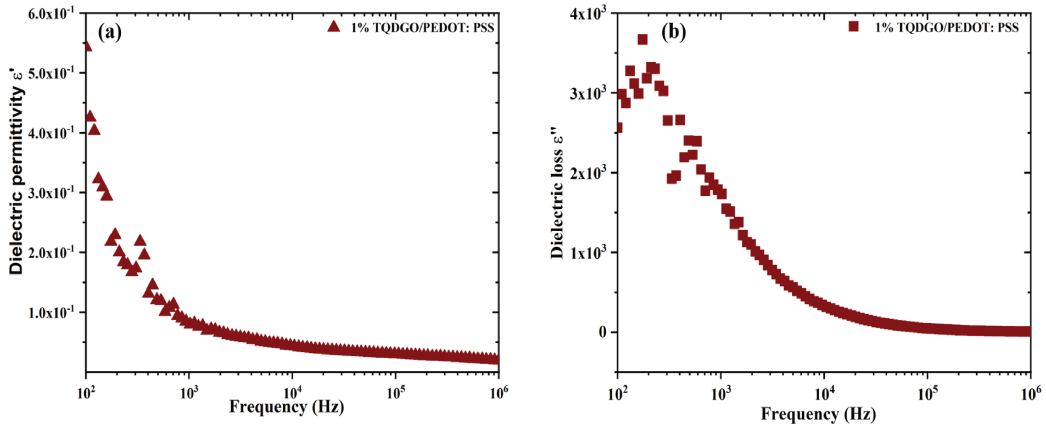

Figure 6.20: (a) Dielectric permittivity and (b) Dielectric loss of 1 wt.% TQDGO/PEDOT: PSS as a function of frequency.

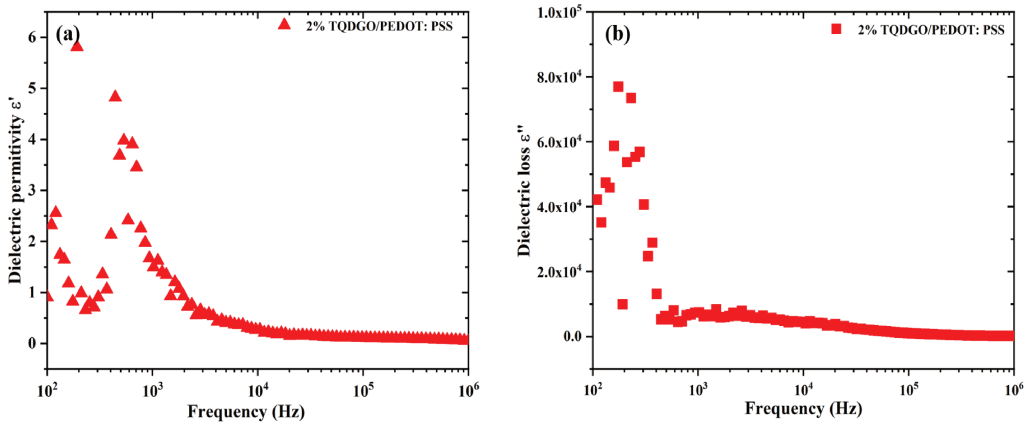

Figure 6.21: (a) Dielectric permittivity and (b) Dielectric loss of 2 wt.% TQDGO/PEDOT: PSS as a function of frequency.

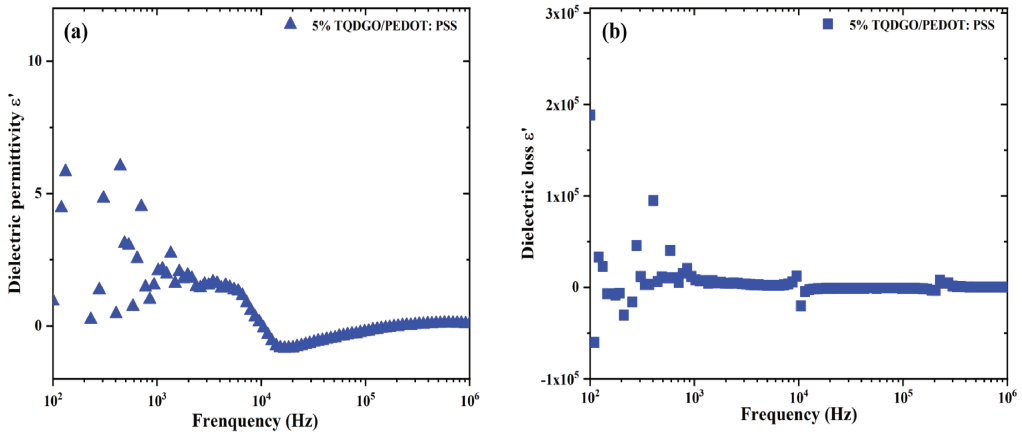

Figure 6.22: (a) Dielectric permittivity and (b) Dielectric loss of 5 wt.% TQDGO/PEDOT: PSS as a function of frequency.

The findings revealed an increase in mobility values with the filler, which may be attributed to the energy-filtering effect in pellets. In-homogeneity and the existence of sharp grain boundaries are crucial to the energy filtering effect, resulting in an increase in electrical conductivity and Seebeck coefficient simultaneously. Only a handful of studies have successfully demonstrated the energy filtering effect, and the phenomenon underlying it remains unknown. [337, 338]. The schematic diagram of the energy filtering effect at the polymer-filler interface is illustrated in figure 6.19. The work function of the samples could not be measured, hence the values from the previous reports were taken into account. Literature shows that the work function of PEDOT: PSS is around 5 eV [339] and $GO - TiO_2$ is around 4.2 eV [340]. It is worth mentioning that the explanation of the energy filtering effect is based on the assumption that the work function values are the same as the reported literature values.

Generally, including nanostructures in a matrix has two effects on the Seebeck coefficient. First, it can enhance the internal energy difference of charge carriers on the hot and cold sides. A larger energy difference induces larger charge diffusion, leading to an achieved higher Seebeck coefficient. In addition, nanostructures

decrease the phonon mean free path due to the change in the lattice constant at the interface and reduce the lattice thermal conductivity κ_l. As discussed earlier, in our case, thermal conductivity was observed to be decreased with filler and could potentially enhance the Seebeck coefficient. In addition, hydrangea like TQDGO nanostructure can also enhance the density of state near the Fermi level via the quantum confinement effect. The combined outcome of the above hypotheses leads to the increment in Seebeck coefficient and a decrement in thermal conductivity [112].

6.5 Thermoelectric power factor (PF)

The electrical conductivity and the Seebeck coefficient have a significant impact on the thermoelectric *power factor (PF)*. However, the impact of the Seebeck coefficient is slightly lesser than the electrical conductivity. Figure 6.23 depicts the effect of TQDGO on the power factor of PEDOT:PSS. A manifold growth for all the samples was observed. The power factor of non-treated pellets was increased from 3.09 10^{-8} $\mu Wm^{-1}K^{-2}$ to 0.013 $\mu Wm^{-1}K^{-2}$. The acid treatment increased the electrical conductivity while decreasing the Seebeck coefficient, resulting in a slight increase in the power factor (0.0418 $\mu Wm^{-1}K^{-2}$). The commercial PEDOT: PSS pellets have the power factor of 0.003 $\mu Wm^{-1}K^{-2}$, however, it did not change significantly after the addition of 5 wt.% TQDGO compared to non-treated and acid-treated pellets. Even with the highest TQDGO content, all pellet samples exhibited a low power factor due to their low electrical conductivities. Consequently, they were incompatible with the TE applications.

Nevertheless, the large values of electrical conductivities in thin films leads to a enormous increase in power factor up to 91.26 $\mu Wm^{-1}K^{-2}$ with 0.0059 vol. fraction of TQDGO. The obtained PF is considerably greater than that of previously re-

ported quantum dot-based thermoelectric polymer nanocomposites [261,341–343]. Since the Seebeck coefficient did not change significantly, the electrical conductivity played a crucial role in increasing the power factor of thin films. The enhanced PF further verifies the strengthened filler-matrix interactions. Similar results were obtained by Dong et al. by using SnOx-NPs in the PEDOT: PSS matrix and a large PF of 116 μWm^{-1}K^{-2} was accomplished with the assistance of dedoping and energy filtering effects [344].

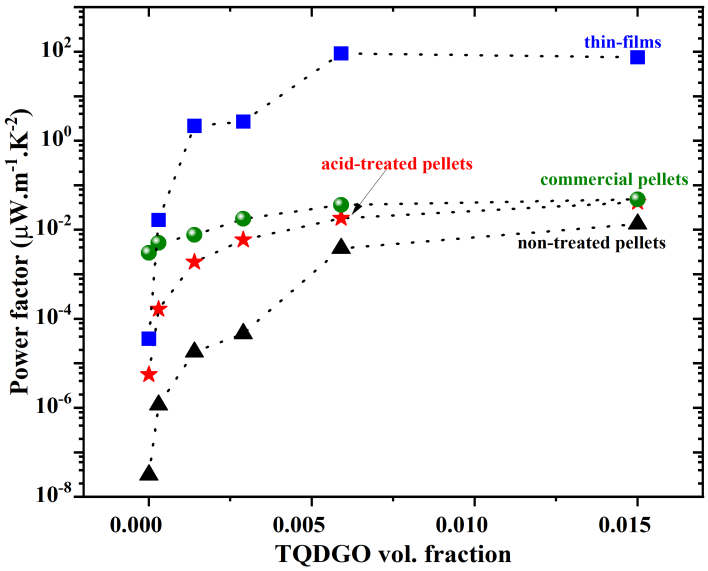

Figure 6.23: The effect of TQDGO filler on the thermoelectric power factor of non-treated (black triangles), acid-treated (red stars), commercial pellets (olive spheres), and thin films (blue squares) of PEDOT: PSS.

6.6 Thermoelectric properties of ethylene glycol treated TQDGO/PEDOT: PSS pellets

As described previously, ethylene glycol and annealing treatment improved the thermoelectric properties of TQDGO/PEDOT: PSS films. Consequently, we analyzed the thermoelectric properties of TQDGO/PEDOT: PSS pellets using the same method as thin films. Figure 6.24 shows the Seebeck coefficient, electrical conductivity, and power factor of the ethylene-glycol treated TQDGO/PEDOT: PSS pellets. The enhancement in the electrical conductivity was observed compared to untreated pellets as shown in figure 6.24 (b). However, the performance was still inferior to thin films because organic materials can control charge transport in thin films more efficiently than in bulk form (pellets) [345, 346].

6.7 Effect of aging

Generally, good thermoelectric materials need to have good stability in the air. Therefore, we analysed the samples with the FTIR spectroscopy and measured the Seebeck coefficient of one-year-old samples kept in an ambient environment for 1 year for the aging process (in North Europe climate) to prove the long-term stability of the samples.

6.7.1 FTIR after aging process

For comparison, figure 6.25 depicts the FTIR of PEDOT: PSS and TQDGO/ PEDOT: PSS before and after the aging process. The FTIR demonstrated that the samples did not degrade chemically. However, it showed that the aged samples exhibited a broad hump corresponding to the OH group as indicated by the blue color. This indicates that the samples have absorbed the environmental water due

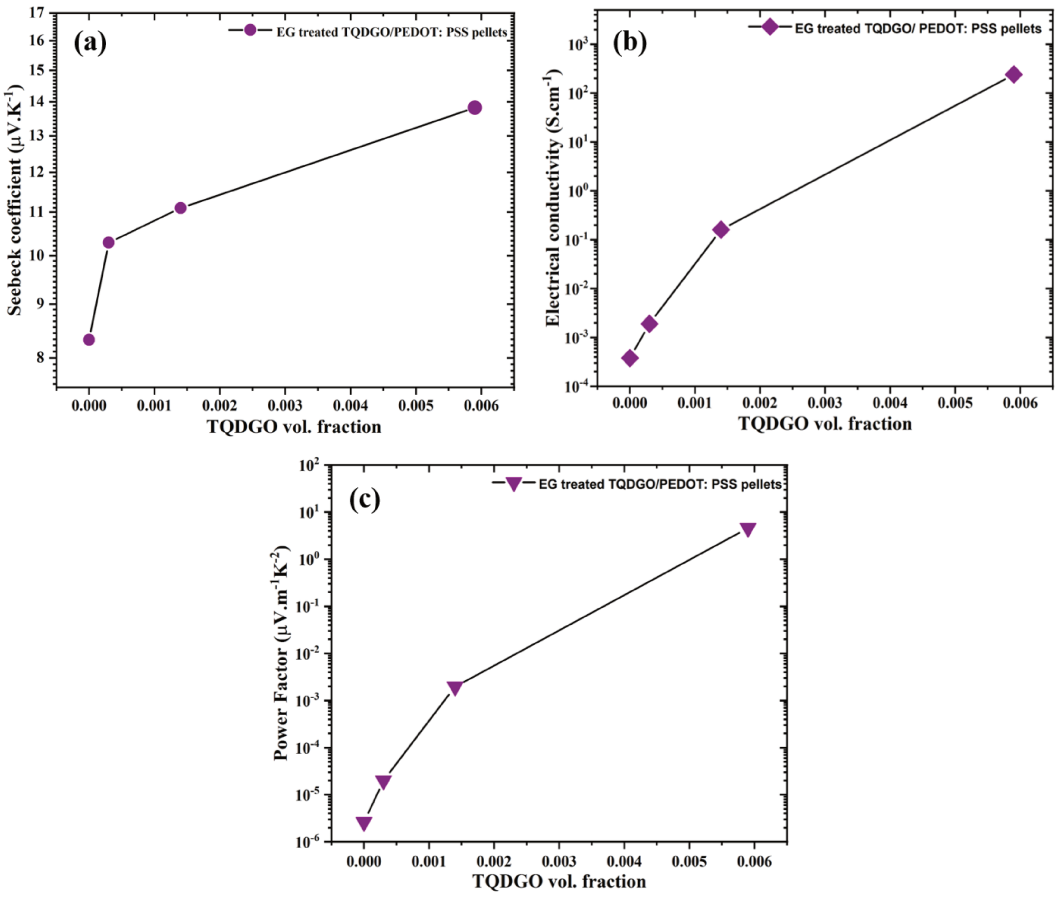

Figure 6.24: (a) Seebeck coefficient, (b) Electrical conductivity, and (c) Power factor of ethylene glycol treated TQDGO/PEDOT: PSS pellets as a function of TQDGO vol. fraction.

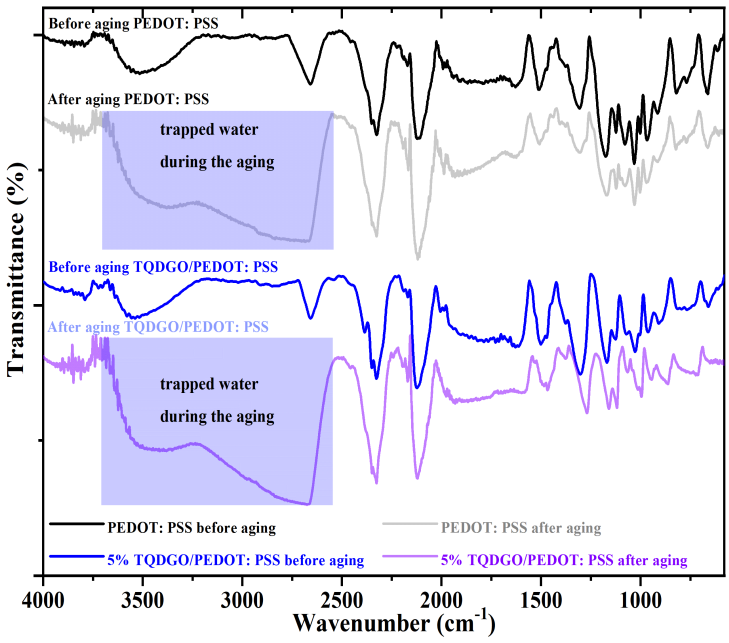

Figure 6.25: FTIR of PEDOT: PSS and TQDGO/ PEDOT: PSS before and after aging in ambient environment.

to the humidity.

6.7.2 Seebeck coefficient measurements after aging process

The Seebeck coefficient measurement is shown in figure 6.26. It shows that the performance of the 5 wt.% TQDGO/PEDOT: PSS has decreased from 37 to 26.7 μVK^{-1} (32.43 %). The observed degradation in the Seebeck coefficient may have been caused by the trapped water as detected by the FTIR.

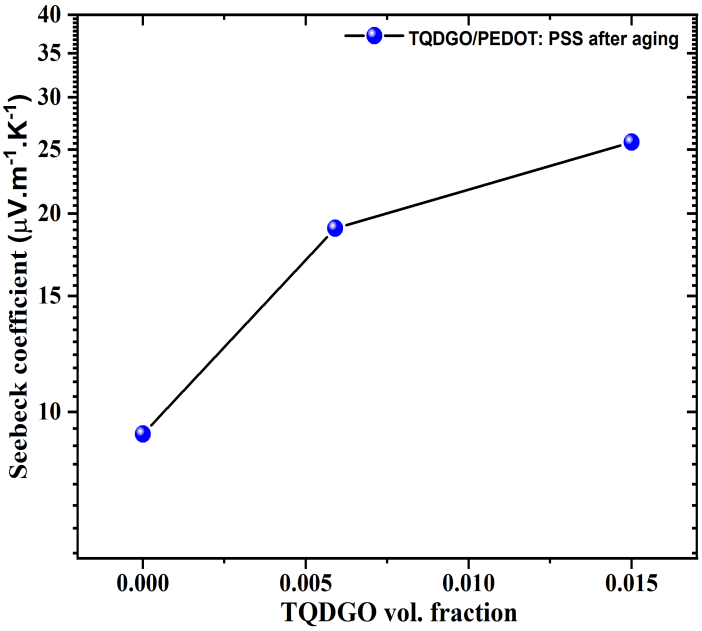

Figure 6.26: Long term stability performance of TQDGO/PEDOT: PSS pellets Seebeck coefficient as a function of TQDGO vol. fraction.

6.8 Discussion

So far, we have observed that the TE properties were improved with the TQDGO filler, and that the performance of the samples in pellets was different than that of the thin films. Interestingly, we noticed the existing dual phenomenon behind the increase in electrical conductivity (could be a long-range PEDOT network) and the Seebeck coefficient (could be energy-filtering) may confer unique thermoelectric properties on PEDOT: PSS based composites. In this section, we will consider some additional analyses, such as, UV-Visible spectroscopy and X-ray diffraction analysis, to confirm our hypothesis. We chose non-treated pellets and thin films for further investigation.

The samples were analysed by XRD to confirm the enhanced crystallinity in thin films compared to the pellets. Figure 6.27 shows the XRD patterns for pristine PEDOT: PSS, TQDGO, 2 wt.%, and 5 wt.% TQDGO/PEDOT: PSS. In pristine polymer, a broad hump starting from $2\theta = 15°$ to $40°$ and centered at $21°$ is associated with the h(020) plane of the polymer backbone, representing the semi-crystalline nature of PEDOT: PSS (JCPDS card no. 00-048-1449). The obtained single peak confirms the uniform mixing and interchain planar ring stacking of PEDOT with PSS [347,348]. The d-spacing of 3.14 Å corresponding to a 2θ value is attributed to the polymer inter-chain distance [349].

Interestingly, this polymeric peak was observed to be shifted towards the higher angle with the addition of TQDGO (from $21°$ to $25°$) which could be attributed to the partial replacement of PSS [350] as shown in figure 6.27 (c). Generally, PSS coils are tangled around the PEDOT, and the surplus PSS places itself at the interface of connecting PEDOT chains [351]. The TQDGO interrupted the excessive PSS chains, as evidenced by the disappearance of the PSS peak with 5wt.% TQDGO in figure 6.27 (d), leaving behind the conducting network of TQDGO-PEDOT-TQDGO chains shown in schematic figure 6.12.

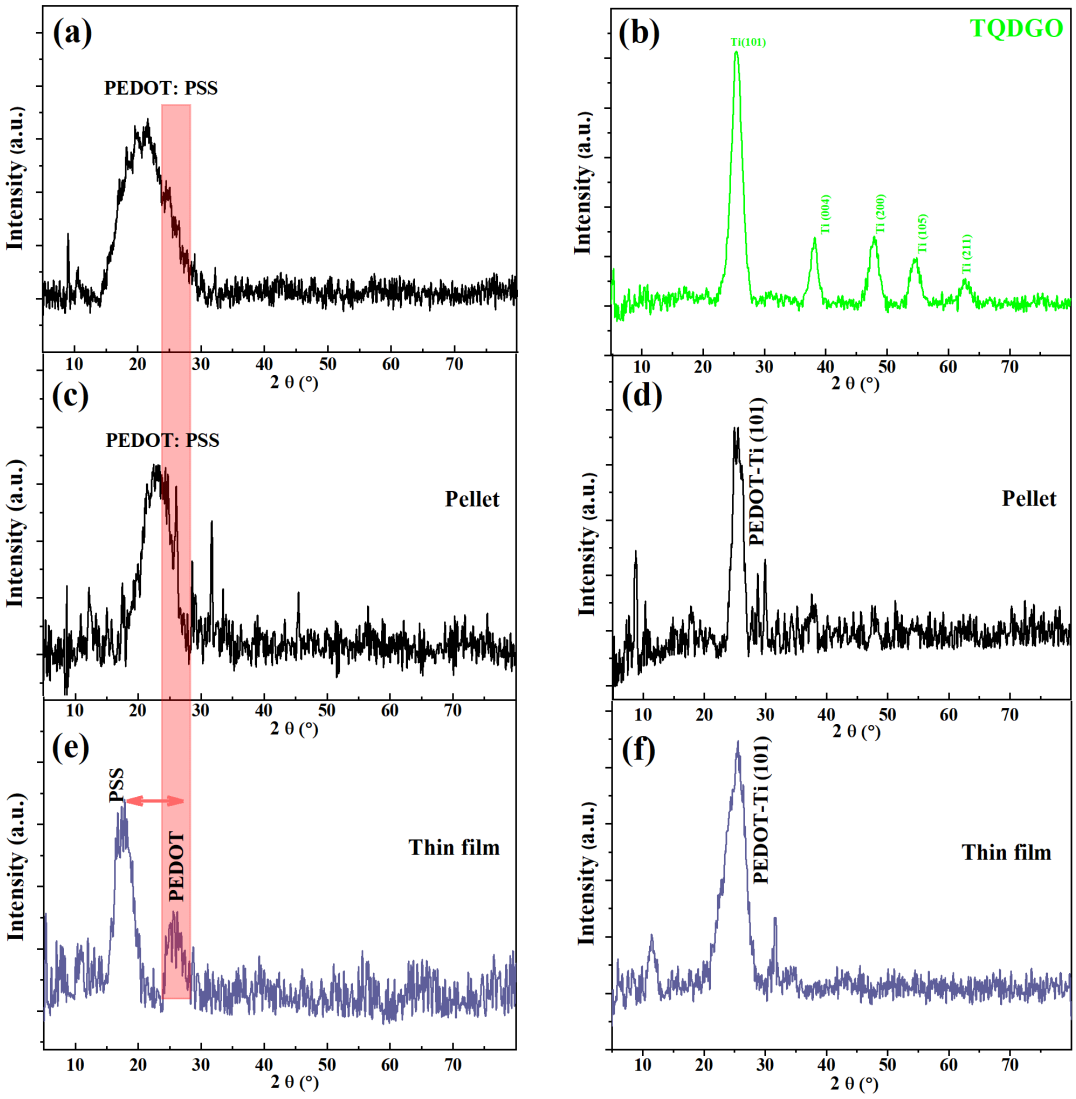

Figure 6.27: X-ray diffractograms of (a) pristine polymer PEDOT: PSS showing single peak corresponding to the strong interaction between PEDOT-PSS, (b) TQDGO filler. XRD for 2 wt.% (c) pellet and (e) thin film indicating the polymeric peak splitting due to the PEDOT-PSS detachments after the addition of TQDGO filler, and 5 wt.% TQDGO/PEDOT: PSS (d) pellet and (f) thin film depicting strong interaction of PEDOT and TQDGO.

Furthermore, in the thin films (figure 6.27 (e)), the polymeric peak in the 2 wt.% TQDGO/PEDOT: PSS pellet (figure 6.27 (c)) was observed to be split into

two, corresponding to the PSS (centering at 17.5°) and PEDOT planes (centering at 25.5°). It is supposed that the ethylene glycol, with a high dielectric constant and a high boiling point, reduced the electrostatic interactions of PEDOT cations with PSS anions due to the screening effect in thin films. [151, 321]. As a result, ethylene glycol and the annealing process might introduce a linear conformation in PEDOT chains to further enhance the crystallinity [352, 353] in thin films from 23.3 % to 41.1 %. Also, in the pellet (figure 6.27 (d)) and the thin film of 5 wt./% TQDGO/PEDOT: PSS (figure 6.27 (f)), there was only one peak that corresponded to the PEDOT phase, indicating that the PSS was already replaced by the TQDGO. Consequently, there was no second peak that matched PSS, and thus there was no peak splitting.

The XRD pattern for TQDGO filler is shown in figure 6.27 (b), and the characteristic peaks for the crystalline planes of the anatase TiO_2 phase were obtained at 2θ values of 25.47 (101), 38.21 (004), 47.89 (200), 54.83 (105), and 62.74 (211) (JCPDS card no. 21-1272). The XRD spectra confirm the anatase phase with a tetragonal crystal structure with no evidence of any other phase or impurity. The main XRD peak for TQDGO belongs to the (101) phase which is in good agreement with the diffraction pattern obtained from the HR-TEM analysis (figure 4.7 (e-f)). Since the peak broadening is solely related to crystalline size, the observed broad peaks imply a smaller particle size for TQDGO in accordance with the Debye-Scherrer's relation $D = 0.9\lambda/\beta\cos(\theta)$ where, D is the mean crystalline size, λ is the incident X-ray wavelength, β is the full width at half maximum (FWHM), and θ is the Bragg's angle [285, 354]. The calculated particle size from the XRD is analogous to the average particle size obtained from the TEM. However, no significant XRD peak was observed for graphene oxide due to the small amount.

Many researchers [355–357] have reported the quantum confinement effect of TiO_2. To confirm the phenomenon, we conducted absorbance studies via

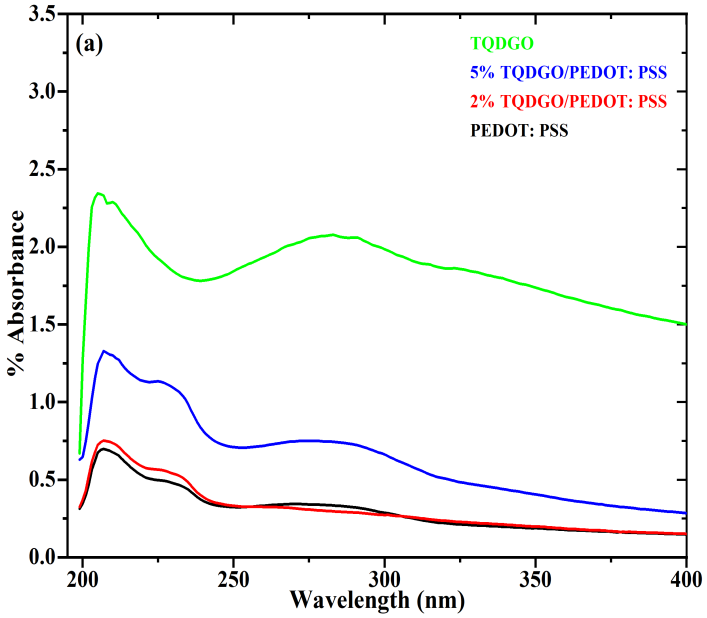

Figure 6.28: Absorption spectrum of TQDGO (green), 5 wt.% TQDGO/PEDOT: PSS (blue), 2 wt.% TQDGO/PEDOT: PSS (red), and pristine PEDOT: PSS (black) as a function of wavelength.

UV-visible spectroscopy. Figure 6.28 shows the absorption spectra for polymer nanocomposites, and no significant variation was observed in the visible range for any sample. The filler undergoes two peaks corresponding, to the $\pi - \pi^*$ transition of the C-C aromatic bond and the $n - \pi^*$ transition of the carbocyclic and carbonyl functional groups. Polymer PEDOT: PSS undergoes the characteristic absorption bands in the UV range from 200 to 350 nm due to the aromatic PSS rings [358].

Semiconductors are classified as direct and indirect band gap semiconductors in accordance with their lowest allowed transitions. The optical band gap of the nanocomposites have been calculated by the Tauc plot equation:

$$(\alpha\ h\nu)^n = A_0\ (h\nu - E_g) \tag{6.9}$$

where, α is the optical absorption coefficient, hν is the incident photon energy, A_0 is the material constant, E_g is the optical band gap and n is the exponent. Here, n posses different values depending on the type of electronic transition for example, n=2 for direct band gap, and n=0.5 for indirect band gap. Figure 6.29 shows the Tauc plots of direct and indirect optical band gaps for TQDGO/PEDOT: PSS by linear extrapolation of $(\alpha h\nu)^n$ vs hν. The obtained results for the optical band gaps are illustrated in table 6.2.

According to the literature, the TiO_2 in anatase phase shows the absorption in the UV regime with an indirect band gap of 3.2 eV [359–361], however, the TQDGO manifest a larger band gap of 3.50 eV. The observed blue shift exhibits a quantum confinement effect and confirms the formation of TiO_2 quantum dots [253]. Similarly, all PNCs showed the absorption in the UV region with a slight decrease in the indirect band gap from 3.88 eV to 3.56 eV with the filler. This may be due to the partial removal of insulating PSS chains (also confirmed by the XRD (figure 6.27)). TQDGO, as the secondary dopant in PEDOT: PSS, has the potential to replace the primary dopant (PSS) if counter ions compensate for the charge on the detached PSS rings. TQDGO undergoes $\pi - \pi$ interaction with PEDOT, and hydrophilic interaction with PSS. TQDGO deduces the Coulombic interaction of PSS with PEDOT and replace PSS to form TQDGO-PEDOT. As PSS is an insulator so establishment of a strong TQDGO-PEDOT interaction forms the conductive pathways [362]. Therefore, a slight decrement in direct (5.42 eV to 5.25 eV) and indirect band gaps (3.88 eV to 3.56 eV) for PEDOT: PSS have been observed with addition of 5 wt.% TQDGO as shown in table 6.2. Furthermore, the elimination of PSS escalates interchain interaction among conducting PEDOT moieties and justifies the enhanced electrical conductivity in the composites, also the contribution

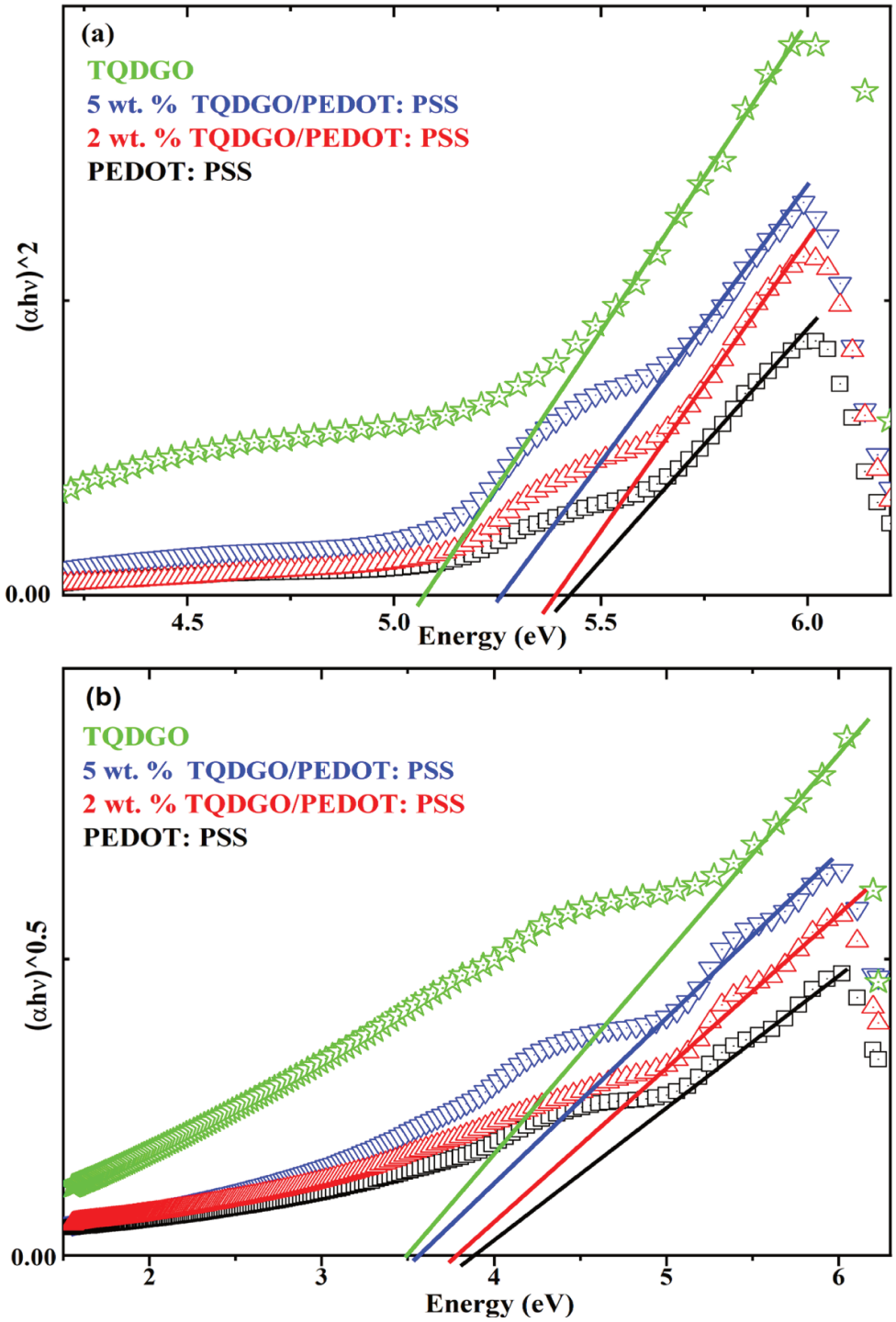

Figure 6.29: Tauc plot by linear extrapolation of (a) $(\alpha h\nu)^2$ vs $h\nu$ for direct band gap and (b) $(\alpha h\nu)^{0.5}$ vs $h\nu$ for direct band gap for TQDGO (green), 5 wt.% TQDGO/PEDOT: PSS (blue), 2 wt.% TQDGO/PEDOT: PSS (red), and pristine PEDOT: PSS (black).

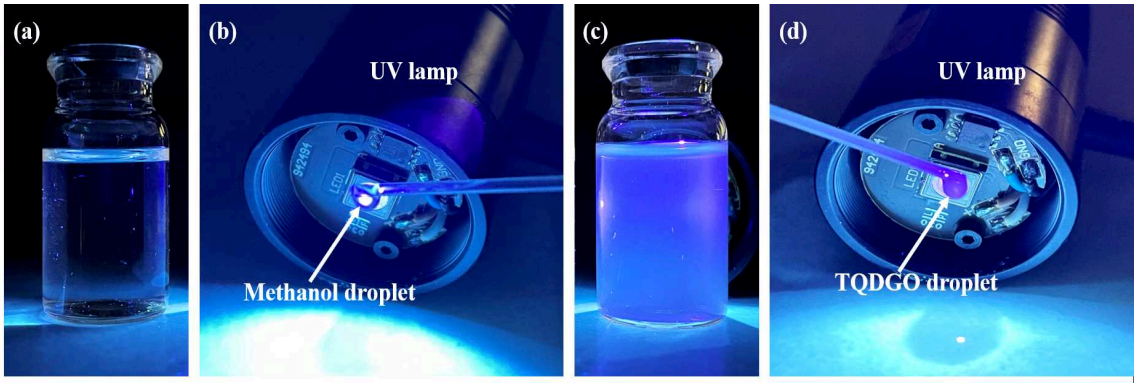

Figure 6.30: Optical image of UV light irradiated (a) methanol (b) methanol droplet, (c) TiO_2 quantum dots decorated graphene oxide (TQDGO) dispersed in methanol, and (d) TQDGO droplet irradiated by UV-light. The blue color of TQDGO confirms the 3.75±0.95 nm particle size.

Sample name	Direct band gap (E_d) (eV)	Indirect band gap (E_{id}) (eV)
PEDOT: PSS	5.42	3.88
2 wt.% TQDGO/PEDOT: PSS	5.38	3.77
5 wt.% TQDGO/PEDOT: PSS	5.25	3.56
Filler TQDGO	5.07	3.50

Table 6.2: Direct and indirect band gap values for TQDGO /PEDOT: PSS nanocomposites by Tauc plot.

of the filler to electrical conductivity cannot be ignored [363]. Figure 6.30(c) and (d) show the unique optical properties of quantum dots by emitting the blue light under the UV illumination. The blue color confirms the 3-4 nm particle size of the as-synthesized TiO_2 quantum dots. Similar size dependant optical properties were observed for the ZnSe quantum dots [364].

6.9 Conclusion

In this chapter, the TE properties of PEDOT: PSS nanocomposites (bulk and thin films) were investigated. Major enhancements in electrical conductivity and the

Seebeck coefficient were achieved, and the issue associated with their interdependence was resolved. In addition, the improved TE performance could be due to the energy filtering effect [365] combined with the long PEDOT chain conformation due to the TQDGO filler. It was discovered that thin films have far superior thermoelectric properties than pellets. The thermal conductivity of the pure and acid treated pellets was investigated. The thermal conductivity of the pure pellets was decreased with the filler indicating that the filler is offering the interfacial resistance to the phonons. However, the acid-treatment had a negative impact on thermal conductivity and it was enhanced from 0.19 $Wm^{-1}K^{-1}$ to 1.36 $Wm^{-1}K^{-1}$. As a consequence, acid treated pellets suffered from the lowest thermoelectric ZT value of around 9.2 x 10^{-6}.

Conclusion and future perspectives

In this thesis, we have provided an in-depth literature review of thermoelectric principles, materials, and their applications. We have covered the conventional high-performance inorganic thermoelectric materials, their properties, advantages, and limitations. We have provided a comprehensive literature review of conducting polymers, their properties, and applications, including thermoelectricity. We then discussed various metal-oxides and their nanostructures for thermoelectric applications, where the research gap was identified as TiO_2 quantum dots have never been used for thermoelectric applications.

We have used a polymer nanocomposite composed of PEDOT: PSS as a matrix and TiO_2 quantum dot decorated graphene oxide as a filler. The thermoelectric performance of the aforementioned composites was investigated by measuring electrical conductivity, thermal conductivity, and the Seebeck coefficient. The TQDGO/PEDOT: PSS hybrid composite was prepared by the oxidative polymerization process and was analysed by XRD, SEM, EDS, FTIR, UV-Vis spectroscopy, and TGA. The thermal conductivity measurements of the materials were done by the PTR method. Seebeck coefficient measurements were done with a home-made

setup based on the two-probe method. The electrical conductivity of the pellets and thin films was measured by impedance spectroscopy and four-point probe methods, respectively.

We have encountered the challenges associated with achieving high thermoelectric performance due to the interdependency of thermoelectric parameters, namely, electrical conductivity, Seebeck coefficient, and thermal conductivity. However, thanks to nanostructures, it was possible to partially break this interdependency by employing an interface phonon scattering approach, which further provided the energy filtering sites. An effort has been made to improve the TE efficiency by reducing the phonon contribution to thermal conductivity without affecting the other parameters. The issues associated with achieving a high Seebeck coefficient, high electrical conductivity, and low thermal conductivity have been successfully resolved in our work. The nanostructuring of TQDGO provided the successive energy filtering sites, also working as phonon scattering sites to effectively enhance the thermoelectric performance.

In summary, we demonstrate an effective and facile method to enhance the TE properties of PEDOT: PSS (bulk and thin films) by incorporation of the titanium di-oxide quantum dot decorated graphene oxide (TQDGO). The best TE composite in our work was 0.0059 vol. fraction of TQDGO in the PEDOT: PSS matrix with an electrical conductivity of 4,413.31 scm^{-1} and a power factor of 91.26 $\mu Wm^{-1}K^{-2}$ which is among the highest values of any quantum dot-based polymer nanocomposites. The fact that titanium di-oxide based quantum dots in PEDOT: PSS have never been reported in thermoelectric applications exemplifies the novelty of the current work. The thermoelectric applications of the flower-like structure composed of quantum dots in PEDOT: PSS were likewise unknown. The as-synthesised PNCs showed their potential applications in waste heat management.

Future research should concentrate on developing new heterogeneous nanostructures embedded in a conducting matrix. Attempts can be made to better understand the energy filtering phenomenon and link it to the thermal conductivity. The barrier height of the inclusions can be optimized in order to attain the maximum thermoelectric *figure of merit*. The obtained results could be explained by using theoretical models to understand the exact mechanism behind the transport properties.

Bibliography

[1] Shiho Kim, Soonseo Park, SunKook Kim, and Seok Ho Rhi. A Thermoelectric Generator Using Engine Coolant for Light-Duty Internal Combustion Engine-Powered Vehicles. *Journal of Electronic Materials*, 40(5):812–816, 2011.

[2] D. Samson, T. Otterpohl, M. Kluge, U. Schmid, and Th. Becker. Aircraft-Specific Thermoelectric Generator Module. *Journal of Electronic Materials*, 39(9):2092–2095, 2010.

[3] Pawel Ziolkowski, Knud Zabrocki, and Eckhard Müller. TEG design for waste heat recovery at an aviation jet engine nozzle. *Applied Sciences*, 8(12):2637–2658, 2018.

[4] Saniya LeBlanc. Thermoelectric generators: Linking material properties and systems engineering for waste heat recovery applications. *Sustainable Materials and Technologies*, 1(1):26–35, 2014.

[5] Fengjiao Zhang, Yaping Zang, Dazhen Huang, Chong-an Di, and Daoben Zhu. Flexible and self-powered temperature–pressure dual-parameter sensors using microstructure-frame-supported organic thermoelectric materials. *Nature Communications*, 6(1):8356–8366, 2015.

[6] Shuankui Li, Zhongyuan Huang, Rui Wang, Chaoqi Wang, Wenguang Zhao, Ni Yang, Fusheng Liu, Jun Luo, Yinguo Xiao, and Feng Pan. Precision grain boundary engineering in commercial $Bi_2Te_{2.7}Se_{0.3}$ thermoelectric materials towards high performance. *Journal of Materials Chemistry A*, 9(1):11442–11449, 2021.

[7] data World, energy. https://www.iea.org/data-and-statistics/data-tables?country=worldenergy=balancesyear=2019. *IEA*, 1(1):1 – 3, 2021.

[8] Lazaros Tzounis. Organic thermoelectrics and thermoelectric generators (tegs). *Intech Open*, 2(1):1–26, 2019.

[9] Abhijit Dey, Om Prakash Bajpai, Arun K. Sikder, Santanu Chattopadhyay, and Md Abdul Shafeeuulla Khan. Recent advances in CNT/graphene based thermoelectric polymer nanocomposite: A proficient move towards waste energy harvesting. *Renewable and Sustainable Energy Reviews*, 53(1):653–671, 2016.

[10] Sebastian Volz. Thermal nanosystems and nanomaterials. *Topics in Applied Physics*, 118(1):1–289, 2009.

[11] Lourdes Ferre Llin and Douglas J. Paul. Thermoelectrics, photovoltaics and thermal photovoltaics for powering ict devices and systems. *Intech Open*, 9(1):1–25, 2017.

[12] Moritz Thielen, Lukas Sigrist, Michele Magno, Christofer Hierold, and Luca Benini. Human body heat for powering wearable devices: From thermal energy to application. *Energy Conversion and Management*, 131(1):44–54, 2017.

[13] V. T Leonov, P. Fiorini, T. Torfs, R. J. M. Vullers, and C. Van Hoof. Thermal matching of a thermoelectric energy harvester with the environment

and its application in wearable self-powered wireless medical sensors. *2009 15th International Workshop on Thermal Investigations of ICs and Systems*, 1(1):95–100, 2009.

[14] Vladimir Leonov. Thermoelectric energy harvesting of human body heat for wearable sensors. *IEEE Sensors Journal*, 13(6):2284–2291, 2013.

[15] Boukai A. Thermal conductivity reduction in silicon fishbone nanowires. *Matrix industries*, 1(1):4452–4460, 2017.

[16] Aime Lay-Ekuakille, Giuseppe Vendramin, Amerigo Trotta, and Gabriella Mazzotta. Thermoelectric generator design based on power from body heat for biomedical autonomous devices. *Institute of Electrical and Electronics Engineers*, 1(1):1–4, 2009.

[17] Takenobu Kajikawa. Overview of thermoelectric power generation technologies in japan. *Shonan Institute of Technology, Kanagawa, Japan*, 1(1):1–33, 2011.

[18] Takenobu Kajikawa. Overview of progress in rd for thermoelectric power generation technologies in japan. *Shonan Institute of Technology, Japan*, 1(1):1–35, 2012.

[19] M. Rull-Bravo, A. Moure, J. F. Fernández, and M. Martín-González. Skutterudites as thermoelectric materials: revisited. *The Royal Society of Chemistry Advances*, 5(52):41653–41667, 2015.

[20] D M de Leeuw, P A Kraakman, P F G Bongaerts, C M J Mutsaers, and D B M Klaassen. Electroplating of conductive polymers for the metallization of insulators. *Synthetic Metals*, 1(1):263–273, 1994.

[21] Hafsa Siddiqui. Modification of physical and chemical properties of titanium dioxide (TiO_2) by ion implantation for dye sensitized solar cells. 1(1):1–24, 2020.

[22] Albert Polman, Mark Knight, Erik C. Garnett, Bruno Ehrler, and Wim C. Sinke. Photovoltaic materials: Present efficiencies and future challenges. *Science*, 352(6283):307–318, 2016.

[23] K.R. Anjana and R.S. Shaji. A review on the features and technologies for energy efficiency of smart grid. *International Journal of Energy Research*, 42(3):936–952, 2018.

[24] Axel Groß. Fundamental challenges for modeling electrochemical energy storage systems at the atomic scale. *Topics in Current Chemistry*, 376(3):376–398, 2018.

[25] Pushker A. Kharecha and James E. Hansen. Prevented mortality and greenhouse gas emissions from historical and projected nuclear power. *Environmental Science & Technology*, 47(9):4889–4895, 2013.

[26] John Asafu-Adjaye, Linus Blomqvist, Stewart Brand, Barry Brook, Ruth DeFries, Erle Ellis, Christopher Foreman, David Keith, Martin Lewis, Mark Lynas, Ted Nordhaus, Roger Pielke, Rachel Pritzker, Joyashree Roy, Mark Sagoff, Michael Shellenberger, Robert Stone, and Peter Teague. An ecomodernist manifesto. *An ecomodernist manifesto*, 1(1):1–33, 2015.

[27] Jeffrey Sachs and Laurence Tubiana. Pathways to deep decarbonization: 2014 report. 1(1):1–232, 2014.

[28] Ruth Shortall, Brynhildur Davidsdottir, and Guni Axelsson. Geothermal energy for sustainable development: A review of sustainability impacts

and assessment frameworks. *Renewable and Sustainable Energy Reviews*, 44(1):391–406, 2015.

[29] Jiangtao Wei, Liangliang Yang, Zhe Ma, Peishuai Song, Mingliang Zhang, Jing Ma, Fuhua Yang, and Xiaodong Wang. Review of current high-ZT thermoelectric materials. *Journal of Materials Science*, 55(27):12642–12704, 2020.

[30] R K Pandey, N Tandon, and R Chaudhary. Effect of top compression piston ring profile on the fuel efficiency of IC engine. (1):1–7, 2009.

[31] Mikhail Vedernikov and E. K. Iordanishvili. A.f. ioffe and origin of modern semiconductor thermoelectric energy conversion. *Seventeenth International Conference on Thermoelectrics*, 1(1):37–42, 1998.

[32] Robert L. Burwell and Ralph G. Pearson. The principle of microscopic reversibility. 70(1):300–302, 1966.

[33] Herbert B. Callen. The Application of Onsager's Reciprocal Relations to Thermoelectric, Thermomagnetic, and Galvanomagnetic Effects. *Phys. Rev.*, 73(11):1349–1359, 1948.

[34] S. R. de Groot. Thermodynamics of Irreversible Processes. *North-Holland Publishing Company Amsterdam*, 8(2):242–244, 1951.

[35] Christophe Goupil, Wolfgang Seifert, Knud Zabrocki, Eckhart Müller, and G. Jeffrey Snyder. Thermodynamics of Thermoelectric Phenomena and Applications. *Entropy*, 13(8):1481–1517, 2011.

[36] Veljko, Rene Zlatic, and Monnier. Modern theory of thermoelectricity. *Oxford University Press*, 1(1):1–256, 2014.

[37] H Julian and Goldsmid. Introduction to thermoelectricity. *Springer*, 1(1):1–233, 2009.

[38] G. Jeffrey Snyder and Tristan S. Ursell. Thermoelectric efficiency and compatibility. *Physical Review Letters*, 91(14):148301–148305, 2003.

[39] Ran He, Gabi Schierning, and Kornelius Nielsch. Thermoelectric devices: A review of devices, architectures, and contact optimization. *Advanced Materials Technologies*, 3(4):1700256–1700273, 2018.

[40] Daniel Champier. Thermoelectric generators: A review of applications. *Energy Conversion and Management*, 140(1):167–181, 2017.

[41] Marlow. Thermoelectric generator (teg) modules. *Matrixindustries*, 1(1):1–2, 2019.

[42] Cronin B. Vining. An inconvenient truth about thermoelectrics. *Nature Materials*, 8(2):83–85, 2009.

[43] Maisam Wahbah, Mohammad Alhawari, Baker Mohammad, Hani Saleh, and Mohammed Ismail. Characterization of human body-based thermal and vibration energy harvesting for wearable devices. *Institute of Electrical and Electronics Engineers Journal on Emerging and Selected Topics in Circuits and Systems*, 4(3):354–363, 2014.

[44] Yang Yang, Xiao-Juan Wei, and Jing Liu. Suitability of a thermoelectric power generator for implantable medical electronic devices. *Journal of Physics D: Applied Physics*, 40(18):5790–5800, 2007.

[45] Achraf Amar, Ammar Kouki, and Hung Cao. Power approaches for implantable medical devices. *Sensors*, 15(11):28889–28914, 2015.

[46] Antonino Proto, Daniele Bibbo, Martin Cerny, David Vala, Vladimir Kasik, Lukas Peter, Silvia Conforto, Maurizio Schmid, and Marek Penhaker. Thermal energy harvesting on the bodily surfaces of arms and legs through a wearable thermo-electric generator. *Sensors*, 18(6):1927–1929, 2018.

[47] Ingo Stark. Converting body heat into reliable energy for powering physiological wireless sensors. *Association for Computing Machinery Press*, 1:1–2, 2011.

[48] Keith D Lind. Understanding the market for implantable medical devices. *American Association of Retired Person Public Policy Institute*, 1(1):1–15, 2017.

[49] Tom Torfs, Vladimir Leonov, Chris Van Hoof, and Bert Gyselinckx. Body-heat powered autonomous pulse oximeter. *IEEE Sensors Journal*, 1(1):427–430, 2006.

[50] Vladimir Leonov. Thermoelectric energy harvesting of human body heat for wearable sensors. *IEEE Sensors*, 13(6):2284–2291, 2013.

[51] A C Myers and J S Jur. Effects of thermal energy harvesting on the human clothing environment microsystem. *IOP Conference Series: Materials Science and Engineering*, 254(1):072015–072021, 2017.

[52] Vladimir Leonov. Thermoelectric energy harvesting of human body heat for wearable sensors. *Institute of Electrical and Electronics Engineers Sensors Journal*, 13(6):2284–2291, 2013.

[53] Brewster S. Body heat powers this smart watch. *Technology Review*, 1(1):1–2, 2016.

[54] Nesrine Jaziri, Ayda Boughamoura, Jens Müller, Brahim Mezghani, Fares Tounsi, and Mohammed Ismail. A comprehensive review of thermoelectric generators: Technologies and common applications. *Energy Reports*, 6:264–287, 2020.

[55] Lars Onsager. Reciprocal relations in irreversible processes. *Physical Review*, 37(4):405–426, 1931.

[56] Shiho Kim, Soonseo Park, SunKook Kim, and Seok-Ho Rhi. A Thermoelectric Generator Using Engine Coolant for Light-Duty Internal Combustion Engine-Powered Vehicles. *Journal of Electronic Materials*, 40(5):812–816, 2011.

[57] D. Samson, T. Otterpohl, M. Kluge, U. Schmid, and Th. Becker. Aircraft-Specific Thermoelectric Generator Module. *Journal of Electronic Materials*, 39(9):2092–2095, 2010.

[58] Hussam Jouhara, Alina Żabnieńska Góra, Navid Khordehgah, Qusay Doraghi, Lujean Ahmad, Les Norman, Brian Axcell, Luiz Wrobel, and Sheng Dai. Thermoelectric generator (TEG) technologies and applications. *International Journal of Thermofluids*, 9(1):100063–100081, 2021.

[59] Xinqing Xiao, Boyu Mu, Guoqing Cao, Yunyue Yang, and Meng Wang. Flexible battery-free wireless electronic system for food monitoring. *Journal of Science: Advanced Materials and Devices*, 7(2):100430–100437, 2022.

[60] K. Charilaou, Th. Kyratsi, and L.S. Louca. Design of an air-cooled thermoelectric generator system through modelling and simulations, for use in cement industries. *Materials Today: Proceedings*, 44(1):3516–3524, 2021.

[61] Zuzana Murčinková, Marek Kosturák, and Jozef Ferenc. Testing of proposed design of stove-powered thermoelectric generator using natural and forced air cooling. *Advances in Mechanical Engineering*, 13(1):1–10, 2021.

[62] Miloš Marjanović, Aneta Prijić, Branislav Randjelović, and Zoran Prijić. A transient modeling of the thermoelectric generators for application in wireless sensor network nodes. *Electronics*, 9(6):1015–1035, 2020.

[63] R K Pandey, N Tandon, and R Chaudhary. The thermoelectric generator from bmw is making use of waste heat. *Springer*, 4(1):4–11, 2009.

[64] Kaleem Ahmad, C. Wan, and Peng-an Zong. Thermoelectric properties of BiSbTe/graphene nanocomposites. *Journal of Materials Science: Materials in Electronics*, 30(13):11923–11930, 2019.

[65] Avto Tavkhelidze. Large enhancement of the thermoelectric figure of merit in a ridged quantum well. *Nanotechnology*, 20(40):405401–405408, 2009.

[66] R. Franz and G. Wiedemann. Ueber die wärme-leitungsfähigkeit der metalle. *Annalen der Physik und Chemie*, 165(8):497–531, 1853.

[67] Yanzhong Pei, Heng Wang, and G. J. Snyder. Band engineering of thermoelectric materials. *Advanced Materials*, 24(46):6125–6135, 2012.

[68] Eric S. Toberer, Lauryn L. Baranowski, and Chris Dames. Advances in thermal conductivity. *Annual Review of Materials Research*, 42(1):179–209, 2012.

[69] Jolly Jacob, U. Rehman, K. Mahmood, A. Ali, A. Ashfaq, Nasir Amin, Salma Ikram, Meshal Alzaid, and Khurram Mehboob. Simultaneous enhancement of Seebeck coefficient and electrical conductivity in ZnSnO by the engineering

of grain boundaries using post annealing. *Physics Letters A*, 388:127034–127040, 2021.

[70] Jonathan Atoyo, Matthew R. Burton, James McGettrick, and Matthew J. Carnie. Enhanced electrical conductivity and Seebeck coefficient in PEDOT:PSS via a two-step ionic liquid and $NaBH_4$ treatment for organic thermoelectrics. *Polymers*, 12(3):559–575, 2020.

[71] Xin Guan, Wei Feng, Xizu Wang, Roshani Venkatesh, and Jianyong Ouyang. Significant enhancement in the Seebeck coefficient and power factor of p-type poly(3,4-ethylenedioxythiophene): Poly(styrenesulfonate) through the incorporation of n-type MXene. *American Chemical Society: Applied Material Interfaces*, 12(11):13013–13020, 2020.

[72] Zeng Fan and Jianyong Ouyang. Thermoelectric properties of PEDOT:PSS. *Advanced Electronic Materials*, 5(11):1800769–1800792, 2019.

[73] K. Xiong, R.C. Longo, W. Wang, R.P. Gupta, B.E. Gnade, and K. Cho. Enhancement of the thermoelectric efficiency of PbTe by selective site doping: Effect of group VA impurities. *Computational Materials Science*, 97(1):159–164, 2015.

[74] Won-Yong Lee, No-Won Park, Ji-Eun Hong, Soon-Gil Yoon, Jung-Hyuk Koh, and Sang-Kwon Lee. Effect of electronic contribution on temperature-dependent thermal transport of antimony telluride thin film. *Journal of Alloys and Compounds*, 620(1):120–124, 2015.

[75] Kyung Kuk Jung and Jong Soo Ko. Thermoelectric generator based on a bismuth-telluride alloy fabricated by addition of ethylene glycol. *Current Applied Physics*, 14(12):1788–1793, 2014.

[76] Tiantian Jia, Jesús Carrete, Georg K. H. Madsen, Yongsheng Zhang, and Suhuai Wei. Chemical trends in the high thermoelectric performance of the pyrite-type dichalcogenides: ZNS_2, CdS_2 and $CdSe_2$. *ArXiv Physics*, 1(1):1–7, 2020.

[77] G-H. Kim, L. Shao, K. Zhang, and K. P. Pipe. Engineered doping of organic semiconductors for enhanced thermoelectric efficiency. *Nature Materials*, 12(8):719–723, 2013.

[78] Fiseha Tesfaye. An Overview of Advanced Chalcogenide Thermo- electric Materials and Their Applications. *Journal of Electronic Research and Application*, 2(2):1–8, 2018.

[79] Yixuan Shi, Cheryl Sturm, and Holger Kleinke. Chalcogenides as thermoelectric materials. *Journal of Solid State Chemistry*, 270(1):273–279, 2019.

[80] Naziah Latiff, Wei Zhe Teo, Zdenek Sofer, Štěpán Huber, Adrian C. Fisher, and Martin Pumera. Toxicity of layered semiconductor chalcogenides: beware of interferences. *Royal Society of Chemistry Advances*, 5(83):67485–67492, 2015.

[81] Murugan Saranya, Chella Santhosh, Rajendran Ramachandran, Pratap Kollu, Padmanapan Saravanan, Mari Vinoba, Soon Kwan Jeong, and Andrews Nirmala Grace. Hydrothermal growth of CuS nanostructures and its photocatalytic properties. *Powder Technology*, 252(1):25–32, 2014.

[82] F. Yakuphanoglu and B. F. Şenkal. Electronic and thermoelectric properties of polyaniline organic semiconductor and electrical characterization of al/PANI MIS diode. *The Journal of Physical Chemistry C*, 111(4):1840–1846, 2007.

[83] Mario Culebras, Belén Uriol, Clara M. Gómez, and Andrés Cantarero. Controlling the thermoelectric properties of polymers: application to PEDOT and polypyrrole. *Physical Chemistry Chemical Physics*, 17(23):15140–15145, 2015.

[84] Junjie Wang, Yuchao Liu, Huihui Li, Shouke Yan, Xiaoli Sun, Dandan Tu, Xin Guo, and Zhongjie Ren. Enhanced charge transport and thermoelectric performance of P(NDI2OD − T2) by epitaxial crystallization on highly oriented polyethylene substrates. *Materials Chemistry Frontiers*, 4(2):661–668, 2020.

[85] S.A. Mansour, M. Hussein, and A.H. Moharram. Thermoelectric power properties of graphite-loaded nitrile rubber/poly(vinyl chloride) blends above the percolation threshold. *Advances in Polymer Technology*, 33(1):21439–21448, 2014.

[86] Liming Wang, Zimeng Zhang, Yuchen Liu, Biran Wang, Lei Fang, Jingjing Qiu, Kun Zhang, and Shiren Wang. Exceptional thermoelectric properties of flexible organicinorganic hybrids with monodispersed and periodic nanophase. *Nature Communications*, 9(1):3817–3825, 2018.

[87] Jiwon Kim and Jae-Hong Lim. Organic-inorganic hybrid thermoelectric material synthesis and properties. *Journal of the Korean Ceramic Society*, 54(4):272–277, 2017.

[88] G. Prunet, F. Pawula, G. Fleury, E. Cloutet, A.J. Robinson, G. Hadziioannou, and A. Pakdel. A review on conductive polymers and their hybrids for flexible and wearable thermoelectric applications. *Materials Today Physics*, 18(1):100402–100462, 2021.

[89] Chang-Jiang Yao, Hao-Li Zhang, and Qichun Zhang. Recent progress in thermoelectric materials based on conjugated polymers. *Polymers*, 11(1):107–126, 2019.

[90] Jinji Luo, Detlef Billep, Thomas Blaudeck, Evgeniya Sheremet, Raul D. Rodriguez, Dietrich R. T. Zahn, Marius Toader, Michael Hietschold, Thomas Otto, and Thomas Gessner. Chemical post-treatment and thermoelectric properties of poly(3,4-ethylenedioxylthiophene): poly(styrenesulfonate) thin films. *Journal of Applied Physics*, 115(5):054908–054914, 2014.

[91] Zeng Fan, Donghe Du, Xin Guan, and Jianyong Ouyang. Polymer films with ultrahigh thermoelectric properties arising from significant Seebeck coefficient enhancement by ion accumulation on surface. *Nano Energy*, 51(1):481–488, 2018.

[92] Wan Sik Kim, Gopinathan Anoop, Il-Seok Jeong, Hye Jeong Lee, Hyun Bin Kim, Soo Hyeon Kim, Gi Won Goo, Hyunmyung Lee, Hyeon Jun Lee, Chingu Kim, Joo-Hyoung Lee, Bongjin Simon Mun, Ji-Woong Park, Eunji Lee, and Ji Young Jo. Feasible tuning of barrier energy in PEDOT:PSS/Bi_2Te_3 nanowires-based thermoelectric nanocomposite thin films through polar solvent vapor annealing. *Nano Energy*, 67:104207–104214, 2020.

[93] Md. Saidul Islam, Hitomi Ohmagari, Mohammad Atiqur Rahman, Yuta Shudo, Masahiro Fukuda, Junya Yagyu, Yoshihiro Sekine, Leonard F. Lindoy, and Shinya Hayami. Enhanced thermoelectric properties exhibited by unreduced freestanding graphene oxide/carbon nanotube membranes. *Materials Advances*, 2(17):5645–5649, 2021.

[94] Tamás Szabó, Ottó Berkesi, Péter Forgó, Katalin Josepovits, Yiannis Sanakis, Dimitris Petridis, and Imre Dékány. Evolution of surface functional groups in a series of progressively oxidized graphite oxides. *Chemistry of Materials*, 18(11):2740–2749, 2006.

[95] D. Yu. Kornilov and S. P. Gubin. Graphene oxide: Structure, properties, synthesis, and reduction (a review). *Russian Journal of Inorganic Chemistry*, 65(13):1965–1976, 2020.

[96] Zhidong Han and Alberto Fina. Thermal conductivity of carbon nanotubes and their polymer nanocomposites: A review. *Progress in Polymer Science*, 36(7):914–944, 2011.

[97] Bogumiła Kumanek and Dawid Janas. Thermal conductivity of carbon nanotube networks: a review. *Journal of Materials Science*, 54(10):7397–7427, 2019.

[98] Xiaojian Tan, Huijun Liu, Yanwei Wen, Hongyan Lv, Lu Pan, Jing Shi, and Xinfeng Tang. Optimizing the thermoelectric performance of zigzag and chiral carbon nanotubes. *Nanoscale Research Letters*, 7(1):116, 2012.

[99] Haiyan Yan and Kaichang Kou. Enhanced thermoelectric properties in polyaniline composites with polyaniline-coated carbon nanotubes. *Journal of Materials Science*, 49(3):1222–1228, 2014.

[100] Ruben Sarabia-Riquelme, Gloria Ramos-Fernández, Ignacio Martin-Gullon, and Matthew C. Weisenberger. Synergistic effect of graphene oxide and wet-chemical hydrazine/deionized water solution treatment on the thermoelectric properties of PEDOT:PSS sprayed films. *Synthetic Metals*, 222(1):330–337, 2016.

[101] Jikun Chen, Liming Wang, Xuchun Gui, Zhiqiang Lin, Xinyou Ke, Feng Hao, Yulong Li, Yong Jiang, Yong Wu, Xun Shi, and Lidong Chen. Strong anisotropy in thermoelectric properties of CNT/PANI composites. *Carbon*, 114(1):1–7, 2017.

[102] Lian Ji. Metal oxide-based thermoelectric materials. *Elsevier*, 2(1):49–72, 2018.

[103] Yinong Yin, Bharati Tudu, and Ashutosh Tiwari. Recent advances in oxide thermoelectric materials and modules. *Vacuum*, 146(1):356–374, 2017.

[104] G.-D. Yuan, W.-J. Zhang, J.-S. Jie, X. Fan, J.-X. Tang, I. Shafiq, Z.-Z. Ye, C.-S. Lee, and S.-T. Lee. Tunable n-Type Conductivity and Transport Properties of Ga-doped ZnO Nanowire Arrays. *Advanced Materials*, 20(1):168–173, 2008.

[105] Sten Andersson, Bengt Collén, Ulf Kuylenstierna, Arne Magnéli, et al. Phase analysis studies on the titanium-oxygen system. *Acta chem. scand*, 11(10):1641–1652, 1957.

[106] Haiqiang Liu, Hongan Ma, Taichao Su, Yuewen Zhang, Bing Sun, Binwu Liu, Lingjiao Kong, Baomin Liu, and Xiaopeng Jia. High-thermoelectric performance of TiO_{2-x} fabricated under high pressure at high temperatures. *Journal of Materiomics*, 3(4):286–292, 2017.

[107] Jinke Tang, Wendong Wang, Guang-Lin Zhao, and Qiang Li. Colossal positive Seebeck coefficient and low thermal conductivity in reduced TiO_2. *Journal of Physics: Condensed Matter*, 21(20):205703, 2009.

[108] Fengyuan Li, Kefeng Cai, Shirley Shen, and Song Chen. Preparation and thermoelectric properties of reduced graphene oxide/PEDOT:PSS composite films. *Synthetic Metals*, 197(1):58–61, 2014.

[109] Woo Hyun Nam, Young Soo Lim, Woochul Kim, Hyeon Kook Seo, Kyun Seong Dae, Soonil Lee, Won-Seon Seo, and Jeong Yong Lee. A gigantically increased ratio of electrical to thermal conductivity and synergistically enhanced thermoelectric properties in interface-controlled TiO_2 –RGO nanocomposites. *Nanoscale*, 9(23):7830–7838, 2017.

[110] Mariam K. Ali and A.A. Moneim. Investigation of Thermoelectric Performance of MoS_2-Templated Polyaniline Nanocomposites. *Key Engineering Materials*, 821(1):103–110, 2019.

[111] George S. Nolas, Jeffrey Sharp, and H. Julian Goldsmid. The phonon—glass electron-crystal approach to thermoelectric materials research. *Springer Berlin Heidelberg*, 45(1):177–207, 2001.

[112] Shivani Shisodia, Benoit Duponchel, Gérard Leroy, Abdelhak Hadj Sahraoui, Dharmendra Pratap Singh, Christophe Poupin, Lucette Tidahy, Renaud Cousin, Patrick Ropa, and Michael Depriester. Synthesis of quantum dot-based polymer nanocomposites: assessment of their thermoelectric performances. *Sustainable Energy Fuels*, 7:3158–3168, 2022.

[113] Hideki Shirakawa, Edwin J. Louis, Alan G. MacDiarmid, Chwan K. Chiang, and Alan J. Heeger. Synthesis of electrically conducting organic polymers: halogen derivatives of polyacetylene, ch_x. *Journal of the Chemical Society, Chemical Communications*, 1(16):578–581, 1977.

[114] Namsheer K and Chandra Sekhar Rout. Conducting polymers: a comprehensive review on recent advances in synthesis, properties and applications. *The Royal Society of Chemistry Advances*, 11(10):5659–5697, 2021.

[115] Tapan K. Das and Smita Prusty. Review on conducting polymers and their applications. *Polymer-Plastics Technology and Engineering*, 51(14):1487–1500, 2012.

[116] Youn Soo Kim, Jong Hyeok Park, Soo-Hyoung Lee, and Youngkwan Lee. Polymer photovoltaic devices using highly conductive poly(3,4-ethylenedioxythiophene-methanol) electrode. *Solar Energy Materials and Solar Cells*, 93(8):1398–1403, 2009.

[117] Graeme A. Snook, Pon Kao, and Adam S. Best. Conducting-polymer-based supercapacitor devices and electrodes. *Journal of Power Sources*, 196(1):1–12, 2011.

[118] Hua Bai and Gaoquan Shi. Gas sensors based on conducting polymers. *Sensors*, 7(1):267–307, 2007.

[119] Dinesh D. Borole, U. R. Kapadi, P. P. Mahulikar, and D. G. Hundiwale. Conducting polymers: an emerging field of biosensors. *Designed Monomers and Polymers*, 9(1):1–11, 2006.

[120] Nara Kim, Samuel Lienemann, Ioannis Petsagkourakis, Desalegn Alemu Mengistie, Seyoung Kee, Thomas Ederth, Viktor Gueskine, Philippe Leclère, Roberto Lazzaroni, Xavier Crispin, and Klas Tybrandt. Elastic conducting polymer composites in thermoelectric modules. *Nature Communications*, 11(1):1424–1434, 2020.

[121] Ottavia Bettucci, Giovanni Maria Matrone, and Francesca Santoro. Conductive polymer-based bioelectronic platforms toward sustainable and biointegrated devices: A journey from skin to brain across human body interfaces. *Advanced Materials Technologies*, 7(2):2100293–2100331, 2022.

[122] Ponce C. de León, S. A. Campbell, J. R. Smith, and F. C. Walsh. Conducting polymer coatings in electrochemical technology part 2 – application areas. *Transactions of the IMF*, 86(1):34–40, 2008.

[123] Huizhi Lu, Xunlai Li, and Qingquan Lei. Conjugated conductive polymer materials and its applications: A mini-review. *Frontiers in Chemistry*, 9(1):732132–732138, 2021.

[124] Timothy M. Swager. 50th anniversary perspective : Conducting/semiconducting conjugated polymers. a personal perspective on the past and the future. *Macromolecules*, 50(13):4867–4886, 2017.

[125] Hugo Bronstein, Christian B. Nielsen, Bob C. Schroeder, and Iain McCulloch. The role of chemical design in the performance of organic semiconductors. *Nature Reviews Chemistry*, 4(2):66–77, 2020.

[126] Xugang Guo and Antonio Facchetti. The journey of conducting polymers from discovery to application. *Nature Materials*, 19(9):922–928, 2020.

[127] Richard D. McCullough. The chemistry of conducting polythiophenes. *Advanced Materials*, 10(2):93–116, 1998.

[128] Thaneshwor P. Kaloni, Patrick K. Giesbrecht, Georg Schreckenbach, and Michael S. Freund. Polythiophene: From fundamental perspectives to applications. *Chemistry of Materials*, 29(24):10248–10283, 2017.

[129] Seth C Rasmussen. Early history of polypyrrole: The first conducting organic polymer. *Bulletin for the History of Chemistry*, 40(1):45–57, 2015.

[130] Marcus Remmers, Beate Müller, Kai Martin, Hans-Joachim Räder, and Werner Köhler. Poly(*p* -phenylene)s. synthesis, optical properties, and quan-

titative analysis with HPLC and MALDITOF mass spectrometry. *Macromolecules*, 32(4):1073–1079, 1999.

[131] Seth C. Rasmussen. The early history of polyaniline: Discovery and origins. *Substantia*, 1(2):99–110, 2017.

[132] Laura-Bianca Enache, Veronica Anăstăsoaie, Cecilia Lete, Alina Giorgiana Brotea, Ovidiu-Teodor Matica, Cristina-Andreea Amarandei, Jérémy Brandel, Eleonora-Mihaela Ungureanu, and Marius Enăchescu. Polyazulene-based materials for heavy metal ion detection. 3. (E)-5-((6-t-butyl-4,8-dimethylazulen-1-yl) diazenyl)-1H-tetrazole-based modified electrodes. *Symmetry*, 13(9):1642–1658, 2021.

[133] Jarmila Vilčáková, Petr Sáha, Otakar Quadrat, and Jaroslav Stejskal. Conductivity of polyaniline/1,2,4-trichlorobenzene composites during freezing and melting transitions. *Physica A: Statistical Mechanics and its Applications*, 301(1):29–36, 2001.

[134] Mario Leclerc and Karim Faid. Electrical and optical properties of processable polythiophene derivatives: Structure-property relationships. *Advanced Materials*, 9(14):1087–1094, 1997.

[135] N S Sundaresan, Sanjay Basak, Martin Pomerantz, and John R Reynolds. Electroactive copolymers of pyrrole containing covalently bound dopant ions: Poly{ pyrrole-co-[3-(pyrrol-I -yl)propanesulphonate]}. *Journal of the Chemical Society, Chemical communications*, 1(1):621–623, 1987.

[136] Taegeun Kim, Sumin Park, Joonsik Seo, Chan Woo Lee, and Jong-Man Kim. Highly conductive PEDOT:PSS with enhanced chemical stability. *Organic Electronics*, 74(1):77–81, 2019.

[137] Yijie Xia and Shuyang Dai. Review on applications of PEDOTs and PEDOT:PSS in perovskite solar cells. *Journal of Materials Science: Materials in Electronics*, 32(10):12746–12757, 2021.

[138] Xi Fan, Wanyi Nie, Hsinhan Tsai, Naixiang Wang, Huihui Huang, Yajun Cheng, Rongjiang Wen, Liujia Ma, Feng Yan, and Yonggao Xia. PEDOT:PSS for flexible and stretchable electronics: Modifications, strategies, and applications. *Advanced Science*, 6(19):1900813–1900854, 2019.

[139] Magatte N. Gueye, Alexandre Carella, Jérôme Faure-Vincent, Renaud Demadrille, and Jean-Pierre Simonato. Progress in understanding structure and transport properties of PEDOT-based materials: A critical review. *Progress in Materials Science*, 108(1):100616–100656, 2020.

[140] AG Bayer. In situ polymerization of conducting poly(3,4-ethylenedioxythiophene). *European Patent*, 339(1), 1988.

[141] F. Jonas and L Schrader. Conductive modifications of polymers with polypyrroles and polythiophenes. *Synthetic Metals*, 41(1):831–836, 1991.

[142] Gerhard Heywang and Friedrich Jonas. Poly(alkylenedioxythiophene)s—new, very stable conducting polymers. *Advanced Materials*, 4(2):116–118, 1992.

[143] I. Winter, C. Reese, J. Hormes, G. Heywang, and F. Jonas. The thermal ageing of poly(3,4-ethylenedioxythiophene). an investigation by x-ray absorption and x-ray photoelectron spectroscopy. *Chemical Physics*, 194(1):207–213, 1995.

[144] Michael Dietrich, Jürgen Heinze, Gerhard Heywang, and Friedrich Jonas. Electrochemical and spectroscopic characterization of polyalkylenedioxythiophenes. *Journal of Electroanalytical Chemistry*, 369(1):87–92, 1994.

[145] L. Groenendaal, F. Jonas, D. Freitag, H. Pielartzik, and J. R. Reynolds. Poly(3,4-ethylenedioxythiophene) and Its Derivatives: Past, Present, and Future. *Advanced Materials*, 12(7):481–494, 2000.

[146] Kuan Sun, Shupeng Zhang, Pengcheng Li, Yijie Xia, Xiang Zhang, Donghe Du, Furkan Halis Isikgor, and Jianyong Ouyang. Review on application of PEDOTs and PEDOT:PSS in energy conversion and storage devices. *Journal of Materials Science: Materials in Electronics*, 26(7):4438–4462, 2015.

[147] X. Crispin, F. L. E. Jakobsson, A. Crispin, P. C. M. Grim, P. Andersson, A. Volodin, C. van Haesendonck, M. Van der Auweraer, W. R. Salaneck, and M. Berggren. The origin of the high conductivity of poly(3,4-ethylenedioxythiophene): Poly(styrenesulfonate) (PEDOTPSS) plastic electrodes. *Chemistry of Materials*, 18(18):4354–4360, 2006.

[148] Rupali Gangopadhyay, Bidisa Das, and Mijanur Rahaman Molla. How does PEDOT combine with PSS? Insights from structural studies. *The Royal Society of Chemistry Advances*, 4(83):43912–43920, 2014.

[149] Desalegn Alemu Mengistie, Pen-Cheng Wang, and Chih-Wei Chu. Effect of molecular weight of additives on the conductivity of PEDOT:PSS and efficiency for ITO-free organic solar cells. *Journal of Materials Chemistry A*, 1(34):9907–9916, 2013.

[150] Alexandre Mantovani Nardes, René A. J. Janssen, and Martijn Kemerink. A morphological model for the solvent-enhanced conductivity of PEDOT:PSS thin films. *Advanced Functional Materials*, 18(6):865–871, 2008.

[151] Takumi Takano, Hiroyasu Masunaga, Akihiko Fujiwara, Hidenori Okuzaki, and Takahiko Sasaki. PEDOT nanocrystal in highly conductive PEDOT:PSS polymer films. *Macromolecules*, 45(9):3859–3865, 2012.

[152] Claudia M. Palumbiny, Christoph Heller, Christoph J. Schaffer, Volker Körstgens, Gonzalo Santoro, Stephan V. Roth, and Peter Müller-Buschbaum. Molecular reorientation and structural changes in cosolvent-treated highly conductive PEDOT:PSS electrodes for flexible indium tin oxide-free organic electronics. *The Journal of Physical Chemistry C*, 118(25):13598–13606, 2014.

[153] Hui Shi, Congcong Liu, Qinglin Jiang, and Jingkun Xu. Effective approaches to improve the electrical conductivity of PEDOT:PSS: A review. *Advanced Electronic Materials*, 1(4):1500017–1500033, 2015.

[154] G Greczynski, Th Kugler, and W.R Salaneck. Characterization of the PEDOT-PSS system by means of x-ray and ultraviolet photoelectron spectroscopy. *Thin Solid Films*, 354(1):129–135, 1999.

[155] S.K.M Jönsson, J Birgerson, X Crispin, G Greczynski, W Osikowicz, A.W Denier van der Gon, W.R Salaneck, and M Fahlman. The effects of solvents on the morphology and sheet resistance in poly(3,4-ethylenedioxythiophene)–polystyrenesulfonic acid (PEDOT–PSS) films. *Synthetic Metals*, 139(1):1–10, 2003.

[156] Lorico D.S. Lapitan, Bernard John V. Tongol, and Shueh-Lin Yau. In situ scanning tunneling microscopy imaging of electropolymerized poly(3,4-ethylenedioxythiophene) on an iodine-modified Au(111) single crystal electrode. *Electrochimica Acta*, 62(1):433–440, 2012.

[157] Asli Ugur, Ferhat Katmis, Mingda Li, Lijun Wu, Yimei Zhu, Kripa K. Varanasi, and Karen K. Gleason. Low-dimensional conduction mechanisms in highly conductive and transparent conjugated polymers. *Advanced Materials*, 27(31):4604–4610, 2015.

[158] Stephan Kirchmeyer and Knud Reuter. Scientific importance, properties and growing applications of poly(3,4-ethylenedioxythiophene). *Journal of Materials Chemistry*, 15(21):2077–2089, 2005.

[159] Anil Kumar and John R. Reynolds. Soluble Alkyl-substituted Poly(ethylenedioxythiophenes) as electrochromic materials. *Macromolecules*, 29(23):7629–7630, 1996.

[160] Phimchanok Sakunpongpitiporn, Katesara Phasuksom, Nophawan Paradee, and Anuvat Sirivat. Facile synthesis of highly conductive PEDOT:PSS *via* surfactant templates. *The Royal Society of Chemistry Advances*, 9(11):6363–6378, 2019.

[161] Jian Zhou, Tadashi Fukawa, and Mutsumi Kimura. Directional electromechanical properties of PEDOT/PSS films containing aligned electrospun nanofibers. *Polymer Journal*, 43(10):849–854, 2011.

[162] Yong Zhang, Siqi Liu, J. Justin Koh, and Chaobin He. Construction of a hierarchical multiscale conducting network for enhanced thermoelectric response in organic PEDOT:PSS based nanocomposites. *Journal of Materiomics*, 7(1):34–39, 2021.

[163] Desalegn Alemu, Hung-Yu Wei, Kuo-Chuan Ho, and Chih-Wei Chu. Highly conductive PEDOT:PSS electrode by simple film treatment with methanol for ITO-free polymer solar cells. *Energy & Environmental Science*, 5(11):9662–9672, 2012.

[164] Tsu-Ruey Chou, Szu-Hua Chen, Yen-Te Chiang, Yi-Ting Lin, and Chih-Yu Chao. Highly conductive PEDOT:PSS films by post-treatment with dimethyl sulfoxide for ITO-free liquid crystal display. *Journal of Materials Chemistry C*, 3(15):3760–3766, 2015.

[165] Qingduan Li, Jianwei Yang, Shuangshuang Chen, Jizhao Zou, Weiguang Xie, and Xierong Zeng. Highly conductive PEDOT:PSS transparent hole transporting layer with solvent treatment for high performance silicon/organic hybrid solar cells. *Nanoscale Research Letters*, 12(1):506–514, 2017.

[166] Jens Neu and Charles A. Schmuttenmaer. Tutorial: An introduction to terahertz time domain spectroscopy (THz-TDS). *Journal of Applied Physics*, 124(23):231101–231116, 2018.

[167] Brendan T. McGrail, Alp Sehirlioglu, and Emily Pentzer. Polymer composites for thermoelectric applications. *Angewandte Chemie International Edition*, 54(6):1710–1723, 2015.

[168] Siyao Liu, Hua Deng, Yun Zhao, Shijie Ren, and Qiang Fu. The optimization of thermoelectric properties in a PEDOT:PSS thin film through post-treatment. *The Royal Society of Chemistry Advances*, 5(3):1910–1917, 2015.

[169] Jinji Luo, Detlef Billep, Thomas Waechtler, Thomas Otto, Marius Toader, Ovidiu Gordan, Evgeniya Sheremet, Joerg Martin, Michael Hietschold, Dietrich R. T. Zahn, and Thomas Gessner. Enhancement of the thermoelectric properties of PEDOT:PSS thin films by post-treatment. *Journal of Materials Chemistry A*, 1(26):7576–7584, 2013.

[170] Yan Yang, Hua Deng, and Qiang Fu. Recent progress on PEDOT:PSS based polymer blends and composites for flexible electronics and thermoelectric devices. *Materials Chemistry Frontiers*, 4(11):3130–3152, 2020.

[171] Hongkwan Park, Seung Hwan Lee, Felix Sunjoo Kim, Hyang Hee Choi, In Woo Cheong, and Jung Hyun Kim. Enhanced thermoelectric proper-

ties of PEDOT:PSS nanofilms by a chemical dedoping process. *Journal of Material Chemistry A*, 2(18):6532–6539, 2014.

[172] Thomas Stöcker, Anna Köhler, and Ralf Moos. Why does the electrical conductivity in PEDOT:PSS decrease with PSS content? A study combining thermoelectric measurements with impedance spectroscopy. *Journal of Polymer Science Part B: Polymer Physics*, 50(14):976–983, 2012.

[173] Joseph P. Heremans, Vladimir Jovovic, Eric S. Toberer, Ali Saramat, Ken Kurosaki, Anek Charoenphakdee, Shinsuke Yamanaka, and G. Jeffrey Snyder. Enhancement of thermoelectric efficiency in PbTe by distortion of the electronic density of states. *Science*, 321(5888):554–557, 2008.

[174] Joseph P. Heremans, Bartlomiej Wiendlocha, and Audrey M. Chamoire. Resonant levels in bulk thermoelectric semiconductors. *Energy Environmental Science*, 5(2):5510–5530, 2012.

[175] Qinyong Zhang, Hui Wang, Weishu Liu, Hengzhi Wang, Bo Yu, Qian Zhang, Zhiting Tian, George Ni, Sangyeop Lee, Keivan Esfarjani, Gang Chen, and Zhifeng Ren. Enhancement of thermoelectric figure-of-merit by resonant states of aluminium doping in lead selenide. *The Royal Society of Chemistry: Energy Environmental Science*, 5(1):5246–5251, 2012.

[176] Qinyong Zhang, Siqi Yang, Qian Zhang, Shuo Chen, Weishu Liu, Hui Wang, Zhiting Tian, David Broido, Gang Chen, and Zhifeng Ren. Effect of aluminum on the thermoelectric properties of nanostructured PbTe. *Nanotechnology*, 24(34):345705–345711, 2013.

[177] Q. Zhang, B. Liao, Y. Lan, K. Lukas, W. Liu, K. Esfarjani, C. Opeil, D. Broido, G. Chen, and Z. Ren. High thermoelectric performance by res-

onant dopant indium in nanostructured SnTe. *Proceedings of the National Academy of Sciences*, 110(33):13261–13266, 2013.

[178] Duong Nguyen Nguyen, Seung Hun Roh, Dong-Hwan Kim, Jun Young Lee, Dong Hwan Wang, and Jung Kyu Kim. Molecular manipulation of PEDOT:PSS for efficient hole transport by incorporation of n-doped carbon quantum dots. *Dyes and Pigments*, 194(1):109610–109620, 2021.

[179] Gert Krauss, Adrian Hochgesang, John Mohanraj, and Mukundan Thelakkat. Highly efficient doping of conjugated polymers using multielectron acceptor salts. *Macromolecular Rapid Communications*, 42(22):2100443–2100454, 2021.

[180] Marisol Reyes-Reyes, Isidro Cruz-Cruz, and Román López-Sandoval. Enhancement of the electrical conductivity in PEDOT:PSS films by the addition of dimethyl sulfate. *The Journal of Physical Chemistry C*, 114(47):20220–20224, 2010.

[181] Youngno Kim, Yunryeol Kim, and Jung Kim. Highly conductive PEDOT:PSS thin films with two-dimensional lamellar stacked multi-layers. *Nanomaterials*, 10(11):2211–2221, 2020.

[182] Temesgen Atnafu Yemata, Yun Zheng, Aung Ko Ko Kyaw, Xizu Wang, Jing Song, Wee Shong Chin, and Jianwei Xu. Modulation of the doping level of PEDOT:PSS film by treatment with hydrazine to improve the Seebeck coefficient. *The Royal Society of Chemistry Advances*, 10(3):1786–1792, 2020.

[183] Chao Yi, Abigail Wilhite, Long Zhang, Rundong Hu, Steven S. C. Chuang, Jie Zheng, and Xiong Gong. Enhanced thermoelectric properties of poly(3,4-ethylenedioxythiophene): poly(styrenesulfonate) by binary sec-

ondary dopants. *American Chemical Society: Applied Material Interfaces*, 7(17):8984–8989, 2015.

[184] Olga Bubnova, Zia Ullah Khan, Hui Wang, Slawomir Braun, Drew R. Evans, Manrico Fabretto, Pejman Hojati-Talemi, Daniel Dagnelund, Jean-Baptiste Arlin, Yves H. Geerts, Simon Desbief, Dag W. Breiby, Jens W. Andreasen, Roberto Lazzaroni, Weimin M. Chen, Igor Zozoulenko, Mats Fahlman, Peter J. Murphy, Magnus Berggren, and Xavier Crispin. Semi-metallic polymers. *Nature Materials*, 13(2):190–194, 2014.

[185] Yani Chen, Yan Zhao, and Ziqi Liang. Solution processed organic thermoelectrics: towards flexible thermoelectric modules. *Energy & Environmental Science*, 8(2):401–422, 2015.

[186] Soo-Kwan Kim, Jun-Hyun Mo, Jae-Yeop Kim, and Kwang-Suk Jang. Improving the thermoelectric power factor of PEDOT:PSS films by a simple two-step post-treatment method. *e-Polymers*, 17(6):501–506, 2017.

[187] Sasha Stankovich, Dmitriy A. Dikin, Richard D. Piner, Kevin A. Kohlhaas, Alfred Kleinhammes, Yuanyuan Jia, Yue Wu, SonBinh T. Nguyen, and Rodney S. Ruoff. Synthesis of graphene-based nanosheets via chemical reduction of exfoliated graphite oxide. *Carbon*, 45(7):1558–1565, 2007.

[188] T. Nakajima, A. Mabuchi, and R. Hagiwara. A new structure model of graphite oxide. *Carbon*, 26(3):357–361, 1988.

[189] Tapas Kuilla, Sambhu Bhadra, Dahu Yao, Nam Hoon Kim, Saswata Bose, and Joong Hee Lee. Recent advances in graphene based polymer composites. *Progress in Polymer Science*, 35(11):1350–1375, 2010.

[190] Andrew T. Smith, Anna Marie LaChance, Songshan Zeng, Bin Liu, and Luyi Sun. Synthesis, properties, and applications of graphene oxide/reduced

graphene oxide and their nanocomposites. *Nano Materials Science*, 1(1):31–47, 2019.

[191] Masukazu Hirata, Takuya Gotou, and Michio Ohba. Thin-film particles of graphite oxide. 2: Preliminary studies for internal micro fabrication of single particle and carbonaceous electronic circuits. *Carbon*, 43(3):503–510, 2005.

[192] Tamás Szabó, Etelka Tombácz, Erzsébet Illés, and Imre Dékány. Enhanced acidity and pH-dependent surface charge characterization of successively oxidized graphite oxides. *Carbon*, 44(3):537–545, 2006.

[193] G.I. Titelman, V. Gelman, S. Bron, R.L. Khalfin, Y. Cohen, and H. Bianco-Peled. Characteristics and microstructure of aqueous colloidal dispersions of graphite oxide. *Carbon*, 43(3):641–649, 2005.

[194] Sasha Stankovich, Richard D. Piner, SonBinh T. Nguyen, and Rodney S. Ruoff. Synthesis and exfoliation of isocyanate-treated graphene oxide nanoplatelets. *Carbon*, 44(15):3342–3347, 2006.

[195] N. Vats, S. Rauschenbach, W. Sigle, S. Sen, S. Abb, A. Portz, M. Dürr, M. Burghard, P. A. van Aken, and K. Kern. Electron microscopy of polyoxometalate ions on graphene by electrospray ion beam deposition. 10(10):4952–4961, 2018.

[196] Cristina Gómez-Navarro, Jannik C. Meyer, Ravi S. Sundaram, Andrey Chuvilin, Simon Kurasch, Marko Burghard, Klaus Kern, and Ute Kaiser. Atomic structure of reduced graphene oxide. *Nano Letters*, 10(4):1144–1148, 2010.

[197] Dongxing Yang, Aruna Velamakanni, Gülay Bozoklu, Sungjin Park, Meryl Stoller, Richard D. Piner, Sasha Stankovich, Inhwa Jung, Daniel A. Field,

Carl A. Ventrice, and Rodney S. Ruoff. Chemical analysis of graphene oxide films after heat and chemical treatments by X-ray photoelectron and micro-raman spectroscopy. *Carbon*, 47(1):145–152, 2009.

[198] Hannes C. Schniepp, Je-Luen Li, Michael J. McAllister, Hiroaki Sai, Margarita Herrera-Alonso, Douglas H. Adamson, Robert K. Prud'homme, Roberto Car, Dudley A. Saville, and Ilhan A. Aksay. Functionalized single graphene sheets derived from splitting graphite oxide. *The Journal of Physical Chemistry B*, 110(17):8535–8539, 2006.

[199] Michael J. McAllister, Je-Luen Li, Douglas H. Adamson, Hannes C. Schniepp, Ahmed A. Abdala, Jun Liu, Margarita Herrera-Alonso, David L. Milius, Roberto Car, Robert K. Prud'homme, and Ilhan A. Aksay. Single sheet functionalized graphene by oxidation and thermal expansion of graphite. *Chemistry of Materials*, 19(18):4396–4404, 2007.

[200] Félix Mouhat, François-Xavier Coudert, and Marie-Laure Bocquet. Structure and chemistry of graphene oxide in liquid water from first principles. *Nature Communications*, 11(1):1566–1575, 2020.

[201] E. Jaafar, Muhammad Kashif, S.K. Sahari, and Z. Ngaini. Study on morphological, optical and electrical properties of graphene oxide (GO) and reduced graphene oxide (rGO). *Materials Science Forum*, 917:112–116, 2018.

[202] Junjie Chen and Linke Li. Effect of oxidation degree on the thermal properties of graphene oxide. *Journal of Materials Research and Technology*, 9(6):13740–13748, 2020.

[203] Siegfried Eigler, Stefan Grimm, and Andreas Hirsch. Investigation of the thermal stability of the carbon framework of graphene oxide. *Chemistry - A European Journal*, 20(4):984–989, 2014.

[204] Xin Mu, Xufei Wu, Teng Zhang, David B. Go, and Tengfei Luo. Thermal transport in graphene oxide–from ballistic extreme to amorphous limit. *Scientific Reports*, 4(1):3909–3918, 2015.

[205] Shangchao Lin and Markus J. Buehler. Thermal transport in monolayer graphene oxide: Atomistic insights into phonon engineering through surface chemistry. *Carbon*, 77(1):351–359, 2014.

[206] Pampi Majumder, Kakoli Dutta ., and Partha Dutta . Synthesis, properties of graphene oxide-metal oxide mixed nanocomposites and their applications - review. *International Journal of Advanced Science and Engineering*, 5(3):1032–1039, 2019.

[207] Bin Feng, Jian Xie, Gaoshao Cao, Tiejun Zhu, and Xinbing Zhao. Enhanced thermoelectric properties of p-type $CoSb_3$/graphene nanocomposite. *Journal of Materials Chemistry A*, 1(42):13111–13120, 2013.

[208] Pritam Dey, Subhra Sourav Jana, Farheen Anjum, Tathagata Bhattacharya, and Tanmoy Maiti. Effect of semiconductor to metal transition on thermoelectric performance in oxide nanocomposites of $SrTi_{0.85}Nb_{0.15}O_3$ with graphene oxide. *Applied Materials Today*, 21(1):100869–100878, 2020.

[209] F. A. Grant. Properties of rutile (titanium dioxide). *Reviews of Modern Physics*, 31(3):646–674, 1959.

[210] Agatino Di Paola, Marianna Bellardita, and Leonardo Palmisano. Brookite, the least known TiO_2 photocatalyst. *Catalysts*, 3(1):36–73, 2013.

[211] R. Sanjines, H. Tang, H. Berger, F. Gozzo, G. Margaritondo, and F. Levy. Electronic-structure of anatase TiO_2 oxide. *Journal of Applied Physics*, 75(6):2945–2951, 1994.

[212] Tanujjal Bora, Adrien Dousse, Kunal Sharma, Kaushik Sarma, Alexander Baev, G. Louis Hornyak, and Guatam Dasgupta. Modeling nanomaterial physical properties: theory and simulation. *International Journal of Smart and Nano Materials*, 10(2):116–143, 2019.

[213] L. Miao, S. Tanemura, R. Huang, C.Y. Liu, C.M. Huang, and G. Xu. Large Seebeck coefficients of protonated titanate nanotubes for high-temperature thermoelectric conversion. *American Chemical Society: Applied Material Interfaces*, 2(8):2355–2359, 2010.

[214] Frederick W. Dynys, Marie-Helene Berger, and Alp Sehirlioglu. Thermoelectric properties of undoped and doped $(Ti_{0.75}Sn_{0.25})O_2$. *Journal of the American Ceramic Society*, 95(2):619–626, 2012.

[215] David Portehault, Vasana Maneeratana, Christophe Candolfi, Niels Oeschler, Igor Veremchuk, Yuri Grin, Clément Sanchez, and Markus Antonietti. Facile general route toward tunable magnéli nanostructures and their use as thermoelectric metal oxide/carbon nanocomposites. *American Chemical Society Nano*, 5(11):9052–9061, 2011.

[216] Ling Xu, Matthew P. Garrett, and Bin Hu. Doping effects on internally coupled Seebeck coefficient, electrical, and thermal conductivities in aluminum-doped TiO_2. *The Journal of Physical Chemistry C*, 116(24):13020–13025, 2012.

[217] Monika Backhaus-Ricoult, James R. Rustad, Deenamma Vargheese, Indrajit Dutta, and Kim Work. Levers for thermoelectric properties in titania-based ceramics. *Journal of Electronic Materials*, 41(6):1636–1647, 2012.

[218] Hiroyuki Kitagawa, Toshimitsu Kunisada, Yasuji Yamada, and Shugo Kubo. Effect of boron-doping on thermoelectric properties of rutile-type titanium

dioxide sintered materials. *Journal of Alloys and Compounds*, 508(2):582–586, 2010.

[219] Shunta Harada, Katsushi Tanaka, and Haruyuki Inui. Thermoelectric properties and crystallographic shear structures in titanium oxides of the magnèli phases. *Journal of Applied Physics*, 108(8):083703–083710, 2010.

[220] Alexandre Verchère, Stéphane Pailhès, Sylvie Le Floch, Sandrine Cottrino, Régis Debord, Gilbert Fantozzi, Shantanu Misra, Christophe Candolfi, Bertrand Lenoir, Stéphane Daniele, and Shashank Mishra. Optimum in the thermoelectric efficiency of nanostructured Nb-doped TiO_2 ceramics: from polarons to Nb–Nb dimers. *Physical Chemistry Chemical Physics*, 22(23):13008–13016, 2020.

[221] M. K. Nowotny, T. Bak, and J. Nowotny. Electrical properties and defect chemistry of TiO_2 single crystal. II. Thermoelectric Power. *The Journal of Physical Chemistry B*, 110(33):16283–16291, 2006.

[222] Isao Tsuyumoto, Taisuke Hosono, and Masataka Murata. Thermoelectric power in nonstoichiometric orthorhombic titanium oxides. *Journal of the American Ceramic Society*, 1(1):2301–2304, 2006.

[223] Daisuke Kurita, Shingo Ohta, Kenji Sugiura, Hiromichi Ohta, and Kunihito Koumoto. Carrier generation and transport properties of heavily Nb-doped anatase TiO_2 epitaxial films at high temperatures. *Journal of Applied Physics*, 100(9):096105–096109, 2006.

[224] Sophie Laurent, Delphine Forge, Marc Port, Alain Roch, Caroline Robic, Luce Vander Elst, and Robert N. Muller. Magnetic iron oxide nanoparticles: Synthesis, stabilization, vectorization, physicochemical characteri-

zations, and biological applications. *Chemical Reviews*, 108(6):2064–2110, 2008.

[225] Won-Kyung Shin, Jinhyun Cho, Aravindaraj G. Kannan, Yoon-Sung Lee, and Dong-Won Kim. Cross-linked composite gel polymer electrolyte using mesoporous methacrylate-functionalized SiO_2 nanoparticles for lithium-ion polymer batteries. *Scientific Reports*, 6(1):26332–26342, 2016.

[226] Ji Eun Lee, Nohyun Lee, Taeho Kim, Jaeyun Kim, and Taeghwan Hyeon. Multifunctional mesoporous silica nanocomposite nanoparticles for theranostic applications. *Accounts of Chemical Research*, 44(10):893–902, 2011.

[227] Haythem Barrak, Taieb Saied, Pascale Chevallier, Gaétan Laroche, Adel M'nif, and Ahmed Hichem Hamzaoui. Synthesis, characterization, and functionalization of ZnO nanoparticles by n-(trimethoxysilylpropyl) ethylenediamine triacetic acid (TMSEDTA): Investigation of the interactions between phloroglucinol and ZnO@TMSEDTA. *Arabian Journal of Chemistry*, 12(8):4340–4347, 2019.

[228] Muhammad Mansha, Ahsanulhaq Qurashi, Nisar Ullah, Fatai Olawale Bakare, Ibrahim Khan, and Zain H. Yamani. Synthesis of In_2O_3/graphene heterostructure and their hydrogen gas sensing properties. *Ceramics International*, 42(9):11490–11495, 2016.

[229] Ishpal Rawal and Amarjeet Kaur. Synthesis of mesoporous polypyrrole nanowires/nanoparticles for ammonia gas sensing application. *Sensors and Actuators A: Physical*, 203(1):92–102, 2013.

[230] F D Utami, D Y Rahman, Sutisna, Kamirul, D O Margareta, and M Abdullah. Photocatalyst based on TiO_2 and its application in organic wastewater

treatment using simple spray method. *Journal of Physics: Conference Series*, 1204(1):012086–012094, 2019.

[231] Suman Dutta. Wastewater treatment using TiO_2-based photocatalysts. *Elsevier*, 1(1):303–323, 2020.

[232] Alex Weir, Paul Westerhoff, Lars Fabricius, Kiril Hristovski, and Natalie von Goetz. Titanium dioxide nanoparticles in food and personal care products. *Environmental Science & Technology*, 46(4):2242–2250, 2012.

[233] Dui Yanto Rahman, Mamat Rokhmat, Elfi Yuliza, Euis Sustini, and Mikrajuddin Abdullah. New design of potentially low-cost solar cells using TiO_2/graphite composite as photon absorber. *International Journal of Energy and Environmental Engineering*, 7(3):289–296, 2016.

[234] Adawiyah J. Haider, Zainab N. Jameel, and Imad H.M. Al-Hussaini. Review on: Titanium dioxide applications. *Energy Procedia*, 157(1):17–29, 2019.

[235] Muhammad Tayyab Noman, Muhammad Azeem Ashraf, and Azam Ali. Synthesis and applications of nano-TiO_2: a review. *Environmental Science and Pollution Research*, 26(4):3262–3291, 2019.

[236] Ibrahim Khan, Khalid Saeed, and Idrees Khan. Nanoparticles: Properties, applications and toxicities. *Arabian Journal of Chemistry*, 12(7):908–931, 2019.

[237] Jiai Ning, Di Wu, and Degang Zhao. Synthesis and thermoelectric properties of TiO_2/Cu_2SnSe_3 composites. *Applied Sciences*, 7(10):1043–1054, 2017.

[238] D. Cederkrantz, N. Farahi, K. A. Borup, B. B. Iversen, M. Nygren, and A. E. C. Palmqvist. Enhanced thermoelectric properties of Mg_2Si by addition

of TiO_2 nanoparticles. *Journal of Applied Physics*, 111(2):023701–023709, 2012.

[239] Ajit Debnath, Krishna Deb, Kamanashis Sarkar, and Biswajit Saha. Improved thermoelectric performance in TiO_2 incorporated polyaniline: A polymer-based hybrid material for thermoelectric generators. *Journal of Electronic Materials*, 49(8):5028–5036, 2020.

[240] Andrey V. Lashkov, Fedor S. Fedorov, Mikhail Yu. Vasilkov, Alexey V. Kochetkov, Ilia V. Belyaev, Ilia A. Plugin, Alexey S. Varezhnikov, Anastasia N. Filipenko, Stepan A. Romanov, Albert G. Nasibulin, Ghenadii Korotcenkov, and Victor V. Sysoev. The ti wire functionalized with inherent TiO_2 nanotubes by anodization as one-electrode gas sensor: A proof-of-concept study. *Sensors and Actuators B: Chemical*, 306:127615–127624, 2020.

[241] Khuzaimah Arifin, Rozan Mohamad Yunus, Lorna Jeffery Minggu, and Mohammad B. Kassim. Improvement of TiO_2 nanotubes for photoelectrochemical water splitting: Review. *International Journal of Hydrogen Energy*, 46(7):4998–5024, 2021.

[242] Marcel F. Kunrath, Roberto Hubler, Rosemary S. A. Shinkai, and Eduardo R. Teixeira. Application of TiO_2 nanotubes as a drug delivery system for biomedical implants: A critical overview. *Chemistry Select*, 3(40):11180–11189, 2018.

[243] Yuehong Li, Yue Yang, Ruiyan Li, Xiongfeng Tang, Deming Guo, Yun'an Qing, and Yanguo Qin. Enhanced antibacterial properties of orthopedic implants by titanium nanotube surface modification: a review of current techniques. *International Journal of Nanomedicine*, 14(1):7217–7236, 2019.

[244] Lusheng Su and Yong X. Gan. Formation and thermoelectric property of TiO_2 nanotubes covered by Te-Bi-Pb nanoparticles. *Electrochimica Acta*, 56(16):5794–5803, 2011.

[245] Youfu Wang and Aiguo Hu. Carbon quantum dots: synthesis, properties and applications. *Journal of Materials Chemistry C*, 2(34):6921–6940, 2014.

[246] Yadong Yin and A. Paul Alivisatos. Colloidal nanocrystal synthesis and the organic–inorganic interface. *Nature*, 437(7059):664–670, 2005.

[247] Motonari Adachi, Yusuke Murata, Fumin Wang, and Jinting Jiu. Synthesis of titania nanocrystals: Application for dye-sensitized solar cells. *Springer*, 1(1):71–100, 2006.

[248] Renyuan Zhang, Ahmed A. Elzatahry, Salem S. Al-Deyab, and Dongyuan Zhao. Mesoporous titania: From synthesis to application. *Nano Today*, 7(4):344–366, 2012.

[249] Abhijit Biswas, Alice Corani, Arunkumar Kathiravan, Yingyot Infahsaeng, Arkady Yartsev, Villy Sundstrom, and Swati De. Control of the size and shape of TiO_2 nanoparticles in restricted media. *Nanotechnology*, 24(19):195601–195616, 2013.

[250] Sofia Javed, Mohammad Mujahid, Mohammad Islam, and Umair Manzoor. Morphological effects of reflux condensation on nanocrystalline anatase gel and thin films. *Materials Chemistry and Physics*, 132(2):509–514, 2012.

[251] Sofia Javed, Muhammad Aftab Akram, and Mohammad Mujahid. Environment friendly template-free microwave synthesis of submicron-sized hierarchical titania nanostructures and their application in photovoltaics. *Crystal Engineering Communication*, 16(48):10937–10942, 2014.

[252] Xing Wang, Subin Jiang, Xuejian Huo, Rui Xia, Elisée Muhire, and Meizhen Gao. Facile preparation of a TiO_2 quantum dot/graphitic carbon nitride heterojunction with highly efficient photocatalytic activity. *Nanotechnology*, 29(20):205702–205718, 2018.

[253] Lalitha Gnanasekaran, R. Hemamalini, and K. Ravichandran. Synthesis and characterization of TiO_2 quantum dots for photocatalytic application. *Journal of Saudi Chemical Society*, 19(5):589–594, 2015.

[254] Rehan Danish, Faheem Ahmed, and Bon Heun Koo. Rapid synthesis of high surface area anatase titanium oxide quantum dots. *Ceramics International*, 40(8):12675–12680, 2014.

[255] Amandeep Kaur, Ahmad Umar, and Sushil Kumar Kansal. Sunlight-driven photocatalytic degradation of non-steroidal anti-inflammatory drug based on TiO_2 quantum dots. *Journal of Colloid and Interface Science*, 459(1):257–263, 2015.

[256] Young-Jae Shim and Gyoung-Jin Choi. Characterization of TiO_2 quantum dots synthesized by hydrothermal method. *Transactions on Electrical and Electronic Materials*, 17(2):125–127, 2016.

[257] Jana Drbohlavova, Marina Vorozhtsova, Radim Hrdy, Rene Kizek, Ota Salyk, and Jaromir Hubalek. Self-ordered TiO_2 quantum dot array prepared via anodic oxidation. *Nanoscale Research Letters*, 7(1):123–127, 2012.

[258] Gencai Shen, Zhonglin Du, Zhenxiao Pan, Jun Du, and Xinhua Zhong. Solar paint from TiO_2 particles supported quantum dots for photoanodes in quantum dot–sensitized solar cells. *American Chemical Society Omega*, 3(1):1102–1109, 2018.

[259] Zion Tachan, Idan Hod, Menny Shalom, Larissa Grinis, and Arie Zaban. The importance of the TiO_2/quantum dots interface in the recombination processes of quantum dot sensitized solar cells. *Physical Chemistry Chemical Physics*, 15(11):3841–3845, 2013.

[260] Lun Pan, Ji-Jun Zou, Songbo Wang, Zhen-Feng Huang, Ao Yu, Li Wang, and Xiangwen Zhang. Quantum dot self-decorated TiO_2 nanosheets. *Chemical Communications*, 49(59):6593–6597, 2013.

[261] Fei-Peng Du, Nan-Nan Cao, Yun-Fei Zhang, Ping Fu, Yan-Guang Wu, Zhi-Dong Lin, Run Shi, Abbas Amini, and Chun Cheng. PEDOT:PSS/graphene quantum dots films with enhanced thermoelectric properties via strong interfacial interaction and phase separation. *Scientific Reports*, 8(1):6441–6453, 2018.

[262] Liying Zhu, Woo-Jin An, Joseph W. Springer, Luis B. Modesto-Lopez, Sravani Gullapalli, Dewey Holten, Michael S. Wong, and Pratim Biswas. Linker-free quantum dot sensitized TiO_2 photoelectrochemical cells. *International Journal of Hydrogen Energy*, 37(8):6422–6430, 2012.

[263] Björn Sothmann, Rafael Sánchez, and Andrew N Jordan. Thermoelectric energy harvesting with quantum dots. *Nanotechnology*, 26(3):032001–0320026, 2015.

[264] Wei Shi, Sanyin Qu, Hongyi Chen, Yanling Chen, Qin Yao, and Lidong Chen. One-step synthesis and enhanced thermoelectric properties of polymer–quantum dot composite films. *Angewandte Chemie*, 130(27):8169–8174, 2018.

[265] Qinglin Jiang, Xiaoqi Lan, Congcong Liu, Hui Shi, Zhengyou Zhu, Feng Zhao, Jingkun Xu, and Fengxing Jiang. High-performance hybrid organic

thermoelectric SWNTs/PEDOT:PSS thin-films for energy harvesting. *Materials Chemistry Frontiers*, 2(4):679–685, 2018.

[266] Fei Peng Du, Nan-Nan Cao, Yun-Fei Zhang, Ping Fu, Yan-Guang Wu, Zhi-Dong Lin, Run Shi, Abbas Amini, and Chun Cheng. PEDOT:PSS/graphene quantum dots films with enhanced thermoelectric properties via strong interfacial interaction and phase separation. *Scientific Reports*, 8(1):6441–6453, 2018.

[267] Amr Tayel, Adham Ramadan, and Omar El Seoud. Titanium dioxide/graphene and titanium dioxide/graphene oxide nanocomposites: Synthesis, characterization and photocatalytic applications for water decontamination. *Catalysts*, 8(11):491–536, 2018.

[268] Nay Ming Huang, Chang, and Nay Ming Huang. Facile hydrothermal preparation of titanium dioxide decorated reduced graphene oxide nanocomposite. *International Journal of Nanomedicine*, 7(1):3379–3388, 2012.

[269] Liangjun Chen, Wei Liu, Xianli Su, Shengqiang Xiao, Hongyao Xie, Ctirad Uher, and Xinfeng Tang. Chemical synthesis and enhanced electrical properties of bulk poly(3,4-ethylenedioxythiophene)/reduced graphene oxide nanocomposites. *Synthetic Metals*, 229(1):65–71, 2017.

[270] Xinyu Zhang, Jeong-Soo Lee, Gil S. Lee, Dong-Kyu Cha, Moon J. Kim, Duck J. Yang, and Sanjeev K. Manohar. Chemical Synthesis of PEDOT Nanotubes. *Macromolecules*, 39(2):470–472, 2006.

[271] Dimitrios Konios, Minas M. Stylianakis, Emmanuel Stratakis, and Emmanuel Kymakis. Dispersion behaviour of graphene oxide and reduced graphene oxide. *Journal of Colloid and Interface Science*, 430(1):108–112, 2014.

[272] Jianyong Ouyang. "secondary doping" methods to significantly enhance the conductivity of PEDOT:PSS for its application as transparent electrode of optoelectronic devices. *Displays*, 34(5):423–436, 2013.

[273] Rui Chen, Kuan Sun, Qi Zhang, Yongli Zhou, Meng Li, Yuyang Sun, Zhou Wu, Yuyang Wu, Xinlu Li, Jialei Xi, Chi Ma, Yiyang Zhang, and Jianyong Ouyang. Sequential solution polymerization of Poly(3,4-ethylenedioxythiophene) using V_2O_5 as oxidant for flexible touch sensors. *iScience*, 12(1):66–75, 2019.

[274] Manrico Fabretto, Kamil Zuber, Colin Hall, Peter Murphy, and Hans J. Griesser. The role of water in the synthesis and performance of vapour phase polymerised PEDOT electrochromic devices. *Journal of Materials Chemistry*, 19(42):7871–7879, 2009.

[275] Xiang J. and Drazil L.T. Electrical and thermal conductivities of au nanoparticle decorated graphene nanoplatelet. *Composite Structures*, 1(1):1–6, 2015.

[276] Addis Tessema, Dan Zhao, Joseph Moll, Shansan Xu, Ronggui Yang, Chen Li, Sanat K. Kumar, and Addis Kidane. Effect of filler loading, geometry, dispersion and temperature on thermal conductivity of polymer nanocomposites. *Polymer Testing*, 73(1):448–449, 2019.

[277] Nikhil Satyala and Daryoosh Vashaee. The effect of crystallite size on thermoelectric properties of bulk nanostructured magnesium silicide (Mg_2Si) compounds. *Applied Physics Letters*, 100(7):073107–073112, 2012.

[278] Graeme Williams, Brian Seger, and Prashant V. Kamat. TiO_2-Graphene nanocomposites. UV-Assisted photocatalytic reduction of graphene oxide. *American Chemical Society Nano*, 2(7):1487–1491, 2008.

[279] Yi Zhang, Adam M. Schwartzberg, Kevin Xu, Claire Gu, and Jin Z. Zhang. Electrical and thermal conductivities of gold and silver nanoparticles in solutions and films and electrical field enhanced Surface-Enhanced Raman Scattering (SERS). *Proceedings of SPIE Physical Chemistry of Interfaces and Nanomaterials IV*, 5929(1):592912–592920, 2005.

[280] Yandong Sun, Yanguang Zhou, Ramya Gurunathan, Jin-Yu Zhang, Ming Hu, Wei Liu, Ben Xu, and G. Jeffrey Snyder. Phonon scattering in the complex strain field of a dislocation in PbTe. *Journal of Materials Chemistry C*, 9(27):8506–8514, 2021.

[281] Xing Wang, Rui Xia, Elisée Muhire, Subin Jiang, Xuejian Huo, and Meizhen Gao. Highly enhanced photocatalytic performance of TiO_2 nanosheets through constructing TiO_2 /TiO_2 quantum dots homojunction. *Applied Surface Science*, 459(1):9–15, 2018.

[282] Sofia Javed, Mohammad Islam, and Mohammad Mujahid. Synthesis and characterization of TiO_2 quantum dots by sol gel reflux condensation method. *Ceramics International*, 45(2):2676–2679, 2019.

[283] Swati Sood, Sandeep Kumar, Ahmad Umar, Amandeep Kaur, Surinder Kumar Mehta, and Sushil Kumar Kansal. TiO_2 quantum dots for the photocatalytic degradation of indigo carmine dye. *Journal of Alloys and Compounds*, 650(1):193–198, 2015.

[284] Di He, Yongli Li, Jinshu Wang, Yilong Yang, and Qier An. Tunable Nanostructure of TiO_2 /Reduced Graphene Oxide Composite for High Photocatalysis. *Applied Microscopy*, 46(1):37–44, 2016.

[285] Chanbasha Basheer. Application of titanium di-oxide-graphene composite material for photocatalytic degradation of alkylphenols. *Journal of Chemistry*, 2013(1):1–10, 2013.

[286] Sadiye Sener, Murat Erdemog, Meltem Asilturk, and Hikmet Sayilkan. The effect of silane modification on the adsorptive properties of natural pyrophyllite and synthetic titanium-based powders prepared by the sol-gel process. *Turkish Journal of Chemistry*, 29(5):487–495, 2005.

[287] Julien Vaillant, Monica Lira-Cantu, Karina Cuentas-Gallegos, Nieves Casañ-Pastor, and Pedro Gómez-Romero. Chemical synthesis of hybrid materials based on PAni and PEDOT with polyoxometalates for electrochemical supercapacitors. *Progress in Solid State Chemistry*, 34(2-4):147–159, 2006.

[288] Dona Jacob, P A Mini, Avinash Balakrishnan, S V Nair, and K R V Subramanian. Electrochemical behaviour of graphene–poly (3,4-ethylenedioxythiophene) (PEDOT) composite electrodes for supercapacitor applications. *Bulletin of Materials Science*, 37(1):61–69, 2014.

[289] Kipyo Hong, Se Hyun Kim, Chanwoo Yang, Won Min Yun, Sooji Nam, Jaeyoung Jang, Chanjun Park, and Chan Eon Park. Photopatternable poly(4-styrene sulfonic acid)-wrapped MWNT thin-film source/drain electrodes for use in organic field-effect transistors. *American Chemical Society: Applied Materials & Interfaces*, 3(1):74–79, 2011.

[290] Jianyong Ouyang, Qianfei Xu, Chi-Wei Chu, Yang Yang, Gang Li, and Joseph Shinar. On the mechanism of conductivity enhancement in poly(3,4-ethylenedioxythiophene):poly(styrene sulfonate) film through solvent treatment. *Polymer*, 45(25):8443–8450, 2004.

[291] Mario Culebras, Clara M. Gómez, and Andrés Cantarero. Thermoelectric measurements of PEDOT:PSS/expanded graphite composites. *Journal of Materials Science*, 48(7):2855–2860, 2013.

[292] José Luceño Sánchez, Rafael Peña Capilla, and Ana Díez-Pascual. High-performance PEDOT:PSS/hexamethylene diisocyanate-functionalized graphene oxide nanocomposites: Preparation and properties. *Polymers*, 10(10):1169–1188, 2018.

[293] J A Garcia, A Mandelis, B Farahbakhsh, C Lebowitz, and I Harris. Thermophysical Properties of Thermal Sprayed Coatings on Carbon Steel Substrates by Photothermal Radiometry. 20(1):1587–1603, 1999.

[294] M. Depriester, P. Hus, S. Delenclos, and A. Hadj Sahraoui. New methodology for thermal parameter measurements in solids using photothermal radiometry. *Review of Scientific Instruments*, 76(7):074902–074909, 2005.

[295] M. Depriester, P. Hus, S. Delenclos, and A. Hadj Sahraoui. Study of thermal parameters' temperature dependence in solids using photothermal radiometry. *Review of Scientific Instruments*, 78(3):036101–036105, 2007.

[296] Yimin Zhao, Chunlin Zhu, Sigen Wang, J. Z. Tian, D. J. Yang, C. K. Chen, Hao Cheng, and Peter Hing. Pulsed photothermal reflectance measurement of the thermal conductivity of sputtered aluminum nitride thin films. *Journal of Applied Physics*, 96(8):4563–4568, 2004.

[297] Andrzej Kusiak, Jiri Martan, Jean-Luc Battaglia, and Rostislav Daniel. Using pulsed and modulated photothermal radiometry to measure the thermal conductivity of thin films. *Thermochimica Acta*, 556(1):1–5, 2013.

[298] K.L. Ngai. Introduction to the Problems of Relaxation and Diffusion in Complex Systems. *Springer*, 1(1):1–47, 2011.

[299] J. Ross Macdonald. Impedance spectroscopy. *Annals of Biomedical Engineering*, 20(1):289–306, 1992.

[300] Andrew K. Jonscher. Dielectric relaxation in solids. *Journal of Physics D: Applied Physics*, 32(14):57–70, 1999.

[301] Amine Bendahhou, Karim Chourti, Rachid El Bouayadi, Soufian El Barkany, and Mohamed Abou-Salama. Structural, dielectric and impedance spectroscopy analysis of $Ba_5CaTi_{1.94}Zn_{0.06}Nb_8O_{30}$ ferroelectric ceramic. *The Royal Society of Chemistry Advances*, 10(47):28007–28018, 2020.

[302] Leopoldo B Valdes. Resistivity measurements on germanium for transistors. *Proceedings of the IRE*, 42(2):420–427, 1954.

[303] FM Smits. Measurement of sheet resistivities with the four-point probe. *Bell System Technical Journal*, 37(3):711–718, 1958.

[304] Nassima Radouane, Michael Depriester, Abdelhak Hadj Sahraoui, Bennaceur Ouaki, Benoit Escorne, Benoît Duponchel, Dharmendra Pratap Singh, and Abdelkrim Maaroufi. Thermoelectric improvement of the figure of merit of zinc phosphate glass composites by a likely tunnel percolation mechanism. *Journal of Applied Physics*, 129(15):155110–155120, 2021.

[305] H. Takahashi, R. Okazaki, S. Ishiwata, H. Taniguchi, A. Okutani, M. Hagiwara, and I. Terasaki. Colossal Seebeck effect enhanced by quasi-ballistic phonons dragging massive electrons in $FeSb_2$. *Nature Communications*, 7(1):12732–12738, 2016.

[306] Qin Wang and Morteza Eslamian. Improving uniformity and nanostructure of solution-processed thin films using ultrasonic substrate vibration post treatment (SVPT). *Ultrasonics*, 67(1):55–64, 2016.

[307] Qin Wang and Morteza Eslamian. Improving uniformity and nanostructure of solution-processed thin films using ultrasonic substrate vibration post treatment (SVPT). *Ultrasonics*, 67(1):55–64, 2016.

[308] Aung Ko Ko Kyaw, Temesgen A. Yemata, Xizu Wang, Siew Lay Lim, Wee Shong Chin, Kedar Hippalgaonkar, and Jianwei Xu. Enhanced thermoelectric performance of PEDOT:PSS films by sequential post-treatment with formamide. *Macromolecular Materials and Engineering*, 303(2):1700429–1700445, 2018.

[309] Yong Zhang, Siqi Liu, J. Justin Koh, and Chaobin He. Construction of a hierarchical multiscale conducting network for enhanced thermoelectric response in organic PEDOT:PSS based nanocomposites. *Journal of Materiomics*, 7(1):34–39, 2021.

[310] Eun Jin Bae, Young Hun Kang, Kwang-Suk Jang, and Song Yun Cho. Enhancement of thermoelectric properties of PEDOT:PSS and tellurium-PEDOT:PSS hybrid composites by simple chemical treatment. *Scientific Reports*, 6(1):18805–18815, 2016.

[311] Sung Hyun Kim. Control of the charge carrier concentration and hall mobility in PEDOT:PSS thermoelectric films: Control of the charge carrier concentration and hall mobility in PEDOT:PSS thermoelectric films. *Bulletin of the Korean Chemical Society*, 38(12):1460–1464, 2017.

[312] Hui Shi, Congcong Liu, Qinglin Jiang, and Jingkun Xu. Effective approaches to improve the electrical conductivity of PEDOT:PSS: A review. *Advanced Electronic Materials*, 1(4):1500017–1500033, 2015.

[313] Jian Zhou, Tadashi Fukawa, and Mutsumi Kimura. Directional electromechanical properties of PEDOT/PSS films containing aligned electrospun nanofibers. *Polymer Journal*, 43(10):849–854, 2011.

[314] Desalegn Alemu, Hung-Yu Wei, Kuo-Chuan Ho, and Chih-Wei Chu. Highly conductive PEDOT:PSS electrode by simple film treatment with methanol for ITO-free polymer solar cells. *Energy & Environmental Science*, 5(11):9662–9672, 2012.

[315] Tsu-Ruey Chou, Szu-Hua Chen, Yen-Te Chiang, Yi-Ting Lin, and Chih-Yu Chao. Highly conductive PEDOT:PSS films by post-treatment with dimethyl sulfoxide for ITO-free liquid crystal display. *Journal of Materials Chemistry C*, 3(15):3760–3766, 2015.

[316] Qingduan Li, Jianwei Yang, Shuangshuang Chen, Jizhao Zou, Weiguang Xie, and Xierong Zeng. Highly conductive PEDOT:PSS transparent hole transporting layer with solvent treatment for high performance silicon/organic hybrid solar cells. *Nanoscale Research Letters*, 12(1):506–514, 2017.

[317] Jian Zhou, Tadashi Fukawa, Hirofusa Shirai, and Mutsumi Kimura. Anisotropic motion of electroactive papers coated with PEDOT/PSS. *Macromolecular Materials and Engineering*, 295(7):671–675, 2010.

[318] Jian Zhou, Tadashi Fukawa, and Mutsumi Kimura. Directional electromechanical properties of PEDOT/PSS films containing aligned electrospun nanofibers. *Polymer Journal*, 43(10):849–854, 2011.

[319] Jian Zhou and Mutsumi Kimura. Electromechanical actuation of highly conductive PEDOT/PSS-coated cellulose papers. *Sen'i Gakkaishi*, 67(6):125–131, 2011.

[320] Kun Zhang, Jingjing Qiu, and Shiren Wang. Thermoelectric properties of PEDOT nanowire/PEDOT hybrids. *Nanoscale*, 8(15):8033–8041, 2016.

[321] Syang-Peng Rwei, Yi-Huan Lee, Jia-Wei Shiu, Ragu Sasikumar, and Uin-Ting Shyr. Characterization of solvent-treated PEDOT:PSS thin films with enhanced conductivities. *Polymers*, 11(1):134–144, 2019.

[322] Paramita Kar Choudhury, Debjani Bagchi, C. S. Suchand Sangeeth, and Reghu Menon. Modified conformation and physical properties in conducting polymers due to varying conjugation and solvent interactions. *Journal of Material Chemistry*, 21(5):1607–1614, 2011.

[323] Scott T. Huxtable, David G. Cahill, Sergei Shenogin, Liping Xue, Rahmi Ozisik, Paul Barone, Monica Usrey, Michael S. Strano, Giles Siddons, Moonsub Shim, and Pawel Keblinski. Interfacial heat flow in carbon nanotube suspensions. *Nature Materials*, 2(11):731–734, 2003.

[324] Ce-Wen Nan, Gang Liu, Yuanhua Lin, and Ming Li. Interface effect on thermal conductivity of carbon nanotube composites. *Applied Physics Letters*, 85(16):3549–3551, 2004.

[325] Madan Singh, Kopang Khotso Hlabana, Sanjay Singhal, and Kamal Devlal. Grain-size effects on the thermal conductivity of nanosolids. *Journal of Taibah University for Science*, 10(3):375–380, 2016.

[326] Haijun Song, Qiufeng Meng, Yao Lu, and Kefeng Cai. Progress on PEDOT:PSS/nanocrystal thermoelectric composites. *Advanced Electronic Materials*, 5(11):1800822–1800840, 2019.

[327] Biplab Paul, Ajay Kumar V, and P. Banerji. Embedded ag-rich nanodots in PbTe: Enhancement of thermoelectric properties through energy filtering of the carriers. *Journal of Applied Physics*, 108(6):064322–064328, 2010.

[328] Haijun Song and Kefeng Cai. Preparation and properties of PEDOT:PSS/Te nanorod composite films for flexible thermoelectric power generator. *Energy*, 125(1):519–525, 2017.

[329] Jaeyoo Choi, Jang Yeol Lee, Sang-Soo Lee, Chong Rae Park, and Heesuk Kim. High-performance thermoelectric paper based on double carrier-filtering processes at nanowire heterojunctions. *Advanced Energy Materials*, 6(9):1502181–1502189, 2016.

[330] Haijun Song, Qiufeng Meng, Yao Lu, and Kefeng Cai. Progress on PEDOT:PSS/nanocrystal thermoelectric composites. *Advanced Electronic Materials*, 5(11):1800822–1800840, 2019.

[331] Hao He and Jianyong Ouyang. Enhancements in the mechanical stretchability and thermoelectric properties of PEDOT:PSS for flexible electronics applications. *Accounts of Materials Research*, 1(2):146–157, 2020.

[332] Fei Peng Du, Nan-Nan Cao, Yun-Fei Zhang, Ping Fu, Yan-Guang Wu, Zhi-Dong Lin, Run Shi, Abbas Amini, and Chun Cheng. PEDOT:PSS/graphene quantum dots films with enhanced thermoelectric properties via strong interfacial interaction and phase separation. *Scientific Reports*, 8(1):6441–6453, 2018.

[333] Zeng Fan, Pengcheng Li, Donghe Du, and Jianyong Ouyang. Significantly enhanced thermoelectric properties of PEDOT:PSS films through sequential post-treatments with common acids and bases. *Advanced Energy Materials*, 7(8):1602116–1602124, 2017.

[334] Shinsaku Uemura. Ionic contribution to the complex dielectric constant of a polymer under dc bias. *Journal of Polymer Science Part A-2: Polymer Physics*, 10(11):2155–2166, 1972.

[335] Shinsaku Uemura. Low-frequency dielectric behavior of poly(vinylidene fluoride). *Journal of Polymer Science: Polymer Physics Edition*, 12(6):1177–1188, 1974.

[336] Bhupendra Pratap Singh, Samiksha Sikarwar, Kamal Kumar Pandey, Rajiv Manohar, Michael Depriester, and Dharmendra Pratap Singh. Carbon nanotubes blended nematic liquid crystal for display and electro-optical applications. *Electronic Materials*, 2(4):466–481, 2021.

[337] Neophytos Neophytou, Xanthippi Zianni, Hans Kosina, Stefano Frabboni, Bruno Lorenzi, and Dario Narducci. Simultaneous increase in electrical conductivity and Seebeck coefficient in highly boron-doped nanocrystalline Si. *Nanotechnology*, 24(20):205402–205414, 2013.

[338] Yue Lin, Maxwell Wood, Kazuki Imasato, Jimmy Jiahong Kuo, David Lam, Anna N. Mortazavi, Tyler J. Slade, Stephen A. Hodge, Kai Xi, Mercouri G. Kanatzidis, David R. Clarke, Mark C. Hersam, and G. Jeffrey Snyder. Expression of interfacial Seebeck coefficient through grain boundary engineering with multi-layer graphene nanoplatelets. *Energy & Environmental Science*, 13(11):4114–4121, 2020.

[339] Zaifang Li, Ying Liang, Zhicheng Zhong, Jingyu Qian, Guijie Liang, Kun Zhao, Haixin Shi, Shuming Zhong, Yanzhen Yin, and Wenjing Tian. A low-work-function, high-conductivity PEDOT:PSS electrode for organic solar cells with a simple structure. *Synthetic Metals*, 210(1):363–366, 2015.

[340] Joon Seok Lee, Kyeong Hwan You, and Chan Beum Park. Highly photoactive, low bandgap TiO_2 nanoparticles wrapped by graphene. *Advanced Materials*, 24(8):1084–1088, 2012.

[341] Kongli Xu, Guangming Chen, and Dong Qiu. Convenient construction of poly(3,4-ethylenedioxythiophene)–graphene pie-like structure with enhanced thermoelectric performance. *Journal of Materials Chemistry A*, 1(40):12395–12402, 2013.

[342] Chuizhou Meng, Changhong Liu, and Shoushan Fan. A promising approach to enhanced thermoelectric properties using carbon nanotube networks. *Advanced Materials*, 22(4):535–539, 2010.

[343] Ahmed Gamal El-Shamy. New free-standing and flexible PVA/carbon quantum dots (CQDs) nanocomposite films with promising power factor and thermoelectric power applications. *Materials Science in Semiconductor Processing*, 100(1):245–254, 2019.

[344] Jingjin Dong, Dominic Gerlach, Panagiotis Koutsogiannis, Petra Rudolf, and Giuseppe Portale. Boosting the thermoelectric properties of PEDOT:PSS via low-impact deposition of tin oxide nanoparticles. *Advanced Electronic Materials*, 7(5):2001284–2001292, 2021.

[345] Rama Venkatasubramanian, Edward Siivola, Thomas Colpitts, and Brooks O'Quinn. Thin-film thermoelectric devices with high room-temperature figures of merit. *Nature*, 413(1):6–12, 2001.

[346] Qin Yao, Qun Wang, Liming Wang, and Lidong Chen. Abnormally enhanced thermoelectric transport properties of SWNT/PANI hybrid films by the strengthened PANI molecular ordering. *Energy Environmental Science*, 7(11):3801–3807, 2014.

[347] F. Zabihi, Y. Xie, S. Gao, and M. Eslamian. Morphology, conductivity, and wetting characteristics of PEDOT:PSS thin films deposited by spin and spray coating. *Applied Surface Science*, 338(1):163–177, 2015.

[348] Ozlem Yagci, Serco Serkis Yesilkaya, Süreyya Aydin Yüksel, Fatih Ongül, Nurhan Mehmet Varal, Mahmut Kus, Serap Günes, and Orhan Icelli. Effect of boric acid doped PEDOT:PSS layer on the performance of P3HT:PCBM based organic solar cells. *Synthetic Metals*, 212(1):12–18, 2016.

[349] Anusit Keawprajak, Wantana Koetniyom, Phimwipha Piyakulawat, Kanpitcha Jiramitmongkon, Sirapat Pratontep, and Udom Asawapirom. Effects of tetramethylene sulfone solvent additives on conductivity of PEDOT:PSS film and performance of polymer photovoltaic cells. *Organic Electronics*, 14(1):402–410, 2013.

[350] Zhengyou Zhu, Congcong Liu, Fengxing Jiang, Jingkun Xu, and Endou Liu. Effective treatment methods on PEDOT:PSS to enhance its thermoelectric performance. *Synthetic Metals*, 225(1):31–40, 2017.

[351] Sesha Vempati, Yelda Ertas, Asli Celebioglu, and Tamer Uyar. Tuning the degree of oxidation and electron delocalization of poly(3,4-ethylenedioxythiophene): poly(styrenesulfonate) with solid-electrolyte. *Applied Surface Science*, 419(1):770–777, 2017.

[352] Tatsuhiro Horii, Yuechen Li, Yusaku Mori, and Hidenori Okuzaki. Correlation between the hierarchical structure and electrical conductivity of PEDOT/PSS. *Polymer Journal*, 47(10):695–699, 2015.

[353] Hidenori Okuzaki, Yuko Harashina, and Hu Yan. Highly conductive PEDOT/PSS microfibers fabricated by wet-spinning and dip-treatment in ethylene glycol. *European Polymer Journal*, 45(1):256–261, 2009.

[354] Poonam Benjwal, Manish Kumar, Pankaj Chamoli, and Kamal K. Kar. Enhanced photocatalytic degradation of methylene blue and adsorption of arsenic(III) by reduced graphene oxide (rGO)–metal oxide

(TiO_2/Fe_3O_4) based nanocomposites. *The Royal Society of Chemistry Advances*, 5(89):73249–73260, 2022.

[355] Xiangxin Xue, Wei Ji, Zhu Mao, Huijuan Mao, Yue Wang, Xu Wang, Weidong Ruan, Bing Zhao, and John R. Lombardi. Raman investigation of nanosized TiO_2 : Effect of crystallite size and quantum confinement. *The Journal of Physical Chemistry C*, 116(15):8792–8797, 2012.

[356] Libin Yang, Xin Jiang, Weidong Ruan, Bing Zhao, Weiqing Xu, and John R. Lombardi. Observation of enhanced raman scattering for molecules adsorbed on TiO_2 nanoparticles: Charge-transfer contribution. *The Journal of Physical Chemistry C*, 112(50):20095–20098, 2008.

[357] Pilarisetty Tarakeshwar, Daniel Finkelstein-Shapiro, Tijana Rajh, and Vladimiro Mujica. Quantum confinement effects on the surface enhanced raman spectra of hybrid systems molecule-TiO $_2$ nanoparticles: Quantum confinement effects on surface enhanced raman spectra. *International Journal of Quantum Chemistry*, 111(7):1659–1670, 2011.

[358] Yijie Xia, Kuan Sun, and Jianyong Ouyang. Highly conductive poly(3,4-ethylenedioxythiophene):poly(styrene sulfonate) films treated with an amphiphilic fluoro compound as the transparent electrode of polymer solar cells. *Energy Environmental Science*, 5(1):5325–5332, 2012.

[359] Sateesh Prathapani, Venumadhav More, Siva Bohm, Parag Bhargava, Aswani Yella, and Sudhanshu Mallick. TiO_2 colloid-based compact layers for hybrid lead halide perovskite solar cells. *Applied Materials Today*, 7(1):112–119, 2017.

[360] Lijie Zhu, Qipeng Lu, Longfeng Lv, Yue Wang, Yufeng Hu, Zhenbo Deng, Zhidong Lou, Yanbing Hou, and Feng Teng. Ligand-free rutile and anatase

TiO_2 nanocrystals as electron extraction layers for high performance inverted polymer solar cells. *The Royal Society of Chemistry Advances*, 7(33):20084–20092, 2017.

[361] Omar Ricardo Fonseca-Cervantes, Alejandro Pérez-Larios, Víctor Hugo Romero Arellano, Belkis Sulbaran-Rangel, and Carlos Alberto Guzmán González. Effects in band gap for photocatalysis in TiO_2 support by adding gold and ruthenium. *Processes*, 8(9):1032–1047, 2020.

[362] Xinkai Wu, Lu Lian, Shuai Yang, and Gufeng He. Highly conductive PEDOT:PSS and graphene oxide hybrid film from a dipping treatment with hydroiodic acid for organic light emitting diodes. *Journal of Materials Chemistry C*, 4(36):8528–8534, 2016.

[363] Goutham P Raj, Sandhya V Rani, Anil Kanwat, and Jin Jang. Enhanced organic photovoltaic properties via structural modifications in PEDOT:PSS due to graphene oxide doping. *Materials Research Bulletin*, 74(1):346–352, 2016.

[364] Taehyung Kim, Kwang-Hee Kim, Sungwoo Kim, Seon-Myeong Choi, Hyosook Jang, Hong-Kyu Seo, Heejae Lee, Dae-Young Chung, and Eunjoo Jang. Efficient and stable blue quantum dot light-emitting diode. *Nature*, 586(7829):385–389, 2020.

[365] Shasha Wei, Yichuan Zhang, Haicai Lv, Liang Deng, and Guangming Chen. SWCNT network evolution of PEDOT:PSS/SWCNT composites for thermoelectric application. *Chemical Engineering Journal*, 428:131137–131144, 2022.

Amélioration des performances de matériaux thermoélectriques organiques : nouvelle approche basée sur l'utilisation de quantum dots

Mots clés : Nanocomposite polymère, points quantiques, thermoélectricité

Résumé : Le polymère poly(3,4-éthylène dioxythiophène):polystyrène sulfonate (PEDOT:PSS) a été largement étudié en raison de son excellente conductivité électrique. Cependant, jusqu'à présent, il n'y a eu que quelques études sur les polymères contenant des points quantiques pour des applications thermoélectriques (TE). L'étude actuelle décrit une nouvelle méthode pour améliorer les propriétés TE du polymère PEDOT:PSS en utilisant de l'oxyde de graphène décoré de points quantiques de dioxyde de titane (TQDGO). La conductivité électrique, la conductivité thermique et le coefficient Seebeck ont été mesurés pour étudier les propriétés TE. En outre, leurs performances dans les films minces ont été comparées à celles des pastilles en vrac, et il a été constaté que les films minces permettaient de meilleures performances TE que leurs homologues en vrac. Un facteur de puissance maximal de $91.26\,\mu W m^{-1} K^{-2}$ a été atteint en utilisant un film mince TQDGO/PEDOT: PSS à 2 % en poids.

Organic thermoelectric materials: A novel approach to improve performances using quantum dots

Keywords: Polymer nanocomposite, Quantum dots, Thermoelectricity

Abstract: The polymer poly(3,4-ethylene dioxythiophene):polystyrene sulfonate (PEDOT:PSS) has been widely studied because of its excellent electrical conductivity. However, so far there have been only a few studies of polymers containing quantum dots for thermoelectric (TE) applications. The current study describes a new method to improve the TE properties of the PEDOT:PSS polymer using graphene oxide decorated with titanium dioxide quantum dots (TQDGO). Electrical conductivity, thermal conductivity and Seebeck coefficient were measured to study TE properties. Also, their performance in thin films was compared to that of bulk pellets, and thin films were found to provide better TE performance than their bulk counterparts. A maximum power factor of $91.26\ \mu W m^{-1} K^{-2}$ was achieved using a 2 wt% TQDGO/PEDOT: PSS thin film.